ESCUELA POLITÉCNICA SUPERIOR

DEPARTAMENTO DE TEORÍA DE LA SEÑAL Y COMUNICACIONES

Ph. D. Thesis

EXPERIMENTAL CHARACTERIZATION OF THE AIR DECONTAMINATION SYSTEM COUNTERFOG®

Author:

Francisco José Llerena Aguilar

Supervisor:

José Luis Pérez Díaz, Ph. D.

Oct 2019

Abstract

There are numerous health risks to which we are exposed in our environment, and the damage caused by some of them is particularly serious. This is the case with air pollution in major urban centres. There are many episodes in which high levels of air pollution had serious consequences for the population of large cities, causing numerous deaths and countless cases of hospitalization and intoxication.

On the other hand, the use of chemical, biological, radiological and nuclear (CBRN) agents as weapons by terrorist groups with the aim of harming the civilian population represents one of the greatest threats to countries, acquiring a defensive importance of the first order.

Counterfog® is a project created and directed by Prof. Dr. José Luis Pérez Díaz. It is a completely new system designed to give a quick response to all types of dispersed agents: from chemical agents to Diesel particles. The system has been developed mainly to remove CBRN agents from the air in the event of a terrorist attack or accidental release. However, it can also be applied to remove particulate pollutants responsible for respiratory diseases in highly polluted cities. Airborne agents less than 10 μm in diameter are particularly dangerous, as they can penetrate our respiratory system and even reach the bloodstream. The need to remove these pollutants from the air to save lives is the motivation behind the Counterfog® project, which seeks to ensure the safety of people and living things both indoors and outdoors, regardless of the origin of the pollutants.

The work carried out on this thesis consisted in the experimental characterization of the fog generated by the Counterfog® system and its effectiveness in laboratory conditions for the decontamination or removal of suspended particles and CBRN agents indoors.

In the first part of this work, an introduction is made to the different harmful agents that this new system seeks to address: suspended particles and chemical, biological, radiological and nuclear agents. A state of the art on fogs is presented below. Finally, an in-depth description is given of the test laboratory where the experimental work has been carried out and the different materials and equipment used for this purpose.

In the second part, the decontamination tests performed in the laboratory are described and the results obtained are presented. In particular, the following are described: characterization of the fog generated by Counterfog® nozzles, fog dynamics, decontamination tests of particles in suspension resulting from the combustion of Diesel, decontamination tests of biological agents and decontamination tests of chemical agents.

The results obtained in this work are highly promising, as they corroborate the high efficiency of the system developed in interior spaces for all the scenarios proposed. Therefore, this system offers an immense range of real-life application possibilities.

Resumen

Existen numerosos riesgos para la salud a los que estamos expuestos en nuestro entorno, y los daños causados por algunos de ellos son especialmente graves. Es el caso de la contaminación del aire de los grandes centros urbanos. Son numerosos los episodios en los que los altos niveles de contaminación atmosférica tuvieron graves consecuencias para la población de las grandes ciudades, causando numerosas muertes e innumerables casos de hospitalización e intoxicación.

Por otra parte, el uso de agentes químicos, biológicos, radiológicos y nucleares (QBRN) como armas por parte de grupos terroristas con el objetivo de causar daño a la población civil representa una de las mayores amenazas para los países, adquiriendo una importancia defensiva de primer orden.

Counterfog® es un proyecto creado y dirigido por el Prof. Dr. José Luis Pérez Díaz. Se trata de un sistema totalmente novedoso diseñado para dar una respuesta rápida a todo tipo de agentes dispersos: desde agentes químicos hasta partículas de Diésel. El sistema ha sido desarrollado principalmente para retirar del aire a los agentes QBRN en caso de ataque terrorista o liberación accidental. Sin embargo, también puede aplicarse para eliminar las partículas contaminantes responsables de las enfermedades respiratorias en ciudades altamente contaminadas. Los agentes aerotransportados de menos de 10 μm de diámetro son particularmente peligrosos, ya que pueden penetrar nuestro sistema respiratorio e incluso llegar al torrente sanguíneo. La necesidad de eliminar estos contaminantes del aire para salvar vidas es la motivación del proyecto Counterfog® que busca garantizar la seguridad de las personas y los seres vivos tanto en ambientes interiores como exteriores, independientemente del origen de los contaminantes.

El trabajo realizado en esta tesis ha consistido en la caracterización experimental de la niebla generada por el sistema Counterfog® y su eficacia en condiciones de laboratorio para la descontaminación o eliminación de partículas en suspensión y agentes QBRN en interiores.

En la primera parte de este trabajo, se lleva a cabo una introducción a los diferentes agentes nocivos a los que este nuevo sistema busca hacer frente: partículas en suspensión

y agentes químicos, biológicos, radiológicos y nucleares. A continuación, se presenta un estado del arte sobre nieblas. Finalmente, se describe en profundidad el laboratorio de ensayos donde se han desarrollado los trabajos experimentales y los diferentes materiales y equipamientos utilizados para ello.

En la segunda parte, se describen los ensayos de descontaminación realizados en laboratorio y se exponen los resultados obtenidos. En particular, se describirán los siguientes: caracterización de la niebla generada por las boquillas Counterfog®, dinámica de la niebla, ensayos de descontaminación de partículas en suspensión resultantes de la combustión del Diésel, ensayos de descontaminación de agentes biológicos y ensayos de descontaminación de agentes químicos.

Los resultados obtenidos en este trabajo son altamente prometedores, pues corroboran la elevada eficacia del sistema desarrollado en espacios interiores para todos los escenarios planteados. Por tanto, este sistema ofrece una inmensa gama de posibilidades de aplicación en la vida real.

A mi familia, que lo sois todo para mí.

"No se gloríe el sabio en su sabiduría, ni se gloríe el fuerte en su fortaleza, ni se gloríe el rico en su riqueza, sino que el que se gloría gloríese de esto: comprender y conocer que yo soy el Señor, que hago misericordia, juicio y justicia sobre la tierra, porque en eso está, mi voluntad, dice el Señor"

Jr 9,22-23

Agradecimientos

A José Luis Pérez Díaz, mi director de tesis. La persona que me ha guiado durante todo este camino. Son ya cinco años los que nos unen. No he parado de aprender ni un segundo que he estado a tu lado. Agradezco mucho la confianza y el esfuerzo puestos en mí. Gracias por darme esta oportunidad.

Gracias al equipo de la facultad de farmacia: Jorge, Giovanni, José Luis y José María. Habéis sido una parte muy importante de este trabajo.

A Elisa, por ayudarme con el análisis de datos abriéndome las puertas de sus instalaciones.

Gracias al equipo del CIEMAT: Javier y Marta. Por vuestra ayuda y por vuestro tiempo.

Gracias a Tania, José y Miguel. Hubiera sido imposible dar con mejores compañeros de trabajo. Tanto es así que, de grandes compañeros, habéis pasado a ser grandes amigos.

A mi familia: los cimientos que me mantienen en pie. A mis padres, mis referemtes. Gracias por toda una vida de sacrificio para hacernos felices. A mis hermanos: siempre ayudándonos, siempre apoyándonos, siempre juntos. A la alegría de la casa, a mi sobrino Mario. Parece imposible pensar que hasta hace un añito no estabas aún en nuestras vidas. Gracias por traer alegría e ilusión a nuestra casa. A mi pareja, por estar a mi lado y ser un apoyo imprescindible en mi vida. A mis cuñados, por vuestros ánimos y por hacer de esta familia, una familia mejor.

A mis amigos, por estar a mi lado siempre que os he necesitado.

Quisiera dar las gracias a todas y cada una del resto de personas que me habéis ayudado a llegar aquí. Sois tantas, que sería imposible nombraros a todas en tan estas pocas líneas. Por ello, y de todo corazón, muchas gracias.

La investigación que ha dado lugar a estos resultados ha recibido financiación del Séptimo Programa Marco de la Unión Europea (7PM/2007-2013) en virtud del Acuerdo de subvención nº 312804.

Francisco

General Index

Index of Figures

Index of Tables

Chapter 1

Introduction

1.1 Motivation of the study

The use of chemical, biological, radiological and nuclear (CBRN) agents as weapons by terrorist groups with the aim of inflicting harm on the civilian population represents one of the greatest threats to countries, acquiring first-rate defensive importance [Bennett, 2007]. Many serious episodes of severe environmental pollution [Bradley et al., 1958]and the enormous problem currently posed by air pollution in urban centres result in the expulsion of air pollutants into the atmosphere.

The need to remove these pollutants from the air to save lives is the motivation of the Counterfog® project.. tCounterfog® seeks to ensure safety of people and living beings in both indoor and outdoor environments irrespectively of the origin of the pollutants.

In addition, it has been intended to go one step further, developing a system whose application is completely innocuous to people and other living beings, allowing its application in all kinds of situations.

The present study aims to experimentally characterize the fog generated by Counterfog® and their effectiveness in laboratory conditions.

1.2 Counterfog® Project (Device for large scale decontamination)

Counterfog® is a project (Figure 1) created and directed by Prof. Dr. José Luis Pérez Díaz. This is a completely novel system designed to provide a rapid response to all types of dispersed agents: from chemical agents to diesel particles. The system has been developed primarily to remove CBRN agents from air in the event of a terrorist attack or accidental release. However, it can be also applied to remove particulate pollutants responsible for respiratory diseases in highly contaminated cities. Airborne agents less than 10 μm in diameter are particularly dangerous, as they can penetrate our respiratory system and even reach the bloodstream. The research leading to these results has received funding from the European Union Seventh Framework Programme (FP7/2007-2013) under Grant Agreement n° 312804.

Figure 1: Counterfog® Project Logotype.

The main objective of Counterfog® is to design, build and test a rapid response system for collapsing all kinds of dispersed agents (smoke, fog, etc.) by using a fog made of a solution that could eventually also contain some kind of neutralizing component. Not only must it be suitable to be "incorporated" into a fog fire protection system in buildings, but it must also be able to be used in outdoor conditions. Its goal is to provide a very quick and early response. It therefore directly addresses the objective of Topic SEC-2012.4.4-2: "*This project will make available new or improved technology able to decontaminate public areas (e.g. subway stations, railway stations, etc.) and critical infrastructures (e.g. command centres, hospitals, airports, local authorities) in a more efficient way*".

In order to achieve this goal, several specific objectives have been achieved:

- To design and build a prototype nozzle capable of the performances required for Counterfog®.
- To design, build and prepare a laboratory for experimental study of fog dynamics and the effects of the Counterfog® nozzle under different conditions.
- To determine the best solution and products for decontamination –of surrogates- and determine the fog dynamics in laboratory conditions.
- To design and build a portable on a truck prototype

- To install a fixed Counterfog® in a real large building and to test the fog dynamics produced by it.
- To test the dynamics of fog in an outdoor environment with the portable on-truck prototype

Therefore, the main objective is to provide a system or device to physically collapse any dispersed product. Another key goal of this project is the development of a device that measures the degree of neutralization, or how the cleaning process progresses at a given time.

Counterfog® consists of a unique and patented nozzle (E.U. Patent No. EP17382293.3/22.05.17) and a particular set of settings to be able to produce the proper drop size using very limited and simple inputs (energy for pneumatic pressure and water). It can be applied in crisis (both in counter attacks or in pollution crisis) or for prevention within pollution control protocols .This system uses small droplets of liquid of the right size. Additionally, water droplets of the exact size can also be used to effectively hydrolyze gases in the atmosphere. This system has been demonstrated in a laboratory with surrogates and simulants through various decontamination tests. In addition, other chemical elements such as disinfectants can be added to water droplets to improve decontamination results.

The installation of this system consists of deploying a set of nozzles in critical infrastructures, equipped with something as simple as water and compressed air line. The required pressure will not be as high as other fog fire protection systems. In addition, it can also be used in the open field to combat diesel pollution in large areas.

Counterfog® is simple, economical and environmentally friendly. It essentially uses a jet of micron-sized water fog specifically optimized to decontaminate air removing all kind of noxious airborne particles including spores or radioactive particles.

1.3 Air pollutants

1.3.1 Environmental risks

There are quite a few health hazards to which we are exposed in our environment, with damage caused by some of them being particularly serious. This is the case of pollution in the air of large urban centres with several episodes of the last century in which high levels of air pollution had serious consequences for the population of large cities, causing numerous deaths and countless cases of hospitalization and intoxication [Bell and Davis, 2001; Nemery and Nemmar, 2001; EEA, 2012]. These events led to the creation and implementation of legislation to reduce air pollution emission levels. These actions have led to a considerable reduction in the concentration levels reached, but this is not the end of the problem since several epidemiological studies [Pope, 2000; Thatcher and Layton, 1995; Zhou and Cheng, 2005] and computational modeling [Rostami, 2009] have been carried out since then and their results show how air pollution as a result of combustion sources is highly harmful, even when found in low concentrations [WHO, 2002; Sexton, Spengler and Treitman, 1984]. It is remarkable the important relationship between environmental air pollution and cancer deaths [IARC, 2013]. This problem is particularly acute in developding regions, such as Asia, Africa and Ibero America [Cao et al., 2012],

where legislation is more relaxed or at least more recent. Figure 2 shows some of the environmental factors most at risk:

Risk factor	Theoretical minimum exposure	Measured adverse outcomes of exposure
Unsafe water, sanitation and hygiene	Absence of transmission of diarrhoeal disease through water, sanitation and hygiene practices	Diarrhoea
Urban air pollution	7.5 μg/m^3 for $PM_{2.5}$	Cardiovascular mortality, respiratory mortality, lung cancer, mortality from acute respiratory infections in children
Indoor smoke from solid fuels	No solid fuel use	Acute respiratory infections in children, chronic obstructive pulmonary disease, lung cancer
Lead exposure	0.016 μg/dl blood lead levels	Cardiovascular disease, mild mental retardation
Climate change	1961–1990 concentrations	Diarrhoea, flood injury, malaria, malnutrition

Figure 2: Selected major risks to health: environmental factors [WHO 2002]

On the other hand, it should be borne in mind that although the greatest exposure of people to air pollution occurs in outdoor spaces, part of it occurs in indoor spaces [Ezzati and Kammen, 2002]. This pollution comes mainly from the combustion of solid fuels such as coal, firewood, animal excrement, etc. It should be remembered that about 50% of the world's population still cooks with this type of fuel [WHO, 2002].

1.3.2 Classification of air pollutants

Air pollutants can be classified in different ways: by source of origin, particle size, chemical composition and form of emission to the environment. Figure 3 shows a comparison of several of these forms of classification:

A. Primary-secondary pollutants
  (i) Primary: pollutants emitted directly into the atmosphere (eg, SO_2, some NO_x species, CO, PM)
  (ii) Secondary: pollutants that form in the air as a result of chemical reactions with other pollutants and gases (eg, ozone, NO_x, and some particulates)
B. Indoor-outdoor pollutants
  (i) Indoor pollutants
    (a) Sources: cooking and combustion, particle resuspension, building materials, air conditioning, consumer products, smoking, heating, biologic agents
    (b) Products: Combustion products (eg, tobacco and wood smoke), CO, CO_2, SVOC (eg, aldehydes, alcohols, alkanes, and ketones), microbial agents and organic dusts, radon, manmade vitreous fibers
  (ii) Outdoor pollutants
    (a) Sources: industrial, commercial, mobile, urban, regional, agricultural, natural
    (b) Products: SO_2, ozone, NO_x, CO, PM, SVOC
C. Gaseous-particulate pollutants
  (i) Gaseous: SO_2, NO_x, ozone, CO, SVOC (eg, PAH, dioxins, benzene, aldehydes, 1,3-butadiene)
  (ii) Particulate: coarse PM (2.5-10 μm; regulatory standard = PM_{10}), fine PM (0.1-2.5 μm; regulatory standard = $PM_{2.5}$); ultrafine PM (<0.1 μm; not regulated)

NO_x, Nitrogen oxides; *SVOC*, specific volatile organic compounds.

Figure 3: Classification of air pollutants [Bernstein, 2004].

Primary pollutants are defined as those emitted directly into the atmosphere by physical or chemical processes from a specific emission source. These sources can be very varied and range from the industrial sector, such as blast furnaces or gravel crushing, to natural sources, such as forest fires or ocean aerosols [Watson, Chow and Pace, 2000]. On the other hand, pollutants formed by chemical reactions that occur in the atmosphere are called secondary pollutants. These reactions can take place in the gas phase or may occur between gases and particles that already exist. These secondary particles are one of the major sources of Aitken nuclei [Went, 1966], responsible for most of the condensation processes that occur in the atmosphere, as well as one of the main components of urban smog [Fennelly, 1975].

In turn, because the proportion of average time people spend in enclosed spaces is very high (> 80%), outdoor-indoor classification has become very important. The increase in several studies on the exposure of people to pollutants found in indoor spaces has provided an important data set. [Myers and Maynard, 2005].

For suspended particulate pollutants, which are called particulate matter (PM), their classification is a function of their aerodynamic diameter. In this way, three differentiated groups are defined: coarse PM, fine PM and ultrafine PM. Coarse particulate matter ($PM_{10-2.5}$) has an aerodynamic diameter between 2.5 and 10 μm and originates from eroded soil, construction debris, road dust or the aggregation of smaller combustion particles. Fine particulate matter ($PM_{2.5}$) has an aerodynamic diameter up to 2.5 μm while ultrafine particulate matter ($PM_{0.1}$) has an aerodynamic diameter of 0.1 μm or less and both have as their main source the combustion of fossil fuels [Wilson and Suh, 1997; Bernstein, 2004].

Finally, we have the gaseous pollutants. Their main origin is in the combustion of fossil fuels and they have an important influence on the variation of the composition of the atmosphere. Some of the most important gaseous components are nitrogen oxides, ozone, carbon monoxide, sulphur dioxide and volatile organic compounds (VOCs). Nitrogen oxide is emitted into the atmosphere as NO and reacts with ozone and free radicals to produce NO_2. Ozone is produced in the lower layers of the atmosphere as a result of the reaction between NO_2 and volatile organic compounds. CO is the result of incomplete combustion while SO_2 comes from anthropogenic and natural sources, with sulphur fossil fuel combustion being the main anthropogenic source and volcanoes and oceans being the main natural sources. [Kampa and Castanas, 2007].

1.3.3 Human health effects of air pollution

The following is a summary of the harmful effects of air pollutants. They affect different organs and systems: respiratory system, cardiovascular system, nervous system, urinary system, digestive system. Exposed foetuses can also be affected during pregnancy [Kampa and Castanas, 2008; Nel, 2005]. Figure 4 shows the possible mechanisms of harmful health effects associated with pollutants:

1. PM- or ozone-induced pulmonary inflammation
2. Free radical and oxidative stress generation by transition metals and organic chemical compounds (eg, PAH)
3. Covalent modification of key intracellular proteins (eg, enzymes)
4. Biologic compounds, such as endotoxin and glucans, which induce inflammation and innate immune effects
5. Stimulation of nocioreceptor and autonomic nervous system activity, which regulates heart rate variability and airway reactivity
6. Adjuvant effects in the immune system (eg, DEPs and transition metals enhancing responses to common environmental allergens)
7. Procoagulant activity by ultrafine particles after access to the systemic circulation
8. Suppression of normal defense mechanisms (eg, suppression of alveolar macrophage functions)

PAH, Polyaromatic hydrocarbons.

Figure 4: Possible mechanisms of pollutant-associated adverse health effects [Bernstein, 2004].

Due to the enormous complexity of the study of the mixtures of the different atmospheric pollutants, since their study is only in its infancy, this section will be focused on the study of particles and gases that, according to the current criteria, are the most important air pollutants:

- **PARTICULATE MATTER (PM)**

  Mixture of environmental particles of different physical and chemical characteristics. In terms of the most important characteristics, size, surface area and number are the main physical characteristics, while the most important chemical characteristics are the content of transition metals, polycyclic aromatic hydrocarbons, material of the earth's crust, sulphates, nitrates and hydrocarbons. The indicator traditionally used in Europe is Black Smoke (BS) [Quincey, 2007], but the PM_{10} indicator of the Environmental Protection Agency (EPA) is very common as an environmental particulate indicator for regulatory purposes. The $PM_{2.5}$ indicator [Cao et al., 2013] was subsequently also defined. Figure 5 shows the source of $PM_{2.5}$ emissions in the European Union (EU) in 2014 by sectors:

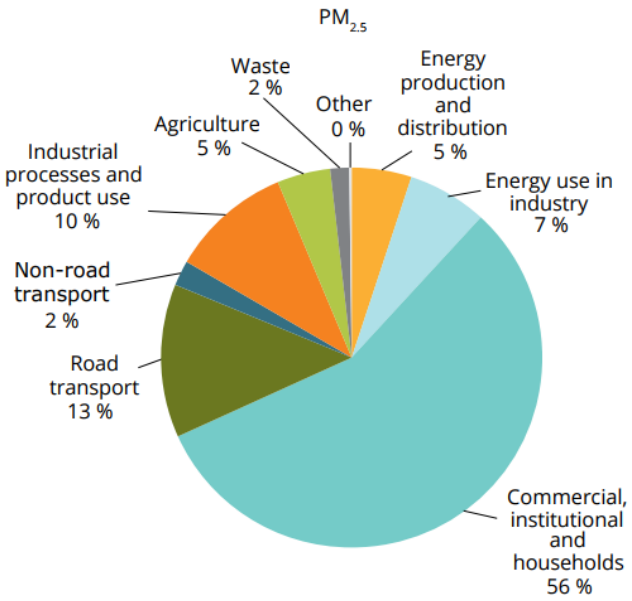

Figure 5: Emissions in the EU-28: share by sector group in 2014 [EEA, 2016].

Fossil fuel combustion particles are generally smaller than those produced by abrasion that tend to be larger in size [Committee of the Environmental and Occupational Health Assembly of the American Thoracic Society, 1996]. Although the regulations were initially based on mass per unit volume of particulate matter, it is now known how the number and surface area of particles have a greater impact on health [Künzli et al., 2000]. As for its formation, it is necessary to differentiate between primary and secondary particles. The former are emitted directly into the environment while the latter are formed in the atmosphere: sulphates, nitrates, etc. [Katsouyanni, 2003].

- **Short-term effects:** Air Pollution and Health: a European Approach (APHEA) [APHEIS, 2004] provides studies based on 29 cities where the percentage of daily deaths due to this cause is estimated to be between 0.6% and 1.5% of the total [Katsouyanni et al., 2001] and hospital and asthma admissions in elderly people account for 1.1% of the total [Atkinson et al., 2001]. Studies show that people with pre-existing respiratory or cardiac diseases, diabetes or socially disadvantaged are particularly vulnerable [Gouveia et al., 2000; Goldberg et al., 2001; Katsouyanni, 2003].

- **Long-term effects:** The main studies on which the results obtained are based correspond to Dockery et al. (1993) and Pope et al. (1995). Based on these studies it has been estimated that life expectancy can be reduced by several years due to air pollutants [Brunekreef, 1997, Horak et al., 2002]. Subsequently, studies also state that 6% of annual global mortality is caused by exposure to this type of pollutant [Künzli et al., 2000]. The World Health Organization (WHO) estimates premature deaths due to high concentrations of PM at more than one million each year [Ezzati et al., 2002; Gamble, 1996 and 1998; Katsouyanni, 2003].

- **OZONE (O_3)**

  Secondary contaminant formed from the reaction of primary pollutants in the presence of solar radiation. It is therefore a photochemical oxidant resulting mainly from the reaction of nitrogen oxides and volatile organic compounds [Committee of the Environmental and Occupational Health Assembly of the American Thoracic Society, 1996]. The units of measurement used correspond to ppb or $\mu g/m^3$, the equivalence being 1 ppb = 2 $\mu g/m^3$ at 20°C [WHO, 2000; Katsouyanni, 2003].

  Ozone causes short and long-term effects on the body. Epidemiological studies and controlled exposures have been carried out for both cases, with fewer and less consistent results in the long term.

  - **Short-term effects:** increased number of daily deaths, increased hospital airway admissions, increased respiratory symptoms, changes in lung function, inflammation of the airways, and changes in airway responsiveness. Several relevant studies have been carried out, such as those conducted by the Health Effects Institute (HEI) [Samet, Zeger and Dominici 2000] or by Goldberg et al. (2001). In the APHEA project of Touloumi et al. (1997) is shown as an increase in ozone of 50 $\mu g/m^3$ per day represents an increase of 2.9% in mortality [Katsouyanni, 2003].

  - **Long-term effects:** it causes the onset of asthma, changes in lung function and increases the occurrence of lung cancer, as well as increases the mortality rate of this disease [Pope et al., 2002; McConnel et al., 2002; McDonnell et al., 1999; Beeson, Abbey and Knutsen, 1998; Abbey et al., 1999].

- **NITROGEN DIOXIDE (NO_2)**

  Result of fossil fuel combustion in vehicles, industry, heating systems, etc. [Rijnders et al., 2001]. The formation of NO, NO_2 and NO_x occurs during combustion at elevated temperatures [Committee of the Environmental and Occupational Health Assembly of the American Thoracic Society, 1996]. Part of the NO generated reacts with ozone and oxygen producing NO_2. In turn, in the presence of solar radiation, NO_2 reacts with oxygen and hydrocarbons resulting in the formation of ozone and other photochemical secondary oxidants. The units of measurement used correspond to ppb or $\mu g/m^3$, the equivalence being 1 ppb = 1.913 $\mu g/m^3$ at 20°C [WHO, 2000; Katsouyanni, 2003].

  The studies carried out suggest that the effects caused by this gas are not particularly serious, and its regulation is necessary not because of the direct damage it causes to the body, but because it is an indirect ozone precursor.

  - **Short-term effects:** decreased lung function and increased airway reactivity in healthy people with values greater than 1,500 $\mu g/m^3$. These values are much higher than the concentrations in the atmosphere. In the case of particularly vulnerable people, such as asthmatics, the same symptoms have been detected with concentrations of 550 $\mu g/m^3$ [WHO, 2000]. In addition, it is believed that its presence in the atmosphere may alter the behaviour of other air pollutants [Katsouyanni et al., 2001].

- **Long-term effects:** Epidemiological studies show the relationship between increased internal concentration of NO_2 in the body and increased disease, although these results are not clearly demonstrated [Braun-Fahrlander et al., 1992].

▪ **SULPHUR DIOXIDE (SO_2)**

Resulting mostly from coal combustion, its concentration has declined in the West in recent decades due to improved fuel efficiency and reduced coal use. However, in other large areas such as East Asia, high concentrations can be observed due to the current heavy coal consumption [Committee of the Environmental and Occupational Health Assembly of the American Thoracic Society, 1996]. The units of measurement used correspond to ppb or $\mu g/m^3$, the equivalence being 1 ppb = 2.704 $\mu g/m^3$ at 20°C [WHO, 2000; Katsouyanni, 2003].

Numerous studies have been carried out on the effects on humans:

- **Short-term effects:** very short-term effects of high SO_2 levels such as decreased lung function, respiratory symptoms and specific resistance of the airways have been demonstrated. Various studies reflect how it affects mortality and hospital admissions [Katsouyanni et al., 1997; Sunyer, 1991].

- **Long-term effects:** the results from different cohort studies indicate that health effects are predominantly a result of exposure to ambient particles [Dockery et al., 1993].

▪ **CARBON MONOXIDE (CO)**

It comes mainly from the incomplete combustion of fossil fuels such as gasoline. Its outdoors concentration is mostly due to vehicles; while there are various indoors sources such as environmental tobacco smoke (ETS) and gas devices [Committee of the Environmental and Occupational Health Assembly of the American Thoracic Society, 1996]. The units of measurement used correspond to ppb or $\mu g/m^3$, the equivalence being 1 ppb = 1.165 $\mu g/m^3$ at 20°C [WHO, 2000; Katsouyanni, 2003].

Its high affinity with hemoglobin causes approximately 80-90% of the absorbed CO to bind with it, resulting in carboxyhemoglobin (COHb). High concentrations of CO cause acute episodes of poisoning, but such concentrations are not present in the atmosphere. Its toxic effects on the lungs appear to be non-existent, but it does have harmful effects on interference with oxygen transport [WHO, 2000; COMEAP, 2006]. Studies show the relationship between CO and cardiac arrhythmia, cardiovascular hospital admissions and mortality [Schwartz, 1999; Touloumi, Samoli and Katsouyanni, 1996; Katsouyanni 2003].

Finally, the mechanisms involved in the cardiovascular effects of gases and particulate matter are presented in Figure 6:

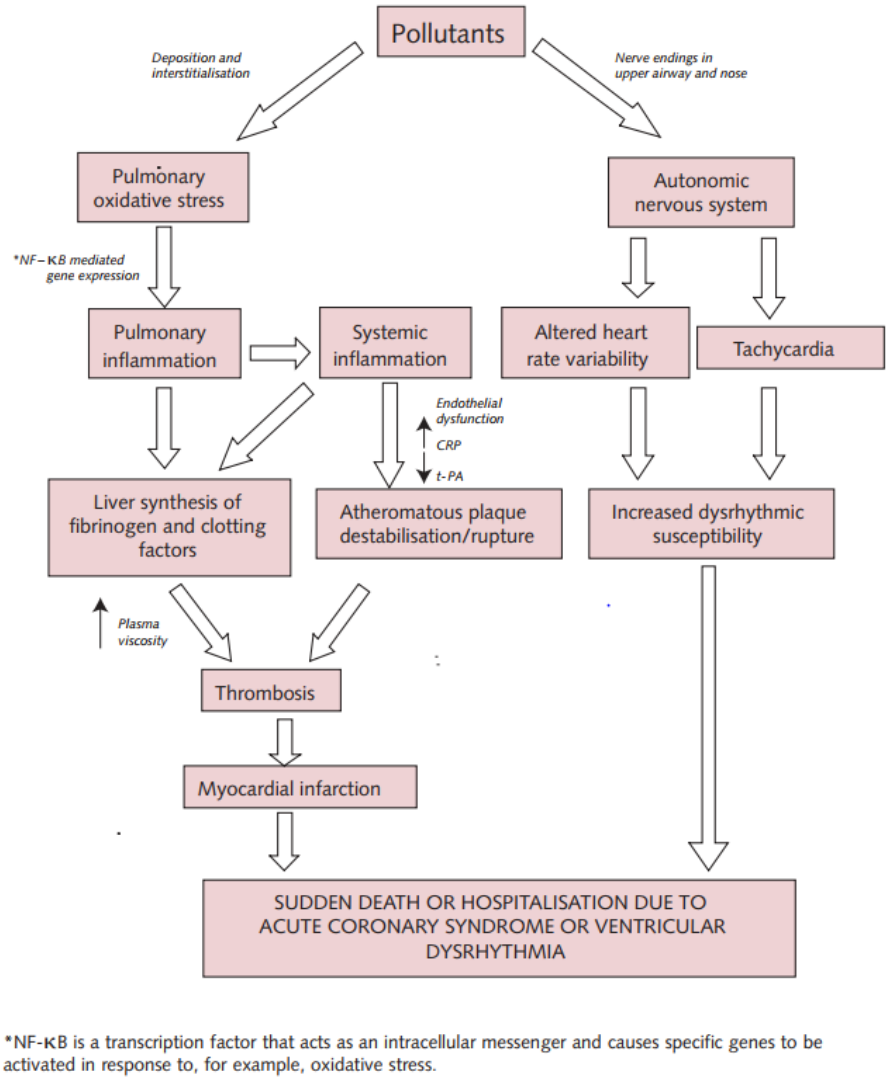

Figure 6: Toxicological mechanisms involved in the cardiovascular effects of particles and gases – two current hypotheses [COMEAP, 2006].

1.3.4 European context

The European continent has been suffering from serious environmental pollution problems for several decades. Already in the first half of the 20th century, some of the first episodes occurred that led countries to develop a special sensitivity on this subject. Although the trend in air pollutant emissions over the last decade has been decreasing as can be seen in Figure 7, Figure 8 shows how the population is still exposed to high concentrations of pollutants:

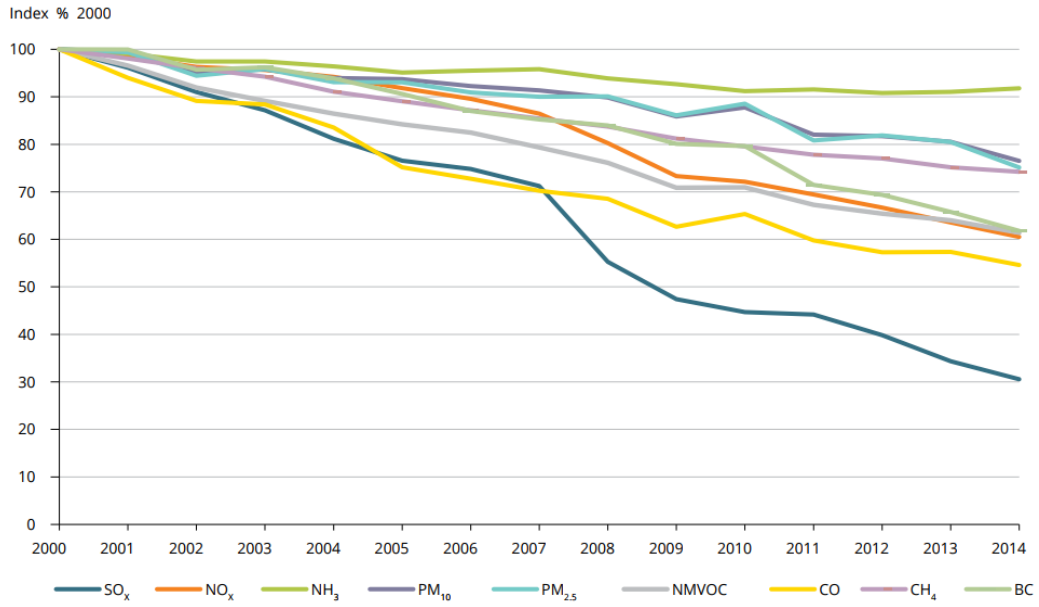

Figure 7: Development in EU-28 emissions, 2000–2014 (% of 2000 levels): (a) SO_X, NO_X, NH_3, PM_{10}, $PM_{2.5}$, NMVOCs, CO, CH_4 and BC [EEA, 2016].

Pollutant	EU reference value (a)	Exposure estimate (%)	WHO AQG (a)	Exposure estimate (%)
$PM_{2.5}$	Year (25)	8–12	Year (10)	85–91
PM_{10}	Day (50)	16–21	Year (20)	50–63
O_3	8-hour (120)	8–17	8-hour (100)	96–98
NO_2	Year (40)	7–9	Year (40)	7–9
BaP	Year (1)	20–24	Year (0.12) (RL)	88–91
SO_2	Day (125)	< 1	Day (20)	35–49

Key: < 5 % | 5–50 % | 50–75 % | > 75 %

Notes: (a) In µg/m³; except BaP, in ng/m³.

The reference concentrations include EU limit or target values, WHO air-quality guidelines (AQGs) and estimated reference levels (RLs).

For some pollutants, EU legislation allows a limited number of exceedances. This aspect is considered in the compilation of exposure in relation to EU air-quality limit and target values.

The comparison is made for the most stringent EU limit or target values set for the protection of human health. For PM_{10}, the most stringent limit value is for 24-hour mean concentration, and for NO_2 it is the annual mean limit value.

The estimated exposure range refers to a recent 3-year period (2012–2014) and includes variations attributable to meteorology, as dispersion and atmospheric conditions differ from year to year.

As the WHO has not set AQGs for BaP, the reference level in the table was estimated assuming WHO unit risk for lung cancer for PAH mixtures, and an acceptable risk of additional lifetime cancer risk of approximately 1 in 100 000.

Sources: EEA, 2016f.

Figure 8: Percentage of the urban population in the EU-28 exposed to air pollutant concentrations above certain EU and WHO reference concentrations (2012–2014) [EEA, 2016].

- **PARTICULATE MATTER (PM)**

The annual average of PM_{10} levels reached in European countries ranged between 14 and 65 µg/m^3, while black smoke levels ranged between 10 and 65 µg/m^3. In several cities, the level of 50 µg/m^3 is exceeded for more than 35 days per year [Katsouyanni, 2001; Katsouyanni et al. 2003]. Figure 9 and Figure 10 show the values for various European countries compared to the limit value established by the EU for PM_{10} and $PM_{2.5}$ respectively.

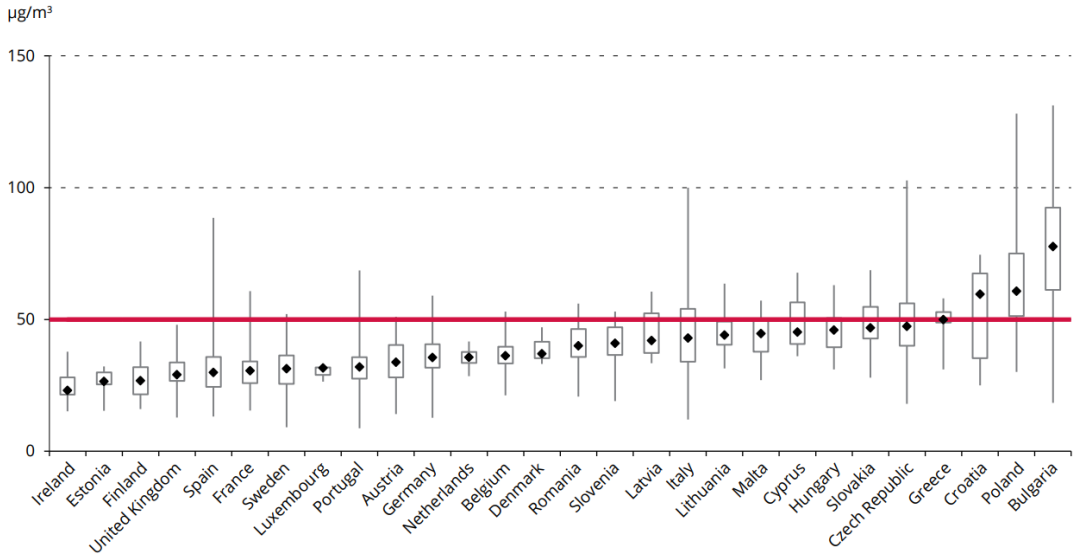

Notes: The graph is based, for each Member State, on the 90.4 percentile of daily mean concentration values corresponding to the 36th highest daily mean. For each country, the lowest, highest and median percentile 90.4 values (in µg/m³) at the stations are given. The rectangles mark the 25th and 75th percentiles. At 25 % of the stations, levels are below the lower percentile; at 25 % of the stations, concentrations are above the upper percentile. The daily limit value set by EU legislation is marked by the red line.

Figure 9: PM_{10} concentrations in relation to the daily limit value in 2014 in the EU-28 [EEA, 2016].

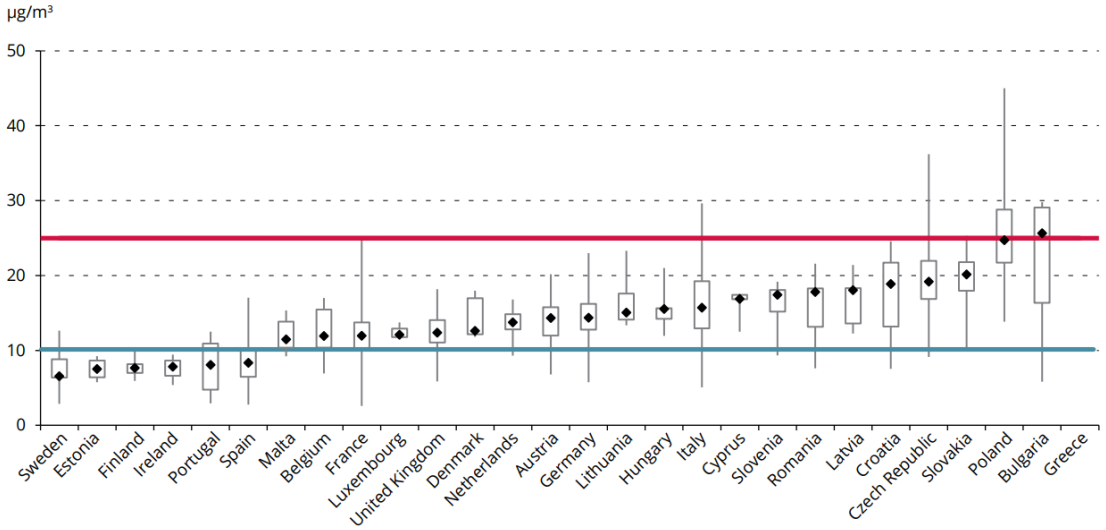

Notes: The graph is based on annual mean concentration values. For each country, the lowest, highest and median values (in µg/m³) at the stations are given. The rectangles mark the 25th and 75th percentiles. At 25 % of the stations, levels are below the lower percentile; at 25 % of the stations, concentrations are above the upper percentile. The target value set by EU legislation is marked by the red line. The WHO AQG is marked by the blue line.

Figure 10: $PM_{2.5}$ concentrations in relation to the target value in 2014 in the EU-28 [EEA, 2016].

- **OZONE (O_3)**

In the first decade of the 21st century, many European cities had a 90th percentile of ozone 1-h concentrations exceeding 120 µg/m^3 and maximum values reaching more than 200–µg/m^3 [Katsouyanni, 2001; Katsouyanni et al. 2003]. Figure 11 shows the values for various European countries compared to the EU limit value for O_3.

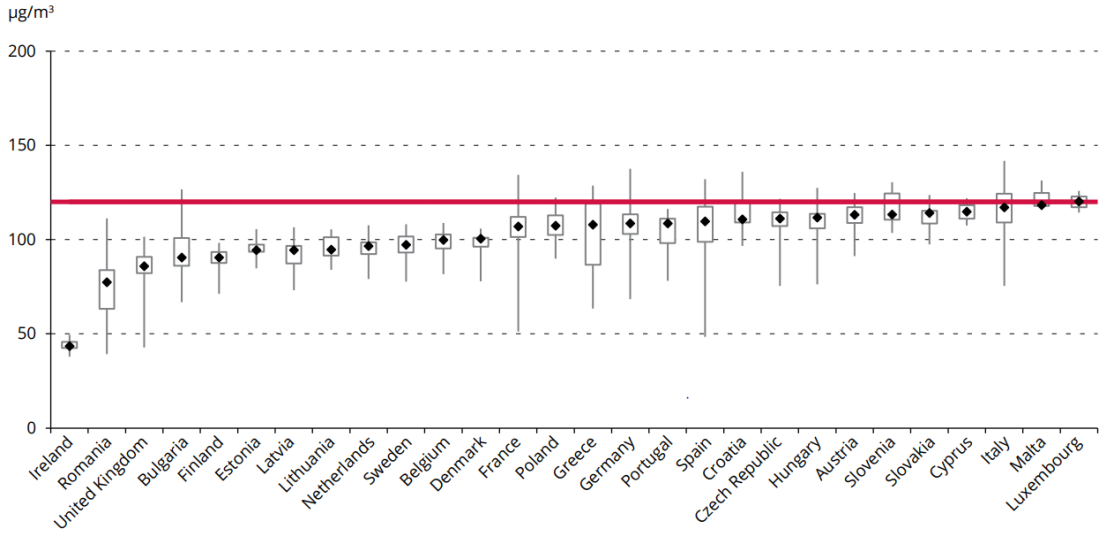

Notes: The graph is based, for each Member State, on the 93.2 percentile of maximum daily 8-hour mean concentration values, corresponding to the 26th highest daily maximum of the running 8-hour mean. For each country, the lowest, highest and median values (in µg/m³) at the stations are given. The rectangles mark the 25th and 75th percentiles. At 25 % of the stations, levels are below the lower percentile; at 25 % of the stations, concentrations are above the upper percentile. The target value threshold set by the EU legislation is marked by the red line.

Figure 11: O_3 concentrations in relation to the target value in 2014 in the EU-28 [EEA, 2016].

- **NITROGEN DIOXIDE (NO_2)**

At the beginning of this century, the average of 24-h NO_2 concentration ranges from about 30 to about 90 µg/m^3 and the 90th percentile from about 40 to about 140 µg/m^3 in European cities.The higher traffic density is, the higher concentrations , particularly in southern European cities [Katsouyanni, 2001; Katsouyanni et al. 2003]. Figure 12 shows the values for various European countries compared to the EU limit value for NO_2.

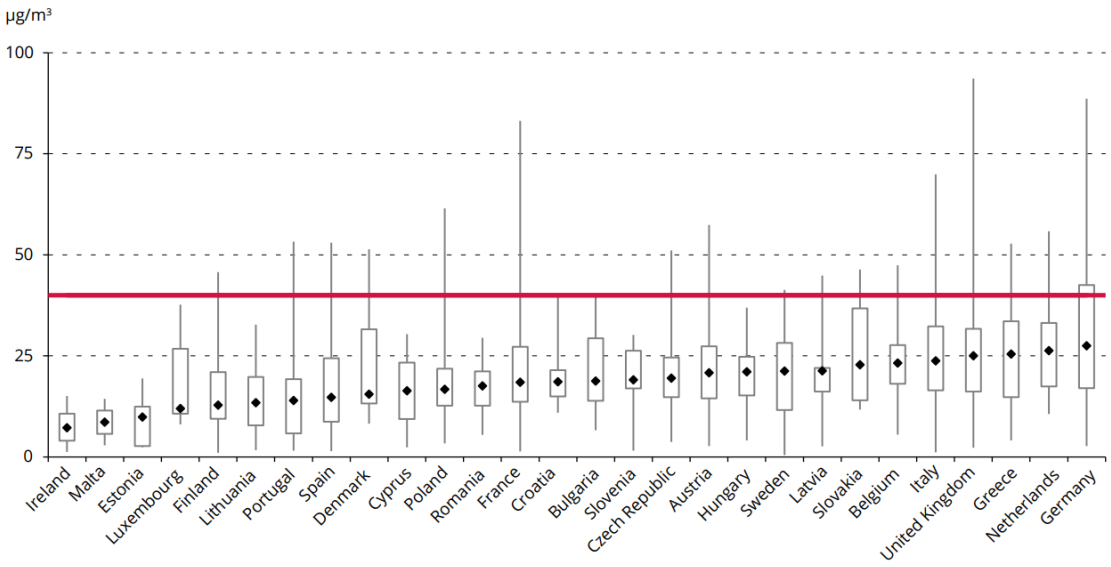

Notes: The graph is based on the annual mean concentration values for each Member State. For each Member State, the lowest, highest and median values (in µg/m³) at the stations are given. The rectangles mark the 25th and 75th percentiles. At 25 % of the stations, levels are below the lower percentile; at 25 % of the stations, concentrations are above the upper percentile. The limit value set by EU legislation (equal to the WHO AQ guideline) is marked by the red line.

Figure 12: NO_2 concentrations in relation to the target value in 2014 in the EU-28 [EEA, 2016].

- **SULPHUR DIOXIDE (SO_2)**

  Already at the turn of the century, the 24-h percentiles of SO_2 were below 50 µg/m^3 in European cities in most cases but there were some values above 100 µg/m^3 on a 24-h basis, mainly in the cities of Central and Eastern Europe [Katsouyanni, 2001; Katsouyanni et al. 2003].

- **CARBON MONOXIDE (CO)**

  In the case of urban traffic environments of European cities, the 8-hour average carbon monoxide concentrations are in general lower than 20 mg/m^3 with short-lasting peaks below 60 mg/m^3 [WHO 2000].

1.3.5 European legislation

This section summarizes the limit values stipulated in current legislation. The following data are taken from Council Directive 2002/3/EC (of 12 February 2002) [UECD, 2002] and the European Parliament and Council Directive 2008/50/EC (of 21 May 2008) [UECD, 2008] and WHO (2006) and apply to the whole territory of the European Union. It is important to note that the current WHO air quality guidelines for Europe accept that available information does not allow a judgment of concentrations below which no effects are to be expected.

- **PARTICULATE MATTER (PM)**

Table 1: Limit values for PM_{10}.

PM_{10}			
Averaging Period	**Limit value**	**Margin of tolerance**	**Date by which limit value is to be met**
One hour	50 µg/m^3 , not to be exceeded more than 35 times a calendar year	50 %	— (1)
Calendar year	40 µg/m^3	20 %	— (1)

(1) Already in force since 1 January 2005

(2) The maximum daily eight hour mean concentration will be selected by examining eight hour running averages, calculated from hourly data and updated each hour. Each eight hour average so calculated will be assigned to the day on which it ends i.e. the first calculation period for any one day will be the period from 17:00 on the previous day to 01:00 on that day; the last calculation period for any one day will be the period from 16:00 to 24:00 on that day.

(3) Already in force since 1 January 2005. Limit value to be met only by 1 January 2010 in the immediate vicinity of the specific industrial sources situated on sites contaminated by decades of industrial activities. In such cases, the limit value until 1 January 2010 will be 1,0 µg/m3 . The area in which higher limit values apply must not extend further than 1 000 m from such specific sources.

The limit values for $PM_{2.5}$ are:

Table 2: Limit values for $PM_{2.5}$.

$PM_{2.5}$		
Averaging Period	**Limit value**	**Margin of tolerance** **Margin of tolerance and date by which limit value is to be met**
Calendar year	25 µg/m^3	To be met by 1 January 2015 (until then, margin of tolerance)
Calendar year	Exposure concentration obligation (b), 20 µg/m3	To be met by 2015
Calendar year	Exposure reduction target (b), 0–20 % reduction in exposure (depending on the average exposure indicator in the reference year) to be met by 2020	

(a) 99th percentile (3 days/year).
(b) Based on a 3-year average.

- **OZONE (O_3)**

The EU regulation for ozone for the protection of human health is still in under consideration:

Table 3: Limit value: O_3.

Ozone		
	Parameter	**Target value for 2010 (a) [(1)]**
Target value for the protection of human health	Maximum daily 8-hour mean (b)	120 µg/m^3 not to be exceeded on more than 25 days per calendar year averaged over three years (c)

a) Compliance with target values will be assessed as of this value. That is, 2010 will be the first year the data for which is used in calculating compliance over the following three or five years, as appropriate.
(b) The maximum daily 8-hour mean concentration shall be selected by examining 8-hour running averages, calculated from hourly data and updated each hour. Each 8-hour average so calculated shall be assigned to the day on which it ends. i.e. the first calculation period for any one day will be the period from 17:00 on the previous day.
(c) If the three or five year averages cannot be determined on the basis of a full and consecutive set of annual data, the minimum annual data required for checking compliance with the target values will be as follows: — for the target value for the protection of human health: valid data for one year, — for the target value for the protection of vegetation: valid data for three years.
(1) These target values and permitted exceedance are set without prejudice to the results of the studies and of the review, provided for in Article 11, which will take account of the different geographical and climatic situations in the European Community

- **NITROGEN DIOXIDE (NO_2)**

Table 4: Limit values: NO_2.

NITROGEN DIOXIDE

Averaging Period	Limit value	Margin of tolerance	Date by which limit value is to be met
One hour	200 µg/m^3 , not to be exceeded more than 18 times a calendar year	50 % on 19 July 1999, decreasing on 1 January 2001 and every 12 months thereafter by equal annual percentages to reach 0 % by 1 January 2010	1 January 2010
Calendar year	40 µg/m^3	5 µg/m^3 (100 %) on 13 December 2000, decreasing on 1 January 2006 and every 12 months thereafter by 1 µg/m^3 to reach 0 % by 1 January 2010	1 January 2010

(1) Already in force since 1 January 2005

(2) The maximum daily eight hour mean concentration will be selected by examining eight hour running averages, calculated from hourly data and updated each hour. Each eight hour average so calculated will be assigned to the day on which it ends i.e. the first calculation period for any one day will be the period from 17:00 on the previous day to 01:00 on that day; the last calculation period for any one day will be the period from 16:00 to 24:00 on that day.

(3) Already in force since 1 January 2005. Limit value to be met only by 1 January 2010 in the immediate vicinity of the specific industrial sources situated on sites contaminated by decades of industrial activities. In such cases, the limit value until 1 January 2010 will be 1,0 µg/m3 . The area in which higher limit values apply must not extend further than 1 000 m from such specific sources.

- **SULPHUR DIOXIDE (SO_2)**

Table 5: Limit values: SO_2.

SULPHUR DIOXIDE

Averaging Period	**Limit value**	**Margin of tolerance**	**Date by which limit value is to be met**
One hour	350 µg/m^3 , not to be exceeded more than 24 times a calendar year	150 µg/m^3 (43 %)	— (1)
One day	125 µg/m^3 , not to be exceeded more than 3 times a calendar year	None	— (1)

(1) Already in force since 1 January 2005

(2) The maximum daily eight hour mean concentration will be selected by examining eight hour running averages, calculated from hourly data and updated each hour. Each eight hour average so calculated will be assigned to the day on which it ends i.e. the first calculation period for any one day will be the period from 17:00 on the previous day to 01:00 on that day; the last calculation period for any one day will be the period from 16:00 to 24:00 on that day.

(3) Already in force since 1 January 2005. Limit value to be met only by 1 January 2010 in the immediate vicinity of the specific industrial sources situated on sites contaminated by decades of industrial activities. In such cases, the limit value until 1 January 2010 will be 1,0 µg/m3 . The area in which higher limit values apply must not extend further than 1 000 m from such specific sources.

- **CARBON MONOXIDE (CO)**

Table 6: Limit values: CO.

Carbon monoxide:			
Averaging Period	Limit value	Margin of tolerance	Date by which limit value is to be met
Maximum daily eight hour mean (2)	10 µg/m^3	60 %	— (1)

(1) Already in force since 1 January 2005
(2) The maximum daily eight hour mean concentration will be selected by examining eight hour running averages, calculated from hourly data and updated each hour. Each eight hour average so calculated will be assigned to the day on which it ends i.e. the first calculation period for any one day will be the period from 17:00 on the previous day to 01:00 on that day; the last calculation period for any one day will be the period from 16:00 to 24:00 on that day.
(3) Already in force since 1 January 2005. Limit value to be met only by 1 January 2010 in the immediate vicinity of the specific industrial sources situated on sites contaminated by decades of industrial activities. In such cases, the limit value until 1 January 2010 will be 1,0 µg/m3 . The area in which higher limit values apply must not extend further than 1 000 m from such specific sources.

The WHO air quality guidelines are set to prevent levels of COHb in the blood exceeding 2.5%.

1.4 CBRN agents

- **CHEMICAL AGENTS**

The different chemical agents used as weapons can be classified according to their form of attack on the organism:

- **Nerve agents:** they attack the central nervous system. Sarin gas is an example of this type of particularly dangerous chemical weapon [Lee, 2003; Sidell and Borak, 1992].
- **Blood agents:** they prevent blood from absorbing oxygen. Cyanide is an example of this type of agent [Geoghegan and Tong, 2006].
- **Blister agents:** they attack the airways and skin. As an example, the mustard gas can be named [Khatery et al., 2003].
- **Choking agents:** they attack the lung membranes. Phosgene is an example of this type of chemical weapon [Geoghegan and Tong, 2006].

The wide variety of toxic agents, as well as their legitimate use in industrial applications, facilitates their acquisition, processing and preparation in many cases and makes them a major threat to society. This type of weapon can be produced in solid, liquid and gaseous form and can be released in the form of powder, drop or vapour by multiple methods. Although their large-scale production would be highly complicated, small-scale manufacture of low-performance agents for use in terrorist

acts is plausible, as evidenced by attacks such as those in Japan during the 1990s [Cornish, 2007].

- **BIOLOGICAL AGENTS**

The different biological agents can be classified into two types:

- **Microorganisms:** they can be contagious like smallpox and Ebola or non-contagious like anthrax. They need a body for reproduction and survival [Cunha, 2002].
- **Toxins:** they are inanimate, poisonous and cannot reproduce. Botulinum is an example of such a biological weapon [Arnon, 2001].

As in the case of chemical weapons, their simple acquisition, processing and preparation in many cases, coupled with their dual use, i. e. their legitimate use in industrial applications, make such agents a major threat to society [Rotz et al., 2002].

Although their large-scale production would be complex, small-scale manufacture of agents would be even more plausible than for chemical weapons and their much greater public impact. This is manifested in the fact that many experts consider that biological weapons are becoming the terrorist's "weapon of choice" [Cornish, 2007].

- **RADIOLOGICAL AGENTS**

The use of this type of agent consists in its dissemination over wide areas with the objective of subjecting people within it to high doses of radiation. Its short-term effects are more limited [Eliseo et al., 2008].

The procurement of radiological agents is feasible through industry, laboratory, etc.. Some authors say that the technology required for their application requires a high level of complexity, making them difficult to use as a weapon in the case of terrorist groups [Cornish, 2007]. However, it seems not so difficult to disperse a Cobalt radioactive source, Iodine or others with an improvised explosive device – particulaly if the terrorist do not care of being irradiated.

- **NUCLEAR AGENTS**

There are four main methods by which to carry out a nuclear attack:

- Acquisition and use of a complete nuclear weapon.
- Manufacture of a nuclear weapon.
- Attack on a nuclear power station.
- Manufacture of an Improvised Nuclear Device (IND) that would require much more quantity of uranium of lower quality.

The effects of such agents are catastrophic, although their use as weapons would be a major complication for terrorist groups [Kollel, 2003; Cornish, 2007].

1.5 Scope of work

The main objective of this thesis is the exerimental characterization of the Counterfog® performance and its effectivity for the decontamination or removal of airborne particulate matter (PM) indoors .

Biological and chemical agents decontamination tests in laboratory are also described.. In particular, the following topics will be described:

- Characterization of the fog generated by Counterfog® nozzles.
- Fog Dynamics.
- Diesel PM decontamination tests.
- Biological agents decontamination tests.
- Chemical agent decontamination tests.

The work presented in this thesis has been the basis for further development and research on Counterfog® systems, more particularly on the application to outdoors scenarios, the improvement of the nozzles and their use for decontamination of surfaces. These are clearly research and development lines with an interesting future.

1.6 Outline of the thesis

The present thesis consists of 9 chapters, a bibliography and 2 annexes. Listed below are the titles of the different chapters that make up this work.

- **Chapter 1:** Introduction
- **Chapter 2:** State of the Art
- **Chapter 3:** Materials and methods
- **Chapter 4:** Characterization of system Counterfog®
- **Chapter 5:** Analysis of the behaviour of the fog generated by the Counterfog® system
- **Chapter 6:** Decontamination of Diesel particles from air by using the Counterfog® system
- **Chapter 7:** Decontamination of biological agents from air by using the Counterfog® system
- **Chapter 8:** Decontamination of chemical agents from air by using the Counterfog® system
- **Chapter 9:** Conclusions

The document concludes with a list of bibliographical references and details the publications in journals, conferences and patents that have led or are related to this thesis and research projects that have funded this study. It ends with a glossary and 2 annexes with more details.

Chapter 2

State of the Art

2.1 Aerosols in the atmosphere

Aerosols are made of small particles of either liquid, solid or mixtures of solid and liquid dispersed in a gas. The dispersed droplets are typically much larger than the size of a molecule but too small to be seen with the naked eye. Thus, atmospheric aerosols are dispersions of PM in the air. As indicated in the previous chapter, sources of aerosols can be natural or anthropogenic [Seinfeld and Pandis, 2006]. They can also be formed in the atmosphere when gas conversion to particles takes place: two or more gaseous species react producing a low vapour pressure compound –below its dew point-. This new compound can condense onto a pre-existing particle or nucleate forming a new ultra-fine particle.

Some examples of aerosols of interest for us are the following:

- **Fog/mist:** made up of small drops of liquid dispersed in a gas. They can be generated by dispersion or condensation.

- **Dust:** consisting of solid particles suspended in a gas. Generally as a result of the mechanical disintegration of materials and their subsequent dispersion.

- **Smoke:** consisting of solid particles suspended in a gas. They originate from pyrolitical, combustion and complex processes involved in fire –even in smouldering flameless fires-..

The main parameters determining the properties of aerosols are:

- **Chemical composition**
  It is conditioned by its origin

- **Concentration**
  It can be expressed as :

  - **Mass concentration**: mass of particles per unit volume of aerosol.

  - **Numerical concentration**: number of particles per unit volume of aerosol.

- **Density.**
  It is the density of the particle itself. The density may be lower than that of the original compound due to the possible presence of structural voids or bubbles..

- **Particle morphology**
  Shape of solid particles may deviate from spheres. Liquid particles shape can also dynamically oscillate.
- **Particle size**
  Typical aerosol particles size ranges from 0.1 to 100 µm as shown in Figure 13.

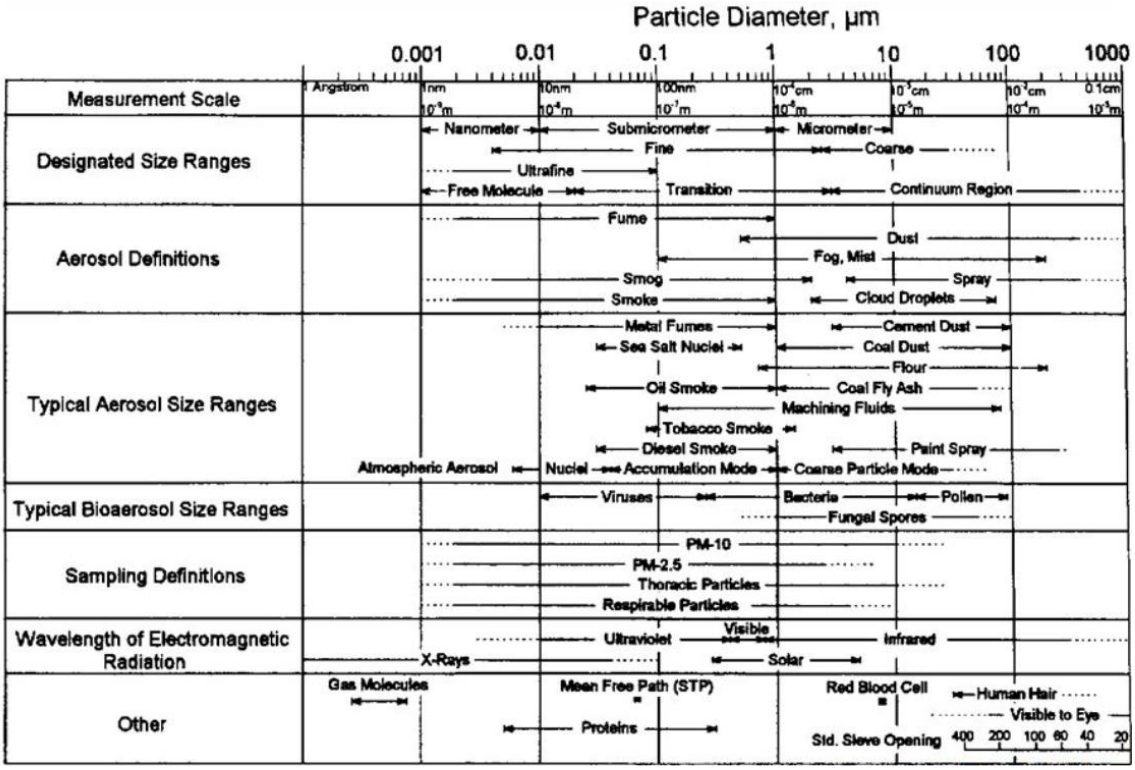

Figure 13: Typical aerosol particle size ranges [Hinds, 1999]

2.1.1 Free fall dynamics of a droplet in air

Diameter is the most important parameter determining aerodynamical properties of the droplet and its final settling velocity (V_s).

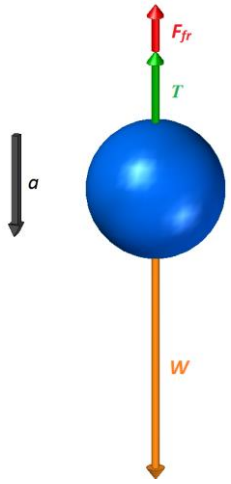

Figure 14: Schematic of the set of forces acting on a spherical particle in free fall within a viscous fluid

The vertical movement of a spherical element with a mass m and a diameter d within a viscous fluid is determined by are weight (W), buoyancy (B) and friction force (F_{fr}), the latter being proportional to the speed of the spherical element(Figure 14). The friction force is given by the expression:

$$F_{fr} = \frac{1}{2}\rho_f A_p C_D v_p^2 \quad \textbf{(1)}$$

where:

- ρ_f : fluid density
- A : cross-sectional area of the particle in the direction of motion
- C_D : drag coefficient
- v_p : velocity of the particle relative to the fluid

C_D is given by numerical expressions that approximate its value for different ranges of the Reynolds number (Figure 15). This number is defined as the quotient between inertial and viscous forces and makes it possible to differentiate between the laminar and turbulent regime situation:

$$Re = \frac{\rho_f d_p v_p}{\mu_f} \quad \textbf{(2)}$$

with:

- d_p: particle diameter
- μ_f : dynamic fluid viscosity

The following expressions are therefore obtained for the coefficient of friction:

$$C_{D1} = \frac{24}{Re} + \frac{2.6\left(\frac{Re}{5}\right)}{1+\left(\frac{Re}{5}\right)^{1.52}} + \frac{0.411\left(\frac{Re}{263{,}000}\right)^{-7.94}}{1+\left(\frac{Re}{263{,}000}\right)^{-8}} + \frac{Re^{0.8}}{461{,}000} \quad \textbf{(3)}$$

$$\text{if } 2.5.10^6 < Re \simeq 2.10^6$$

$$C_{D2} = \left[\left(\frac{24}{Re}\right)^{0.52} + 0.32^{0.52}\right]^{\frac{1}{0.52}} \quad \text{if } Re < 2.10^5 \quad \textbf{(4)}$$

$$C_{D3} = \frac{24}{Re} \quad if\ Re < 1 \quad \textbf{(5)}$$

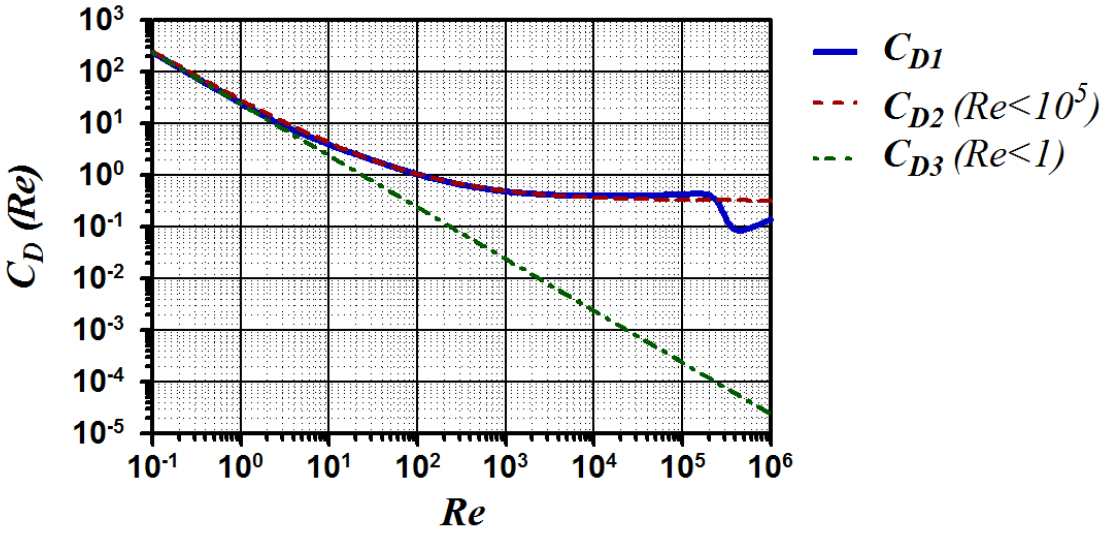

Figure 15: Approximations for C_D given by the expressions C_{D1} and C_{D2} for different Reynolds number values for the air case

In the case of particles under 100 μm falling down by gravity$Re \leq 1$. And since this value will not be exceeded in any case throughout this work, the following approximation can be assumed to be valid: $C_D = \frac{24}{Re}$. Substituting the value in the expression that allows to obtain the friction force, the Stokes formula is reached:

$$F_{fr} = 6\pi\left(\frac{d_P}{2}\right)\mu_a v_p$$

where μ_a is the dynamic viscosity of the air (fluid over which the particle will move).

Buoyancy is due to Archimedes Principle, it is equal to the product of the volume of the element times the gravity and density of the fluid. In this way, the equation of motion will result:

$$m_P a_P = W - B - F_{fr} \quad \textbf{(6)}$$

where:

$$W = m_P g = \rho_p \frac{4}{3}\pi \left(\frac{d_P}{2}\right)^3 g$$

$$B = \rho_a \frac{4}{3}\pi \left(\frac{d_P}{2}\right)^3 g$$

In this way, the final settling velocity (V_s) will be reached in the limit when the acceleration of the particle is zero and, therefore, that resulting from the forces acting on the element is zero. Then, it can be written

$$V_s = \frac{2g(\rho_p - \rho_a)\left(\frac{d_P}{2}\right)^2}{9\mu_a} = \frac{g(\rho_p - \rho_a)d_p^2}{18\mu_a} \quad \textbf{(7)}$$

and, therefore, the equation of motion is defined by:

$$m_P \frac{dv_p}{dt} = W - E - F_{fr} = \rho_p \frac{4}{3}\pi \left(\frac{d_P}{2}\right)^3 g - \rho_a \frac{4}{3}\pi \left(\frac{d_P}{2}\right)^3 g - 6\pi\left(\frac{d_P}{2}\right)\mu_a v_p$$
$$= \left(\rho_p - \rho_a\right)\frac{4}{3}\pi \left(\frac{d_P}{2}\right)^3 g - 6\pi\left(\frac{d_P}{2}\right)\mu_a v = \rho_p \frac{4}{3}\pi \left(\frac{d}{2}\right)^3 \frac{dv_p}{dt}$$

Integrating the previous equation between the initial instant and any instant *t* (it will be assumed in Counterfog® laboratory tests that the initial vertical speed is zero), it is obtained:

$$\int_0^t dt = \int_0^{v_p} \frac{\rho_p \frac{4}{3}\pi \left(\frac{d_P}{2}\right)^3}{\left(\rho_p - \rho_a\right)\frac{4}{3}\pi \left(\frac{d_P}{2}\right)^3 g - 6\pi\left(\frac{d_P}{2}\right)\mu_a v} dv$$

Therefore:

$$t = \frac{-2\rho_p \left(\frac{d_P}{2}\right)^2}{9\mu_a} ln \left| \left(1 - \frac{\rho_a}{\rho_e}\right) g - \frac{9\mu_a}{2\rho_p \left(\frac{d_P}{2}\right)^2} v \right|_0^{v_p}$$

(8)

$$v_p = \frac{\left(1-\frac{\rho_a}{\rho_p}\right)g}{\frac{9\mu_a}{2\rho_p\left(\frac{d_P}{2}\right)^2}}\left(1-e^{\frac{-9\mu_a}{2\rho_p\left(\frac{d_P}{2}\right)^2}t}\right)$$

The vertical distance travelled by the particle in relation to the time elapsed is now calculated:

$$v_p = \frac{\mathrm{d}x_p}{\mathrm{dt}}$$

$$\int_0^{x_p} dx = \int_0^t \frac{\left(1-\frac{\rho_a}{\rho_p}\right)g}{\frac{9\eta_a}{2\rho_e\left(\frac{d}{2}\right)^2}}\left(1-e^{\frac{-9\eta_a}{2\rho_p\left(\frac{d_P}{2}\right)^2}t}\right)dt$$

$$x = \frac{\left(1-\frac{\rho_a}{\rho_p}\right)g}{\frac{9\eta_a}{2\rho_p\left(\frac{d_P}{2}\right)^2}}\left(t+\frac{e^{\frac{-9\eta_a}{2\rho_p\left(\frac{d_P}{2}\right)^2}t}}{\frac{9\eta_a}{2\rho_p\left(\frac{d_P}{2}\right)^2}}-\frac{1}{\frac{9\eta_a}{2\rho_p\left(\frac{d_P}{2}\right)^2}}\right) \quad \textbf{(9)}$$

From the results obtained, it is concluded that in a viscous fluid:

- The velocity of the element tends to a constant value V_s (Figure 16).
- Displacement can be considered almost proportional to the time spent with an offset of the order of the settling time (Figure 17).

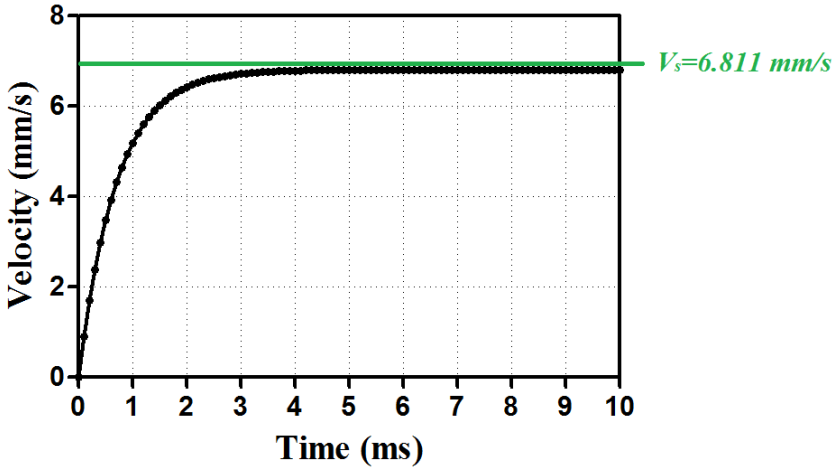

Figure 16: Velocity of fall as a function of time for a particle with d_p=*20 μm*, ρ_p=*350 kg/m*^{3} suspended in the air with T_{atm}=*293.15 K* and P_{atm}=*101,325 Pa*

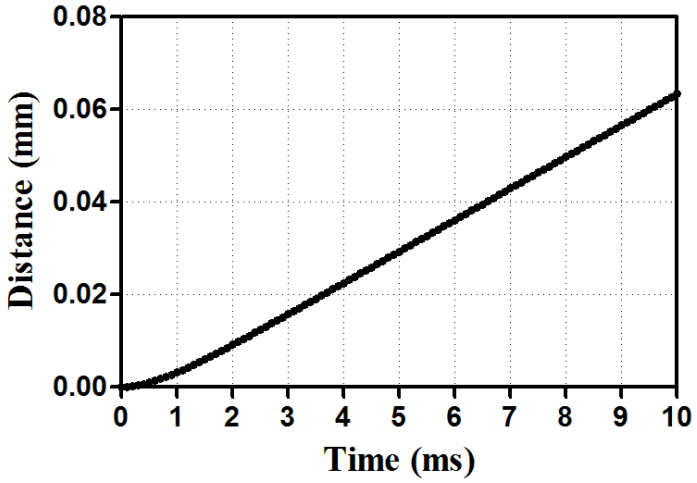

Figure 17: Distance covered as a function of time for a particle with d_p=20 μm, ρ_p=350 kg/m^3 suspended in the air with T_{atm}=293.15 K and P_{atm}=101,325 Pa

The different diameters used for the characterisation of aerosol particles are now defined:

- **Spherical aerosol particles:**
  - **Geometric diameter (d_g):** particle diameter when viewed under a microscope
  - **Aerodynamic diameter (d_a):** diameter of the sphere with density of value unit and same sedimentation velocity than the aerosol particle. The expression that determines the value of this diameter is:

$$d_a = \sqrt{\frac{18\eta_a V_s}{g(1-\rho_a)d_p^2}} \quad \textbf{(10)}$$

- **Non-spherical aerosol particles:**
  - **Volume equivalent diameter (d_{eq}):** diameter of the sphere with the same volume as the particle.
  - **Projected surface diameter (d_{pa}):** diameter of the circle having the same surface as projected by the particle
  - **Stokes diameter (d_s):** diameter of the sphere with the same density and final settling velocity (V_s) as the aerosol particle. The expression that determines the value of this diameter is:

$$d_s = \sqrt{\frac{18\eta_a V_s}{g(\rho_p-\rho_a)d^2}} \quad \textbf{(11)}$$

- **Aerodynamic diameter (d_a):** diameter of the sphere with density of value unit and final settling velocity (V_s) as the aerosol particle. The expression that determines the value of this diameter is:

$$d_a = \sqrt{\frac{18\eta_a V_s}{g(1-\rho_a)d^2}} \quad \textbf{(12)}$$

2.1.2 Interaction between particles and droplets

Aerosols can also be classified according to their size in different sub-distributions or modes as can be seen in Figure 18 [Whitby, 1978; Pérez-Díaz et al., 2017; Wilson and Suh, 1997]:

- **Nucleation mode** ($d_p < 0.01\ \mu m$)
  These particles are newly emitted or in situ formed in the atmosphere. They have short lifetimes as they coagulate to form Aitken and accumulation mode particles.

- **Aitken mode** ($0.01\ \mu m < d_p < 0.1\ \mu m$)
  These are sulfates, elemental carbon, metal and organic compounds with very low saturation vapor pressure at ambient temperature.

- **Accumulation mode** ($0.1\ \mu m < d_p < 1\ \mu m$)
  Different metallic compounds, organic compounds, elemental carbon, as well as coagulated particles from Aitken nuclei are part of this group. These particles have the longest lifetime.

- **Coarse mode** ($1\ \mu m < d_p < 10\ \mu m$)
  Composed of soil dust, nitrates, chlorides, marine salts, oxides of elements of the earth's crust, pollen, mould, etc. Particularly important are the ashes and soot generated from the combustion of fossil fuels such as coal, oil and other fuels such as wood. These particles have high sedimentation velocities and do not stay suspended in the atmosphere for a long time.

- **Giant particles** ($d_p > 10\ \mu m$)

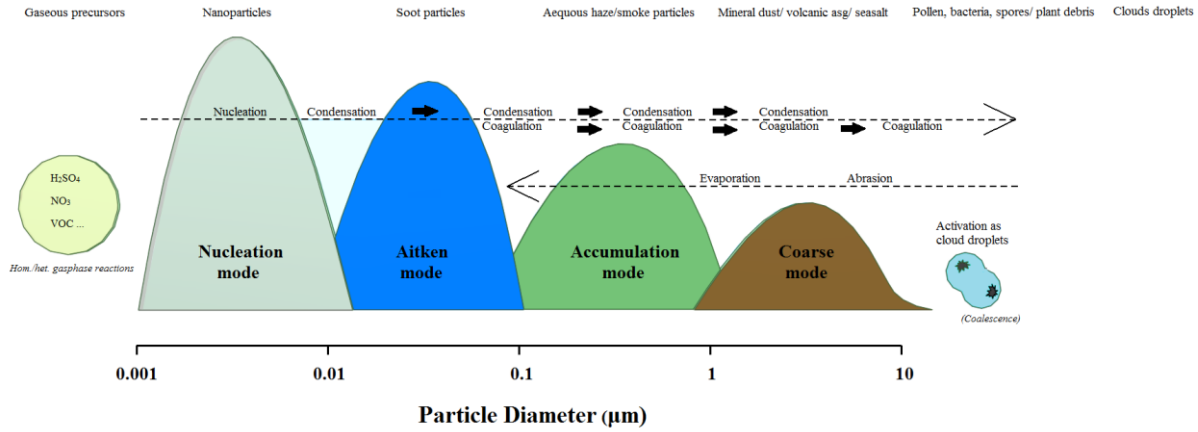

Figure 18: Schematic multimodal particle size distribution with typical transformations of sample particle types of the individual modes. Adapted from DWD (2018)

Two series of mechanisms are responsible for natural aerosol removal (Figure 19):

- **Dry removal:** sedimentation, turbulence and impact.
- **Wet removal:** incorporation in clouds and deposition through precipitation.

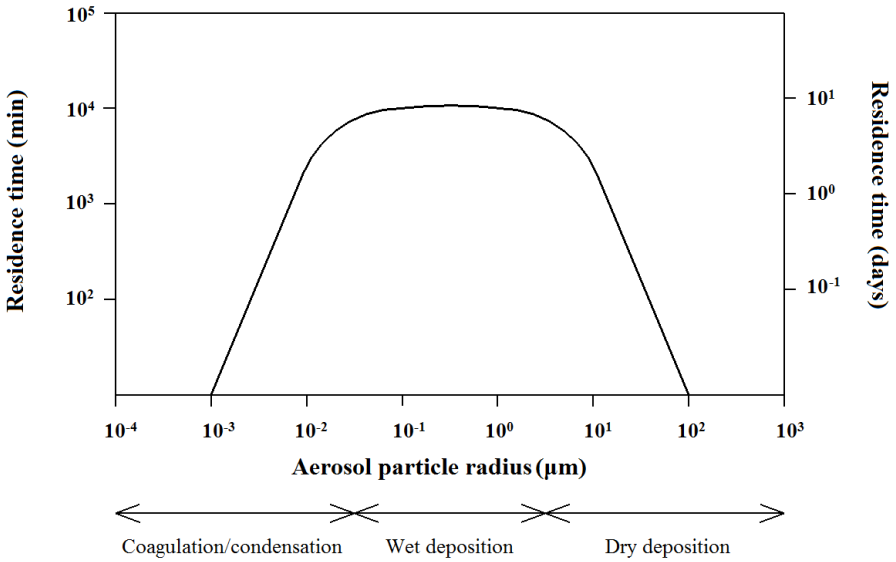

Figure 19: Residence time of aerosol particles in the troposphere as a function of particle radius. The approximate size ranges for the predominant elimination mechanisms are also shown. This figure has been generated using data from Jaenicke (1978)

The behaviour of aerosol particles in the atmosphere includes their interaction with clouds as well as their interaction with precipitation. With respect to clouds, aerosol particles can act as cloud condensation nuclei (CCN) and ice nucleating particles (INP). In the case of rainfall, the aerosol particles can be scavenged by the raindrops. Therefore, aerosol particles can be scavenged from the atmosphere by nucleation scavenging when they act as CCN or INP or by impaction scavenging [Leong et al. 1982]. Aerosol particle scavenging is a critical mechanism that cleans atmospheric air [Radke et al. 1980].

We are interested on the case of aerosol particles swept by droplets during their fall. In this way, the information presented in this chapter will be directed to cleaning air by means of falling water droplets. The theoretical formulations carried out presuppose a flow around spherical drops. The aerosol particles in the models will also be considered spherical.

2.1.2.1 Collision mechanisms between droplets and aerosol particles

Several collision mechanisms have been proposed to describe scavenging[Seinfeld and Pandis, 2012]. (Figure 20):

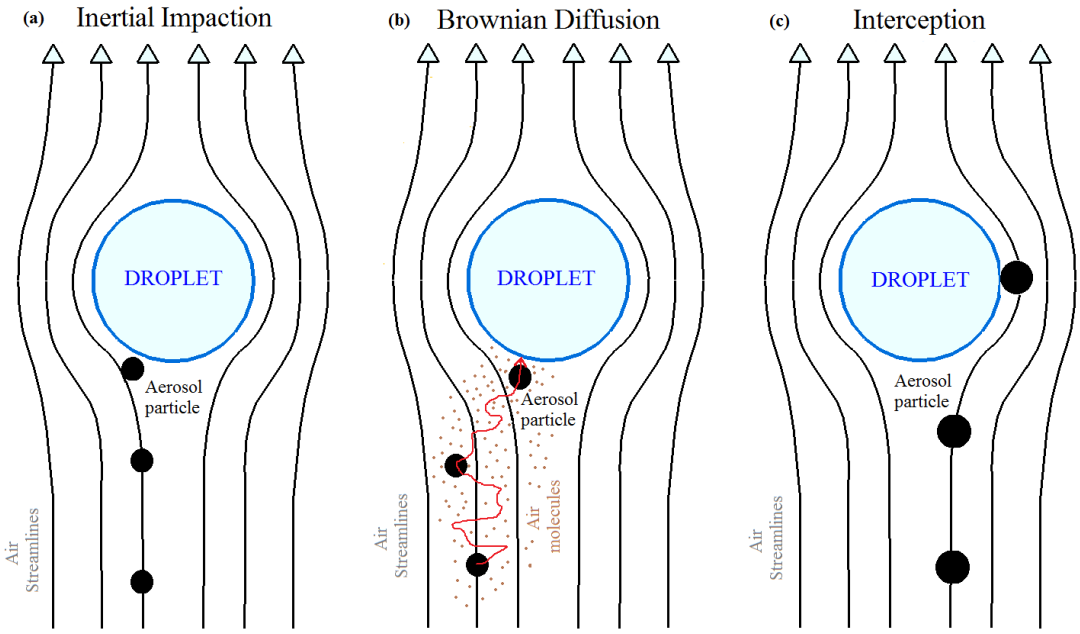

Figure 20: Schematic of the different mechanisms due to inertial effects that can contribute to a collision between an aerosol particle and a droplet: (a) Inertial impactation; (b) Brownian diffusion; (c) Interception. Adapted from Lohman et al. (2016)

- **Inertial impaction**
  This collision mechanism allegedly occurs when the aerosol particle contained in the airflow does not follow the streamlines. This is supposed to take place as a consequence of the inertia of the particle. The particle would deviate from the air streamline and collide with the droplet. This effect increases with increasing particle size.

- **Brownian diffusion**
  It is defined as the chaotic and irregular movement of a particle immersed in a fluid, caused by its collisions with the surrounding molecules of much smaller size. The air molecules hit the aerosol particles, generating this type of movement in the latter. Due to this chaotic movement, aerosol particles can modify their trajectory and be captured by a droplet. This effect increases as the particle size decreases, and is only relevant for particles with a diameter lower than 0.2 μm.

- **Interception**

  The collision of the aerosol particle with the droplet is possible if the aerosol particle does not deviate from the air streamline. If the streamline carries the particle at a distance from the drop below its radius, the particle will collide with the droplet. [Kulkarni et al., 2011].

Wang and Pruppacher (1977) showed that in the absence of electrical forces and by increasing the droplet size for the same particle size, the collision efficiency reached a minimum and then increased to a maximum. This maximum was supposed to be the result of a Reynolds number of drops large enough to cause eddies to fall off the back of the drops (Figure 22). Beard (1974) also speculated that the capture of small particles by eddies in the back of sufficiently large droplets occurred in Reynolds 30 < Re(drop) < 300 intervolute number.

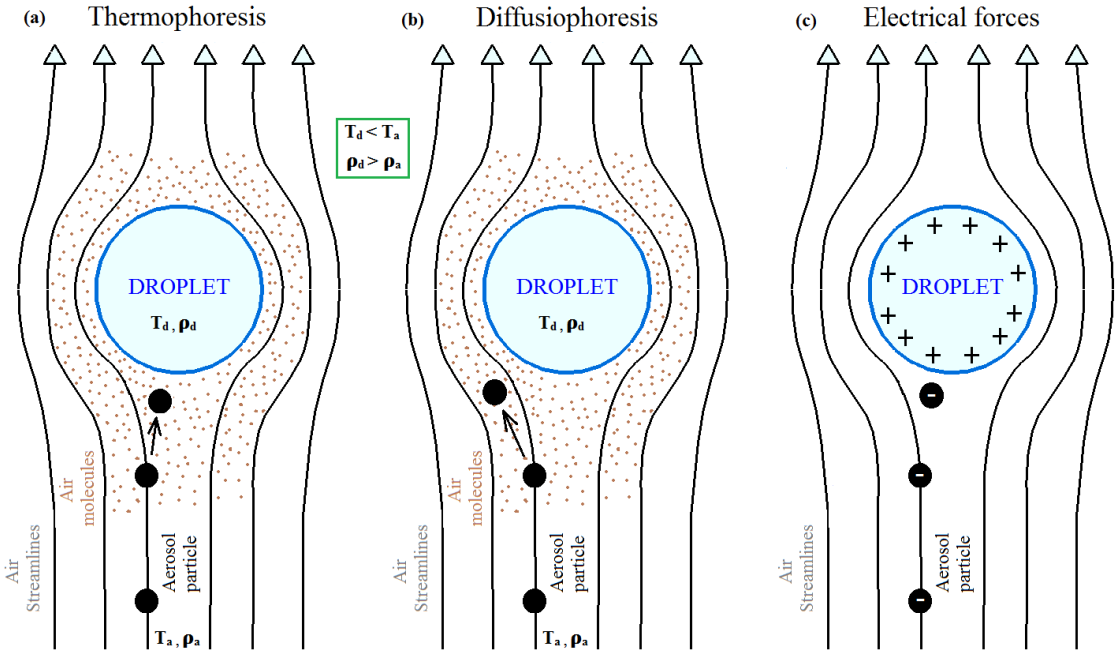

Figure 21: Schematic of the different mechanisms due to environmental effects that can contribute to a collision between an aerosol particle and a droplet: (a) Thermophoresis; (b) Diffusiophoresis; (c) Electrical forces. Adapted from Lohman et al. (2016)

As indicated, particle size dependent collision mechanisms show greater effectiveness for aerosol particles with radii lower than 0.2 μm or upper than 1 μm. The range of diameters between 0.2 μm and 1 μm is referred to as Greenfield Gap [Greenfield, 1957]. This decrease in collision efficiency can be compensated for by collision mechanisms dependent on environmental conditions or particle and droplet electrical charge [Tinsley et al., 2006a; Ladino, 2011]. These mechanisms are set out below (Figure 21):

- **Thermophoresis**

  When a relatively large particle encounters a gradient of temperature in the surrounding fluid, it tends to move towards lower temperature zones. This is because the particle is pushed by collisions with the air molecules –the higher temperature the faster they go. Some authros say that evaporating dropletswould

be cooler than the environment. This would drive particles into the droplets. Theoretical investigations have shown that thermophoretic velocity depends on many factors: the temperature gradient, the thermal conductivity of gas and particle, the Knudsen number ($Kn = \lambda/r$, where λ is the molecular mean free path of the gas surrounding an aerosol particle, and r is the radius of the particle), the momentum and the energy accommodation coefficients of gas molecules on the particle surface [Talbot et al., 1980; Yamamoto and Ishihara, 1988; Beresnev and Chernyak, 1995]. Also, experimental data have shown that the thermophoretic process of the aerosol in the gases depends to a large extent on the number of Knudsen [Tinsley et al., 2001]. Knudsen number is defines as:

$$K_n = \frac{2\lambda_a}{d_p} \quad \textbf{(13)}$$

where:

- d_p: diameter of the aerosol particle.
- λ_a: mean free path of an air molecule (Table 7).

Depending on the value of the Knudsen number, a different work regime will be presented, corresponding to those set out below:

- Continuum regime $(K_n \to 0)$
- Slip-flow region $(0 < K_n < 0.1)$
- Intermediate region $(0.1 < K_n < 10)$
- Free molecule regime $(K_n \to \infty)$

Table 7: Mean free path in air in nanometers for different temperatures, pressures and relative humidity values. Adapted from Jennings (1988)

Mean free path air (nm)				
Temperature (K)	Pressure (Pa)	Relative humidity		
		0%	50%	100%
288.15	1.011325×10^5	63.91	63.89	63.86
293.15	1.011325×10^5	65.43	65.44	65.48
296.15	1.011325×10^5	66.35	66.38	66.47
298.15	1.011325×10^5	66.91	67.01	67.14

Where the characteristics of each regime can be summarized [Wen, 1996]:

- In the continuum flow regime, the macroscopic properties (pressure, temperature and flow velocity etc.) are the mean values of a large number of molecules.
- In the slip flow regime, the fluid still behaves as a continuous medium but there is a slip of velocity on the solid boundary. There is a jump in temperature on the solid boundary due to rarefied effects

- In the intermediate regimen the flow largely depends on the discrete character of the fluid.
- In the free molecule regime the collision between molecules can be considered as negligible.

- **Diffusiophoresis**

  The gradient of vapor in the fluid surrounding the particles exerts a force from the areas of greatest saturation to those of low saturation due to vapor diffusion. Pure diffusiophoresis concerns the movement of an aerosol particle due to the gas momentum transfer process in an isothermal gas mixture with concentration gradients of chemical species. Experimental and theoretical results prevalently show that the diffusiophoretic velocity is independent of particle radius, for both large ($Kn < 1$) and small aerosol particles, i.e. $Kn > 1$ [Schmitt and Waldmann, 1960; Schmitt, 1961; Chernyak et al., 2001]. In the case of a binary mixture in steady condition (pure diffusiophoresis), the aerosol particle should move in the direction of the diffusive flux of the heavier gas molecules [Waldmann, 1959].

  As the evaporation of a droplet causes its temperature to fall, this will cause a temperature gradient to appear with the surrounding air. Therefore, for RH below 100% the aerosol particles are attracted to the droplets by the effect of temophoresis. In turn, this evaporation process will lead to the appearance of a gradient of vapor concentrations, as there is a flow of water molecules coming out of the drop. This is compensated for by a flow of air molecules moving in the opposite direction in order to maintain a constant total pressure.

  Thermo and diffusiophoresis were predicted by Stefan (1881) and subsequently observed by Facy (1958). If the only factor determining the temperature gradient between the droplet and the ambient is the water vapour condensation or evaporation, thermophoresis and diffusiophoresis will act in opposite directions. Therefore, it is important to evaluate the strength of thermophoretic and diffusiophoretic forces to assess which one is prevalent. Diffusiophoresis and thermophoresis act in the opposite way for both droplets in the evaporation process and for droplets in the condensation growth process. According to Slinn and Hales the effect of diffusiophoresis is predominant over thermophoresis for aerosol particle sizes less lower than 1 μm [Slinn and Hales, 1971]. Figure 22 shows how the collision efficiency decreases with increasing relative humidity for a particle diamenter of 50 μm.

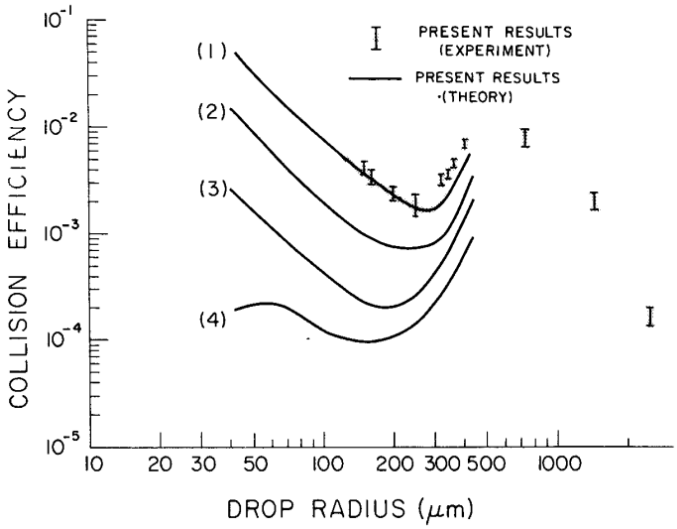

Figure 22*:* Efficiency with wich uncharged aerosol partciles of r_p=*0.25 μm* are collected by uncharged water drops as a function of collector drop size. Comparison of experiments [*RH = (23±2)%, T = (22±2)°C*] with values computed from theory of Grover at al. (1977) relative humidities of (1) *20%*, (2) *75%*, (3) *95%* and (4) *100%* [Wang and Pruppacher, 1977]

- **Electrical forces**

  This collision mechanism has been described when the aerosol particle and the droplet have opposite electrical charges. This generates forces of attraction that lead to the collision of the particles with the drop. In addition, this collision mechanism can also occur if either the droplet or the particle is not charged or even slightly with the same sign due to the formation of image charges [Tinsley and Leddon, 2013] as can be seen in Figure 23 .

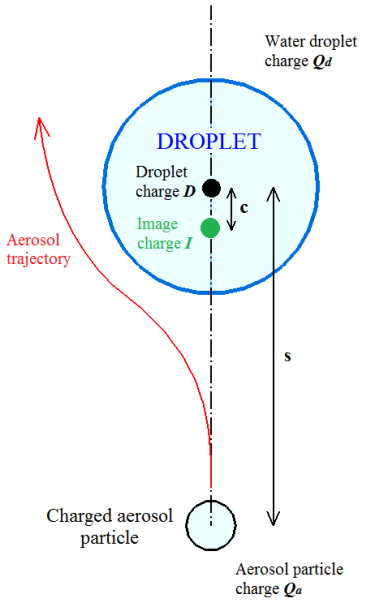

Figure 23: Scheme of the charged aerosol and image charge construction within a water droplet. The aerosol and falling droplet carry charges, Q_a and Q_d, respectively, with $Q_d = I + D$, where D is the non-image charge considered at the centre of the droplet. Adapted from Tripathi and Harrios (2002).

Lay, Dayan and Kerker (1977) measured the results with the application of electric charge, improving up to five times the efficiency previously calculated. This led to the conclusion that the elimination of micro-particles in the atmosphere could be substantially improved when rain was accompanied by thunderstorms. As for the electrical charge, it is observed in Figure 24 as for the particle size used in the experiment and with no charge, the collision efficiency increased with the increase in the density of the surface electrical charge of the droplet, independently of its sign, as a result of the attraction between droplets and particles by the charge induced in the latter. It is worth noting the appearance of a maximum, from which efficiency decreases as the absolute value of the load increases. This effect was already observed by Dennis, Lewis and Matteson (1975) and was justified by the charge transfer theory developed by Sartor (1954) in which it was considered that from a certain surface charge density value in the droplet there was a charge transfer from the droplet to the particles so that the induced charge attraction was reduced. In addition, the smaller the droplet size, the greater the collision efficiency and the lower the surface charge density required to reach its maximum value.

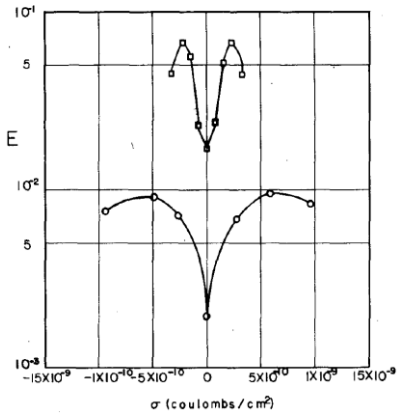

Figure 24: Collision efficiency E at terminal velocity versus surface charge density for drop radii A= 0.62 mm (□) and 1.82 mm (o) when aerosol particles are uncharged [Lay, Dayan and Kerker; 1977].

2.1.2.2 Collision efficiency

The collision efficieny (E) is an important parameter defined as the fraction of particles that collide with the drop in the cylindrical volume swept by it during the fall. Lohman et al. (2016) defines this parameter as the probability of a droplet colliding with a randomly placed particle in the droplet sweep volume. E can be quantitatively defined by the expression:

$$E = \frac{4x_0^2}{(D_d + d_p)^2} \quad \textbf{(14)}$$

where it is defined:

- D_d: diameter of the droplet
- d_p: diameter of the aerosol particle
- x_0: impact parameter

The impact parameter x_0 is defined as the maximum horizontal distance between the center of a droplet and the center of an aerosol particle to achieve the collision (Figure 25).

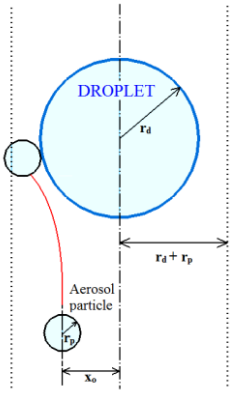

Figure 25: Schematic representation of the impact parameter $\mathbf{x_0}$ in a collision process between a droplet and an aerosol particle.

The collision efficiency will reach a value equal to the unit only when the droplet is capable of sweeping away all aerosol particles present in its sweeping volume. Otherwise, the value of this parameter will be less than the unit. The value of E can only reach a value upper than the unit when particles get scavenged by wake capture, that is, the rear capture of particles by the standing eddy at the downstream side of a drop [Beard, 1974; Beard and Grover, 1974]. Coalescence efficiency is the fraction of particles that are retained by the droplet after the collision. The product of this value by the collision coefficient is called the ***collection coefficient***. In many works, the scavenging of the particle after the collision with the drop is assumed. In this way, the coalescence factor would have a unit value and, therefore, the collision and collection coefficients would coincide.

Most of the theoretical models developed to obtain total collision efficiency have chosen to consider it as the sum of the individual values of each of the collision mechanisms as if they could be considered independently [Andronache et al., 2006; Bae et al., 2009; Croft et al., 2010]. However, the experimental results obtained show that in not all cases this approach can be considered adequate. Thus, in the case of particles belonging to the accumulation mode, which are those contained in the Greenfield Gap range [Greenfield, 1957], the estimates are only accurate when there are phoretic and/or electrical effects that compensate for the inefficiency of inertial mechanisms.

Taking the total collision efficiency as the sum of the different individual collision efficiencies due to the different collision mechanisms, it is obtained:

$$E_{Tot} = E_{imp} + E_{Br} + E_{int} + E_{Th} + E_{Diff} + E_{El} = E_{Br,I} + E_{Ph,E} \qquad \textbf{(15)}$$

where it is defined:

- E_{Tot}: total collision efficiency
- E_{Imp}: inertial impaction collision efficiency
- E_{Int}: interception collision efficiency

- E_{Th}: thermophoresis collision efficiency
- E_{Diff}: diffusiophoresis collision efficiency
- E_{El}: electrical forces collision efficiency
- $E_{Br,I}$: inertial collision mechanisms efficiency
- $E_{Ph,E}$: phoretic and electrical collision mechanisms efficiency

From the value of E_{Tot} ,the number of collisions between particles and droplets can be calculated [Lohman et al., 2016] by means of the expression:

$$N = KCt \quad \textbf{(16)}$$

where it is defined:

- N: number of collisions between particles and droplets
- C: concentration of particles
- t: elapsed time
- K: Collision Kernel. It is defined as:

$$K = \frac{\pi}{4} E_{Tot} \left(D_d + d_p\right)^2 \left|V_S(D_d) - v_S(d_p)\right| \quad \textbf{(17)}$$

where:

- $V_S(D_d)$: terninal fall velocity of the droplet
- $v_S(d_p)$: terminal fall velocity of the aerosol particle

From the above expressions it is evident that the collision number increases with the increase in droplet size due to the increase in volume swept by the droplet. However, collision efficiency increases with decreasing droplet size. Various formulations have been developed for the different components of collision efficiency to achieve mathematical expressions over the years. Park et al. (2005), Jung and Lee (1998) y Slinn (1983) provided expressions for the components of collision efficiency corresponding to the inertial phenomenon, i.e. Brownian motion, interception and impaction. For its part, Andronache et al. (2006), Wang and Pruppacher (1977) and Wang et al. (1978) provided expressions for the phoretic and electrical charge components. Various experimental studies were conducted to validate these expressions [Wang et al., 1978; Ladino et al. 2011a and 2013]. In turn, several studies measuring the concentration of aerosol particles in the air before and after their precipitation sweeping were performed [Laakso et al., 2003; Chate and Pranesha, 2004; Maria and Russell, 2005]. These studies obtained washout values higher than those estimated by theoretical formulations [Andronache et al., 2006].

2.1.2.2.1 Inertial collision mechanisms formulations:

The collision efficiencies corresponding to the Brownian motion mechanisms, interception and impaction are calculated independently and then summed into a single parameter corresponding to the efficiency of the inertial collision mechanisms (Figure 26):

$$E_{Br,I} = E_{Br} + E_{Int} + E_{Imp} \quad \textbf{(18)}$$

The numerical solution to this problem consists of calculating the collision efficiency for an isolated drop and then adding the number of drops present per unit volume of gas flow. This can be solved by applying the Stokes equation for air flow around a drop of water. However, obtaining a solution to this system of equations is extremely complex due to the great difficulty of the flow patterns that are influenced by the internal circulation of the droplets. Because of this, Slinn (1983) proposed a solution in which he combined experimental data with a theoretical dimensional analysis, making the solution to the problem significantly easier. Jung and Lee (1998) studied the collision efficiency due to Brownian diffusion and interception for a multiple fluid sphere system. They used the extended Kuwabara free vorticity model including the effects of induced internal circulation inside a liquid drop and of neighboring collectors. After comparing the results obtained with Slinn's formula, a high level of agreement was observed [Jung, Kim, and Lee, 2002].

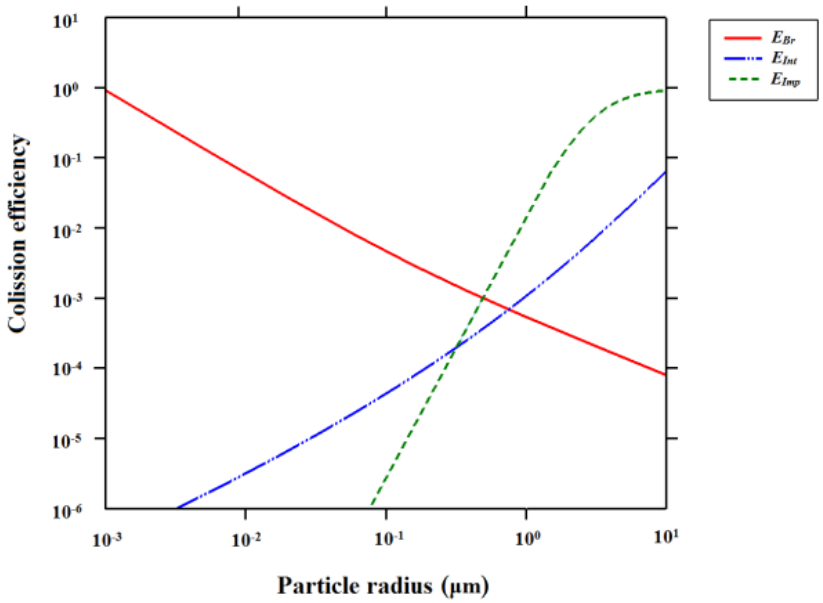

Figure 26: Comparison of collection efficiencies due to Brownian diffusion, interception and inertial impaction. Drop mass concentration is 50 g/m^3 and D_d is 1 mm. Adapted from Park et al. (2005)

Thus, the expression that calculates the collision efficiency due to Brownian movements is taken from Park et. al (2005) and it is given by [Nagare, 2016]:

$$E_{Br}(d_p, D_d) = 2\left(\frac{\sqrt{3}\pi}{4P_e}\right)^{\frac{2}{3}}\left[\frac{(1-\alpha)(3\sigma+4)}{J+\sigma K}\right]^{\frac{1}{3}} \quad \textbf{(19)}$$

where:

- α: packing density. Is it defined as the water volume present in a unit volume of air.
- σ: viscosity.
- J *and* K are the hydrodynamic factors given by:

$$J = 1 - \frac{6}{5}\alpha^{\frac{1}{3}} + \frac{1}{5}\alpha^2$$

$$K = 1 - \frac{9}{5}\alpha^{\frac{1}{3}} + \alpha + \frac{1}{5}\alpha^2$$

- P_e: Peclet number. It is defined as the ratio between the advective and diffusive transport rate and it is given by:

$$P_e = \frac{D_d V_S(D_d)}{D_{diff}} \quad \textbf{(20)}$$

where:

- D_{diff}: diffusion coefficient of aerosol particles. It is given by:

$$D_{diff} = \frac{k_B T_a \, C_c(d_p)}{3\pi\mu_a d_p} \quad \textbf{(21)}$$

where:

- k_B: Boltzmann constant
- T_a : air temperature
- k_B: Boltzmann constant
- T_a : air temperature
- $C_c(d_p)$: Cunningham slip correction factor. It is given by:

$$C_c(d_p) = 1 + \frac{2\lambda_a}{d_p}\left(1.257 + 0.4e^{\frac{-1.1 d_p}{2\lambda_a}}\right) \quad \textbf{(22)}$$

where λ_a is the mean free path of air molecules.

Furthermore, the expression that calculates the collision efficiency due to interaction effects is given by:

$$E_{Int}(d_p, D_d) = \frac{1-\alpha}{J + \sigma K}\left[\frac{\xi}{1+R} + \frac{1}{2}\left(\frac{\xi}{1+\tau}\right)^2 (3\sigma + 4)\right] \quad \textbf{(23)}$$

where $\xi = \frac{d_p}{D_d}$ is the ratio between particle and droplet diameters.

In the case of larger aerosol particles, the impact mechanism is predominant. Through the Stokes number (St), which defines the inertial impact properties of a particle, Calvert (1984) obtained the following expression for impact collision efficiency:

$$E_{Imp}(d_p, D_d) = \left(\frac{St}{St + 0.35}\right)^2 \quad \textbf{(24)}$$

with:

$$St = \frac{\rho_p d_p^{\,2} V_S(D_d)}{18\mu_a D_d} \quad \textbf{(25)}$$

In turn, from the formulation proposed by Slinn (1983) the following expressions for inertial collision efficiencies are obtained [Seinfield and Pandis, 2006; Wang et al., 2010]:

$$E_{Br}(d_p, D_d) = \frac{4}{ReSc}\left(1 + 0.4Re^{\frac{1}{2}}Sc^{\frac{1}{3}} + 0.16Re^{\frac{1}{2}}Sc^{\frac{1}{2}}\right) \quad \textbf{(26)}$$

$$E_{Int}(d_p, D_d) = 4\frac{d_p}{D_d}\left[\frac{\mu_a}{\mu_w} + \left(1 + 2Re^{\frac{1}{2}}\right)\frac{d_p}{D_d}\right] \quad \textbf{(27)}$$

$$E_{Imp}(d_p, D_d) = \left(\frac{\rho_w}{\rho_p}\right)^{\frac{1}{2}}\left(\frac{St - St^*}{St - St^* + \frac{2}{3}}\right)^{\frac{3}{2}} \quad \textbf{(28)}$$

where ρ_w and the ρ_p are water and particle densities, respectively and μ_w is the dynamic viscosity of water. Re is the Reynolds number which is defined as the ratio of inertial forces to viscous forces. This number si taken from Pruppacher and Klett (1997) as:

$$Re = \mathrm{e}^{Y}$$

where:

$$Y = -3.18657 + 0.992696X - 0.00153193X^2 - 0.000987059X^3 - 0.000578878X^4 + 0.000085517X^5 - 0.00000327815X^6$$

$$X = \ln(C_d R_e^2)$$

$$C_d R_e^2 = \frac{4D_d^3(\rho_w - \rho_a)g}{3\mu_a^2}$$

where $\rho_a$is the density of air and g is the gravity acceleration.

$$St = \frac{2\tau\left[V_S(D_d) - v_S(d_p)\right]}{D_d}$$

Wang et al. (2010) defines the relaxation times as:

$$\tau = \frac{(\rho_p - \rho_a)d_p^2 C_c}{18\mu_a}$$

Finally, it is defined as the critical Stokes number as the value from which a particle can be deposited in a droplet. Therefore, the impaction mechanism could only occur if it is met that $St > St^*$ where:

$$St^* = \frac{1.2 + \frac{1}{12} ln(1 + Re)}{1 + ln(1 + Re)} \quad \textbf{(29)}$$

2.1.2.2.2 Phoretic and electrical collision mechanisms formulations:

The collision efficiencies corresponding to the phoretic and electrical effects mechanisms are calculated independently and then summed into a single parameter corresponding to the efficiency of the phoretic and electrical collision mechanisms [Nagare, 2016]:

$$E_{Ph,E} = E_{Th} + E_{Df} + E_{El} \quad \textbf{(30)}$$

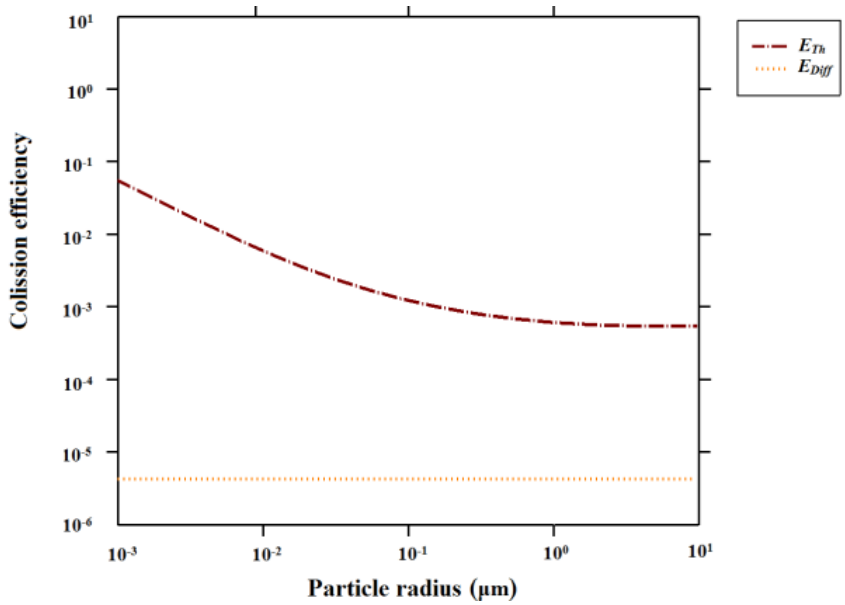

Figure 27: Comparison of collection efficiencies due to phoretic effects. Drop mass concentration is 50 g/m^3 and D_d is 1 mm. Adapted from formulation of Andronache et al. (2006).

The expression for thermophoresis collision efficiency is given by (Andronache et al. 2006):

$$E_{Th}(d_p, D_d) = \frac{4\gamma(2 + 0.6Re^{\frac{1}{2}}Pr^{\frac{1}{3}})(T_a - T_s)}{U(D_d)D_d} \quad \textbf{(31)}$$

where:

- T_a : air temperature
- T_s : droplet surface temperature

- P_r : Prandtl number. It is given by:

$$Pr = \frac{C_p \mu_a}{k_a} \tag{32}$$

- γ is defined as:

$$\gamma = \frac{2C_c \left(k_a + 5\frac{\lambda_a}{D_d} k_p\right) k_a}{5P_a \left(1 + 6\frac{\lambda_a}{D_d}\right)\left(2k_a + k_p + 10\frac{\lambda_a}{D_d} k_p\right)}$$

where:

- k_a: air thermal conductivity
- k_p: aerosol particle thermal conductivity
- P_a: atmospheric pressure
- λ_a: mean free path of an air molecule
- C_p: specific heat of air at constant pressure

The expression for diffusiophoresis collision efficiency is given by Andronache et al. 2006:

$$E_{Diff}(d_p, D_d) = \frac{4\beta(2 + 0.6Re^{\frac{1}{2}} Sc_w{}^{\frac{1}{3}}) \left(\frac{P_s^0}{T_s} - \frac{P_a^0 RH}{T_a}\right)}{U(D_d) D_d} \tag{33}$$

where:

- P_a^0: environment saturation vapor pressure
- P_s^0: droplet surface saturation vapor pressure
- β is defined as:

$$\beta = \frac{T_a D_w}{p}\left(\frac{M_w}{M_a}\right)^{\frac{1}{2}}$$

- Sc_w : Schmidt number for water vapor. It is given by:

$$Sc_w = \frac{\mu_a}{\rho_a D_w} \tag{34}$$

where:

- D_{Diff}: Diffusivity of water vapor in air.

The expression that calculates the collision efficiency due to electric charges is taken from Andronache (2004) and Davenport and Peters (1978) and it is given by:

$$E_{El}(d_p, D_d) = \frac{16KC_C Q_q}{3\pi\mu_a D_d^2 d_p U(D_d)} \tag{35}$$

where:

- Q: mean charges on the droplet.
- q: mean charges on the aerosol particle.

$$K = 9x10^9 Nm^2 C^{-2}$$

As can be observed, this formulation is based on the on Coulomb interactions.

Alternative expressions for forces due to thermophoresis and diffusiophoresis [Tinsley et al., 2006b] are given below:

$$F_{Th} = -\frac{6\pi\mu_a d_p (k_a + 2.5k_p Kn)k_a}{5(1+3Kn)\left(k_p + 2k_a + 5k_p Kn\right)p}\frac{2(T_a - T_s)}{D_d r^2} \quad \textbf{(36)}$$

$$F_{Df} = -\frac{3\pi\mu_a d_p (0.74) D_w M_a}{(1+\alpha Kn)M_w \rho_a}\frac{2\left(\rho_{v,a} - \rho_{v,s}\right)}{D_d r^2} \quad \textbf{(37)}$$

where:

- r: distance between the center of the droplet and the aerosol particle
- K_n : Knudsen number
- M_a: molecular weight of air
- M_w: molecular weight of water
- $\rho_{v,a}$: water vapor density in the air far from the droplet
- $\rho_{v,s}$: water vapor density at the droplet surface
- $\rho_{v,s}$: water vapor density at the droplet surface
- $\frac{2(T_a - T_s)}{D_d r^2}$: temperature gradient between the absolute temperature of the surrounding and the droplet surface
- $\frac{2\left(\rho_{v,a} - \rho_{v,s}\right)}{D_d r^2}$: vapor density gradient between the surrounding and the droplet surface

Wang et al. (1978) gave the α parameter as:

$$\alpha = 1.26 + 0.40\exp(-1.10Kn^{-1})$$

These expressions are only valid when a spherically symmetric inverse square fields is presented. This condition is not met if the drops are moving and therefore corrections to these formulas are necessary. The introduction of the coefficients of mean heat (f_h) and vapor ventilation (f_v) are introduced to take into account the movement of air in the flow of heat and water vapor [Tinsley, 2010], being obtained:

$$F_{Th} = \frac{C_{Th}}{r^2 f_h} \rightarrow C_{Th} = F_{Th} r^2 f_h \quad \textbf{(38)}$$

$$F_{Df} = \frac{C_{Df}}{r^2 f_v} \rightarrow C_{Df} = F_{Df} r^2 f_v \quad \textbf{(39)}$$

and, therefore [Wang et al. 1978]:

$$C_{Th} = -\frac{3\pi\mu_a d_p (k_a + 2.5 k_p Kn) k_a D_d (T_a - T_s) f_h}{5(1 + 3Kn)\left(k_p + 2k_a + 5k_p Kn\right) p} \quad \textbf{(40)}$$

$$C_{Df} = -\frac{3\pi\mu_a d_p (0.74) D_w M_a D_d \left(\rho_{v,a} - \rho_{v,s}\right) f_v}{2(1 + \alpha Kn) M_w \rho_a} \quad \textbf{(41)}$$

where:

- C_{Th}: thermophoresis inverse square force
- C_{Df}: diffusiophoresis inverse square force

In addition, the electric inverse square force is defined as [Tinsley, 2010]:

$$C_{El} = \frac{Qq}{4\pi\varepsilon_0} \quad \textbf{(42)}$$

It is important to know that in this expression the attraction of charges of opposite sign and the repulsion of charges of the same sign has been assumed. However, the image charge effect has not been taken into account. Taking each of the previously defined constants individually and from the definition of the Kernel collision it can be obtain its value for each of them [Ladino el al. 2011a]:

$$K_i = \frac{4\pi B_P C_i}{exp\left(\frac{2B_P C_i}{D_{diff} f_p d_p}\right) - 1} \quad \textbf{(43)}$$

where B_P corresponds to the mobility of particles.

Finally, the expression for the collision efficiency of each force is obtained as:

$$E_i = \frac{4K_i}{\pi\left(D_d + d_p\right)^2 \left[V_s(D_d) - v_s\left(d_p\right)\right]} \quad \textbf{(44)}$$

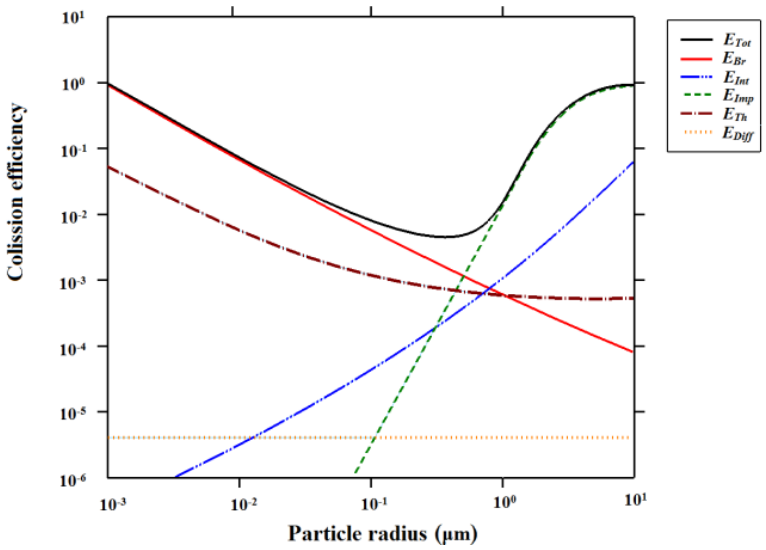

Figure 28: Comparison of collection efficiencies due to inertial and phoretic effects with the total collection efficiency as a sum of the individual efficiencies. Drop mass concentration is 50 g/m^3 and D_d is 1 mm. Adapted from formulation of Park et al. (2005) and Andronache et al. (2006)

A comparison of the different individual collision efficiencies for different particle sizes and the total efficiency resulting from the sum of all of them can be seen in Figure 28.

2.1.3 Aerosols size distribution

When all particles in a system have the same size or well-defined molecular weight, it is called monodisperse. But if the particles are not of the same size, the system is subdivided into parts each made up of uniform particles. Each of the parts into which the system is subdivided is a monodisperse system. If the number of fractions is small, the system is paucidisperse, and if it is very large, the system is polydisperse. It is the case of polydispersed aerosols that is most common. In this way, the aerosol particle characterization method will be carried out by means of a statistical study that will allow to obtain a numerical distribution of the different radii of particles [Grainger, 2017]. Note that any of the radii defined above in the equations may be used. The geometric and aerodynamic radius will be used in this work. Assuming that the number of droplets in a given size range $N(r)$ can be obtained integrally from a differential density distribution function of particle sizes $n(r)$, it would be obtained:

$$\mathrm{N(r)} = \int_{\mathrm{r}}^{\mathrm{r+dr}} \mathrm{n(r)dr} \qquad \textbf{(45)}$$

Thus obtaining the number of particles with a radius between r and $r + dr$. In this way and by clearing the previous equation, it is obtained:

$$\mathrm{n(r)} = \frac{\mathrm{dN(r)}}{\mathrm{dr}}$$

To obtain the total number of particles N_0, the integral should be extended to all possible size ranges:

$$N_0 = \int_0^\infty n(r)dr$$

Morove, the effective radius of the aerosol particle distribution shall be defined as the ratio of the third moment of the patcile size distribution function considered between the second moment. This effective radius, understood as the average radius weighted by the area of the drop, will therefore be expressed as:

$$r_e = \frac{m_3}{m_2} = \frac{\int_0^\infty r^3 n(r)dr}{\int_0^\infty r^2 n(r)dr} \tag{46}$$

Analogous to that used in the calculation of the effective particle radius, it will be applied a similar reasoning for the calculation of other characteristics of the aerosol, such as the particle surface, its volume and mass distribution. In this way, by means of the application of a differential density distribution function of particle area, a(r), it would be obtained:

$$A(r) = \int_r^{r+dr} a(r)dr \tag{47}$$

Note that function $A(r)$ represents the area of particles per unit volume such that their radii are between r and $r + dr$. In this way and by clearing the previous equation, it will be obtained:

$$a(r) = \frac{dA(r)}{dr}$$

To obtain the total area particles A_0 per unit volume, the integral should be extended to all possible size ranges:

$$A_0 = \int_0^\infty a(r)dr$$

Since the spherical particle hypothesis is considered, it can be deduced that:

$$a(r) = \frac{dA(r)}{dr} = \frac{dA(r)}{dN}\frac{dN}{dr} = 4\pi r^2 n(r) \tag{48}$$

And, therefore, it is concluded that:

$$A_0 = \int_0^\infty 4\pi r^2 n(r)dr = 4\pi \int_0^\infty r^2 n(r)dr \tag{49}$$

Similarly, the volume of the particles of the aerosol may be calculated by applying a differential density distribution function of droplet volume, $v(r)$:

$$V(r) = \int_r^{r+dr} v(r)dr \tag{50}$$

Note that the $V(r)$ function represents the volume of particles per unit volume such that their radii are between r and $r + dr$. In this way and by clearing the previous equation, it is obtained:

$$\mathrm{v(r)} = \frac{\mathrm{dV(r)}}{\mathrm{dr}}$$

To obtain the total area of aerosol particles V_0 per unit volume, the integral should be extended to all possible size ranges:

$$\mathrm{V_0} = \int_0^\infty \mathrm{v(r)dr}$$

Since the spherical particle hypothesis is considered, it can be deduced that:

$$\mathrm{v(r)} = \frac{\mathrm{dV(r)}}{\mathrm{dr}} = \frac{\mathrm{dV(r)}}{\mathrm{dN}}\frac{\mathrm{dN}}{\mathrm{dr}} = \frac{4}{3}\pi \mathrm{r^3 n(r)} \quad \textbf{(51)}$$

And, therefore, it is concluded that:

$$\mathrm{V_0} = \int_0^\infty \frac{4}{3}\pi \mathrm{r^3 n(r)dr} = \frac{4}{3}\pi \int_0^\infty \mathrm{r^3 n(r)dr} \quad \textbf{(52)}$$

Finally, and following the same reasoning, the droplet mass of the aerosol can be calculated by applying a differential density distribution function of droplet mass $m(r)$:

$$\mathrm{M(r)} = \int_\mathrm{r}^{\mathrm{r+dr}} \mathrm{m(r)dr} \quad \textbf{(53)}$$

Note that the $M(r)$ function represents the volume of the particles per unit volume such that their radii are between r and $r + dr$. In this way and by clearing the previous equation, it is obtained:

$$\mathrm{m(r)} = \frac{\mathrm{dM(r)}}{\mathrm{dr}}$$

To obtain the total mass of particles M_0 per unit volume, the integral should be extended to all possible size ranges:

$$\mathrm{M_0} = \int_0^\infty \mathrm{m(r)dr}$$

From the particle density of the aerosol ρ_p and that this can be defined as:

$$\rho_p = \frac{\mathrm{dM(r)}}{\mathrm{dV(r)}} = \frac{\mathrm{dM(r)}}{\mathrm{dr}}\frac{\mathrm{dr(r)}}{\mathrm{dV(r)}} = \frac{\mathrm{m(r)}}{\mathrm{v(r)}}$$

So that:

$$m(r) = \rho_p v(r)$$

Since the spherical particle hypothesis is considered, it can be deduced that:

$$m(r) = \frac{4}{3}\pi r^3 \rho_p n(r) \quad \textbf{(54)}$$

And, therefore, assuming that the particle density remains unchanged, it is concluded that:

$$M_0 = \int_0^\infty \frac{4}{3}\pi r^3 \rho n(r) dr = \frac{4}{3}\pi\rho_p \int_0^\infty r^3 n(r) dr \quad \textbf{(55)}$$

It can therefore be deduced from the above that:

$$r_e = \frac{m_3}{m_2} = \frac{\int_0^\infty r^3 n(r) dr}{\int_0^\infty r^2 n(r) dr} = \frac{\frac{V_0}{\frac{4}{3}\pi}}{\frac{A_0}{4\pi}} = \frac{3V_0}{A_0} \quad \textbf{(56)}$$

And, at the same time:

$$r_e = \frac{m_3}{m_2} = \frac{\int_0^\infty r^3 n(r) dr}{\int_0^\infty r^2 n(r) dr} = \frac{\frac{M_0}{\frac{4}{3}\pi\rho}}{\frac{A_0}{4\pi}} = \frac{3M_0}{\rho A_0} \quad \textbf{(57)}$$

At this point, it is time to consider a differential density distribution function for the calculation of the above properties. As is well known, the distribution functions that can be applied are infinite. Some examples of the most common distribution functions applied in the study of aerosol are shown in
Table 8.

Table 8: Some distribution functions applied to aerosols.

DISTRIBUTION FUNCTION	DIFFERENTIAL DENSITY DISTRIBUTION OF PARTICLE RADII
Normal	$n(r) = \frac{N_0}{\sqrt{2\pi}\sigma_0} e^{-\frac{(r-\mu_0)^2}{2\sigma_0^2}}$
Log-Normal	$n(r) = \frac{N_0}{\sqrt{2\pi}\sigma\, r} e^{-\frac{(\ln r-\mu)^2}{2\sigma^2}}$
Gamma	$n(r) = ab^2 r e^{-br}$

DISTRIBUTION FUNCTION	DIFFERENTIAL DENSITY DISTRIBUTION OF PARTICLE RADII
Modified Gamma	$n(r) = a\dfrac{r^{\alpha}e^{-br^{\gamma}}}{\frac{1}{\gamma}b^{-\frac{\alpha+1}{\gamma}}\Gamma\left(\frac{\alpha+1}{\gamma}\right)}$
Inverse Modified Gamma	$n(r) = a\dfrac{r^{-\alpha}e^{-br^{-\gamma}}}{\frac{1}{\gamma}b^{-\frac{\alpha-1}{\gamma}}\Gamma\left(\frac{\alpha-1}{\gamma}\right)}$
Regularized Power Law	$n(r) = a\,\alpha\,\gamma\,b^{\alpha-2}\dfrac{r^{\alpha-1}}{\left[1+\left(\frac{r}{b}\right)^{\alpha}\right]^{\gamma}}$

For instance, the normal distribution function is given by:

$$f(x) = \frac{1}{\sqrt{2\pi}\sigma}e^{-\frac{(x-\mu)^2}{2\sigma^2}} \quad \text{donde } -\infty < x < +\infty$$

which, when applied to the model, would be obtained:

$$n(r) = \frac{N_0}{\sqrt{2\pi}\sigma_0}e^{-\frac{(r-\mu_0)^2}{2\sigma_0^2}} \tag{58}$$

Due to the nature of this distribution function and the fact that it would allow the use of negative radii (which makes no physical sense for the problem under study), its adjustment results in a very high standard deviation value. In this way, it will be opted for a normal distribution of the neperian logarithm of the particle radius, which will allow to eliminate the problem of negative radii:

$$n_l(\ln r) = \frac{dN(\ln r)}{d\ln r} = \frac{N_0}{\sqrt{2\pi}\sigma}e^{-\frac{(\ln r-\mu)^2}{2\sigma^2}} \tag{59}$$

Where the values of the mean and standard deviation are defined as:

$$\mu = \frac{\int_{-\infty}^{\infty}\ln r\, n_l(\ln r)d(\ln r)}{\int_{-\infty}^{\infty}n_l(\ln r)d(\ln r)} = \frac{1}{N_0}\int_{-\infty}^{\infty}\ln r\, n_l(\ln r)d(\ln r) = \ln r_m \tag{60}$$

$$\sigma^2 = \frac{1}{N_0}\int_0^{\infty}(\ln r-\mu)^2 n_l(\ln r)d(\ln r) \tag{61}$$

With $r_m$being the average radius of the distribution. For reasons of simplicity, it will be able to express the above expressions in terms of r and dispense with the neperian logarithm. To this end, the following equality will be applied:

$$\frac{\mathrm{d}\ln \mathrm{r}}{\mathrm{dr}} = \frac{1}{\mathrm{r}}$$

And substituting in the equations:

$$\begin{aligned} \mathrm{n(r)} &= \frac{\mathrm{dN(r)}}{\mathrm{dr}} = \frac{\mathrm{dN(ln\,r)}}{\mathrm{dr}} = \frac{\mathrm{dN(ln\,r)}}{\mathrm{d(ln\,r)}}\frac{\mathrm{d(ln\,r)}}{\mathrm{dr}} = \mathrm{n_l(ln\,r)}\frac{\mathrm{d(ln\,r)}}{\mathrm{dr}} \\ &= \frac{\mathrm{N_0}}{\sqrt{2\pi}\sigma\,\mathrm{r}}\mathrm{e}^{\left[-\frac{(\ln \mathrm{r}-\mu)^2}{2\sigma^2}\right]} = \frac{N_0}{\sqrt{2\pi}\ln\sigma_g\ r}e^{\left[-\frac{(\ln r-\ln r_m)^2}{2(\ln\sigma_g)^2}\right]} \end{aligned} \quad \textbf{(62)}$$

It is noted that σ_g must be larger than the unit for σ to be positive. When its value is the unit, it will be a monodispersed distribution, while for values above it, it will be a polydispersed distribution. The most common values are between 1.5 and 2.

Finally, Table 9 shows the properties of the normal and log-normal distributions that will be applicable for the treatment of aerosol particles.

Table 9: Properties of the normal and log-normal distributions applied to aerosols.

	MOST COMMON PROBABILITY DISTRIBUTIONS IN AEROSOLS	
	NORMAL	**LOG-NORMAL**
Differential density distribution of particle radii	$\mathrm{n(r)} = \frac{\mathrm{N_0}}{\sqrt{2\pi}\sigma_0}\mathrm{e}^{-\frac{(\mathrm{r}-\mu_0)^2}{2\sigma_0^2}}$	$\mathrm{n(r)} = \frac{\mathrm{N_0}}{\sqrt{2\pi}\sigma\,\mathrm{r}}\mathrm{e}^{-\frac{(\ln \mathrm{r}-\mu)^2}{2\sigma^2}}$
	μ_0	$\mu = \ln \mu_g$
	σ_0	$\sigma = \ln \sigma_g$
	$\mathrm{r_m} = \mu_0$ | $\mathrm{r_M} = \mu_0$	$\ln(\mathrm{r_m}) = \mu$ | $\ln(\mathrm{r_M}) = \mu - \sigma^2$
	$\mathrm{m_i} = \mathrm{N_0 e}^{\left(\mathrm{i}\mu_0 + \frac{\mathrm{i}^2\sigma_0^2}{2}\right)}$	$\mathrm{m_i} = \mathrm{N_0 e}^{\left(\mathrm{i}\mu + \frac{\mathrm{i}^2\sigma^2}{2}\right)}$
Differential density distribution of particle areas	$\mathrm{a(r)} = \frac{\mathrm{A_0 r}^2}{\sqrt{2\pi}\sigma_\mathrm{a}}\mathrm{e}^{-\frac{(\mathrm{r}-\mu_\mathrm{a})^2}{2\sigma_\mathrm{a}^2}}$	$\mathrm{a(r)} = \frac{\mathrm{A_0}}{\sqrt{2\pi}\sigma_\mathrm{a}\,\mathrm{r}}\mathrm{e}^{-\frac{(\ln \mathrm{r}-\mu_\mathrm{a})^2}{2\sigma_\mathrm{a}^2}}$
	$\mathrm{A_0} = 4\pi\mathrm{N_0}$	$\mathrm{A_0} = 4\pi\mathrm{N_0 e}^{(2\mu+2\sigma^2)}$
	$\mu_\mathrm{a} = \mu_0$	$\mu_\mathrm{a} = \mu + 2\sigma^2$
	$\sigma_\mathrm{a} = \sigma_0$	$\sigma_\mathrm{a} = \sigma$
Differential density distribution of particle volumes	$\mathrm{v(r)} = \frac{\mathrm{V_0 r}^3}{\sqrt{2\pi}\sigma_\mathrm{v}}\mathrm{e}^{-\frac{(\mathrm{r}-\mu_\mathrm{v})^2}{2\sigma_\mathrm{v}^2}}$	$\mathrm{v(r)} = \frac{\mathrm{V_0}}{\sqrt{2\pi}\sigma_\mathrm{v}\,\mathrm{r}}\mathrm{e}^{-\frac{(\ln \mathrm{r}-\mu_\mathrm{v})^2}{2\sigma_\mathrm{v}^2}}$
	$\mathrm{V_0} = \frac{4}{3}\pi\mathrm{N_0}$	$\mathrm{V_0} = \frac{4}{3}\pi\mathrm{N_0 e}^{\left(3\mu+\frac{9}{2}\sigma^2\right)}$
	$\mu_\mathrm{a} = \mu_0$	$\mu_\mathrm{v} = \mu + 3\sigma^2$
	$\sigma_\mathrm{a} = \sigma_0$	$\sigma_\mathrm{v} = \sigma$

	MOST COMMON PROBABILITY DISTRIBUTIONS IN AEROSOLS	
	NORMAL	**LOG-NORMAL**
Differential density distribution of particle mass	$m(r) = \frac{M_0 r^3}{\sqrt{2\pi}\sigma_v} e^{-\frac{\left(r-\mu_m\right)^2}{2\sigma_m^2}}$	$m(r) = \frac{M_0}{\sqrt{2\pi}\sigma_m r} e^{-\frac{\left(\ln r-\mu_m\right)^2}{2\sigma_m^2}}$
	$M_0 = \frac{4}{3}\pi\rho N_0$	$M_0 = \frac{4}{3}\pi\rho N_0 e^{\left(3\mu+\frac{9}{2}\sigma^2\right)}$
	$\mu_m = \mu_0$	$\mu_m = \mu + 3\sigma^2$
	$\sigma_m = \sigma_0$	$\sigma_m = \sigma$

2.2 Characteristics of droplets

2.2.1 Evaporation rate of a droplet

During evaporation, the number of molecules leaving the surface of the droplet exceeds the number of molecules arriving. Pruppacher and Klett (1997) proposed some expressions to estimate the rate of evaporation (droplet size variation as a function of time) and the time required for a droplet to evaporate completely, the latter known as the droplet lifetime or drying time:

$$\frac{dD_d}{dt} = \frac{4D^*_v M_w}{R_v \rho_w D_d}\left(\frac{p_a^0}{T_a} - \frac{p_s^0}{T_s}\right)\phi \quad for\ D_d > \lambda_a \tag{63}$$

where it is defined:

- D_d: diameter of the droplet
- t: residence time of the droplet
- R_v: gas constant for water vapor
- ρ_w: density of water
- p_a^0: environment saturation vapor pressure
- p_s^0: droplet surface saturation vapor pressure
- ϕ: Fuchs correction factor (it is oly needed for $D_d < 1\ \mu m$)
- T_a: environment temperature
- T_s: droplet surface temperature

with:

$$T_s = T_a + \frac{L_e \rho_w}{4k^*_a} D_d \frac{dD_d}{dt} \tag{64}$$

where it is defined:

- k^*_a: Air modified thermal conductivity

- L_e: Evaporation latent heat

As it can be seen, the evaporation rate depends on the rate at which steam can disperse away from the droplet. It should be noted that this equation also applies to the process of droplet condensation and one or the other case will be presented according to the sign of $\left(\frac{p_a^0}{T_a} - \frac{p_s^0}{T_s}\right)$. If there is a negative sign, there will be a process of evaporation of the droplet. Otherwise, condensation will occur. Calculations show how smaller droplets adapt more quickly to environmental conditions [Nagare et al., 2015]. On the other hand, the droplet lifetime it will be obtained as:

$$\int_{D_0}^{0} D_d d(D_d) = \int_0^t \frac{4D_v^* M_w}{R_v \rho_w}\left(\frac{p_a^0}{T_a} - \frac{p_s^0}{T_s}\right) dt$$

and integrating the equation and clearing is obtained:

$$t = \frac{R_v \rho_w D_d^2}{8 D_v^* M_w \left(\frac{p_a^0}{T_a} - \frac{p_s^0}{T_s}\right)} \quad for\ D_d \geq 1\ \mu m \tag{65}$$

2.2.2 Effective surface tension in a water droplet

Due to the ejection of water droplet molecules into the air around them, a phenomenon associated with a net flow of momentum, a "reaction pressure" is produced in the liquid as a result of the law of action and reaction. This phenomenon leads to a modification of the effective surface tension values of the water droplets.

As a result, it is observed that when the relative humidity of the air surrounding the drop increases, the value corresponding to the effective surface tension decreases for the same ambient temperature as can be observed in Figure 29. As shown in the figure, this decrease in the effective surface tension as the relative humidity increases can be considered practically linear.

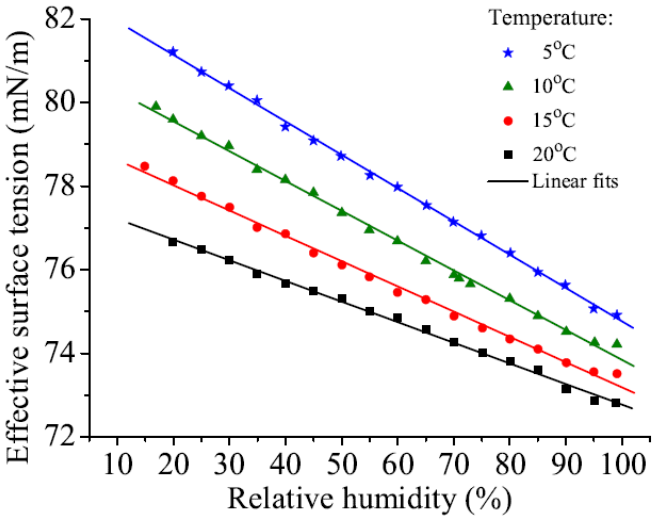

Figure 29: Effective surface tension vs. relative humidity in a 2-8 mm diameter pure water drop [Pérez-Díaz et al., 2017]

This interesting phenomenon that attributes surfactant properties to water steam could be applied in real cases as a way to increase the wetting of solid particles by decreasing the effective surface tension of water droplets on their air-water contact surface. In this way, the effective surface tension could be modified by controlling the ambient humidity, avoiding the use of harmful chemicals that are currently used with this purpose [Pérez-Díaz et al., 2013].

Chapter 3

Materials and methods

3.1 Fog generating nozzle

The Counterfog® fog generation system is based on the use of a nozzle to which coompressed air and water are supplied specifically designed for the project.

3.1.1 Counterfog® Nozzle: nozzle model selection

Six air assisted nozzle models (from model A to model F) were designed during the Counterfog® project (Figure 30). In addition, different features were added to each model typical of other nozzle types with the aim of making better designs [D1.1, 2014]. After carrying out simulation tests with every model using ANSYS Fluent [ANSYS, 2016] software, an analysis was carried out of the results obtained for droplet size, flow rates and type of cones generated. Based on this analysis, the two nozzle models described below were chosen:

- **Nozzle model B**
  This is a mixing nozzle with an air-assisted ring chamber. Water and air interact in a cylindrical mixing chamber where three air jets collide with a single water jet at an angle of 25 - 30°. The nozzle outlet piece produces a hollow fog cone. Additives can be added through a single inlet into the nozzle which forms a 90° angle with the direction of the fog flow.

- **Nozzle model F**
  It is an air-assisted nozzle based on the twin-swirl effect [Omer and Ashgriz, 2011]. From a basic design of a solid conical axial nozzle in spiral, a second chamber was implemented in the nozzle. The water is introduced into the second chamber after a previous rotational movement has been applied. The air then collides tangentially with the water, contributing to the best atomization of the water. In this type of nozzle a full fog cone is generated. Additives are added via four inlets located outside and immediately after the nozzle outlet duct which forms a 90° angle with the direction of fog flow in the nozzle.

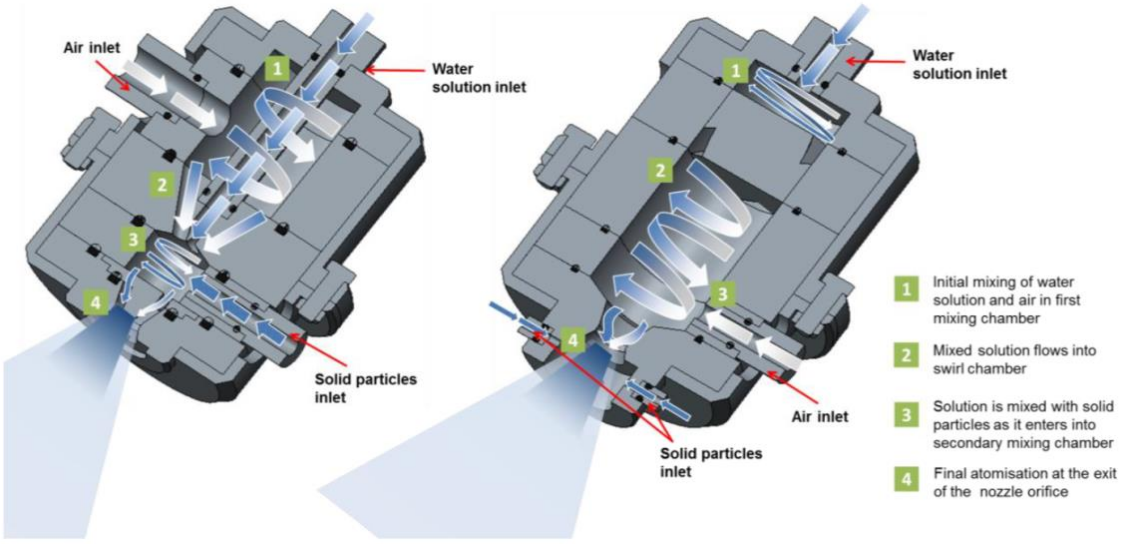

Figure 30: Working principle of the **Counterfog**® nozzle detailed designs [D 1.2, 2014]

3.1.2 Counterfog® Nozzle: nozzle model manufacture

After a series of improvements [D 1.4, 2015], these nozzles were manufactured. These nozzles will now be designated as B1:1 and F1:1 for model B and F respectively. In addition, type AA 6082-T6 aluminium (Table 10) was used for the manufacture of these nozzles (Figure 31 and Figure 32). The selection of this material was based to its good corrosion resistance and ease of machining.

Table 10: Chemical composition of aluminium AA 6082-T6

%	Si	Fe	Cu	Mn	Mg	Cr	Zn	Ti	Other elements		Al
									Each	Total	
Minimum	0.70	0.00	0.00	0.40	0.60	0.00	0.00	0.00	0.00	0.00	95.2
Maximum	1.30	0.50	0.10	1.00	1.20	0.25	0.20	0.10	0.05	0.10	98.3

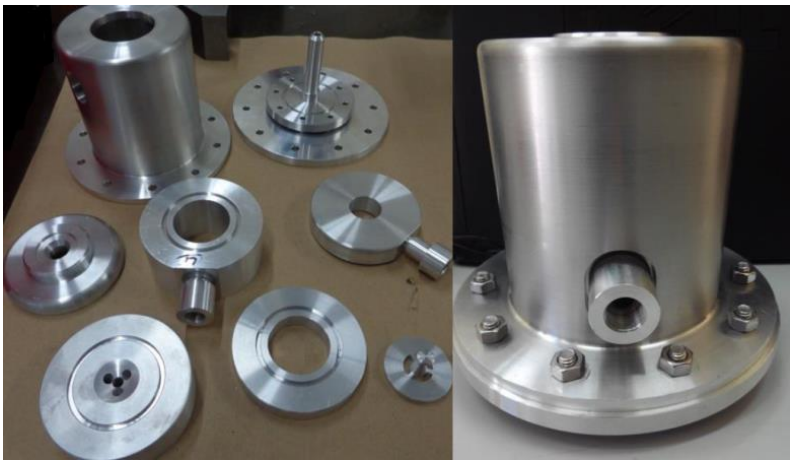

Figure 31: B1:1 nozzle parts and complete assembly

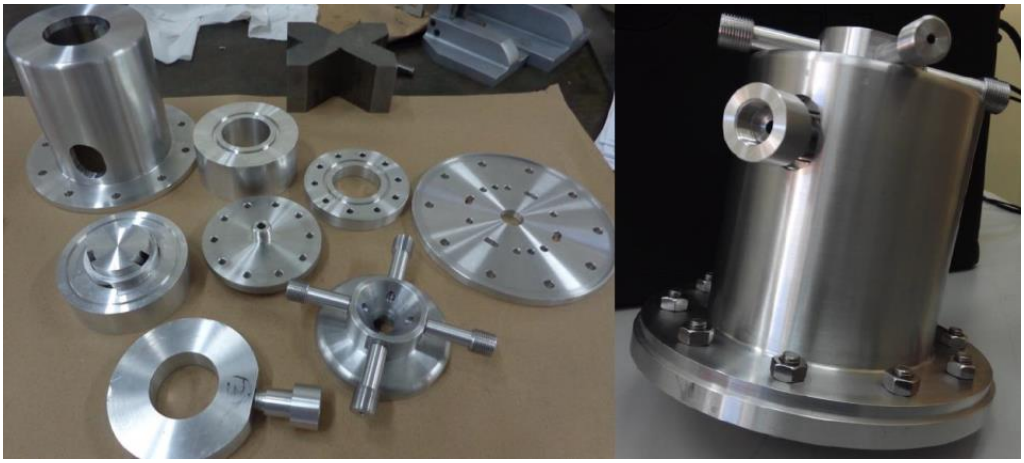

Figure 32: F1:1 nozzle parts and complete assembly

Theoretical results, together with the testing of the B1:1 and F1:1 nozzles outside the laboratory, confirmed the impossibility of their application in the test rooms designed for this purpose (Figure 33). It turned out that the width and length of the cone generated by the nozzles was too large for the dimensions of the rooms. In addition, the required flows exceeded those that could be provided by the facility.

Figure 33: External test with B1:1 nozzle

As a result, the nozzles were redesigned to scale using Solid Edge software, resulting in the following final set of nozzles (Table 11):

Table 11: Final set of **Counterfog**® nozzles.

Nozzle designation	Model	Scale
B1:1	B	1:1
F1:1	F	1:1
B1:2	B	1:2
F1:2	F	1:2
B1:3	B	1:3
F1:3	F	1:3

Each of these nozzles was manufactured (Figure 36 and Figure 37). On this occasion, type AA 7075-T6 aluminium (Table 12) was used for the manufacture of these nozzles (Figure 34 and Figure 35). The choice of this new material was due to its common use and good mechanical properties in relation to its density.

Table 12: Chemical composition of aluminium AA 7075-T6.

%	Si	Fe	Cu	Mn	Mg	Cr	Zn	Ti	Other elements		Al
									Each	Total	
Minimum	0.00	0.00	1.20	0.00	2.10	0.18	5.10	0.00	0.00	0.00	86.92
Maximum	0.40	0.50	2.00	0.30	2.90	0.28	6.10	0.20	0.25	0.15	91.42

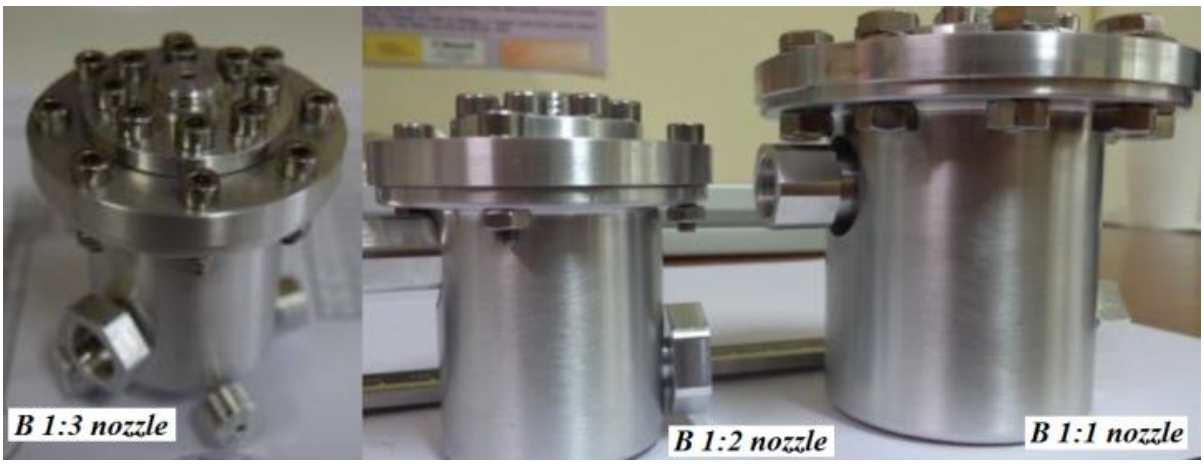

Figure 34: B nozzle model at different scales

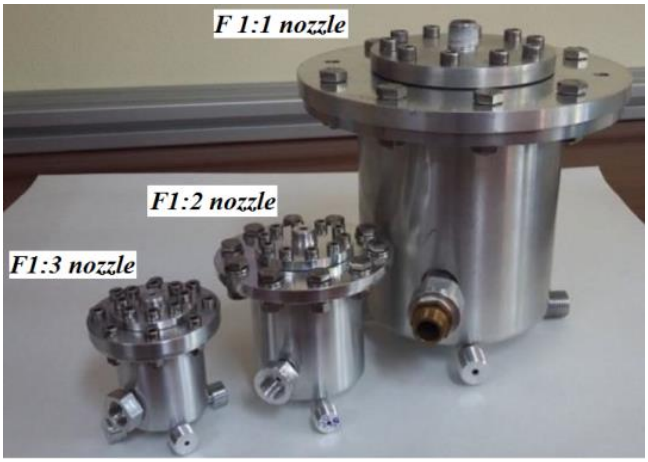

Figure 35: F nozzle model at different scales.

In the work presented in this doctoral thesis, only the B1:2 nozzle will be taken into account, as this work is focused on laboratory tests that prevent the use of the B1:1 nozzle. In addition, and as will be justified below, model B will be chosen over model F for flow reasons. For similar reasons, the use of the B1:2 nozzle will be chosen over the B1:3 nozzle. Figure 36 and Figure 37 show details of the interior of the nozzle models F and B, respectively.

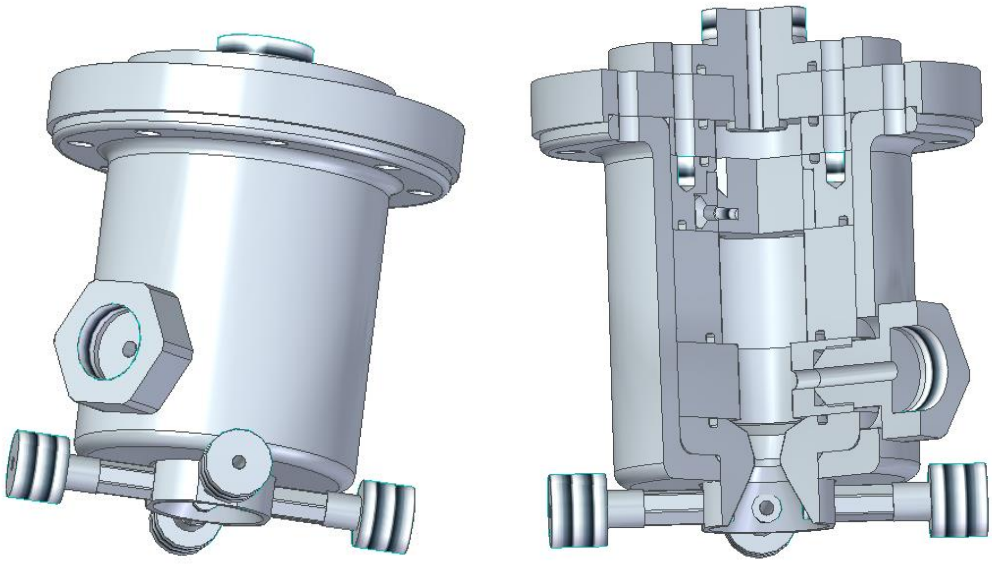

Figure 36: Three-dimensional F1:2 nozzle model design

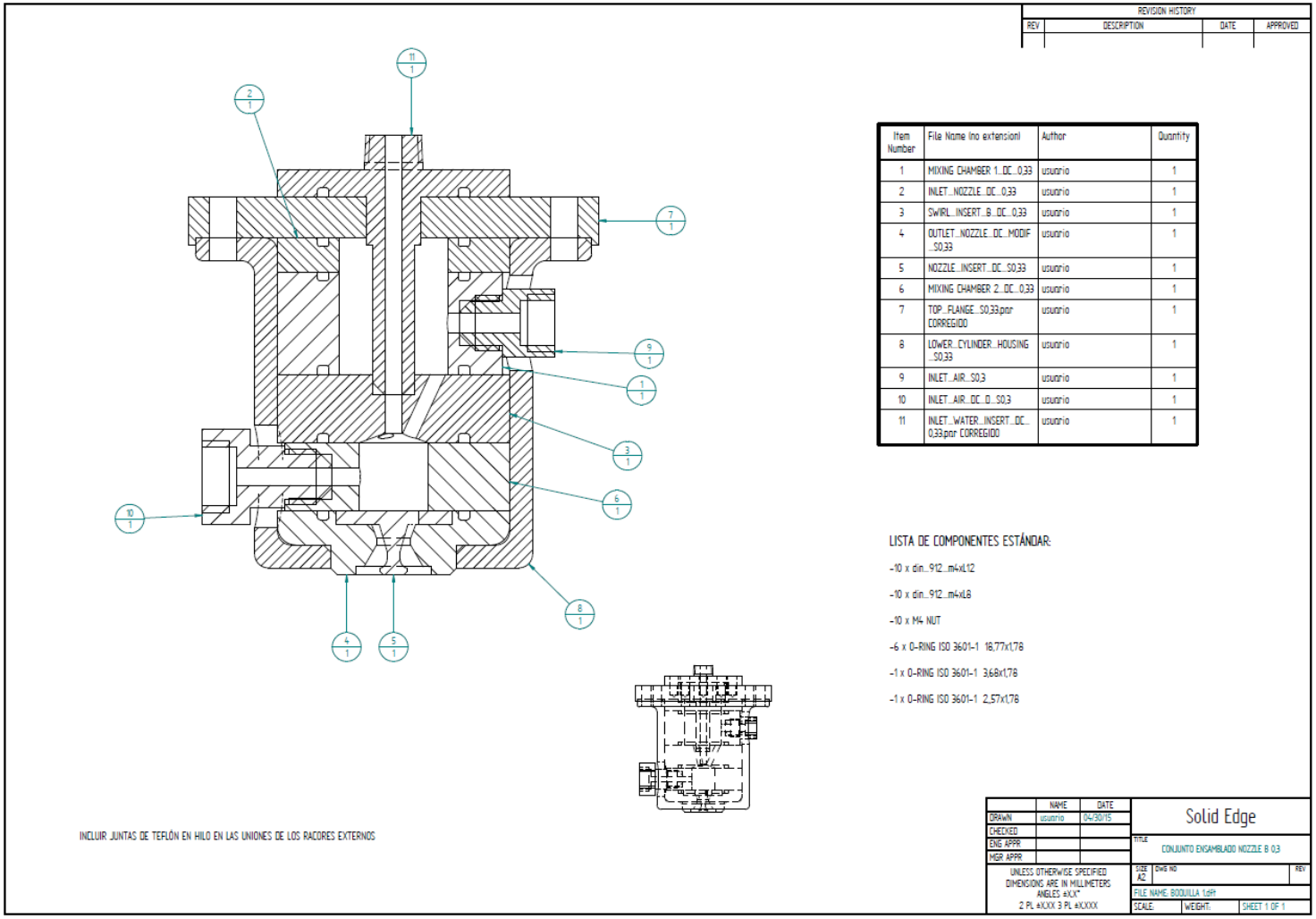

Figure 37: B1:3 nozzle assembly drawing

3.2 Counterfog® Laboratory

3.2.1 Introduction

The fog dynamics laboratory has been developed to carry out experimental measurements of fog dynamics with narrow control of temperature and humidity as well as scavenging and other interaction phenomena between fog and PM.It consists of two test rooms where fog can be generated independently. These two rooms are separated by a sliding door to provide a quick way to connect them and make fog interact.

The control units have been placed in a third room with independent access. This makes it possible to perform the tests without the presence of people in the test rooms. Each test room has an access door with a porthole window that allows observation of the room from outside.

The laboratory is equipped with a heating/cooling system and a humidification/dehumidification system (humidity system). From the control room it is possible to command the desired temperature and humidity in the test room, values that remain stable and homogeneous throughout the volume. The achievable temperature and relative humidity ranges were between 0°C and 40°C and between 30 and 95% respectively for standardized 5^{th} and 95^{th} percentiles external conditions of Madrid-Barajas.

There is also a ventilation and an air filtration system that guarantees that no pollutants are expelled into the atmosphere. The air speed within the test rooms at a height of 1.2 m shall be less than 0.8 m/s.

In addition, the laboratory has a water and air pressure system (see section **¡Error! No se encuentra el origen de la referencia.**) that provides compressed air and water in the range of 0 and 30 bar for both water and air independently or simultaneously.

3.2.2 Description of the Laboratory

The laboratory consists of two standardised portable containers which will be refered as the Test and Control Container and the Machinery Container (see section **¡Error! No se encuentra el origen de la referencia.**). The reason for the construction of the laboratory in this type of containers was the possibility of changing the location of the laboratory to suit the requirements of the project if necessary. The laboratory can therefore be transported by standard intermodal transport means. A third auxiliary container has been placed next to the laboratory just as a storage area. Table 13 shows their dimensions.

Table 13: Dimensions of the containers

INTERNAL DIMENSIONS OF ORIGINAL CONTAINERS	Length	12.031 m
	Width	2.348 m
	Height	2.90 m
DOOR OPENING	Width	2.336 m
	Height	2.28 m
WEIGHT	Max Gross	32,500 kg
	Tare	3,750 kg
	Max Payload	28,750 kg
CAPACITY	Load Capacity	68 m^3

Some of the installation requirements included those listed below:

- Indoor and outdoor coatings must be washable.
- The floor must be non-slip and cleanable including a retractable exterior drain.
- There must be no elements in the rooms that could cause adhesion or disturbance on micro-particles in suspension.
- The external surface must be covered by anticorrosion paint.
- Safety instructions and relevant use of exit, entry, danger and others signs that regulations require must be displayed where needed. It must include the electrical system, protection and control device box and lighting in the three rooms.
- The electrical and lighting installation in the laboratory rooms must have the specifications of wet room.
- The electrical installation, the machinery and control systems, as well as the engine room must have been designed according to the Reglamento Electrotécnico para Baja Tensión (REBT).
- It must be provided with a standardized three phase water-proof plug and socket connection for electrical supply.

Consequently, both containers have been modified according to the needs of the project. Externally they have been painted with a special exterior paint, able to resist extreme weather conditions (Figure 38).

Figure 38: Container before and after exterior paint application

3.2.2.1 Test and Control Container

The container was placed on six reinforced concrete pillars in order to guarantee the perfect horizontality of the same, as well as an access staircase was added to the test rooms to bridge the difference in level created as shown in Figure 39. This container has been divided into three rooms: Test Room 1, Test Room 2 and Control Room (Figure 40).

Figure 39: Test and Control Container

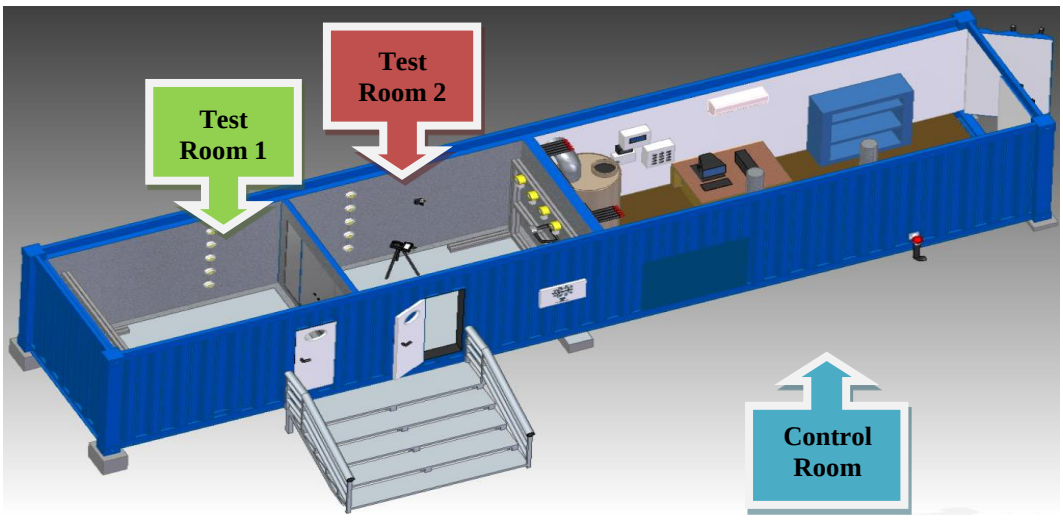

Figure 40: Schematic of the layout of rooms the Test and Control Container

This container is equipped with an independent three-phase current input for power supply (Figure 41).

Figure 41: Independent external three-phase power input in the Test and Control Container

3.2.2.1.1 Test rooms

On the one hand Test Room 1 is located on the left side of the container. Its access is the left white door shown in Figure 40 that connects the room to the outside. The door is equipped with a porthole window allowing the interior room to be viewed from the outside during the test time. On the other hand Test Room 2 is located in the central zone of the container, between Test Room 1 and Control Room. Its access is the right white door shown in Figure 40 and is similar to the door of Test Room 1. The dimensions of the test rooms can be seen in Table 14.

Table 14: Test room dimensions

	TEST ROOM	
DIMENSIONS	**Test Room 1**	**Test Room 2**
Length	3.10 m	3.10 m
Width	2.13 m	2.13 m
Height	2.46 m	2.46 m

Both rooms communicate through a sliding door with electromagnetic lock (Figure 42). This interior door can be opened automatically and almost instantaneously from Control Room, allowing the interaction of two different fogs and avoiding turbulence between them.

Figure 42: Sliding door communicating both test rooms

Temperature and humidity can be controlled between 0 and 40 °C and relative humidity between 30% and 95% respectively, as mentioned above. Homogeneity of temperature and humidity is kept within a margin of 2°C and 5% respectively. A hot/cold water circuit of the heating/cooling system is integrated inside the walls, floor and ceiling, providing maximum homogeneity and soft thermal conditions within the test rooms. Climatization through the surfaces of the rooms allows a perfect isothermal control that avoids temperature gradients and temperature jumps between walls and air. The surfaces are insulated with rock wool of 50 mm thick and 80 kg/m^3 nominal density. In Figure 43 the assembly process of the room is shown.

Figure 43: Assembly process of the test rooms

The walls, floor and ceiling of these rooms are covered with stainless steel sheets. The stainless steel layer protects the chamber from corrosive attacks and facilitates maintenance, cleaning and temperature control of the room. These sheets have a non-slip roughness that prevents laboratory personnel from slipping when walking on them even if the floor is wet.

There is a floor drainage system consisting of a groove that surrounds the entire perimeter of each of the test rooms and collects water and debris deposited during testing and evacuates it through the ducts designed for this purpose to a tarpaulin pool at the bottom of the laboratory (Figure 44) where it is subsequently collected and treated appropriately. This system prevents pollution of the soil, phreatic water or waste water.

Figure 44: Pool for the collection of waste or liquid released during the performance of tests

Test rooms are also provided with a ventilation system (see section **¡Error! No se encuentra el origen de la referencia.**) able to extract and filter 200 m^3/h of air from the rooms of fog laboratory. Two ducts are connected to the ceiling of each room with this purpose: the air can be extracted through them and conduced to a smoke extractor, where after passing through 5 filters is finally thrown out, preventing and minimizing the release of any surrogate product to the atmosphere (Figure 45). In the same way, every test room

has a vent fitted with a filter that controls the entry of air from the outside. These filters are the following:

- G4 EN 779:2012 pre-filter,
- F9 EN 779:2012 high efficiency particle filter,
- Z-BCA/ALPHACARB-B active Carbon for acid and inorganic vapours,
- Z-BCA/ALPHACARB-N active carbon for ammonia derived compounds,
- Z-BCA/ALPHABLEND-8A active carbon for organic vapours and Sulphur dioxide.

In addition, within the ventilation system there is another circuit in parallel to the previous one that allows the recirculation of the air from the rooms through the humidifier/deshumidifier that allows the control of the humidity in the air. This circuit also includes a set of filters for air cleaning. In this way, filtration and humidity systems are connected to the ventilation system.

Figure 45: Ventilation system and filters

Each room is equipped with luminaries (Figure 43) designed to withstand high humidity and direct water application (water-proof IP65). The following items are also available within each of the test rooms and were added to the initial basic laboratory design:

- **Nozzle** (Figure 46). Designed and manufactured as part of the Counterfog® project.

Figure 46: Counterfog® nozzle

- **Mobile and removable aluminium frame** (Figure 47) for nozzle positioning. Standardized profiles provide a convenient connection and continuous position selection for the nozzle position.

Figure 47: Aluminium frame

- **Smoke particle detector system** at different heights (Figure 48). Smoke detectors based on light diffraction working on analog mode with Fire Control Device working as data acquisition system. Five detectors per test room allow to measure the smoke vertical distribution.

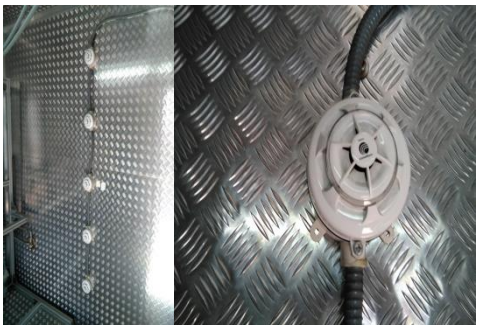

Figure 48: Smoke particle detector system

- **Relative humidity and temperature probe** (Figure 49) with accuracy of 0.1 °C. Temperature and humidity probes on the ceiling provide the external signal for temperature control and actuation of heat pump/water chiller.

Figure 49: Relative humidity and temperature probe

- **Connection hoses** (Figure 50) for connecting the nozzle to the pressurized air and water circuits installed in each of the rooms capable of withstanding the laboratory design air and water pressures. The length of the hoses depend on the test to be carried out and can be exchanged if necessary.

Figure 50: Connection hoses

- **Detectors of chemical substance in gaseous state** (only in test room 2). CO, CO_2, H_2S, CH_4 and O_2 detectors in analogue mode 4-20 mA connectable to the Data acquisition in the control room (Figure 51). Sensitivity in the order of toxic/risk threshold.

Figure 51: Detectors of chemical substance in gaseous state

Particle counter (Figure 52). It is a manual particle counter of the 8000 series (Model 8306) of the company PARTICLE PLUS (see section 3.3.2).

Figure 52: Particle counter

- **Video camera** (Figure 53). Waterproof video camera with 2-hour battery life and an immersive wide-angle field of view.

Figure 53: Waterproof video camera

3.2.2.1.2 Control Room

The control room is located at the right end of the container and immediately after Test Room 2. It has a door on the right side of the container that connects it to the outside, as shown in Figure 54. Without direct communication with the test rooms, this room contains all the different control elements that regulate both test rooms. It also contains part of the laboratory equipment.

Figure 54: Entrance door to the Control Room on the right side of the Test and Control Container

The control room design is based on the comfort and safety of the working staff. For this reason, the floor of this room is covered with wooden sheets. The walls and ceiling of the room are also covered with insulating paint, especially designed for outdoor work environments. The room contains the appropriate furniture for the workers: a table with drawers, chairs, shelves as well as a fully equipped tool trolley, luminaries, a computer with printer for recording and analyzing test data and an air-conditioning system (Figure 55). Luminaries inside the room are designed to withstand high humidity levels, as well as the direct contact with water (water-proof IP65). In the laboratory, a monitoring and control system has been installed in which it is possible to modify, control and acquire the parameters of temperature and relative humidity in each of the test rooms from the control room, as well as to acquire the registers of water and air shooting pressures and water shooting temperature.

Figure 55: Equipment of the Control Room

As for the equipment located in this room, the following elements are available:

- **Heating pump** (Figure 56). It has a maximum water temperature of 60°C and a maximum circuit pressure of 7 bar. The tank capacity is 406.5 litres.

Figure 56: Heating pump

- **Air-cooled chiller** (Figure 57)**.** It has a compact, modular and weatherproof design for outdoor installation IP24 – manufactured according to the ISO 9001 quality standard. Glycol has been added to the water as antifreeze. It is equipped with a twin circuit design (two refrigerant circuits/one water circuit. The plate heat exchanger is thermally insulated to ensure that it is diffusion-proof to prevent any heat loss.

Figure 57: Air-cooled chiller

- **Cooling/heating system water supply** (Figure 58). Flow control and maintenance valves for climatization circuits.

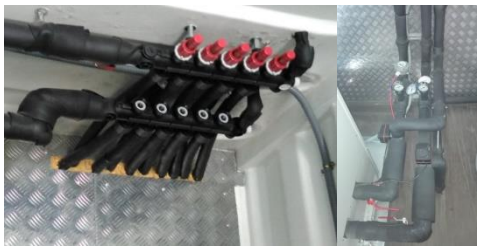

Figure 58: Cooling/heating system water supply

- **Humidifier/dehumidifier** (Figure 59). It has a flow of 700 m^3/h of dry air and 210 m^3/h of wet air.

Figure 59: Humidifier/dehumidifier

- **Electronic systems** (Figure 60). The acquisition system is a PROMUX. It is a modular I/O system which provides a simple, low cost solution to distributed I/O requirements. This type of acquisition system consists of independent digital and analog input modules that are connected to each other via a two wire multipoint RS485 network. The modules communicate via the MODBUS

RTU protocol. A 32-bit ARM CPU is used to provide high-speed data processing and fast communication response times. It plugs directly onto an industry standard DIN rail and has a minimum insulation of 1000VAC rms between field and logic. It is equipped with status LEDs to indicate the status of the inputs or outputs. This visual indication helps with troubleshooting and diagnostics.

Figure 60: PROMUX modular I/O system

The rest of the elements located inside the Control Room of the Test and Control Container are shown below:

- **Electrical protectors box** (Figure 61). Electrical protections according to Electrotechnical Rules and EN standards.

Figure 61: Electrical protectors box of the Test and Control Container

- **Control box** (Figure 62). Temperature automate control unit.

Figure 62: Control box

- **Remote command panel** (Figure 63). Command panel to operate valves of the pressure system and activation of Counterfog®.

Figure 63: Remote command panel

- **Humidifier/dehumidifier control panel** (Figure 64).

Figure 64: Humidifier/dehumidifier control panel

- **Remote smoke alarm control panel** (Figure 65).

Figure 65: Remote smoke alarm control panel

- **Remote control panel for fire detectors** (Figure 66).

Figure 66: Remote control panel for fire detectors

3.2.2.2 Machinery Container

The Machinery Container contains part of the equipment (Figure 67). Its floor is covered with wooden sheets and painted, as in the case of the walls and ceiling, with a special paint suitable for outdoor environments subjected to extreme temperatures, water and humidity resistant. In addition to the first container, the luminaires inside the container are designed to withstand high levels of humidity and direct contact with water (IP65 tightness).

Figure 67: Machinery Container

This container is equipped with an independent three-phase current input for power supply and an external water connection from which water is drawn to the corresponding deposits by means of a hose (Figure 68).

Figure 68: Three-phase current input and external water connection

An air and water pressure supply system has specifically been designed to provide pressurized water and air to both test rooms. The system has capability to keep nozzles working at least 30 s for any pressure combination up to 25 bar. Stability of pressure can be measured with manometers and pressure sensors connected to data acquisition card in the control room. The commands for triggering the valves are in the control room and they can be activated remotely. A second pneumatic circuit is used to supply the command line.

The elements located inside this container are:

- **Pressurized air tank charge compressor** (Figure 69). It has a maximum working pressure of 30 bar and a free air supply flow of 2.5 l/s.

Figure 69: Pressurized air tank charge compressor

- **Pressurized air tank** (Figure 70). It has a maximum allowable pressure of 31 bar and a volume of 500 l. The tank is equipped with a liquid drainage system equipped with a sensor.

Figure 70: Pressurized air tank and drainage sensor

- **Nitrogen compressed cylinders** (Figure 71). Each of them with a pressure of approximately 200 bar and a capacity of 9,373 l. These cylinders are an alternative to the use of the pressurized air tank for water and air shooting in case the

compressor does not work for technical reasons.

Figure 71: Nitrogen compressed cylinders

- **Independent tanks for pressurized water supply** in Test Rooms 1 and 2 (Figure 72). Each of them with a maximum allowable pressure of 45 bar and a capacity of 5 l. The instalation of a filling sensor at the top of these tanks reduced the water inlet capacity to 4.5 l in each of them.

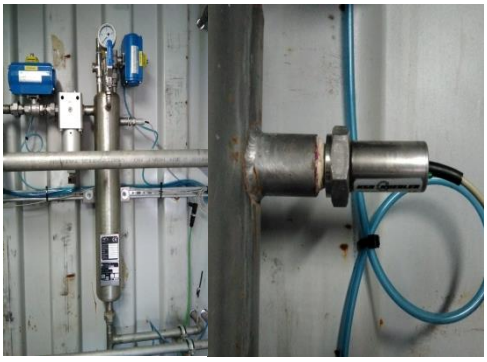

Figure 72: Pressurized water tank and filling sensor

- **Atmospheric water tanks** (Figure 73). Each of them with a capacity of 50 l. A water temperature probe has been installed inthe water tank of Test Room 1 consisting of a sensor with 4-wire transducers with accurate signal output (4-20mA), long wires and low voltage supply (24Vdc).

Figure 73: Atmospheric water tank and water temperature probe

- **Electric submersible water pumps** (Figure 74). They have a maximum flow of 14 m^3/h and a maximum height of 9 m.

Figure 74: Electric submersible water pump

- **Compressor for the operation of pneumatic valves** (Figure 75). It has a maximum working pressure of 8 bar and a air flow of 195 l/min.

Figure 75: Pneumatic valve compressor

The rest of the elements located inside the Control Room of the Test and Control Container are shown below:

- **Electrical protectors box** (Figure 76). Electrical protections according to Electrotechnical Rules and EN standards.

Figure 76: Electrical protectors box of the Machinery Container

- **Air filter and manual ball valves** (Figure 77).

Figure 77: Air filter for the air and water pressure system and ball valves

- **Water pressure manometers** (Figure 78).

Figure 78: Water pressure manometer

- **Pneumatic opening/closing valves for water filling and purging** (Figure 79).

Figure 79: Filling and venting water valves

- **Pneumatic valves for opening/closing water pressure** (Figure 80).

Figure 80: Water pressure valve

- **Manual valve for water pressure regulation** (Figure 81).

Figure 81: Manual water pressure regulation valve

Finally, we present the rest of the elements that are located in the outside of the laboratory. It should be noted that the external pipelines are adequately insulated to avoid any contingency caused by external meteorological factors.

- **Auxiliary external air duct for outdoor fog testing with the 1:1 nozzles** (Figure 82).

Figure 82: External air duct for outdoor testing

- **External air and water ducts connecting both containers and their corresponding weather protection** (Figure 83).

Figure 83: External air and water ducts

- **Air pressure manometers** and **air/ water pressure sensors** (Figure 84).

Figure 84: Water pressure manometer

- **Manual ball valves** (Figure 85).

Figure 85: External circuit manual ball valves

- **Air/water pressure sensors and ball valves** (Figure 86).

Figure 86: Air and water pressure sensors and ball valves

- **Pneumatic opening/closing valves for air and water** (Figure 87).

Figure 87: Air and water pneumatic valves

- **Water flowmeters** (Figure 88).

Figure 88: Flowmeter

- **Manual valve for air pressure regulation** (Figure 89).

Figure 89: Manual air pressure regulation valve

3.3 Measuring devices

The measurement systems used during the tests of this work are presented below. Figure 90 shows the measuring ranges of the different instruments currently available on the market for particle measurement. The particle size range to be measured during the tests, which ranges from 0.1 µm to 10 µm, justifies the choice of a laser particle counter and the Scanning Electron Microscopy (SEM).

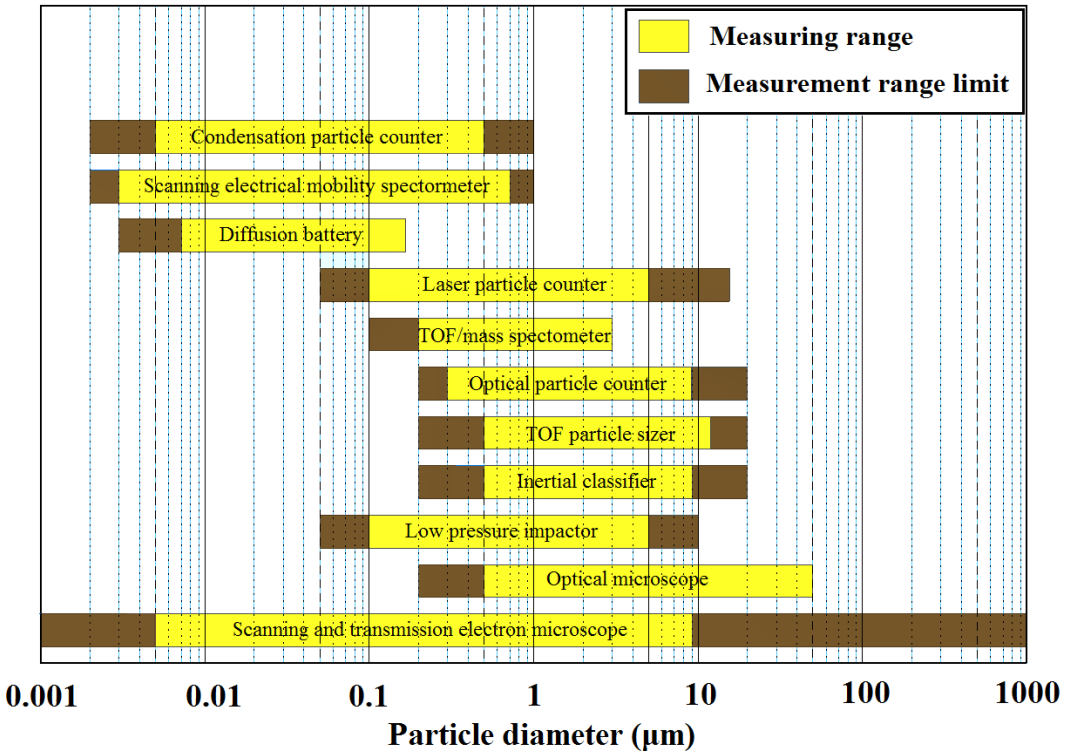

Figure 90: Measurement size range of some principal aerosol instruments. Adapted from Pramod et al. (2011)

3.3.1 Post-sampling measuring instrument

3.3.1.1 Scanning Electron Microscopy (SEM)

Scanning electron microscopy is a very versatile technique that allows the determination of microstructural characteristics of a sample such as topography, morphology and particle size. The image resolution is less than 1 nm. This is a technique that allows electrons to penetrate or escape from the outermost layers of the sample.

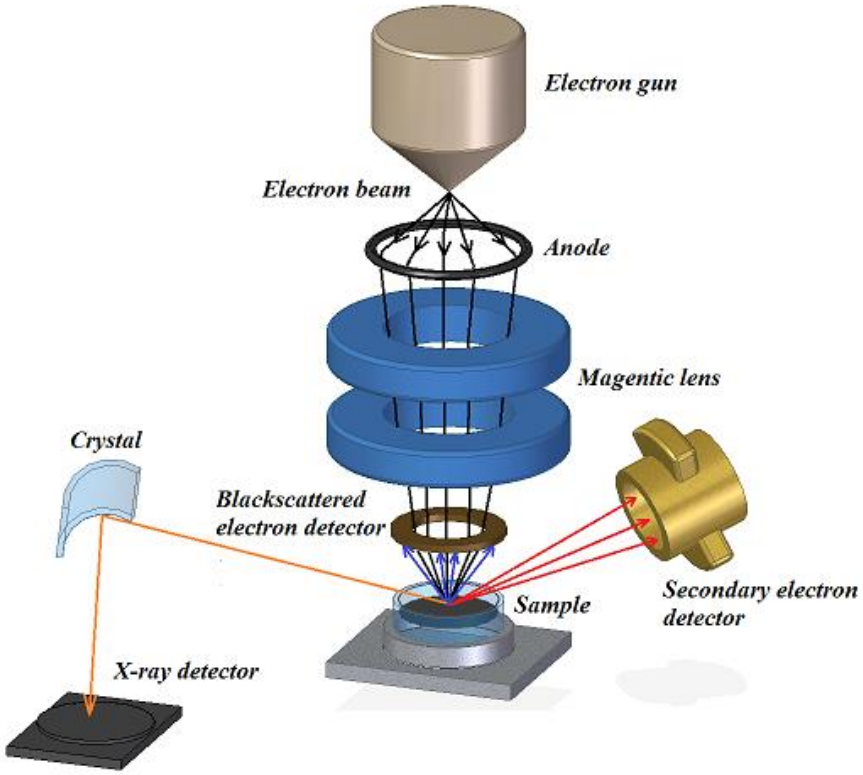

Figure 91: Schematic of a Scanning Electron Microscope and its operating

An electron gun generates an electron beam to the sample. This beam is generated by the application of a high tension difference (1-50 kV) to the ends of a tungsten filament (Figure 91). On its way to the sample, the electron beam passes through a block of electromagnetic lenses that focus the beam on the sample. After passing through the lens, the beam passes through a small metal plate with a tiny hole that allows the beam to be reduced in thickness. Finally, before reaching the sample, the beam passes through an objective lens that provides the final amplification of the beam. This lens consists of a deflector system consisting of sweeping coils for beam steering and an astigmator that eliminates distortions in the signal. The sample is placed in the so-called specimen chamber. Once the beam reaches the sample, the interaction between the two results in (Figure 92):

- **Elastic interactions:** they affect the trajectory of electrons without significantly decreasing their energy:

    - **Backscattered electrons (BSE):** they have higher energy than secondary electrons (Figure 93), therefore provide information on more regions of the sample. They are sensitive to the chemical composition of the sample: the higher the *Z*, the greater the emission of backscattered electrons. Therefore, areas with heavy elements appear bright in the image.

    - **Transmitted electrons (SE):** electrons that escape from the atoms of the sample after their interaction with the electron beam.

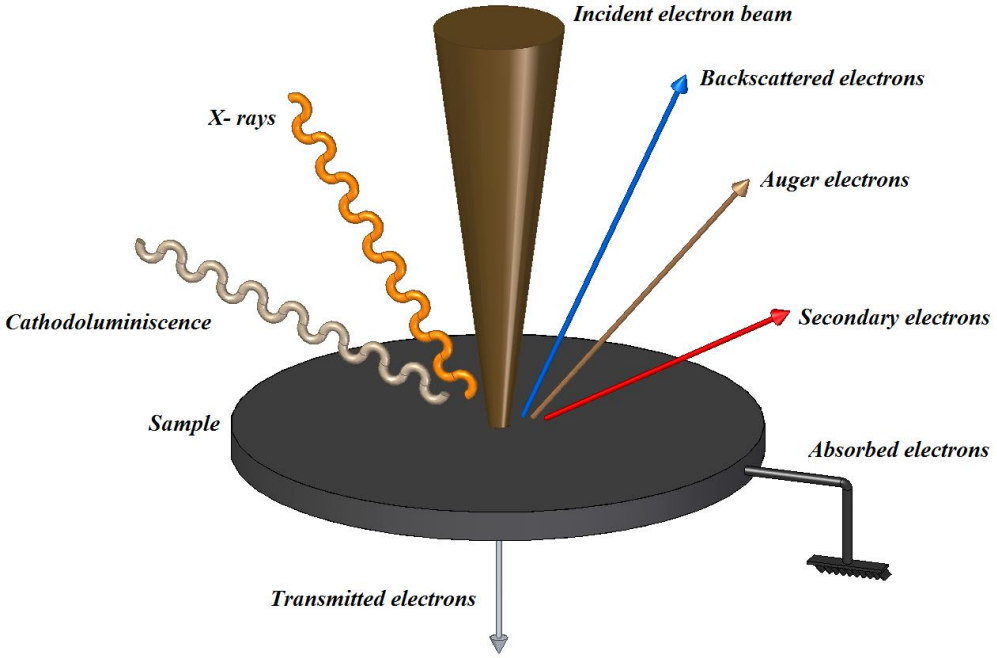

Figure 92: Behaviour of the electron beam in its interaction with the sample

- **Inelastic interactions:** they affect the trajectory of electrons by significantly reducing their energy:

    - **Absorbed electrons:** beam electrons that are absorbed by the atoms of the sample.

    - **Secondary electrons:** they are produced from the emission of electrons of valence of the atoms in the sample. As they are very low energy (< 50 eV) only the most superficial ones get out of the sample. They provide information about the topography of the surface.

As a consequence of the inelastic interactions between beam and sample, electron vacancies occur in the layers of the atoms. This leads to an excess of energy on the part of the atom that seeks its stabilization and can lead to:

- **Auger electrons:** the excess energy is transferred to a second electron of the atoms of the sample producing its expulsion

- **Cathodoluminiscence:** atoms from the outer layers change orbits by filling in vacancies and stabilizing the atom. During electron transfer, energy is released which can be transmitted in the form of long wavelength photons.

- **X-rays:** atoms from the outer layers change orbits by filling in vacancies and stabilizing the atom. During electron transfer, energy is released which can be transmitted in the form of X-rays. They allow an analysis of the composition of the sample.

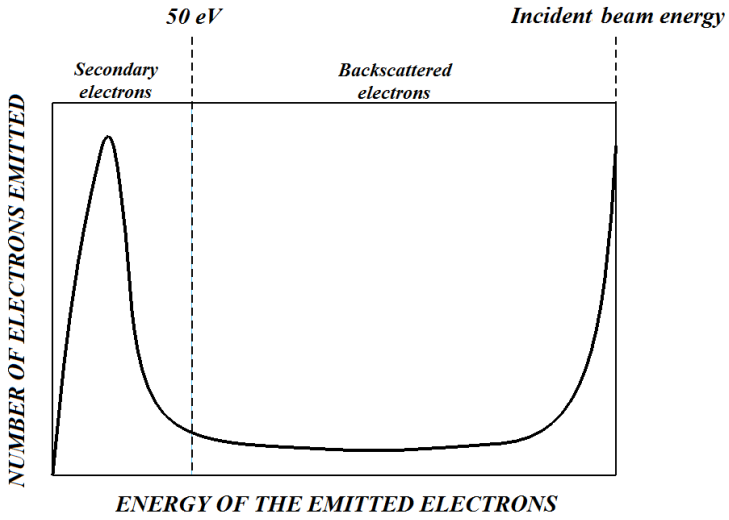

Figure 93: Schematic of energy and number of electrons for secondary and electrodispersed electron

3.3.1.1.1 Secondary-Electron Detector (SED)

The SE type of electrons originates from the surface or the near-surface regions of the sample. They occur due to inelastic interactions between the primary electron beam and the sample and contain lower energy than the backscattered electrons. They provide very important information about the topography of the sample.

This detector comprises of a scintillator within a Faraday cage, which is positively charged and attracts the SE. The scintillator is then used to speed up the electrons and change them into light before reaching a photomultiplier for amplification. The SE detector is positioned at the side of the electron chamber, at an angle, so as to boost the efficiency of detecting secondary electrons.

3.3.1.1.2 Backscattered-Eelectron Detector (BSD)

The BSD detectors are positioned above the sample so that they are concentrically positioned with respect to the electron beam. In this way, the number of backscattered electrons captured is maximized. This detector is divided into different segments that maintain a cylindrical simerty with respect to the axis of the beam. On the one hand, when all the segments are enabled, the image provides a contrast that allows the atomic number *Z* of the atoms in the sample to be obtained. The larger the size of the atom, the more atoms will be dispersed by it after interaction with the electron beam, with the number of restrodispersed electrons being proportional to Z. On the other hand, when only certain segments of the detectors are enabled, beneficial information can also be obtained regarding the topography, crystallography and magnetic field of the sample. The BSE type of electrons originates from a wide region within the interaction volume

The most common BSE detectors are Solid state detectors. They contain p-n junctions. The working principle is based on the production of electron-hole pairs by the backscattered electrons which escape the sample and are captured by the detector. The quantity of these pairs relies on the energy of the backscattered electrons. The p-n junction is linked to two electrodes, one of which attracts the electrons and the other the holes, thus producing an electrical current, which also relies on the quantity of the absorbed backscattered electrons.

3.3.1.2 Enery-dispersive X-ray spectroscopy (EDXS)

This technique can qualitatively anaalyse the composition of a sample using the spectrum of X-ray generated by electrons perturbed by the SME and can be divided into the following stages:

- **Excitation:** the collision between an electron incident of the beam produces the expulsion of an electron located in the inner layers of an atom of the sample. The atom is left in an excited state.

- **Emission:** the excited atom tends to return to its fundamental state. To do this, the electrons in the outermost layers jump between the layers to fill in the gaps left by the ejected electrons. In the realization of this electron jump between layers, energy is released in the form of electromagnetic radiation corresponding to the X-ray region. This energy corresponds to the energy difference between layers.

As the deceleration of the incident electron depends on the force of interaction with the electric field of the atom, the emitted X-ray can have a wide range of energy that can reach the energy value of the incident beam. Therefore, the spectrum is formed by a series of peaks called characteristic rays (which the information is obtained from) on a continuous background of radiation. This type of analysis provides qualitative and quantitative information on the elemental composition of the sample surface:

- **Qualitative analysis**

  Based on the discrimination of the X-ray energies captured by the detector. The heavier an element, the more orbitals and consequently the more electrons transferred with their corresponding higher number of energies measured by the X-ray detector. Since the characteristic energies of the orbital transits of the electrons in the elements are known and well characterized, reliable results are obtained. However, there is the possibility of overlapping peaks in the spectrum due to the similarity of orbital transfer energies between different elements. These effects must be taken into account.

- **Quantitative analysis**

  The signal strength generated by each element of the sample will vary with the depth reached by the electron beam. The X-rays generated must leave the sample through a variable thickness that will be a function of the depth reached by the beam. Some of these lower energy rays can be absorbed by the higher atomic number elements. In addition, higher energy X-rays can generate fluorescence and even excite areas near but outside the electron beam interaction volume. Irregular surfaces and non-homogeneous samples can also make quantitative analysis difficult. With currently available technology and a good calibration of the instrument, the margins of error can vary between 5% and 20%.

3.3.1.3 Laser diffraction particle size analyzer

This method allows the particle size distribution of a sample to be estimated by analysing the angular variation in scattered light intensity when it comes into contact with a laser

beam. Created the dispersion pattern of the sample, it is compared with Mie's dispersion theory. The particle size is obtained as a volume equivalent to the diameter of the sphere obtained. Mie's theory [Ruppin, 1979] makes it possible to evaluate the characteristic intensity distributions of very small particles. In addition, unlike Fraunhofer's theory, such distributions are not limited to angles of dispersion below 90° (forward), but also arise at angles of dispersion above 90° (backward). In order to use the intensity distribution determined in this way to calculate the particle size, Mie's theory requires, unlike Fraunhofer's theory, that the refractive index and absorption index of the material sample be known. The lower limit of the size range that can be recorded with Mie's theory is 10 nm. For smaller particles, the scattering intensity no longer depends on the direction, i.e. the size of the particles can no longer be determined from the distribution of the angles of the scattered light. This is known as Rayleigh scattering. When the values for refractive and absorption indices are unknown, the Franhoufer approach can be used. This method provides accurate particle size results above 50 particles of equivalent diameter and a low degree of transparency. A comparison of particle sizes of 5, 1 and 0.1 is shown in Figure 94. The pattern of light intensity distribution is characteristic for each material and particle size:

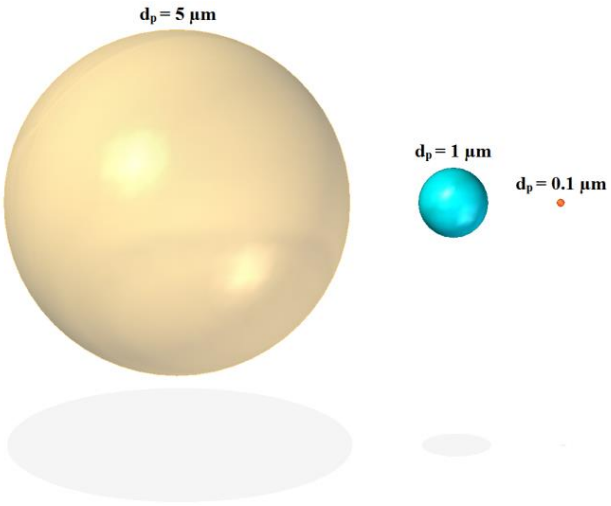

Figure 94: Comparative sizing scheme for particles of different diameters

- **5 µm size particle light intensity distribution pattern:**
  The diffracted light is concentrated in the direction and sense of the laser beam, and the larger the particle size, the greater the effect. Light scattered in other directions is weak.

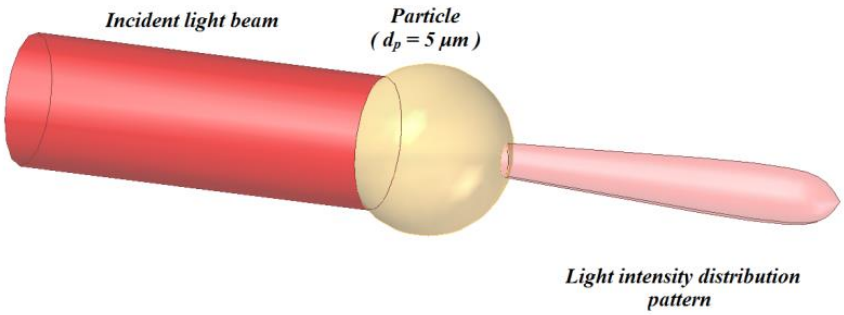

Figure 95: Intensity light pattern for a 5 µm diameter particle

- **1 µm size particle light intensity distribution pattern:**
  The diffracted light continues to be concentrated in the direction and sense of the laser beam, although there is an extension of the pattern towards the periphery. Light scattered in other directions begins to take on importance. The smaller the particle size, the greater the effect.

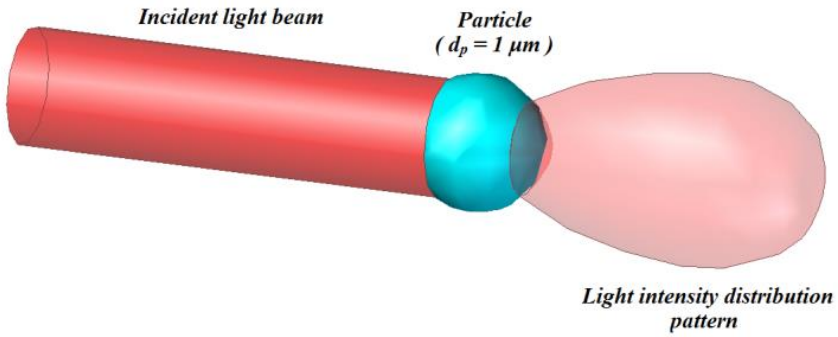

Figure 96: Intensity light pattern for a 1 µm diameter particle

- **0.1 µm size particle light intensity distribution pattern:**
  The light pattern extends even further to the periphery with respect to the previous case, even going in the opposite direction to that of the incident laser beam. The intensity distribution is much more homogeneously distributed. The clear predominance in the direction and sense of the laser ceases to exist and the pattern takes on a shell shape that surrounds the particle.

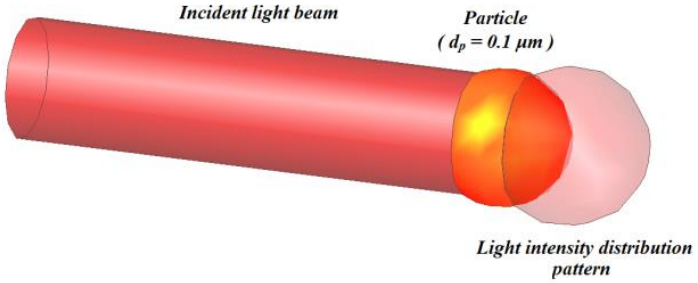

Figure 97: Intensity light pattern for a 0.1 µm diameter particle

- **Particulate conglomerate light intensity distribution pattern:**
  In most cases, particle clusters composed of a large number of independent particles will be found. The corresponding ligth intensity distribution pattern will be the result of the superposition of those corresponding to each of the particles that make up the conglomerate. By detecting and analyzing this pattern of light intensity distribution, it can be found out the particle size distribution, that is, which particle sizes are present and their proportions.

The analysis of the size distribution is carried out by means of Mastersizer2000 (Figure 98). This is laser diffraction particle size analyzer delivers rapid, accurate particle size distributions for both wet and dry dispersions. Measuring over the nanometer to

millimeter particle size ranges. The diffraction light pattern (He-Ne laser) depends on the size of the particle. The laser diffraction pattern is measured and correlated with the particle size distribution based on Fraunhofer's or Mie's theory. The use of Mie's theory presupposes knowledge of the refractive index in light of the particles and the means of dispersion and the imaginary part of the refractive index of the particles. This techniqie is covered by ISO13320 (2009). This instrument has databases with indexes of absorption and refraction of multiple elements, and new values can be entered if necessary.

Figure 98: Laser diffraction particle analyzer model

Techincal information:

- Dispersion media: liquid or air
- Parameters: sonication, stirring speed (liquid) feeding rate, pressure (air)
- Measuring range: 0.02 - 2,000 μm (liquid) and 0.1-2,000 μm (air)
- Sample amount: 10 - 500 mg (liquid) and 0.5 - 10 g (air)

3.3.1.4 Particle impactor

This is a MAS-100 NTTM particle impactor (Figure 99) from Merck. Its mode of operation is explained below: air is aspirated through a perforated lid and impacted onto the surface of growth media in a standard 90 mm Petri dish or 60 mm contact plate. Micro-organisms are trapped on the culture media, and after the incubation period the formed colonies can be counted. It fully complies with the EN ISO 14698 standard parts 1 and 2.

Figure 99: Particle impactor model

Characteristics of the particle impactor:

- Height: 25 cm,
- Diameter: 11 cm ,
- Material/ Weight: Anodized aluminium/ 2.38 kg,
- Diameter of Sampling Head: 10 cm,
- Nominal airflow: 100 l/min ± 2.5%,
- Freely definable sampling volumes: 1 to 2,000 l,
- Running time: approx. 7 hours,
- Total aspiration volumen: approx. 42,000 l

3.3.2 Real-time measuring instrument: particle counter

Particle counters based on laser technology count particles from their responses to a beam of light generated by a laser diode. In this way, these instruments are based on the principle of light scattering, i.e. the changes in direction suffered by light in its interaction with the particle. The light beam passes through an optical compartment consisting of crystals and photodetectors. The air sample is sucked in by the instrument by means of a vacuum pump. On its way through the instrument, the laser beam passes through the sample interacting with the particles. Figure 100 schematizes the interior of a particle counter.

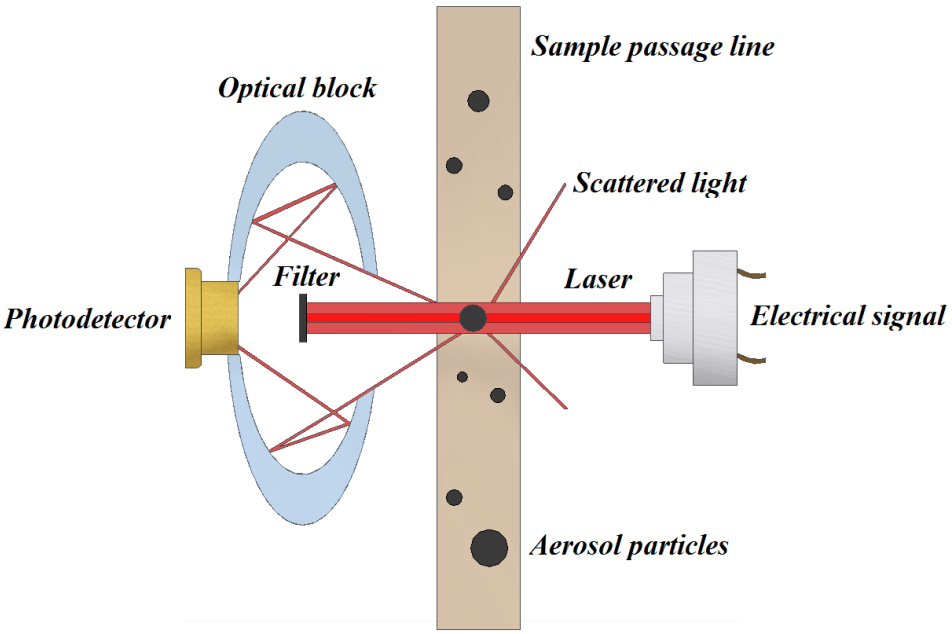

Figure 100: Schematic of the interior and operation of a particle counter based on laser technology

After the interaction of the laser beam with the particle, the light is scattered in different directions. These scattered light beams are directed by the set of crystals that make up the optical compartment to be redirected to the photodetector. The photodetector transforms the energy received by the beams into electrical pulses. From the amplitude of these pulses and by means of a comparison by the system with the calibration curves of the instrument, the particle size is estimated. In addition, depending on the number of pulses, the number of particles passing through the light beam can be counted.

There are three different phenomena that can occur after the interaction of the beam with the particles:

- **Reflection:** a change in the direction of the light beam that occurs on the separation surface between particle and air, so that it returns to the initial medium.

- **Refraction:** a change in direction of the light beam as it passes from air to particle. It is only produced if the beam is oblique to the separation surface of the two media and if they have different refraction indexes. Refraction originates from the change in propagation speed of beam.

- **Diffraction:** is a characteristic phenomenon of waves, it is based on the bending and scattering of the light beam when they encounter an obstacle or when they pass through a slit.

In addition, other possible factors must be taken into account, such as:

- Possible absorption of beam energy by the particle.

- Orientation of non-spherical particles during their interaction with the beam.

- Calibration of the instrument.

3.3.2.1 Calibration of the instrument

Particle counters based on laser technology are calibrated to a reference standardmade of polystyrene latex spheres (PLS). By using monodisperse samples of known size nebulized in HEPA/ULPA grade filtered air a calibration curve is generated for the instrument [Schroth, 1996]. Therefore, the results obtained by the instrument are based on the results obtained for completely spherical latex spheres. This means that the values obtained must be taken as relative and not absolute values, making the corresponding corrections to the data that allow the correct values to be obtained.

3.3.2.2 Particle counter model

A manual particle counter of the 8000 series (Model 8306) manufactured by PARTICLE PLUS (Figure 101) according to ISO 21501-4 and JIS B9921 has been used for measurements of droplet and particle size distribution.

Figure 101: Particle counter model

Characteristics of the particle counter:

- Temperature/ relative humidity (RH) operating conditions: 5° to 40°C / 20% to 95%
- Temperature/ RH probe: (0-50°C ± 0.5°C) / (15-90% ± 2%)
- Isokinetic probe threated (Nickel plated aluminum)
- Flow rate: 2.832 l/min
- Internal HEPA filter
- Calibration: NIST traceable
- Light source: long life laser diode
- Concentration limit: $\frac{4.10^6\ particles}{ft^3} \cong \frac{1.412.10^8\ particles}{m^3}$ and 5% in coincidence loss
- Internal pump with automatic flow control
- ¼ “ -20 threated tripod mounting adapter
- Kick-stand
- Battery compartment with a rechargeable battery 55Wh,
- External purge filter assembly
- Transfer software

Available functions of the particle counter:

- 6 channels for measuring five sizes of particles: 0.3µm, 0.5µm, 1.0µm, 2.5µm, 5.0µm and 10.0µm.
- Real-Time Meter and plotting on screen
- Storage of data in memory (40,000 possible saved records)
- Automatic, manual, continuous, and real-time meter sampling modes
- Establishment of sample time
- Establishment of hold time
- Establishment of delay time
- Establishment of cycle numbers in automatic mode
- Differential and cumulative particle count modes

The particle counter model used in the tests is an advanced instrument for measuring and controlling the content of particles in a given volume. It is suitable for use in clean and controlled environments for the aerospace, life science, data storage, IAQ, and industrial hygiene markets.

This instrument has a dynamic particle size measurement range from 0.3 µm to 10.0 µm. The use of the particle counter allows for high efficiency and real-time particle counting, ensuring high accuracy and high resolution. This instrument allows simultaneous measurement on six different channels, as well as the possibility of intermittent sampling over time. The following table (Table 15) shows the calibration and verification of the device:

Table 15: Size calibration and verification of size setting of the particle counter model

SIZE CALIBRATION AND VERIFICATION OF SIZE SETTING		
Channel	**Nominal Particle Size (µm)**	**Expanded Uncertainty**
1	0.3 µm	2.0 %
2	0.5 µm	1.8 %
3	1.0 µm	1.5 %
4	2.5 µm	1.1 %
5	5.0 µm	0.8 %
6	10.0 µm	0.4 %

3.4 Sampling efficiency coefficients

A theoretical study has been carried out with the objective of quantifying the losses and disturbances obtained in the sampling process carried out during the tests. As indicated in the previous section of this chapter, a particle counter has been used to carry out the tests, which has a thin-walled circular section probe to absorb the volume of air in the sample. Losses that may occur will therefore be considered. Due to the characteristics of the tests,

the existence of a laminar regime will be assumed at all times [Hinds, 1982]. For this purpose, the following parameters will be taken into account and will be detailed later:

- Fractional suction efficiency $(\eta_{suct.})$,
- Gravitational sedimentation efficiency $(\eta_{sed.})$,
- Inertial deposition efficiency $(\eta_{dep.})$,
- Total sampling efficiency$(\eta_{Tot.})$.

In addition, depending on the position of the sampling probe with respect to the direction of the sample flow, the sampling process can be classified as:

1. **Isoaxial sampling.**
   In this type of sampling the streamlines of the sample flow are parallel to the direction of the probe, that is $\theta = 0^{o}$.
2. **Anisoaxial sampling**
   In this type of sampling the current lines of the sample flow are not parallel to the direction of the probe, that is $\theta \neq 0^{o}$.

In turn, three further subcases can be distinguished within each of the two types mentioned above (Figure 102 and Figure 103). Depending on the value obtained for the $\frac{v_o}{v_m}$ ratio (being $\boldsymbol{v_m}$ is the velocity of the sample inside the probe and $\boldsymbol{v_o}$ the velocity of the sample outside the probe), one of the following three cases shall be presented [Vincent, 1989]:

a) Subisokinetic sampling $(\frac{v_o}{v_m} > 1)$

The particle concentration in the probe is higher than that of the sample because the larger particles are diverted from the streamlines of the sample stream by inertial effects and are introduced into the probe, that is, $\eta_{suct.} > 1$.

b) Isokinetic sampling $(\frac{v_o}{v_m} = 1)$

No flow distortion occurs at the probe inlet and therefore the number of particles in the sample matches the number of particles in the probe, that is, $\eta_{suct.} = 1$.

c) Superisokinetic sampling $(\frac{v_o}{v_m} < 1)$

Larger particles deviate from the streamlines of the sample stream due to inertial effects and fail to enter the probe. In this way, the concentration of particles in the sample is higher than that obtained in the probe, that is, $\eta_{suct.} < 1$.

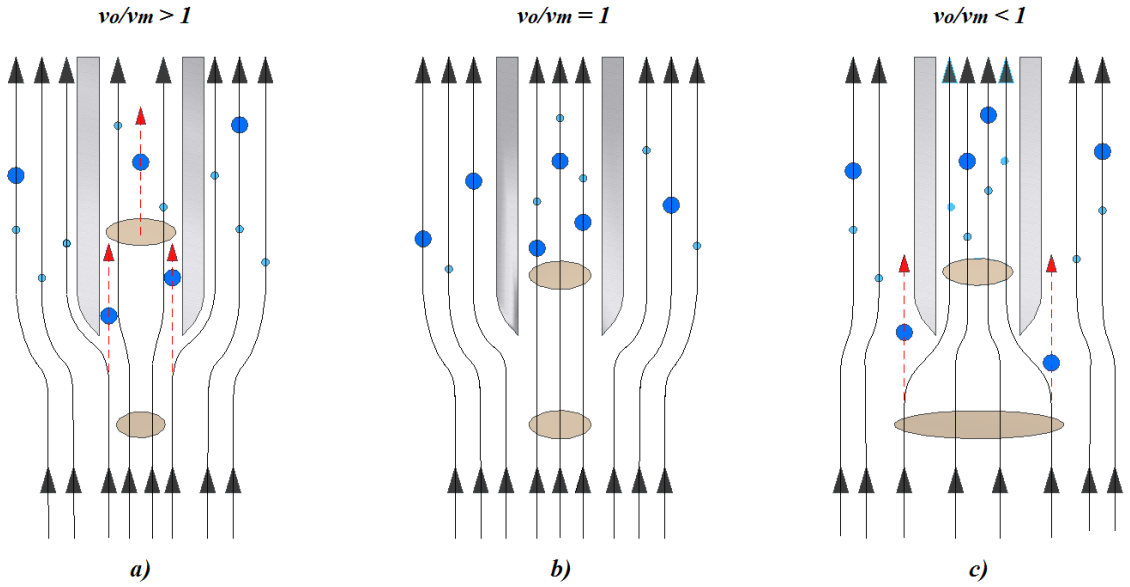

Figure 102: Schematic showing sampling and mainstream stream lines intercepting an isoaxial probe: a) subisokinetic sampling; b) isokinetic sampling; c) superisokinetic sampling.

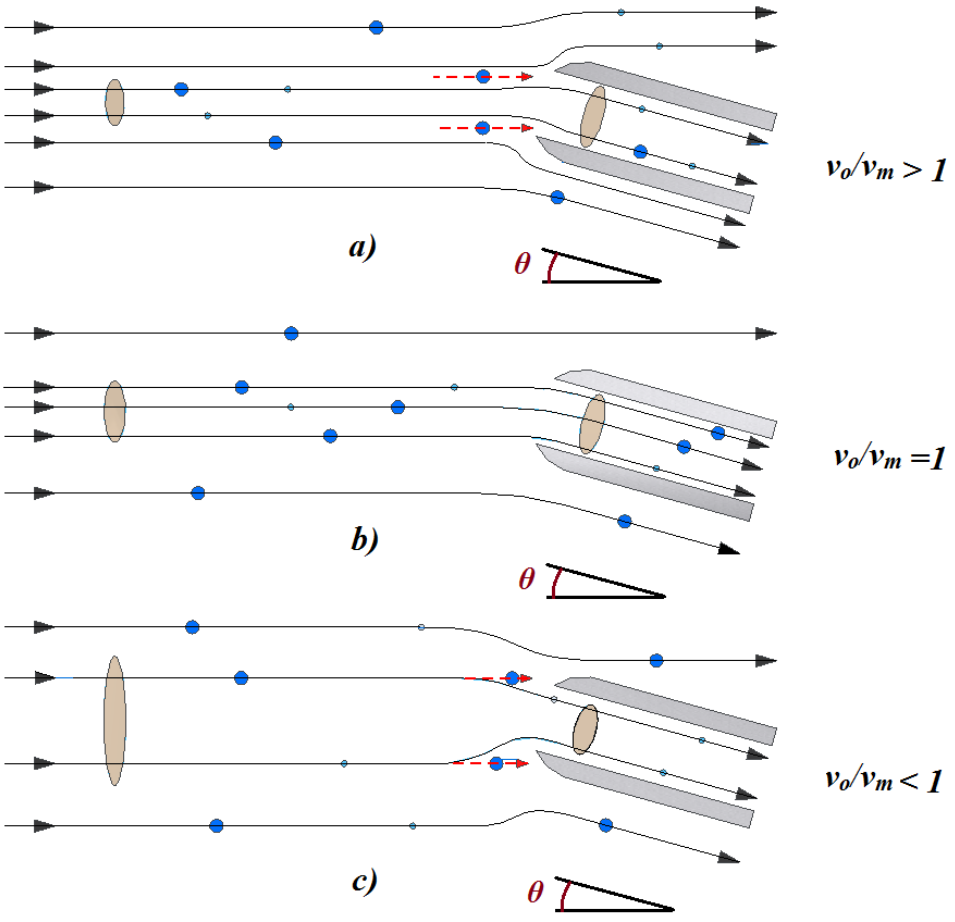

Figure 103: Schematic showing sampling and mainstream stream lines intercepting an anisoaxial probe: a) subisokinetic sampling; b) isokinetic sampling; c) superisokinetic sampling.

3.4.1 Fractional suction efficiency

This parameter is defined as the ratio of the mass concentration of aerosol particles in the probe to the mass concentration of aerosol particles in the sample for the same volume:

$$\eta_{suct.} = \frac{c_m}{c_o} \quad \textbf{(66)}$$

The factors that condition the value of this parameter are:

- Relationship between the velocity of the volume of the sample and and the velocity at the probe: $\frac{\boldsymbol{v_o}}{\boldsymbol{v_m}}$.
- Aerosol particle size (d_p)
- Size and geometry of the sampling probe
- Position of the sampling probe

Each individual case is explained in detail below:

3.4.1.1 Isoaxial sampling

Belyaev and Levin (1972) propose the following mathematical expression to obtain the Fractional suction efficiency :

$$\eta_{suct.} = 1 + \left(\frac{\boldsymbol{v_o}}{\boldsymbol{v_m}} - 1\right)\left\{1 - \left[1 + \left(2 + 0.617\frac{\boldsymbol{v_m}}{\boldsymbol{v_o}}\right)St\right]^{-1}\right\} \quad \textbf{(67)}$$

$$\left(0.18 \leq St \leq 2.03 \;\; ; \;\; 0.17 < \frac{\boldsymbol{v_o}}{\boldsymbol{v_m}} < 5.6\right)$$

where:

- St: Stokes number is defined as:

$$St = \frac{\rho_p d_p^{\,2} v_m C(Kn)}{18\mu_a D_{pr}} \quad \textbf{(68)}$$

Where:

- D_{pr}: probe diameter

- $C(Kn)$: Cunningham slip factor as a function of Knudsen number

$$C(Kn) = 1 + \left[K_n\left(1.142 + 0.558e^{-\frac{0.999}{K_n}}\right)\right] \quad \textbf{(69)}$$

Where:

- Kn: Knudsen number defined as:

$$K_n = \frac{2\lambda_a}{d_p}$$

With:

- λ_a: mean free path of an air molecule. It is given by:

$$\lambda_a = 0.665\left(\frac{101.325}{P}\right)\left(\frac{T}{293.15}\right)\left(\frac{1+\frac{110}{293.15}}{1+\frac{110}{T}}\right) \quad \textbf{(70)}$$

- T: sample temperature
- P: sample pressure

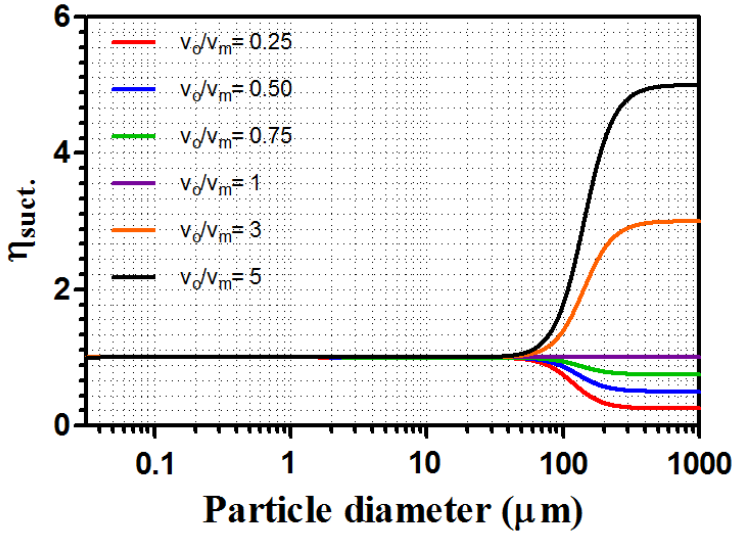

Figure 104: Suction efficiency for an isoaxial sampling with a circular probe of 1 cm in diameter and 6 cm in length as a function of the particle size for a sample at T=298.15 K, P=101,325Pa, RH=50% and different values of v_o/v_m .

Figure 104 shows how the suction efficiency is equal to the unit for particle sizes below $20\,\mu m$ in all cases in the situation under study. However, as the particle size increases, the suction coefficient remains around the unit in the isokinetic case, larger than the unit for the subisokinetic case and smaller than the unit for the superisokinetic case tending in all cases to a limit value coincident with the value of the ratio $\frac{v_o}{v_m}$.

3.4.1.2 Anisoaxial sampling

The mathematical expression that allows this parameter to be obtained was given by Hangal and Willeke (1990) and changes according to the angle formed between the probe and the direction of air flow:

- $\boxed{0^o \leq \theta \leq 45^o}$:

$$\eta_{suct.} = 1 + \left(\frac{v_o}{v_m}\cos\theta - 1\right)\frac{1 - \left[1 + \left(2 + \frac{0.617}{\frac{v_m}{v_o}}\right)St^*\right]^{-1}}{1 - (1 + 2.617St^*)^{-1}}\left[1 - \left(1 + 0.55St^* e^{0.25St^*}\right)^{-1}\right] \quad \textbf{(71)}$$

$$\left(St^* = St\, e^{0.02} \;\; ; \;\; 0.02 \leq St \leq 4 \;\; ; \;\; 0.5 \leq \frac{v_o}{v_m} \leq 2\right)$$

- $\boxed{45^o < \theta \leq 90^o}$:

$$\eta_{suct.} = 1 + \left(\frac{v_o}{v_m}\cos\theta - 1\right)\left[3St^{\left(\frac{v_o}{v_m}\right)^{0.5}}\right] \quad \textbf{(72)}$$

$$\left(0.02 \leq St \leq 0.2 \;\; ; \;\; 0.5 \leq \frac{v_o}{v_m} \leq 2\right)$$

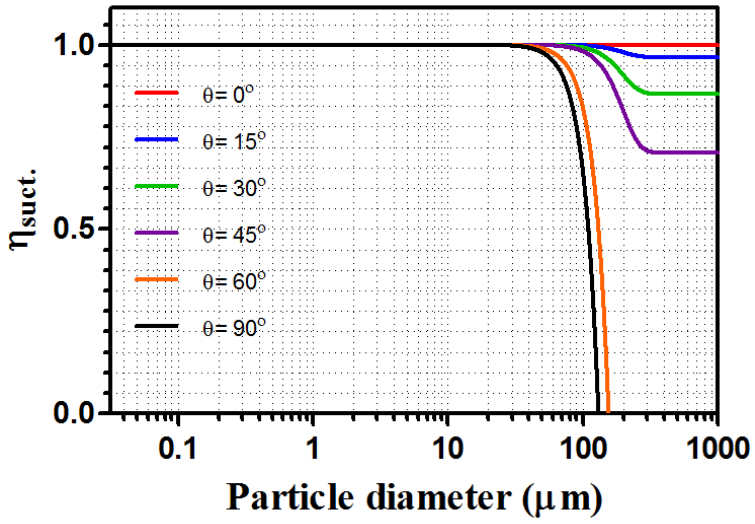

Figure 105: Suction efficiency for an anisoaxial and isokinetic sampling with a circular probe of 1 cm in diameter and 6 cm in length as a function of the particle size for a sample at T=298.15 K, P=101,325Pa, RH=50% and different values of θ.

Figure 105 shows how for isokinetic sampling the suction efficiency is equal to the unit for particle sizes below 20 μm for all θ values. On the other hand, as the particle size increases, the suction coefficient decreases. In the case of angles above 45º it does so quickly reaching a zero value for particles above 100 μm. However, for angles between 0 º and 45 º degrees, the coefficient decreases more gently, tending to a limit value that will be increasingly higher as we approach zero degrees (isoaxial case).

3.4.2 Gravitational sedimentation efficiency

Some of the particles that enter the probe are deposited in its internal walls by gravity. The factor that takes this into account is called gravitational sedimentation efficiency.

3.4.2.1 Isoaxial sampling

The mathematical expression that allows its obtaining was given by Hangal and Willeke (1990):

$$\eta_{sed.} = e^{-4.7\left(Z^{\frac{1}{2}}St^{\frac{1}{2}}Re^{-\frac{1}{4}}\right)^{0.75}} \quad \textbf{(73)}$$

where it is defined:

$$Z = \frac{L_b v_s}{v_m D_{pr}}$$

with:

- L_b: probe length
- v_s: sedimentation rate of the particle
- Re: Reynolds number. It is defined as:

$$Re = \frac{v_m D_{pr} \rho_a}{\mu_a} \quad \textbf{(74)}$$

Being ρ_a the air density.

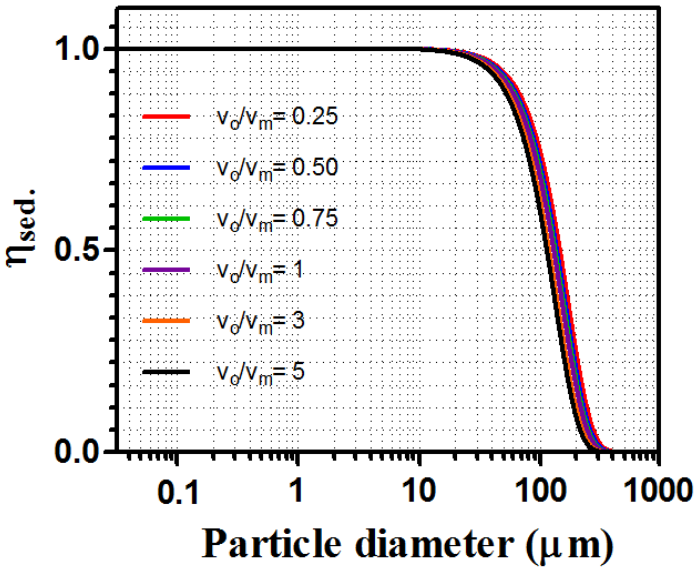

Figure 106: Gravitational sedimentation efficiency for an isoaxial sampling with a circular probe of 1 cm in diameter and 6 cm in length as a function of the particle size for a sample at T=298.15 K, P=101,325Pa, RH=50% and different values of v_o/v_m .

Figure 106 shows how the sedimentation efficiency is equal to the unit for particle sizes up to 10 μm in all cases in the situation under study. However, as particle size increases, the coefficient rapidly decreases to a zero for particles larger than 300 μm.

3.4.2.2 Anisoaxial sampling

The mathematical expression that allows its obtaining was given by Okazaki et al. (1987):

$$\eta_{sed.} = e^{-4.7\left[Z^{\frac{1}{2}}St^{\frac{1}{2}}Re^{-\frac{1}{4}}(cos\,\Theta)^{\frac{1}{2}}\right]^{0.75}} \quad \textbf{(75)}$$

where it is defined:

$$Z = \frac{L_b v_s}{v_m D_{pr}}$$

Figure 107 shows how for isokinetic sampling the sedimentation efficiency is equal to the unit for particle sizes below 10 μm for all θ values. Then, as particle size increases, the coefficient rapidly decreases to zero for particles larger than 300 μm. However, this decrease in the value of the coefficient occurs at larger particle sizes as the value of θ increases, until it is reached the case of $\boldsymbol{\theta}$ =90º, where there are no losses due to gravitational sedimentation and, therefore, its value remains equal to 1 regardless of the particle size. It is interesting to note the important difference in the behavior of the curves for the case of $\boldsymbol{\theta}$ =90º and the rest of the cases. It is observed that even at $\boldsymbol{\theta}$ =60º the behavior of the coefficient value is still very close to the value obtained for $\boldsymbol{\theta}$ =0º, obtaining a very fast change of trend in a very small range of angles.

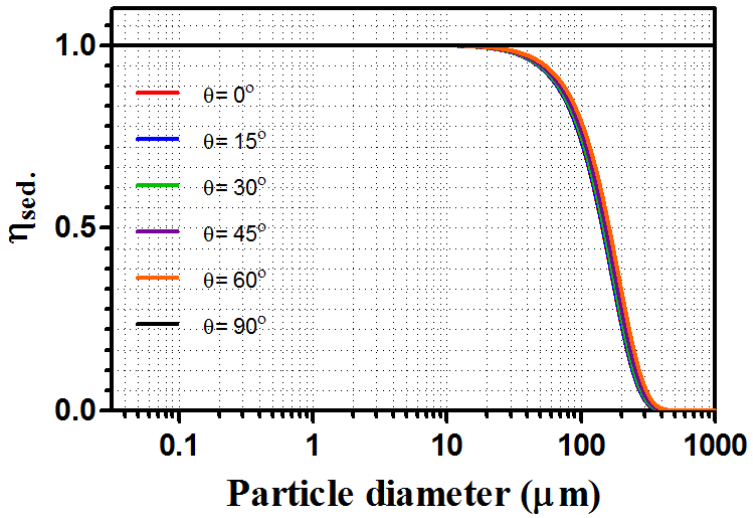

Figure 107: Gravitational sedimentation efficiency for an anisoaxial sampling with a circular probe of 1 cm in diameter and 6 cm in length as a function of the particle size for a sample at T=298.15 K, P=101,325Pa, RH=50% and different values of θ.

3.4.3 Inertial deposition efficiency

Another part of the particles that enter the probe are deposited on its internal walls for inertial reasons. The factor that takes this into account is called inertial deposition efficiency.

3.4.3.1 Isoaxial sampling

The mathematical expression that allows it to be obtained will be different depending on the value $\frac{v_m}{v_o}$.

3.4.3.1.1 Subisokinetic and isokinetic sampling ($v_o/v_m \geq 1$)

The study was conducted by Liu et al. (1989) and it provides the following statement:

$$\eta_{dep.} = \frac{1 + \frac{\left(\frac{v_o}{v_m} - 1\right)}{\frac{1 + 2.66}{St^{\frac{2}{3}}}}}{1 + \frac{\left(\frac{v_o}{v_m} - 1\right)}{\frac{1 + 0.418}{St}}} \quad \textbf{(76)}$$

$$\left(0.01 \leq St \leq 100 \quad ; \quad 1 \leq \frac{v_o}{v_m} \leq 10\right)$$

3.4.3.1.2 Superisokinetic sampling ($v_o/v_m < 1$)

The study was conducted by by Hangal and Willeke (1990) and it provides the following statement:

$$\eta_{dep.} = e^{-75\left[0.09\left(St\frac{v_m - v_o}{v_o}\right)^{0.3}\right]^2} \quad \textbf{(77)}$$

$$\left(0.02 \leq St \leq 4 \quad ; \quad 0.25 < \frac{v_o}{v_m} < 1\right)$$

Figure 108 shows how for isokinetic sampling the suction efficiency is equal to the unit for particle sizes up to $10\ \mu m$ for all $\frac{v_o}{v_m}$. values. On the other hand, as particle size increases, the inertial deposition coefficient decreases in all cases except for the isokinetic, where the value of the coefficient remains constant and equal to the unit for all particle sizes However, the behavior for subisokinetic and superisokinetic cases is very different from $100\ \mu m$ in diameter. While in the case of superisokinetic sampling this performance decreases to zero for values of 200-400 μm, in the case of subisokinetic sampling it reaches a minimum around 200 μm particle sizes and then increases back to values close to the unit.

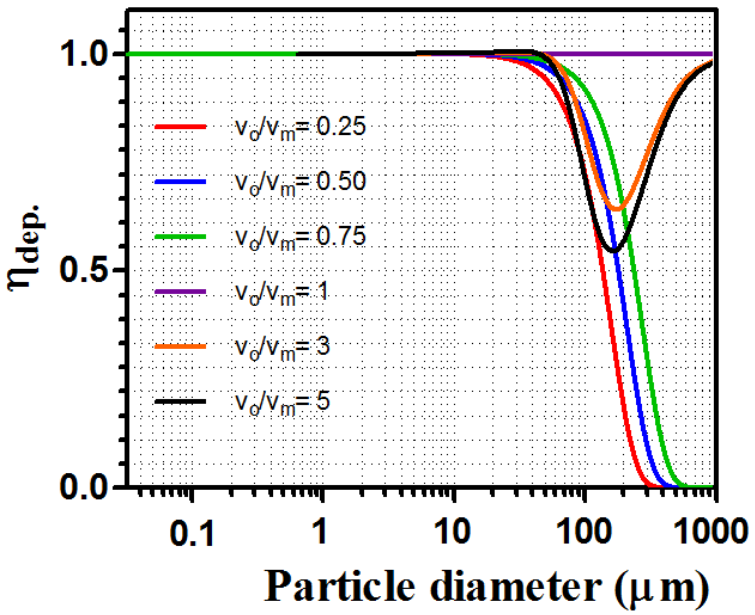

Figure 108: Inertial deposition efficiency for an isoaxial sampling with a circular probe of 1 cm in diameter and 6 cm in length as a function of the particle size for a sample at T=298.15 K, P=101,325Pa, RH=50% and different values of v_o/v_m .

3.4.3.2 Anisoaxial sampling

The mathematical expression that allows its obtaining was given by Hangal and Willeke (1990):

$$\eta_{dep.} = e^{-75\left[0.09\left(St\cos\Theta\frac{v_m - v_o}{v_o}\right)^{0.3} + St\left(\frac{v_o}{v_m}\right)^{0.5}\sin(\theta \mp\alpha)\sin\left(\frac{\Theta\mp\alpha}{2}\right)\right]^2} \qquad \textbf{(78)}$$

$$\left(0.02 \leq St \leq 4 \quad ; \quad 0.25 < \frac{v_o}{v_m} \leq 4\right)$$

with:

$$\alpha = 12\left(1 - \frac{\Theta}{90} - e^{-\Theta}\right)$$

and where the sign of the sinus is chosen according to the criteria:

$$\begin{cases} + & if \;\; 0^0 \leq \Theta \leq 90^0 \\ - & if \;\; -90^0 \leq \Theta < 0^0 \end{cases}$$

Figure 109 shows how for isokinetic sampling the inertial deposition efficiency is equal to the unit for particle sizes below $50\ \mu m$ for all θ values. Then, as particle size increases, the coefficient rapidly decreases to a zero value for particles larger than $100 - 300\ \mu m$ as a function of the angle being studied. However, this decrease in the value of the coefficient occurs at a larger particle size as the value of θ in absolute value decreases, until the case of $\theta = 0^o$ (isoaxial sampling) is reached, where there are no losses due to inertial deposition and, therefore, its value remains equal to 1 regardless of particle size. It is interesting to note the important difference in the behavior of the curves for the case of $\theta = 0^o$ and the rest of the cases. It is observed that even at θ = -30° the

behavior of the coefficient value is still very similar to the value obtained for θ = 0º, obtaining a very fast change of trend in a very small range of angles. Finally, it should be mentioned how, regardless of whether the angle formed between probe and flow is positive or negative, the performance value is quite similar for the same absolute angle value. It is also observed in all cases for the same particle size and for the same sampling angle that inertial efficiency is higher for negative angles than for positive angles.

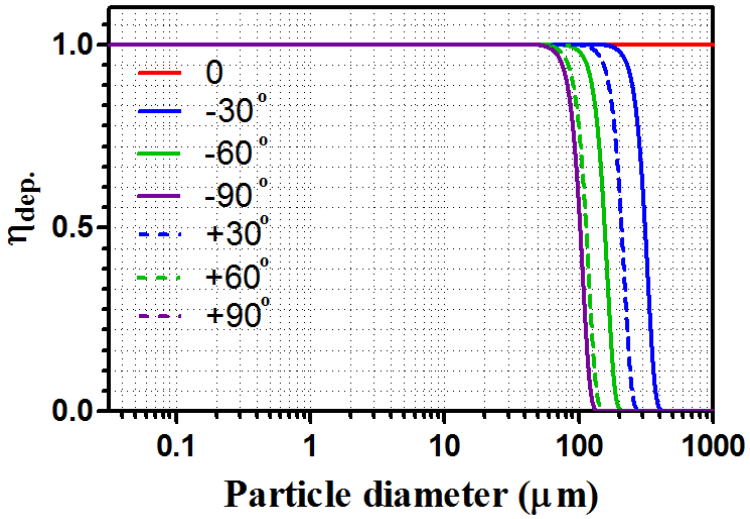

Figure 109: Inertial deposition efficiency for an anisoaxial and isokinetic sampling with a circular probe of 1 cm in diameter and 6 cm in length as a function of the particle size for a sample at T=298.15 K, P=101,325Pa, RH=50% and different values of θ.

3.4.4 Total sampling efficiency

3.4.4.1 Isoaxial sampling

This factor would be the result of the multiplication of the above coefficients, *i.e.*:

$$\eta_{Tot.} = \eta_{suct.}\eta_{sed.}\eta_{dep.} \quad \textbf{(79)}$$

Figure 110 shows how the total efficiency is equal to the unit for particle sizes up to 10 μm in all cases in the situation under study. However, as particle size increases, the coefficient rapidly decreases to zero for particles larger than $200 - 300$ μm as a function of the $\frac{v_o}{v_m}$ ratio.

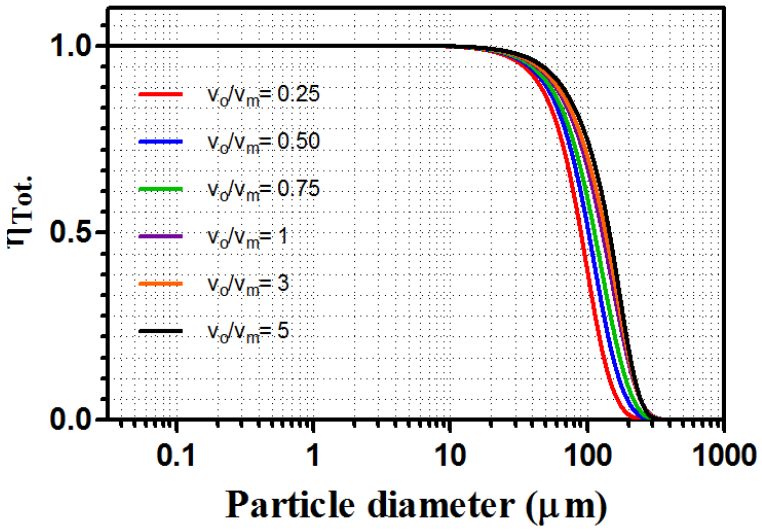

Figure 110: Total efficiency for an isoaxial sampling with a circular probe of 1 cm in diameter and 6 cm in length as a function of the particle size for a sample at T=298.15 K, P=101,325Pa, RH=50% and different values of v_o/v_m .

3.4.4.2 Anisoaxial sampling

This factor would be the result of the multiplication of the above coefficients, *i.e.*:

$$\eta_{Tot.} = \eta_{suct.}\eta_{sed.}\eta_{dep.} \quad \textbf{(80)}$$

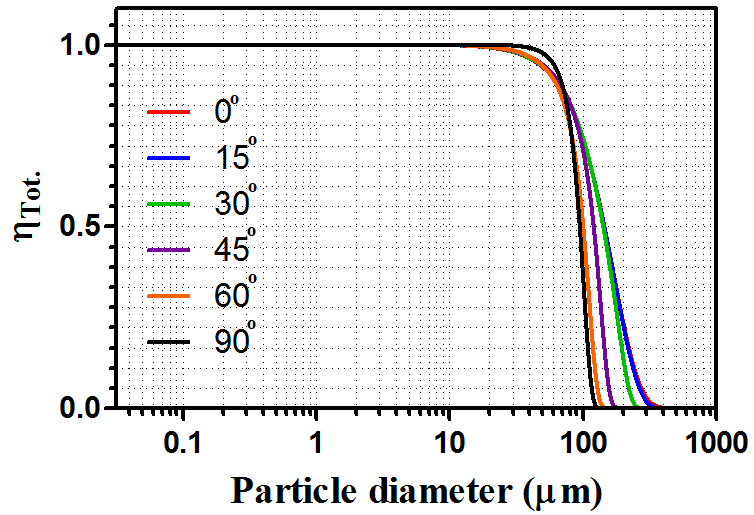

Figure 111: Total efficiency for an anisoaxial sampling with a circular probe of 1 cm in diameter and 8 cm in length as a function of the particle size for a sample at T=298.15 K, P=101,325Pa, RH=50% and different values of θ.

Figure 111 shows how the total efficiency is equal to the unit for particle sizes up to 10 μm in all cases in the situation under study. However, as particle size increases, the coefficient rapidly decreases to a zero for particles larger than $100 - 300$ μm as a function ot the value of θ.

From the results previously obtained and since the range of particle measurements will be contained in the range between 0.1 and 10 μm, it is concluded, therefore, that for the tests carried out for the accomplishment of this work a total efficiency of unit value can be assumed, that is to say, that the number of particles counted in the probe will be equal to the real number of particles of the sample.

Chapter 4

Characterization of the Counterfog® system

This chapter describes the process of characterizing the fog generated by the Counterfog® system. This characterization has been carried out with nozzles B1:2 and F1:2. The results obtained have led to the choice of the B1:2 nozzle for the rest of the tests presented in this thesis as will be appropriately justified below.

4.1 Water flow rate for nozzles B1:2 and F1:2 and different combinations of air and water pressure

In this section, maximum water flows are determined for various combinations of air and water pressures for nozzle models B1:2 and F1:2. In addition, the cone opening angle (Figure 112) will be measured and a visual study of the fog density will be made over time after the activation of the nozzle.

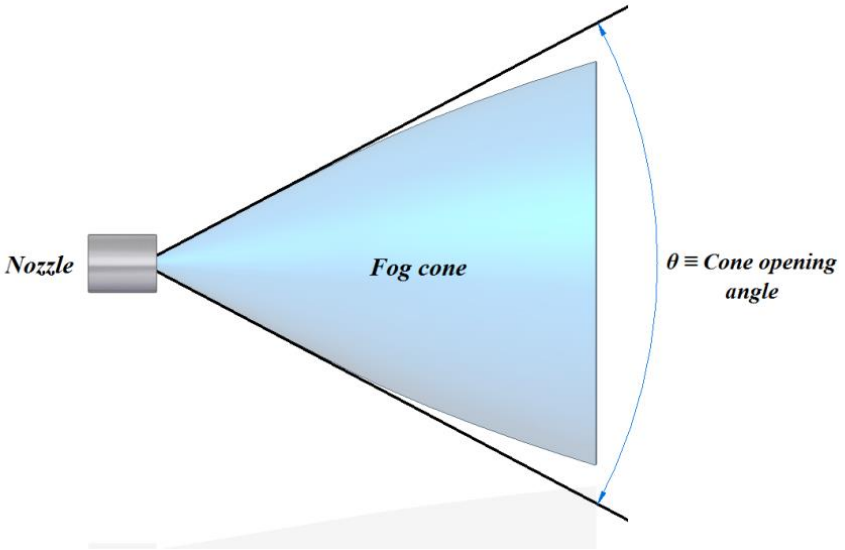

Figure 112: Cone opening angle definition for a fog cone generated by a nozzle.

4.1.1 Experimental setup and procedure

Before performing each test the different parameters of the test room shall be established to ensure that these factors will not affect the fog generation process. In this way, the temperature and relative humidity of the room were set at 25 ºC and 95%, respectively. The temperature of the shooting water will be 12 º C, while the pressures of air and water will vary according to the test. The room temperature has been chosen because it is a temperature contained in the most common range used for air conditioning in large public buildings. On the other hand, it is observed during the tests that the relative humidity reaches values close to 100% almost instantaneously once the shot has been fired. In this way, and since, as will be indicated later on, it is necessary to make shoots prior to carrying out the tests for pressure adjustment, the value of RH close to 100% is chosen.

The composition of the fluid for the generation of the fog was limited to water, not being added any kind of neutralizing compound. The temperature and humidity of the test room, as well as the flow of water used in the generation of fog were monitored at all times during each test. For this porpuse, laboratory equipment (see section 3.2.2) was used during tests. In addition, a video camera recorded everything that happened inside the test room.

Once the factors have been defined, the working procedure used to carry out the tests is explained in detail. Each test begins by ensuring the correct maintenance and cleaning of the different elements of the laboratory (see section 3.2.2), as well as the correct initial position of the pneumatic and manual ball valves. Then it is checked that the pressurized air tank is fully charged and that the pressurized water tank is empty. On the one hand, in the case of the pressurized air tank, it is checked that it is at a pressure of between 26 and 29 bar, as this is the maximum range provided by the compressor. This allows guaranteeing that the pressures that are subsequently imposed for fog generation are met. If this is not the case, the compressor will start up autonomously until it stops once the pressure range in the pressurized air tank defined above has been reached. On the other hand, to check the pressurized water tank, the purge valve is opened to release any remaining pressure inside due to previous tests. The ball valve is then opened to allow the

tank to drain by gravity. Once completely empty, the purge and drain valves are closed. The next step is to check that the atmospheric water tank is full and if necessary fill it with the hose connected to the water inlet. In addition, a pH test and temperature measurement is performed to ensure that the composition and temperature of the water used is the same for the entire test set. After completing the above steps the pressurized water tank is filled with water from the atmospheric water tank. To do this, the purge and fill valves are opened and the pump is activated to allow the pressurized water tank to fill to its maximum level (4.5 l). This maximum level is guaranteed by a sensor and an actuator that stops the pump once it has been reached. Once this process is completed the pump is switched off and the purge and fill valves are closed. Once this is done, the ball valves installed inside the test room for the air and water outlet are closed and the shooting pressures adjusted. In the case of air, the air valve is opened allowing pressurized air to flow from the pressurized air tank through the air circuit. The shooting air pressure is adjusted by means of the manual regulating valve and the pressure manometer located at the same point. Once properly adjusted, the air valve is closed and the air outlet ball valve is opened to release the remaining pressure in the ducts that reach the nozzle. In the case of water, the water pressure valve is opened to allow pressurized air to flow from the pressurized air tank to the pressurized water tanks through the water circuit. The shooting water pressure is adjusted by means of a manual control valve and a pressure manometer located at the same point. Once correctly adjusted, the water outlet ball valve is opened to release the remaining pressure and to remove the residual water contained in the pipes leading to the nozzle. The air and water outlet ball valves will remain open until the next shot is fired. The next step is a short shot (approximately 8 seconds) to fill the water pipes of the water circuit with water without exhausting the pressurized water tank by opening the water valves. In this way, it will be able to ensure that during the test the fog begins to be generated almost instantaneously without a significant delay from the opening of the shooting valves (air and water valves). This is of great importance due to the short test shooting times and the delays observed in fog generation of up to 5 seconds when the water circuit is empty. The air, water and water pressure valves are closed once the shot is finished and the computer in the Control Room is used to check that the air and water shooting pressure obtained match with that established in the settings. Once this process has been completed, it is repeated from the beginning to leave the system ready to perform the test shot. At this point, the test room is closed and completely insulated. The video camera will have been placed and activated inside the test room immediately before the closure of the test room. Figure 113 shows a diagram summarizing the process of setting up the room for testing.

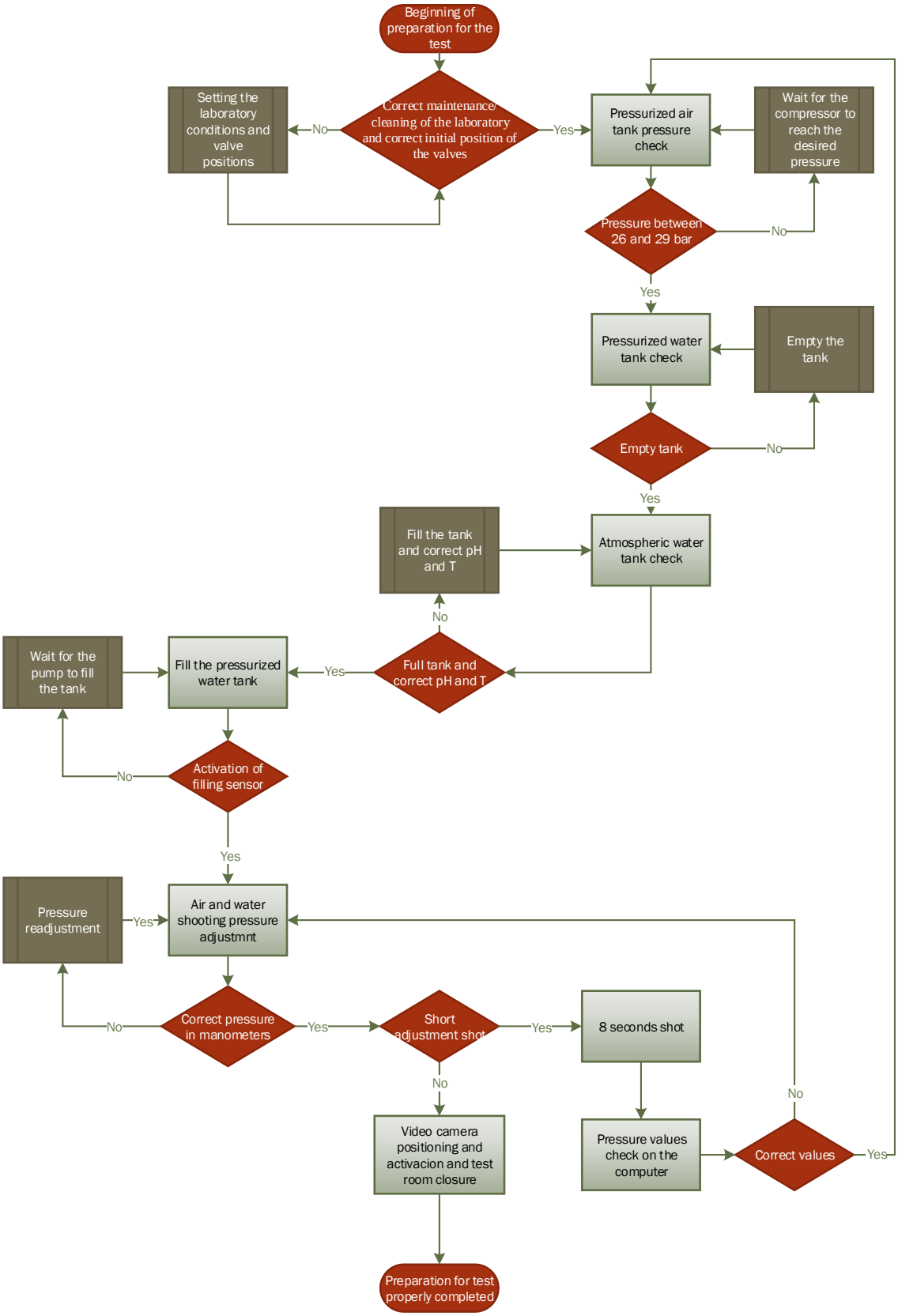

Figure 113: Diagram of the room preparation procedure for water flow rate tests for nozzles B1:2 and F1:2 and different combinations of air and water pressures.

As indicated above, once the video camera has been placed in the room, this is switched on and the test room is closed for perfect isolation from the outside of the laboratory. After this, the fog is generated by shooting the nozzle for 30 seconds at the air and water pressures that have been established during the preparation for the test as shown in Figure 113. After this time, the test is considered complete and the room is opened. At the end of the test, the shooting water and aire pressure data are checked to ensure compliance with test conditions. Furthermore, test videos are reviewed to ensure that no irregularities occur during testing. Once it is verified that everything has happened as stipulated the test is taken as correct and water flow data is collected. Otherwise, the test is automatically discarded and repeated. Figure 114 shows a diagram summarizing the test process.

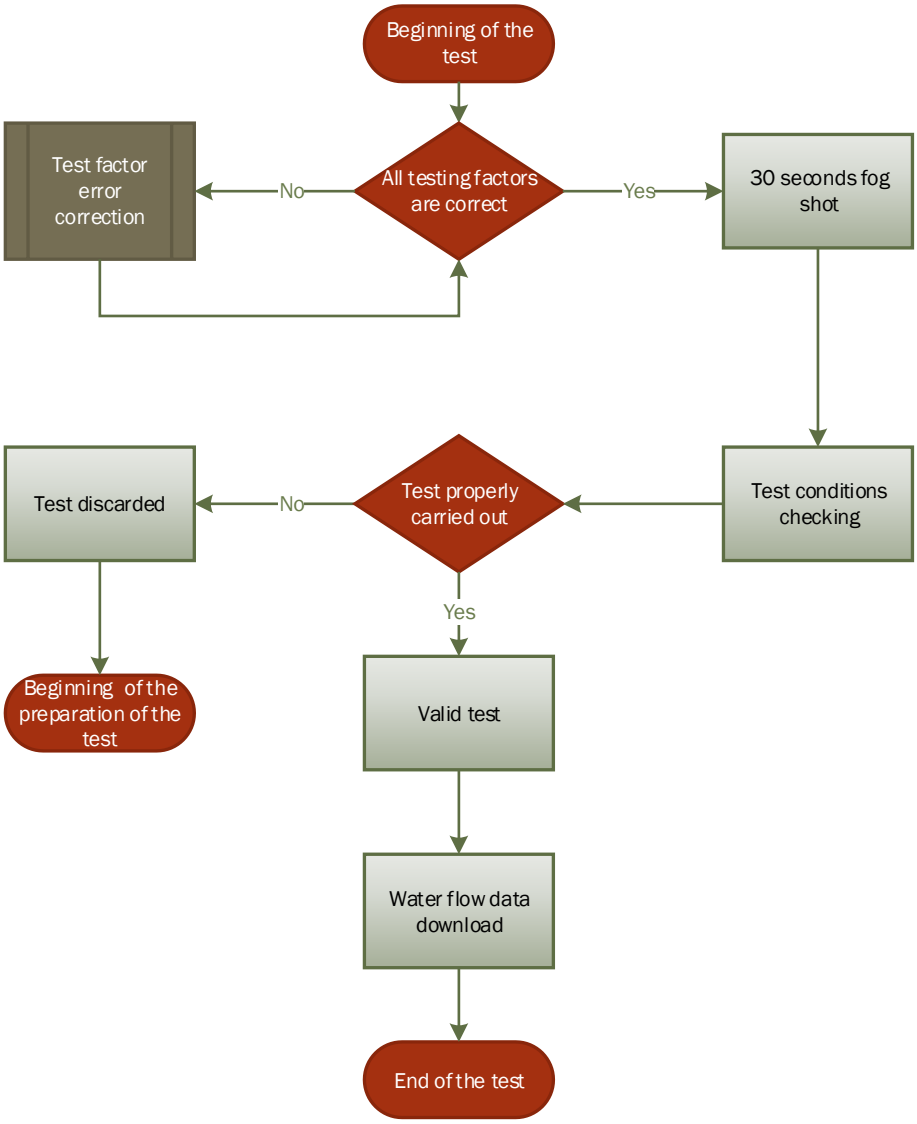

Figure 114: Diagram of the test procedure diagram for water flow rate tests for nozzles B1:2 and F1:2 and different combinations of air and water pressures.

4.1.2 Experimental results and Discussion

A characterization of the fog cones generated for the different nozzle models studied at different combinations of air pressure and water pressure has been carried out. For this purpose, the angle of this cone has been estimated and a visual analyse has been made of the fog density generated and its temporal evolution.

In addition, the maximum flows obtained during the shots were obtained and it was observed whether the water tanks available in the laboratory were emptied during the tests.

By way of example, the results obtained for Test I are shown below. The results obtained for all cases tested are shown in **Annex B** of this work:

TEST I		
NOZZLE	Model	B
	Scale	1:2
AIR PRESSURE		4.5 bar
WATER PRESSURE		1.5 bar

Figure 115: Stabilized cone of nozzle B1:2 for a P_{air}= 4.5 bar and P_{water}= 1.5 bar combination and cone opening angle.

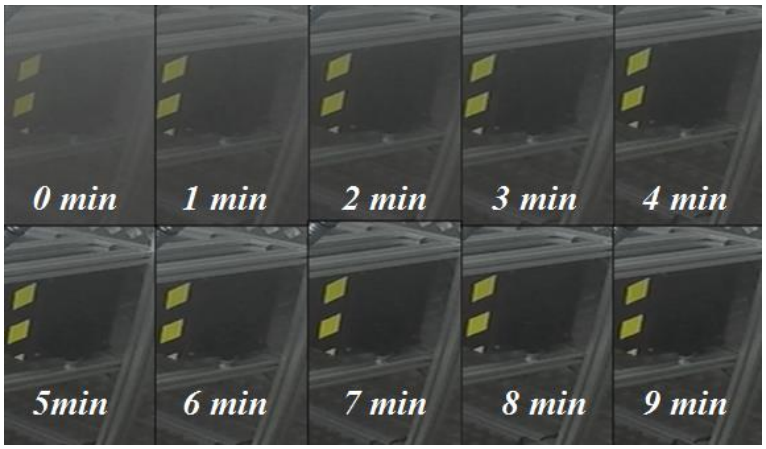

Figure 116: Time evolution of the fog generated with the B1:2 nozzle for a combination of P_{air}= 4.5 bar and P_{water}= 1.5 bar. The images show the concentration of fog in the room every minute since the shot was taken.

For this pressure combination, the pressurized water tank, with a capacity of 4.5 l of water, is not emptied during shooting. The maximun water flow rate obtained is lower than the sensitivity offered by the flowmeters installed in the laboratory. Therefore, it has not been possible to obtain a numerical flow rate value. Figure 115 shows the cone stabilized during the shooting and Figure 116 shows the evolution of the fog with the time elapsed after the shot.

Table 16 shows a comparison of the results obtained in the laboratory for nozzles B1:2 and F1:2.

Table 16: Results obtained for the different pressure combinations tested with the nozzles B1:2 and F1:2.

TEST	Nozzle model	P_{air} (bar)	P_{water} (bar)	Maximum water flow rate (l/s)	Cone opening angle (°)	Pressurized water tank emptied
I	B1:2	4.5	1.5	< 0.01	54.3	No
II	B1:2	5	5	0.13	60.5	No
III	B1:2	5	10	0.23	72.8	Yes
IV	B1:2	5	15	0.30	78.7	Yes
V	B1:2	5	20	0.33	81.5	Yes
VI	B1:2	5	25	0.36	89.1	Yes
VII	B1:2	6	1.5	< 0.01	39.7	No
VIII	B1:2	7	1.5	< 0.01	38.5	No
IX	B1:2	8	1.5	< 0.01	37	No
X	B1:2	9	1.5	< 0.01	26.4	No
XI	B1:2	10	1.5	-	-	No
XII	B1:2	10	5	0.0425	44.7	No
XIII	B1:2	10	10	0.16	50.5	No
XIV	B1:2	10	15	0.24	56.3	Yes
XV	B1:2	10	20	0.33	57.4	Yes
XVI	B1:2	10	25	0.38	62.3	Yes
XVII	B1:2	12	3	< 0.01	35.8	No
XVIII	B1:2	15	3	< 0.01	30.4	No
IXX	B1:2	19	4	< 0.01	27	No
XX	F1:2	5	5	0.01	27.1	No
XXI	F1:2	5	10	0.20	43.9	No
XXII	F1:2	5	15	0.27	31.9	No
XXIII	F1:2	5	20	0.27	58.7	Yes
XXIV	F1:2	10	5	0.14	22.2	No
XXV	F1:2	10	10	0.29	28.3	Yes
XXVI	F1:2	10	15	0.63	34	Yes
XXVII	F1:2	10	20	0.66	45.1	Yes
XVIII	F1:2	15	5	0.44	24.1	No
XXIX	F1:2	15	10	0.28	29.1	Yes
XXX	F1:2	15	15	0.27	33.5	No
XXXI	F1:2	15	20	0.41	36.5	Yes

XXXII	F1:2	20	5	0.33	24	Yes
XXXIII	F1:2	20	10	0.24	25.5	Yes
XXXIV	F1:2	20	15	0.29	28.2	Yes
XXXV	F1:2	20	20	0.40	32.8	Yes

It can be observed that when the air pressure is much higher than the water pressure, the water flow decreases until even fog is not visible in the room. This occurs because the air flow prevents water from flowing out. In fact, a part of the air flow is likely to reverse its direction, entering through the water inlet

The higher density and longer time of the fog are associated to micron sized droplets that were preferred for the next tests. Therefore, the B1:2 nozzle was chosen for the laboratory decontamination tests. A more in-depth characterization of the B1:2 nozzle will be shown below.

4.1.3 Conclusions

From the data and images obtained it can be concluded that:

- As expected, the cone generated by the B1:2 nozzle is a hollow cone while the one generated by the F1:2 nozzle is a solid cone.
- For the same air pressure, the water flow rate increases with increasing water pressure for both nozzles.
- For the same air pressure, the opening angle of the cone increases with increasing water pressure for both nozzles.
- Water flow rates obtained for the B1:2 nozzle are higher than those obtained for the F1:2 nozzle for air pressure below 10 bar; while water flrow rates ofr F1:2 are larger than those of B1:” for air pressure above 10 bar.
- For the same air and water pressure combination, cone opening angles for B1:2 nozzle are larger than those obtained for the F1:2 nozzle.
- For constant water pressure, the lower the air pressure is, the larger cone opening angle for both nozzle models.
- Both nozzle models can generate fog with water flows as low as 0.01 l/s.
- For similar air and water pressure combinations, the fog obtained for the B1:2 nozzle is denser and remains longer than that obtained for the F1:2 nozzle.

4.2 Water flow rate curve for nozzle B1:2 without air application and different water pressures

Tests are conducted on a wide range of water pressures in order to obtain as much information as possible about the required water flows. The object of this section is to delve deeper into the results obtained in section 4.1 for the particular case of the B 1:2 nozzle.

4.2.1 Experimental setup and procedure

Before performing each test the different parameters of the test room shall be established to ensure that these factors will not affect the fog generation process. In this way, the temperature and relative humidity of the room were set at 25 ºC and 95%, respectively. The composition of the fluid for the generation of the fog was limited to water, not being added any kind of neutralizing compound. The temperature and humidity of the test room, as well as the flow of water used in the generation of fog were monitored at all times during each test. For this porpuse, laboratory equipment (see section 3.2.2) was used during tests. In addition, a video camera recorded everything that happened inside the test room.

The temperature of the shooting water will be 12 ºC, while the water pressure will vary according to the test and the air pressure will be not applied.

Once the factors have been defined, the working procedure used to carry out the tests is explained in detail. Each test begins by ensuring the correct maintenance and cleaning of the different elements of the laboratory (see section 3.2.2), as well as the correct initial position of the pneumatic and manual ball valves. Then it is checked that the pressurized air tank is fully charged and that the pressurized water tank is empty. On the one hand, in the case of the pressurized air tank, it is checked that it is at a pressure of between 26 and 29 bar, as this is the maximum range provided by the compressor. This allows guaranteeing that the pressures that are subsequently imposed for fog generation are met. If this is not the case, the compressor will start up autonomously until it stops once the pressure range in the pressurized air tank defined above has been reached. On the other hand, to check the pressurized water tank, the purge valve is opened to release any remaining pressure inside due to previous tests. The ball valve is then opened to allow the tank to drain by gravity. Once completely empty, the purge and drain valves are closed. The next step is to check that the atmospheric water tank is full and if necessary fill it with the hose connected to the water inlet. In addition, a pH test and temperature measurement is performed to ensure that the composition and temperature of the water used is the same for the entire test set. After completing the above steps the pressurized water tank is filled with water from the atmospheric water tank. To do this, the purge and fill valves are opened and the pump is activated to allow the pressurized water tank to fill to its maximum level (4.5 l). This maximum level is guaranteed by a sensor and an actuator that stops the pump once it has been reached. Once this process is completed the pump is switched off and the purge and fill valves are closed. Once this is done, the ball valves installed inside the test room for the air and water outlet are closed and the water

shooting pressures adjusted. In the case of air, and since the tests are carried out without the application of air, the air valve will remain closed at all times. The air outlet ball valve opens to release any remaining pressure in the ducts to the nozzle. In the case of water, the water pressure valve is opened to allow pressurized air to flow from the pressurized air tank to the pressurized water tanks through the water circuit. The shooting water pressure is adjusted by means of a manual control valve and a pressure manometer located at the same point. Once correctly adjusted, the water outlet ball valve is opened to release the remaining pressure and to remove the residual water contained in the pipes leading to the nozzle. The air and water outlet ball valves will remain open until the next shot is fired. The next step is a short shot (approximately 8 seconds) to fill the water pipes of the water circuit with water without exhausting the pressurized water tank by opening the water valves. In this way, it will be able to ensure that during the test the fog begins to be generated almost instantaneously without a significant delay from the opening of the shooting valves (air and water valves). This is of great importance due to the short test shooting times and the delays observed in fog generation of up to 5 seconds when the water circuit is empty. The water and water pressure valves are closed once the shot is finished and the computer in the Control Room is used to check that the water shooting pressure obtained matches with that established in the settings. Once this process has been completed, it is repeated from the beginning to leave the system ready to perform the test shot. At this point, the test room is closed and completely insulated. The video camera will have been placed and activated inside the test room immediately before the closure of the test room. Figure 117 shows a diagram summarizing the process of setting up the room for testing.

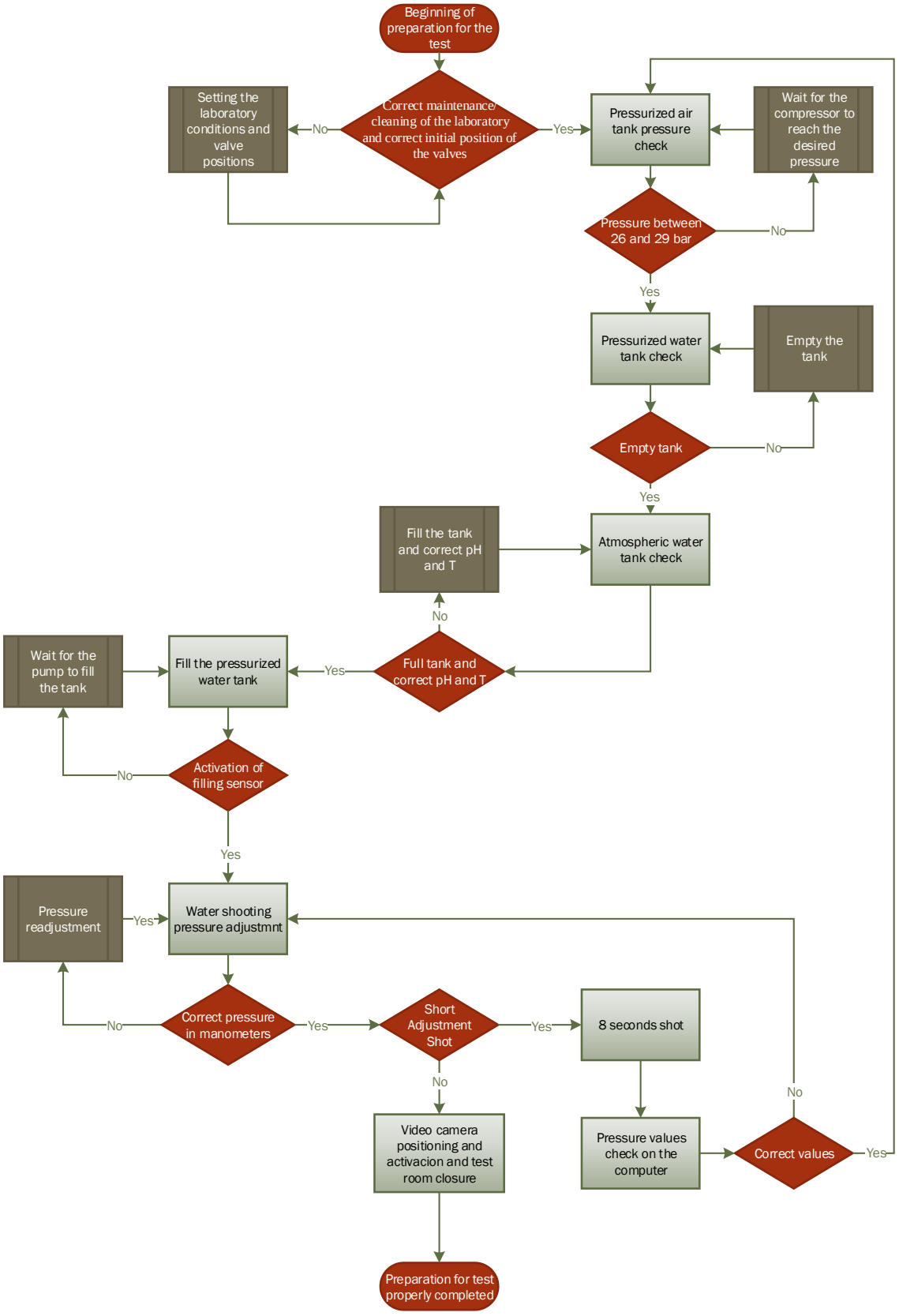

Figure 117: Diagram of the room preparation procedure for water flow rate tests for nozzles B1:2 and different water pressures without air application.

As indicated above, once the video camera has been placed in the room, this is switched on and the test room is closed for perfect isolation from the outside of the laboratory. After this, the fog is generated by shooting the nozzle for 30 seconds at the water pressures that have been established during the preparation for the test as shown in Figure 117. After this time, the test is considered complete and the room is opened. At the end of the test, the shooting water pressure data are checked to ensure compliance with test conditions. Furthermore, test videos are reviewed to ensure that no irregularities occur during testing. Once it is verified that everything has happened as stipulated the test is taken as correct and water flow data is collected. Otherwise, the test is automatically discarded and repeated. Figure 118 shows a diagram summarizing the test process.

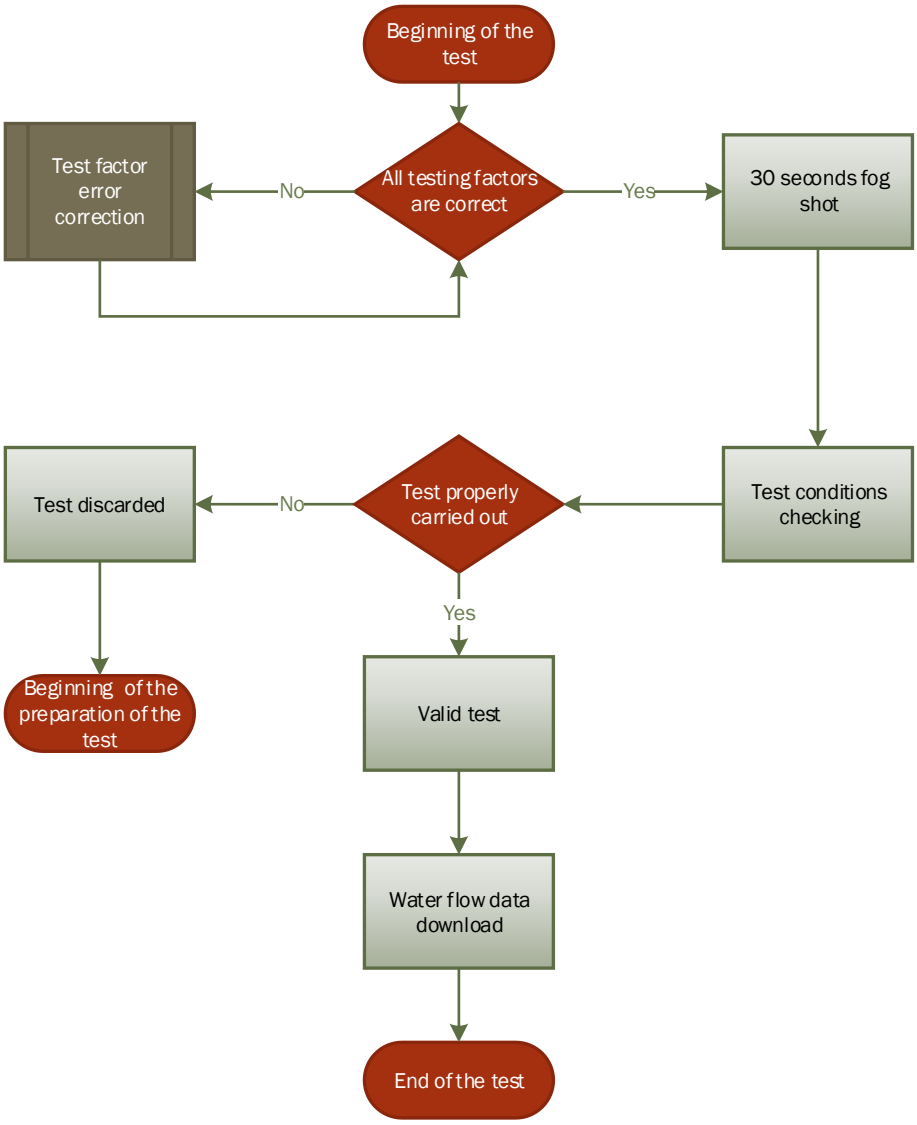

Figure 118: Diagram of the test procedure diagram water flow rate tests for nozzles B1:2 and different water pressures without air application.

4.2.2 Experimental results and Discussion

As previously stated, the shots taken in the execution of these tests will last 30 seconds. The data presented are as follows (**Figure 119**):

- Nominal water pressure imposed prior to the test (P_{water})
- Flow rate of water in liters per seconds collected in real time (Q_{water})

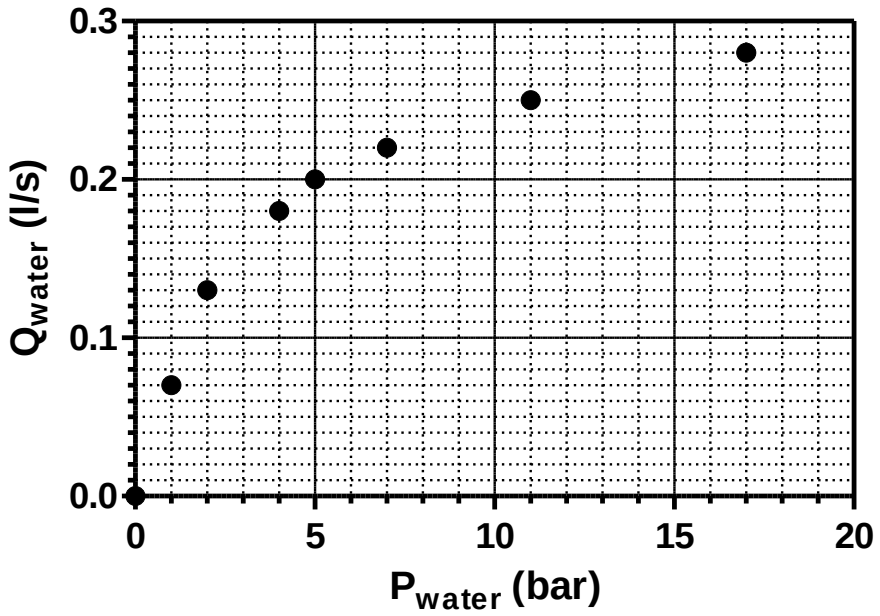

Figure 119: Water flow rate for nozzles B1:2 and different water pressures without air application.

There is a minimum value for the water pressure below which, even if no air pressure is applied, no water flow is appreciated. The value of this threshold is very difficult to obtain due to the precision level of the laboratory. That is why, although this phenomenon has been observed during the tests, the value is not shown in the graph. The need of the fluid to reach a certain kinetic energy for the generation of fog in the nozzle, as well as the need to overcome a certain level of resistance on its way to the nozzle chamber favor the appearance of this phenomenon.

4.2.3 Conclusions

From the data and images obtained it can be concluded that:

- The larger the water pressure is supplied the larger the water flow rate.
- The application of air pressure narrows the cone and reduceds the water flow.
- The water flow approaches asymptotically to a maximum value when water pressure grows.

4.3 Water flow rate curves for nozzle B1:2 with both air and water pressure application

The object of this section is to delve deeper into the results obtained in section 4.1 for the particular case of the B 1: 2 nozzle.

4.3.1 Experimental setup and procedure

Before performing each test the different parameters of the test room shall be established to ensure that these factors will not affect the fog generation process. In this way, the temperature and relative humidity of the room were set at 25 ºC and 95%, respectively. The composition of the fluid for the generation of the fog was limited to water, not being added any kind of neutralizing compound. The temperature and humidity of the test room, as well as the flow of water used in the generation of fog were monitored at all times during each test. For this porpuse, laboratory equipment (see section 3.2.2) was used during tests. In addition, a video camera recorded everything that happened inside the test room.

The temperature of the shooting water will be 12 º C, while the pressures of air and water will vary according to the test.

Once the factors have been defined, the working procedure used to carry out the tests is explained in detail. Each test begins by ensuring the correct maintenance and cleaning of the different elements of the laboratory (see section 3.2.2), as well as the correct initial position of the pneumatic and manual ball valves. Then it is checked that the pressurized air tank is fully charged and that the pressurized water tank is empty. On the one hand, in the case of the pressurized air tank, it is checked that it is at a pressure of between 26 and 29 bar, as this is the maximum range provided by the compressor. This allows to guarantee that the pressures that are subsequently imposed for fog generation are met. If this is not the case, the compressor will start up autonomously until it stops once the pressure range in the pressurized air tank defined above has been reached. On the other hand, to check the pressurized water tank, the purge valve is opened to release any remaining pressure inside due to previous tests. The ball valve is then opened to allow the tank to drain by gravity. Once completely empty, the purge and drain valves are closed. The next step is to check that the atmospheric water tank is full and if necessary fill it with the hose connected to the water inlet. In addition, a pH test and temperature measurement is performed to ensure that the composition and temperature of the water used is the same for the entire test set. After completing the above steps the pressurized water tank is filled with water from the atmospheric water tank. To do this, the purge and fill valves are opened and the pump is activated to allow the pressurized water tank to fill to its maximum level (4.5 l). This maximum level is guaranteed by a sensor and an actuator that stops the pump once it has been reached. Once this process is completed the pump is switched off and the purge and fill valves are closed. Once this is done, the ball valves installed inside the test room for the air and water outlet are closed and the shooting pressures adjusted. In the case of air, the air valve is opened allowing pressurized air to flow from the pressurized air tank through the air circuit. The shooting air pressure is adjusted by means of the manual regulating valve and the pressure manometer located at the same point. Once properly adjusted, the air valve is closed and

the air outlet ball valve is opened to release the remaining pressure in the ducts that reach the nozzle. In the case of water, the water pressure valve is opened to allow pressurized air to flow from the pressurized air tank to the pressurized water tanks through the water circuit. The shooting water pressure is adjusted by means of a manual control valve and a pressure manometer located at the same point. Once correctly adjusted, the water outlet ball valve is opened to release the remaining pressure and to remove the residual water contained in the pipes leading to the nozzle. The air and water outlet ball valves will remain open until the next shot is fired. The next step is a short shot (approximately 8 seconds) to fill the water pipes of the water circuit with water without exhausting the pressurized water tank by opening the water valves. In this way, it will be able to ensure that during the test the fog begins to be generated almost instantaneously without a significant delay from the opening of the shooting valves (air and water valves). This is of great importance due to the short test shooting times and the delays observed in fog generation of up to 5 seconds when the water circuit is empty. The air, water and water pressure valves are closed once the shot is finished and the computer in the Control Room is used to check that the air and water shooting pressure obtained match with that established in the settings. Once this process has been completed, it is repeated from the beginning to leave the system ready to perform the test shot. At this point, the test room is closed and completely insulated. The video camera will have been placed and activated inside the test room immediately before the closure of the test room. Figure 120 shows a diagram summarizing the process of setting up the room for testing.

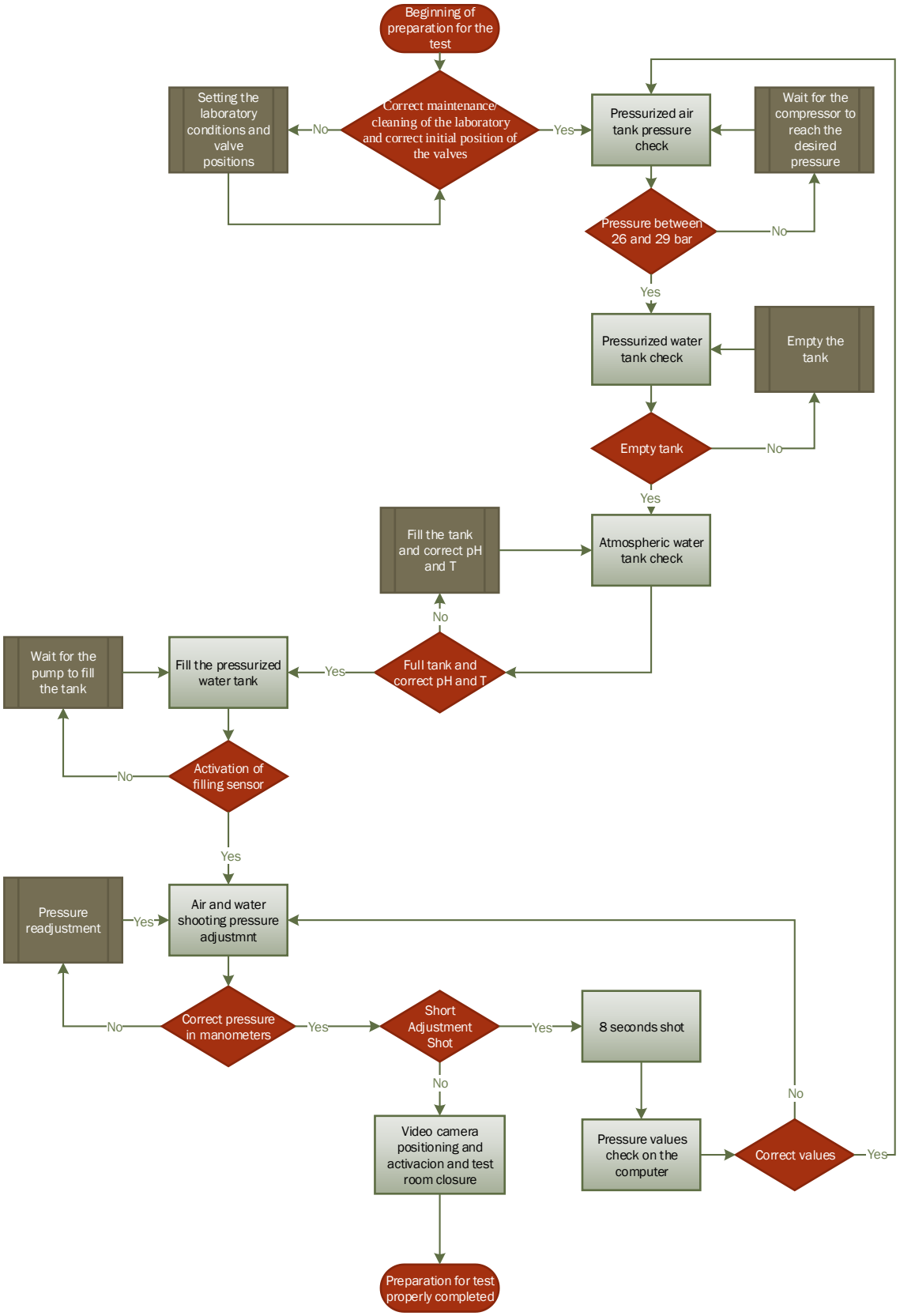

Figure 120: Diagram of the room preparation procedure for water flow rate tests for nozzle B1:2 with different combinations of air and water pressure.

As indicated above, once the video camera has been placed in the room, this is switched on and the test room is closed for perfect isolation from the outside of the laboratory. After this, the fog is generated by shooting the nozzle for 30 seconds at the air and water pressures that have been established during the preparation for the test as shown in Figure 120. After this time, the test is considered complete and the room is opened. At the end of the test, the shooting water and aire pressure data are checked to ensure compliance with test conditions. Furthermore, test videos are reviewed to ensure that no irregularities occur during testing. Once it is verified that everything has happened as stipulated the test is taken as correct and water flow data is collected. Otherwise, the test is automatically discarded and repeated. Figure 121 shows a diagram summarizing the test process.

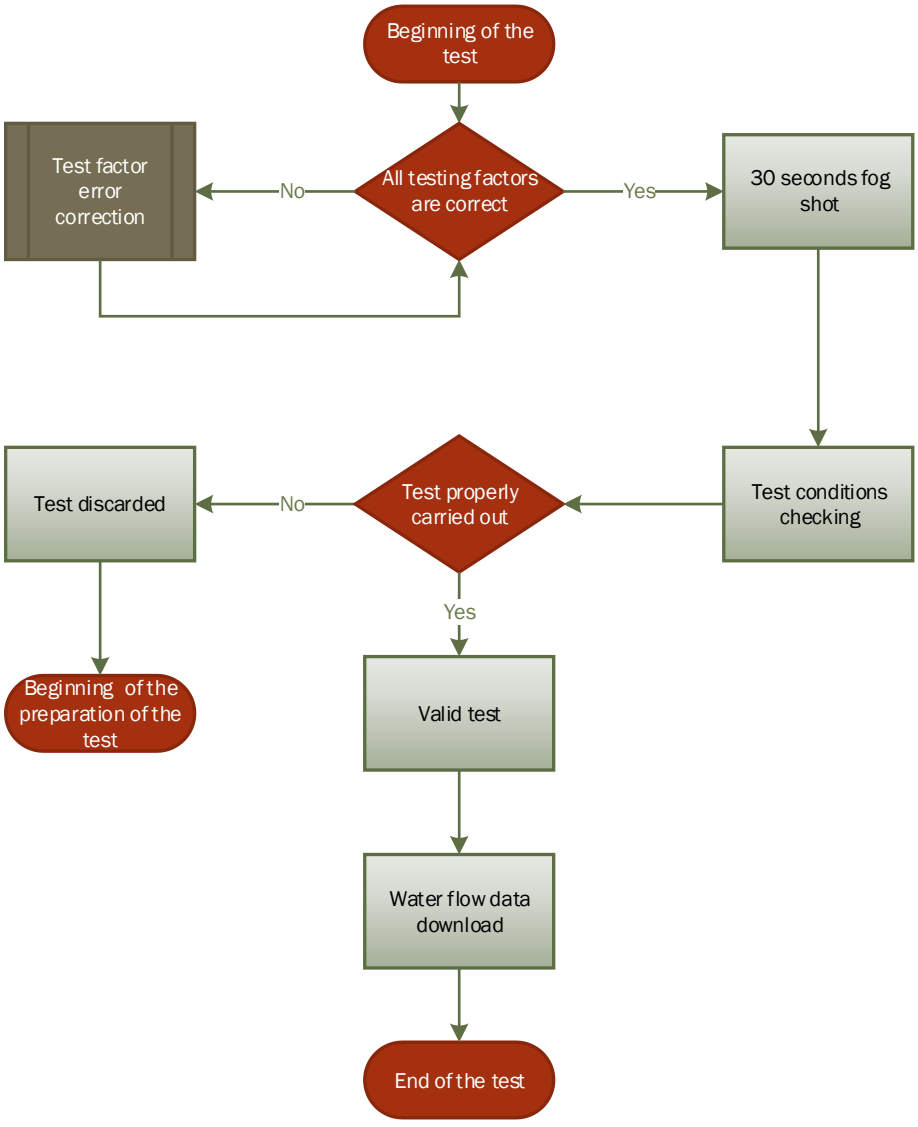

Figure 121: Diagram of the test procedure for water flow rate tests for nozzle B1:2 with different combinations of air and water pressure.

4.3.2 Experimental results and Discussion

As previously mentioned, the shots taken in the execution of these tests will last 30 seconds. The data presented are as follows (Figure 122):

- Nominal water pressure imposed prior to the test (P_{water})
- Nominal air pressure imposed prior to the test (P_{air})
- Flow of water in liters per seconds collected in real time (Q_{water})

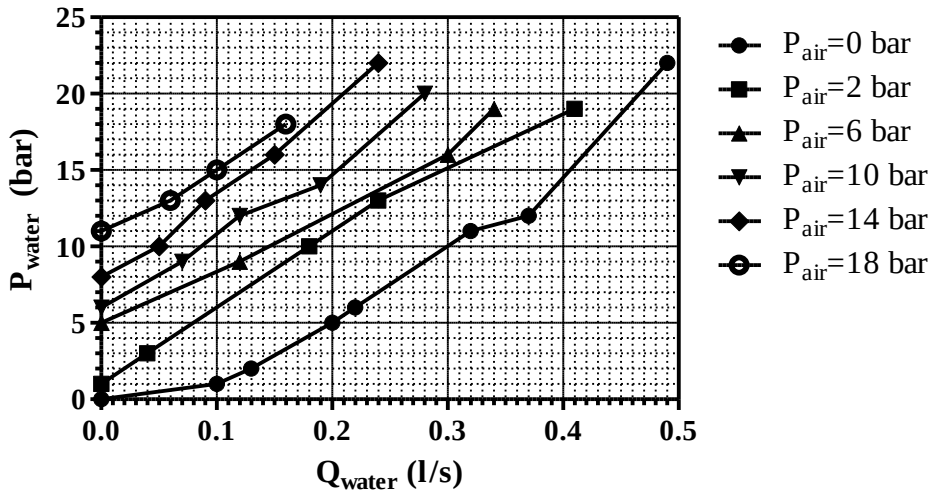

Figure 122: Water flow rate curves for the B1:2 nozzle at constant air pressure as a function of the water pressure used.

There is a minimum value for the water pressure below which no water flow is appreciated. The higher the applied air pressure, the higher the minimum water pressure necessary to generate a visible fog in the room. For a constant air pressure, the water pressure must be high enough to overcome the resistance that the air flow exerts on the water flow. If this value is not exceeded, the air flow blocks the water outlet, possibly also inverse flow of air into the water inlet.

4.3.3 Conclusions

From the data and images obtained it can be concluded that:

- For a constant air pressure, the flow rate obtained increases as the applied water pressure increases.
- For a constant water pressure, the flow rate obtained increases as the applied air pressure decreases.

- The same water flow can be obtained for different combinations of air and water pressures. Increasing one of these pressures will lead to increasing the other to maintain the set flow rate.

- The lower the air pressure applied and the greater the difference with the water pressure, the greater the flow rate obtained.

- There is a minimum water pressure below which no water flow is appreciated. This threshold is higer the higer the aire pressure.

4.4 Particle size distribution of the fog generated with the B1:2 nozzle for different air and water pressure combinations

4.4.1 Experimental setup and procedure

Before performing each test the different parameters of the test room shall be established to ensure that these factors will not affect the fog generation process. In this way, the temperature and relative humidity of the room were set at 25 ºC and 95%, respectively. The composition of the fluid for the generation of the fog was limited to water, not being added any kind of neutralizing compound. The temperature and humidity of the test room, as well as the flow of water used in the generation of fog were monitored at all times during each test.

The number and size of the water droplets was monitored by a particle counter (8306 Handheld Particle Counter, Particles Plus, Massachusetts, U.S.A.). Number of droplets per liter is measured between 0.3 µm and 10 µm. The inclination and height of this counter (Figure 123 and Figure 124), remained unchanged throughout all the tests performed. In addition to the particle counter, laboratory equipment (see section 3.2.2) was used during tests. A video camera recorded everything that happened inside the test room.

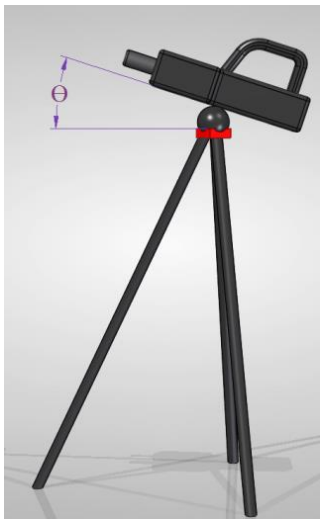

Figure 123: Pitch angle of the particle counter.

Tests will be performed with the B1: 2 nozzle model. The temperature of the shooting water will be 12 º C, while the pressures of air and water will vary accordint to the test. The pitch angle of the particle counter will be + 30º and its height, with respect to the ground level of the test room, of 0.65 m.

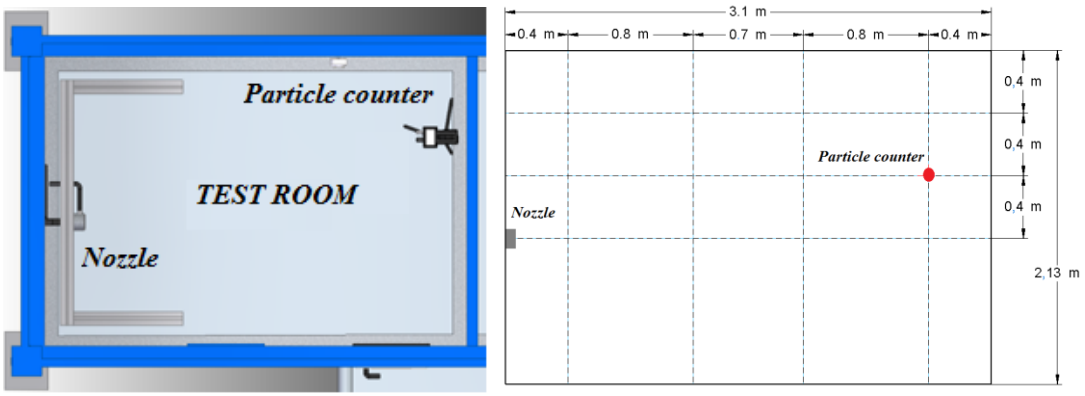

Figure 124: Particle counter position in particle distribution tests for nozzles B1:2 and different water pressures without air application.

Once the factors have been defined, the working procedure used to carry out the tests is explained in detail. Each test begins by ensuring the correct maintenance and cleaning of the different elements of the laboratory (see section 3.2.2), as well as the correct initial position of the pneumatic and manual ball valves. Then it is checked that the pressurized air tank is fully charged and that the pressurized water tank is empty. On the one hand, in the case of the pressurized air tank, it is checked that it is at a pressure of between 26 and 29 bar, as this is the maximum range provided by the compressor. This allows to guarantee that the pressures that are subsequently imposed for fog generation are met. If this is not the case, the compressor will start up autonomously until it stops once the pressure range in the pressurized air tank defined above has been reached. On the other hand, to check the pressurized water tank, the purge valve is opened to release any remaining pressure inside due to previous tests. The ball valve is then opened to allow the

tank to drain by gravity. Once completely empty, the purge and drain valves are closed. The next step is to check that the atmospheric water tank is full and if necessary fill it with the hose connected to the water inlet. In addition, a pH test and temperature measurement is performed to ensure that the composition and temperature of the water used is the same for the entire test set. After completing the above steps the pressurized water tank is filled with water from the atmospheric water tank. To do this, the purge and fill valves are opened and the pump is activated to allow the pressurized water tank to fill to its maximum level (4.5 l). This maximum level is guaranteed by a sensor and an actuator that stops the pump once it has been reached. Once this process is completed the pump is switched off and the purge and fill valves are closed. Once this is done, the ball valves installed inside the test room for the air and water outlet are closed and the water shooting pressures adjusted. In the case of air, and since the tests are carried out without the application of air, the air valve will remain closed at all times. The air outlet ball valve opens to release any remaining pressure in the ducts to the nozzle. In the case of water, the water pressure valve is opened to allow pressurized air to flow from the pressurized air tank to the pressurized water tanks through the water circuit. The shooting water pressure is adjusted by means of a manual control valve and a pressure manometer located at the same point. Once correctly adjusted, the water outlet ball valve is opened to release the remaining pressure and to remove the residual water contained in the pipes leading to the nozzle. The air and water outlet ball valves will remain open until the next shot is fired. The next step is a short shot (approximately 8 seconds) to fill the water pipes of the water circuit with water without exhausting the pressurized water tank by opening the water valves. In this way, it will be able to ensure that during the test the fog begins to be generated almost instantaneously without a significant delay from the opening of the shooting valves (air and water valves). This is of great importance due to the short test shooting times and the delays observed in fog generation of up to 5 seconds when the water circuit is empty. The water and water pressure valves are closed once the shot is finished and the computer in the Control Room is used to check that the water shooting pressure obtained matches with that established in the settings. Once this process has been completed, it is repeated from the beginning to leave the system ready to perform the test shot. At this point, the test room is closed and completely insulated and the air inside it is renewed by activating the corresponding ventilation and air filtration system for 10 minutes.

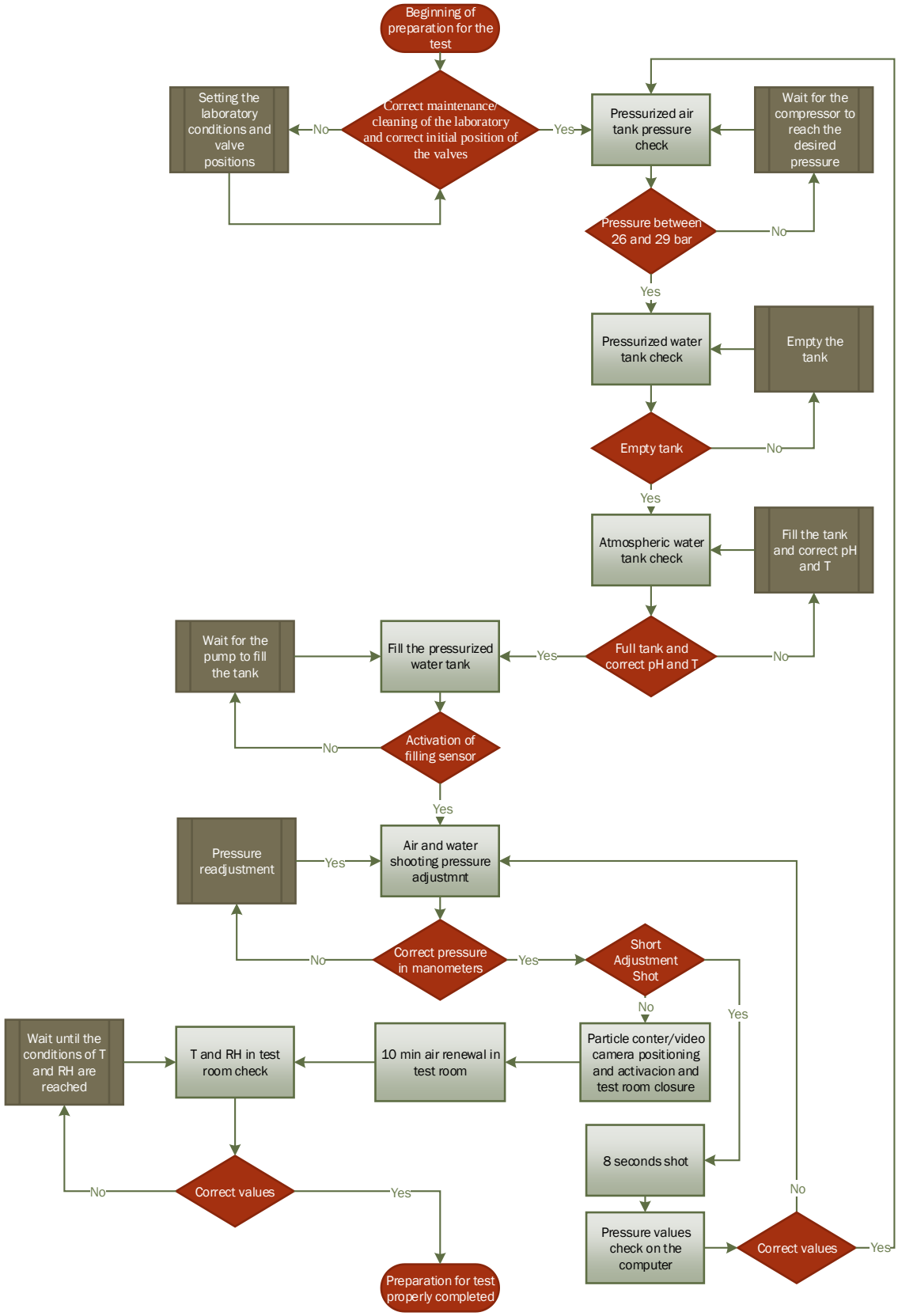

Figure 125: Diagram of the room preparation procedure for particle distribution tests for nozzle B1:2 and different water pressures without air application.

Finally, it is checked that the temperature of the room corresponds to that stipulated for the tests. In the same way, it is verified that the relative humidity in the room is also the desired one. It should be noted that this process is carried out automatically by the control system installed in the Control Room where the desired conditions to be provided by the heat pump and the chiller have been previously defined, thus guaranteeing compliance. The particle counter and video camera will have been placed and activated inside the room immediately prior to the closure of the test room. In the case of the particle counter, with the position, orientation and pitch angle corresponding to the test to be performed. Figure 125 shows a diagram summarizing the test room setup process.

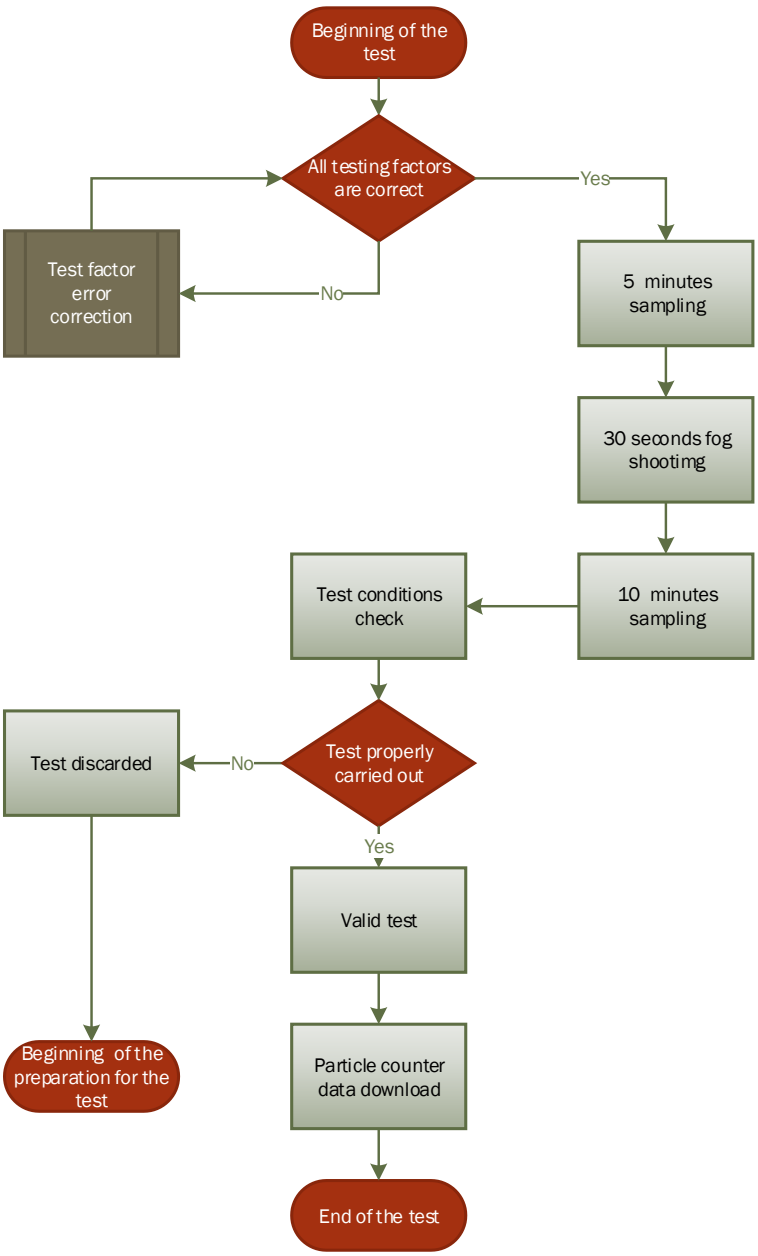

Figure 126: Diagram of the test procedure for particle distribution tests for nozzle B1:2 and different water pressures without air application.

Once the devices have been placed in the room and the correct configuration has been made, the particle counter and the video camera are switched on and the test room is closed for perfect isolation from the outside of the laboratory, as indicated above. The particle counter is maintained by taking 10 second samples every 20 seconds from then until the end of the test. The first stage of the test, once the humidity and temperature conditions in the room have been reached, consists of taking samples with the particle counter for a period of 5 minutes to establish the conditions prior to shooting in the test room, thus ensuring that the initial conditions of all tests are similar. After the specified time has elapsed, the fog is generated by shooting at the nozzle for 30 seconds at the air and water pressures set during test preparation, as shown in Figure 125. Then it has to be waited for 10 minutes from the end of the shoot. During this time the particle counter continues to take samples. After this time, the test is considered complete and the room is opened and the particle counter and video camera are turned off. At the end of the test, the initial temperature and humidity data, as well as the shooting pressure data, are checked to ensure compliance with the test conditions. In addition, test videos are reviewed to ensure that no irregularities occur during testing.Once it is verified that everything has happened as stipulated, the test is taken as correct and the particle counter data is downloaded and processed. Otherwise, the test is automatically discarded and repeated. Figure 126 shows a diagram summarizing the test process.

4.4.2 Experimental results and Discussion

The results obtained are presented below: from Figure 127 to Figure 132 the number of droplets of each size obtained for each of the different combinations of air and water pressures tested are shown. On the other hand, from Figure 133 to Figure 138 the percentajes of droplets of each size obtained for each of the different combinations of air and water pressures tested are represented.

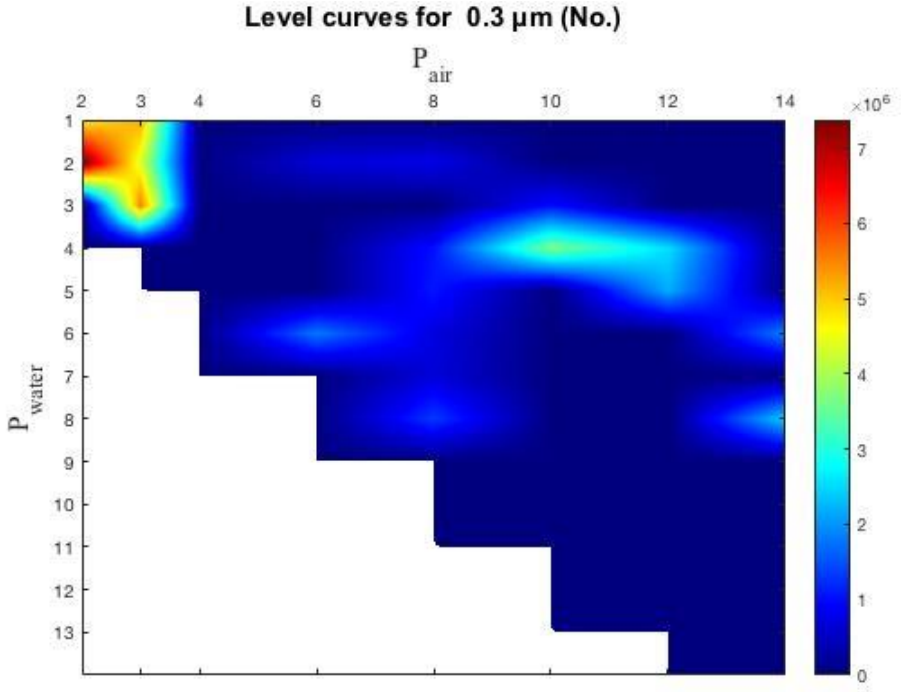

Figure 127: Level curves of the number of droplets of size 0.3 µm produced by the fog generated with the B1:2 nozzle to different combinations of air and water pressures of shot (the white zone represents combinations not studied).

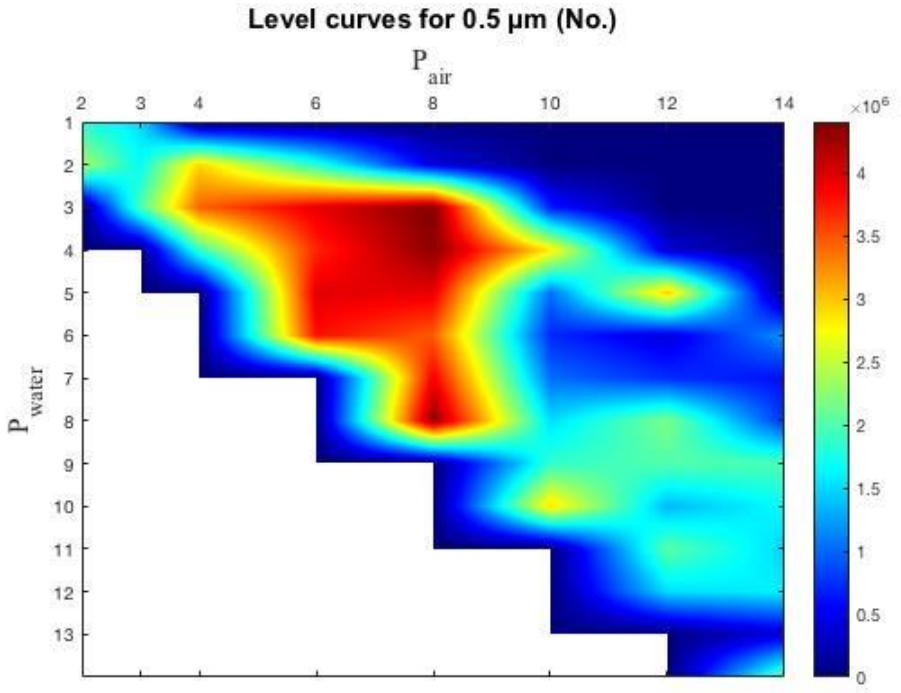

Figure 128: Level curves of the number of droplets of size 0.5 µm produced by the fog generated with the B1:2 nozzle to different combinations of air and water pressures of shot (the white zone represents combinations not studied).

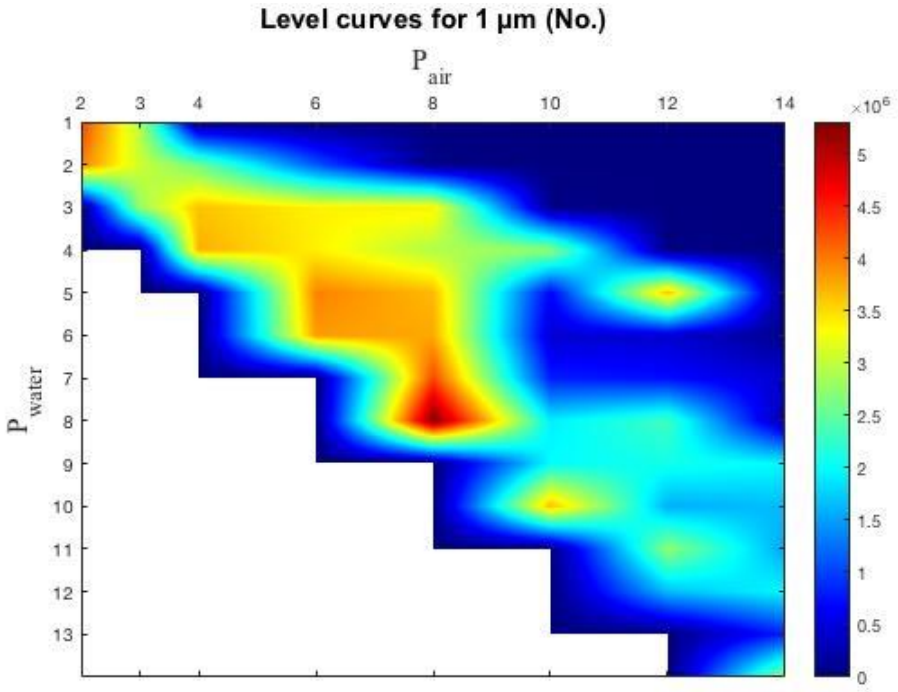

Figure 129: Level curves of the number of droplets of size 1 µm produced by the fog generated with the B1:2 nozzle to different combinations of air and water pressures of shot (the white zone represents combinations not studied).

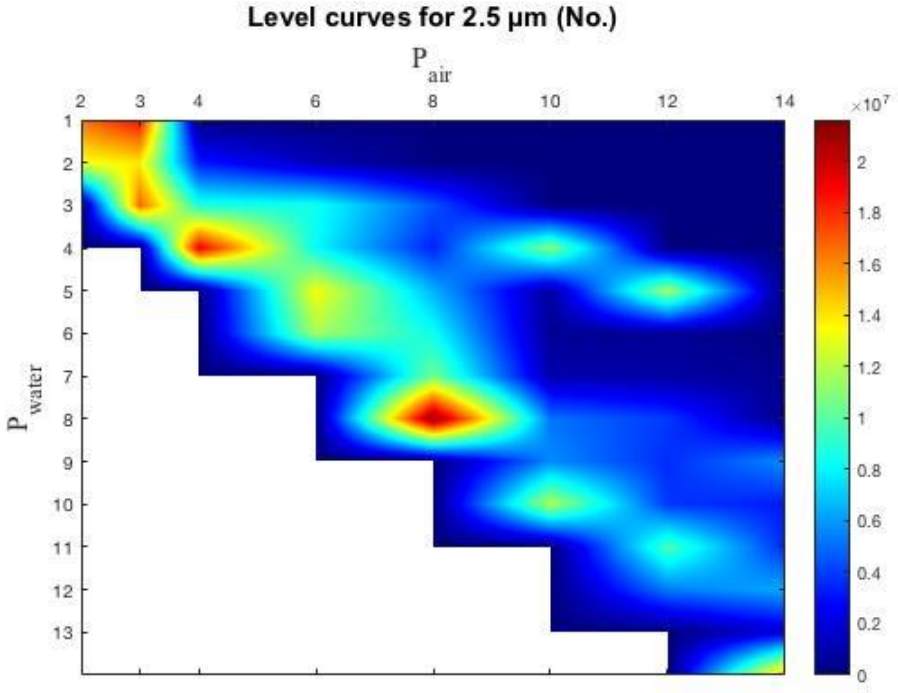

Figure 130: Level curves of the number of droplets of size 2.5 µm produced by the fog generated with the B1:2 nozzle to different combinations of air and water pressures of shot (the white zone represents combinations not studied).

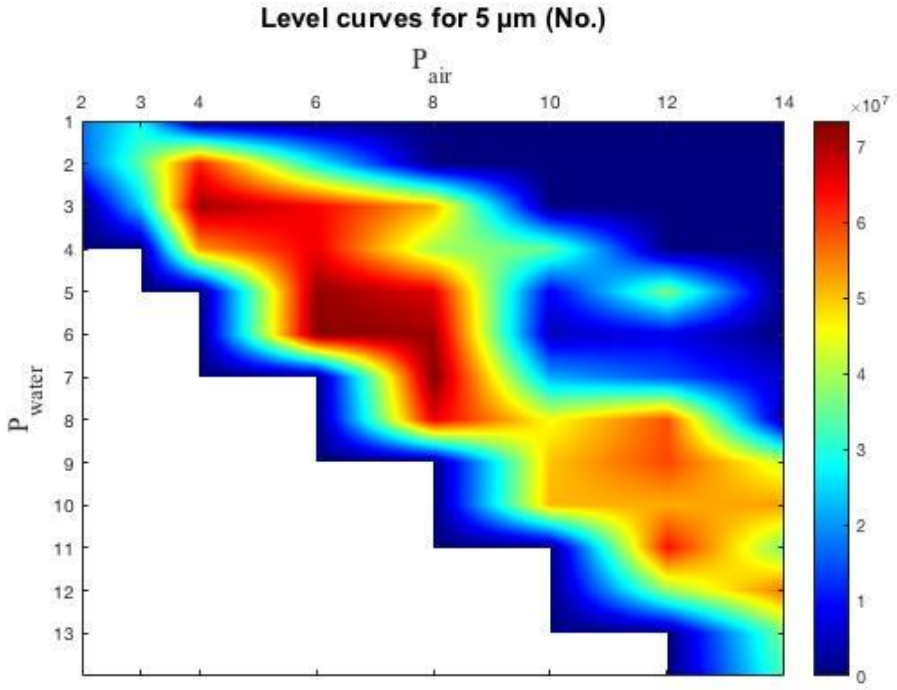

Figure 131: Level curves of the number of droplets of size 5 µm produced by the fog generated with the B1:2 nozzle to different combinations of air and water pressures of shot (the white zone represents combinations not studied).

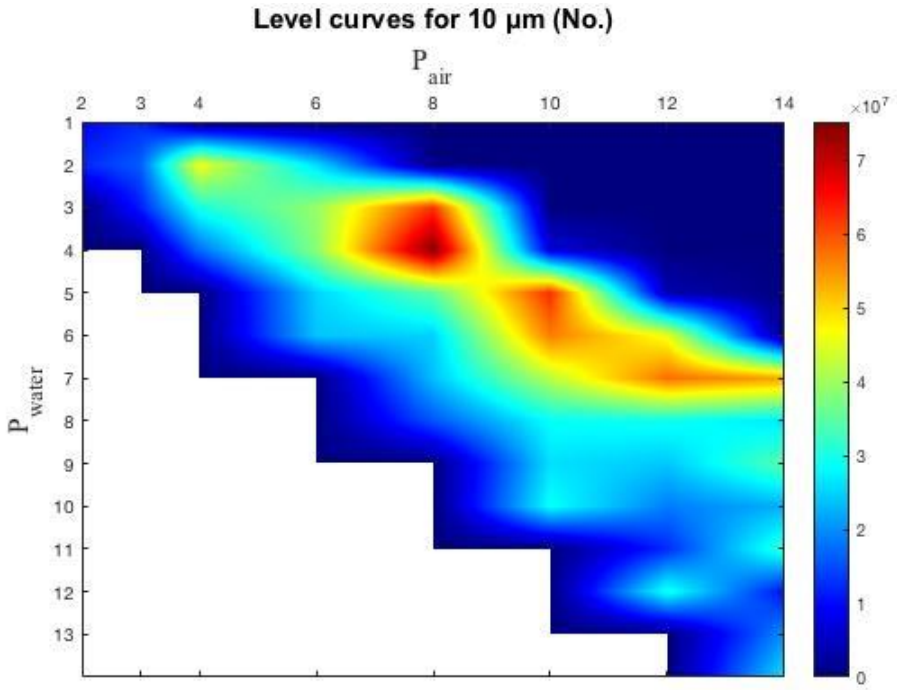

Figure 132: Level curves of the number of droplets of size 10 µm produced by the fog generated with the B1:2 nozzle to different combinations of air and water pressures of shot (the white zone represents combinations not studied).

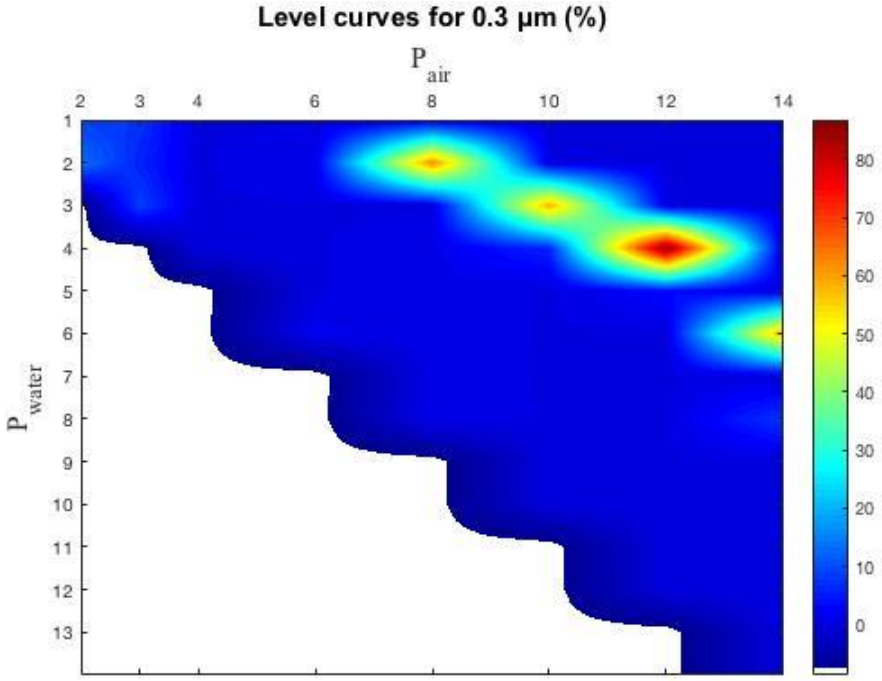

Figure 133: Percentage level curves of 0.3 µm size droplets produced by the fog generated with the B1:2 nozzle to different combinations of air and water pressures of shot (the white zone represents combinations not studied).

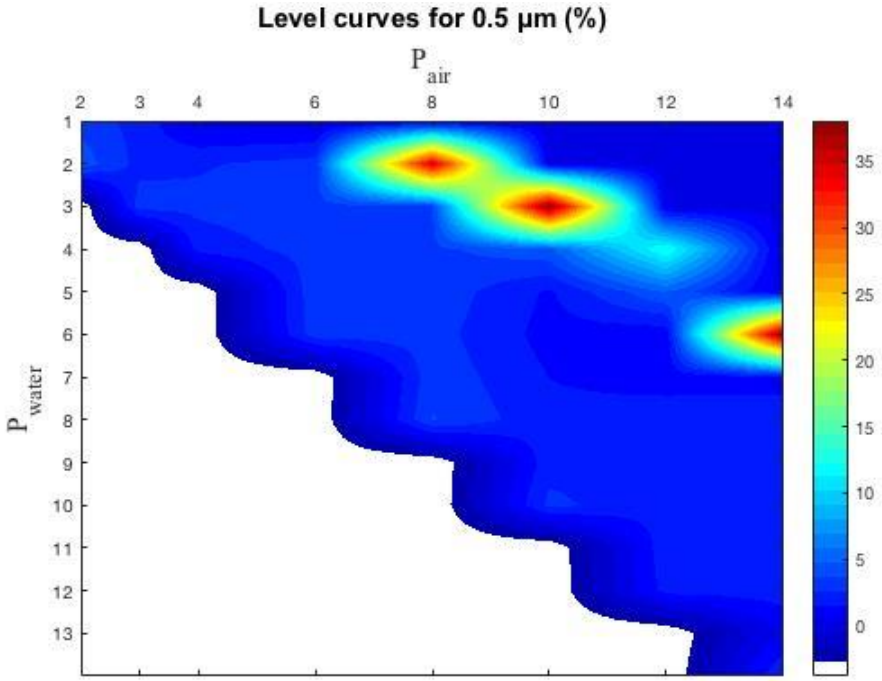

Figure 134: Percentage level curves of 0.5 µm size droplets produced by the fog generated with the B1:2 nozzle to different combinations of air and water pressures of shot (the white zone represents combinations not studied).

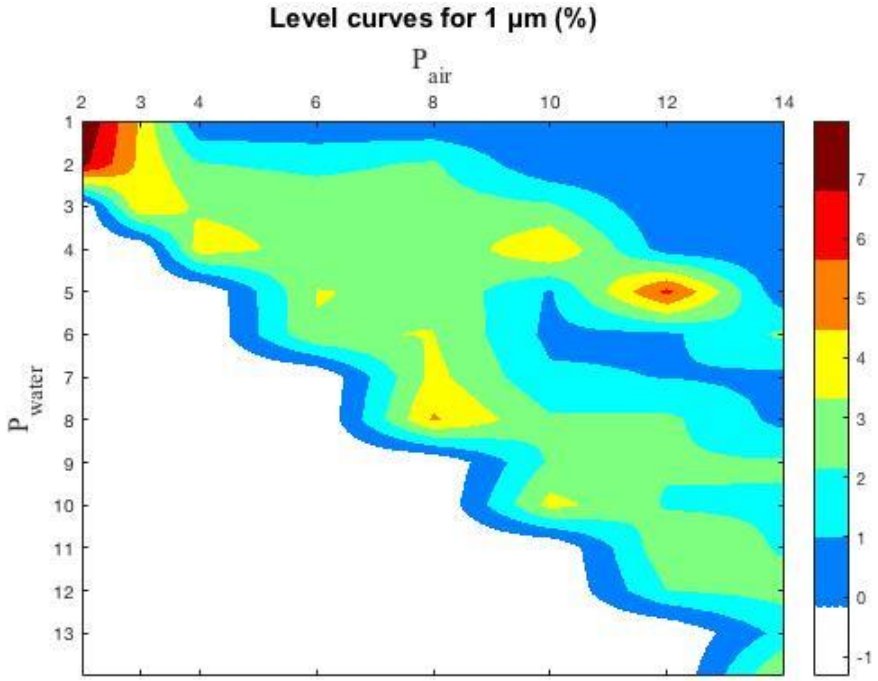

Figure 135: Percentage level curves of 1 µm size droplets produced by the fog generated with the B1:2 nozzle to different combinations of air and water pressures of shot (the white zone represents combinations not studied).

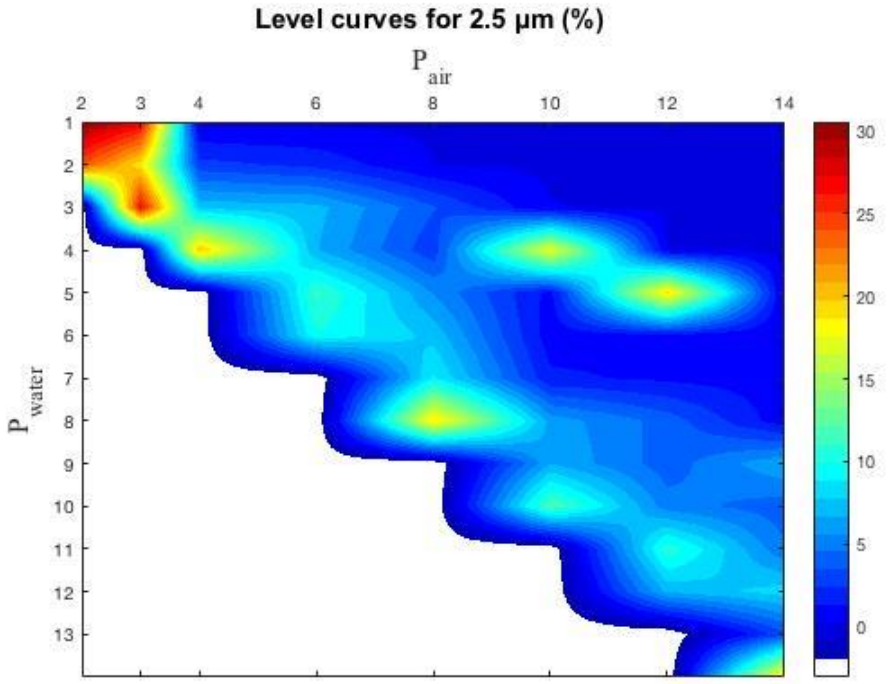

Figure 136: Percentage level curves of 2.5 µm size droplets produced by the fog generated with the B1:2 nozzle to different combinations of air and water pressures of shot (the white zone represents combinations not studied).

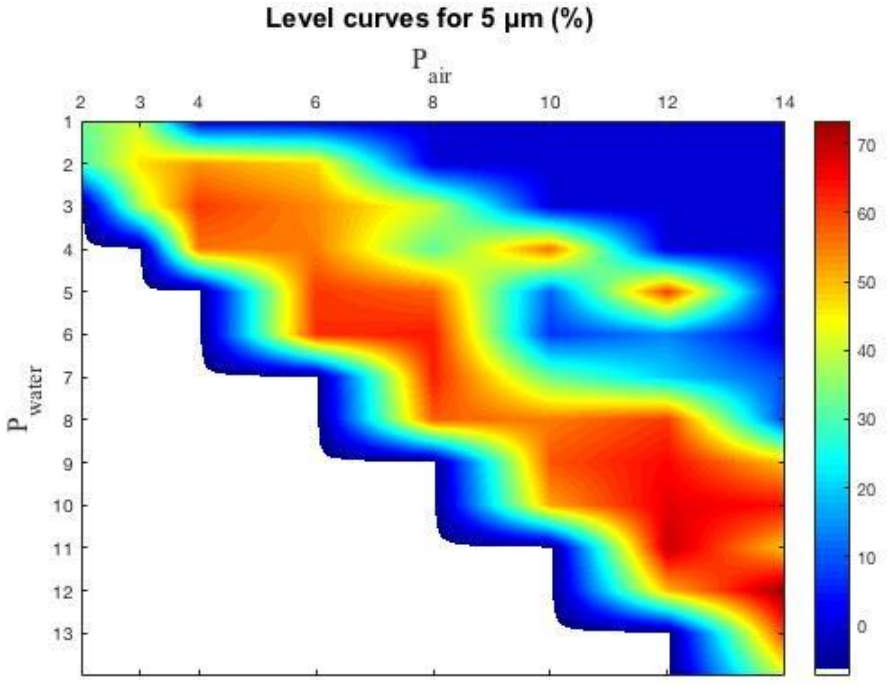

Figure 137: Percentage level curves of 5 µm size droplets produced by the fog generated with the B1:2 nozzle to different combinations of air and water pressures of shot (the white zone represents combinations not studied).

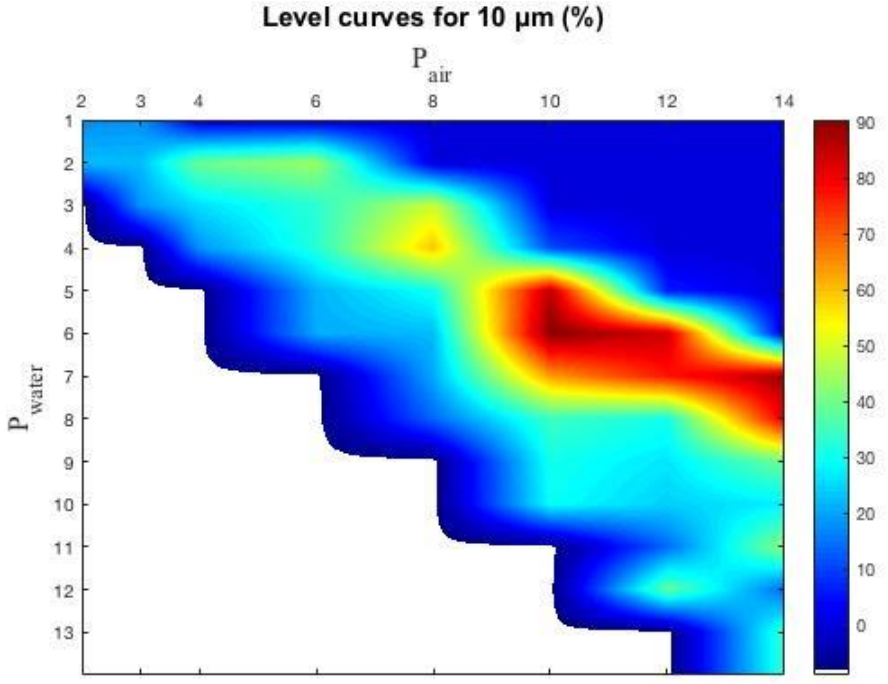

Figure 138: Percentage level curves of 10 µm size droplets produced by the fog generated with the B1:2 nozzle to different combinations of air and water pressures of shot (the white zone represents combinations not studied).

The different graphs with the average values for each pressure combination showing both the number of drops obtained for each measurement channel and their values in percent are shown in Annex B.

4.4.3 Conclusions

From the data and images obtained it can be concluded that:

- The generation of droplets is mainly of sizes 2.5, 5 and 10 μm
- For the same air pressure, it is observed that the production of 5 and 10 μm droplets increases as the water pressure supply is increased up to a maximum and finally decreases.
- Fog density, remaining time and particle size have been characterized as a function of air and water pressure.

4.5 Introduction of the third component into the nozzle B 1:2 during fog generation without the application of pressure

For the B1:2 nozzle and with a predefined combination of air and water pressure, the third component is introduced through the inlet available for this purpose. The third component used for these tests is water tinted with methyl orange. The tests will be separated into two sections: tests in which no pressure is applied to the third component for its entry into the nozzle and tests in which pressure is applied.

4.5.1 Experimental setup and procedure

Before performing each test the different parameters of the test room shall be established to ensure that these factors will not affect the fog generation process. In this way, the temperature and relative humidity of the room were set at 25 ºC and 95%, respectively. The composition of the fluid for the generation of the fog was limited to water, not being added any kind of neutralizing compound. Water tinted with methyl orange will be added at the entrance of the third component inlet to analyze the capacity of the nozzle to integrate a third component into the fog cone generated during the tests. The temperature and humidity of the test room, as well as the flow of water used in the generation of fog were monitored at all times during each test. For this porpuse, laboratory equipment (see section 3.2.2) was used during tests. In addition, a video camera recorded everything that happened inside the test room.

The temperature of the shooting water will be 12 ºC, while the pressures of air and water will be 12 bar and 8 bar, respectively. No third component pressure will be applied.

Different angles formed between the inlet of the third component and the horizontal line will be tested (Figure 139).

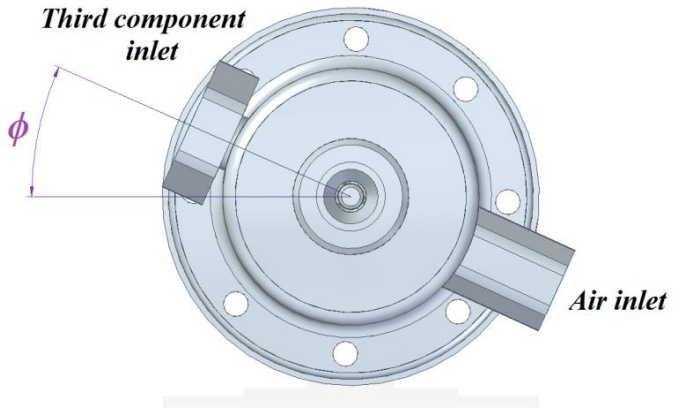

Figure 139: Angle formed between the entrance of the third component and the horizontal line **(ϕ).**

Once the factors have been defined, the working procedure used to carry out the tests is explained in detail. Each test begins by ensuring the correct maintenance and cleaning of the different elements of the laboratory (see section 3.2.2), as well as the correct initial position of the pneumatic and manual ball valves. Then it is checked that the pressurized air tank is fully charged and that the pressurized water tank is empty. On the one hand, in the case of the pressurized air tank, it is checked that it is at a pressure of between 26 and 29 bar, as this is the maximum range provided by the compressor. This allows guaranteeing that the pressures that are subsequently imposed for fog generation are met. If this is not the case, the compressor will start up autonomously until it stops once the pressure range in the pressurized air tank defined above has been reached. On the other hand, to check the pressurized water, the purge valves is opened to release any remaining pressure in the tank due to previous tests and then the ball valve is opened to allow the tank to drain by gravity. Once completely empty, the purge and drain valves are closed. The next step is to check that the atmospheric water tank is full and if necessary fill them with the hose connected to the water inlet. In addition, a pH test and temperature measurement is performed in each of the water tanks to ensure that the composition and temperature of the water used is the same for the entire test set. After completing the above steps the pressurized water tanks are filled with water from the atmospheric water tanks. To do this, the purge and fill valves are opened and the pump is activated to allow the pressurized water tank to fill to their maximum level (4.5 l). This maximum level is guaranteed by a sensor and an actuator that stops the pump once it has been reached. Once this process is completed the pump is switched off and the purge and fill valves are closed. Once this is done, the ball valves installed inside the test room for the air and water are closed and the shooting pressures are adjusted. In the case of air, the air valve is opened allowing pressurized air to flow from the pressurized air tank through the air circuit. The shooting air pressure is adjusted by means of the manual regulating valve and the pressure manometer located at the same point. Once properly adjusted, the air valve is closed and the air outlet ball valve is opened to release the remaining pressure in the

ducts that reach the nozzle. In the case of water, the water pressure valve is opened to allow pressurized air to flow from the pressurized air tank to the pressurized water tank through the water circuit. The shooting water pressure is adjusted by means of the manual control valve and the pressure manometer located at the same point. Once correctly adjusted, the water outlet ball valve is opened to release the remaining pressure and to remove the residual water contained in the pipes leading to the nozzle. The air and water outlet ball valves will remain open until the next shot is fired. The next step is a short shot (approximately 8 seconds) to fill the water pipes of the water circuit with water without exhausting the pressurized water tank by simultaneously opening the air and water valve. In this way, it will be able to ensure that during the test the fog begins to be generated almost instantaneously without a significant delay from the opening of the shooting valves (air and water valves). This is of great importance due to the short test shooting times and the delays observed in fog generation of up to 5 seconds when the water circuit is empty. The air and water pressure valves are closed once the shot is finished and the computer in the Control Room is used to check that the air and water shooting pressures obtained match with that established in the settings. Once this process has been completed, it is repeated from the beginning to leave the system ready to perform the test shot. At this point, the third component container (Figure 140) is placed in the nozzle. The placement is carried out last to avoid that in the most favourable case (ϕ = 90 $^{\circ}$) the methyl orange stained water falls by gravity into the nozzle before the test is carried out. Then, the test room is closed and completely insulated. The video camera will have been placed and activated inside the test room immediately before to the placement of the third component container in the nozzle. Figure 141 shows a diagram summarizing the process of setting up the room for testing.

Figure 140: Third component container in third component tests for nozzle B1:2 with no third component pressure application.

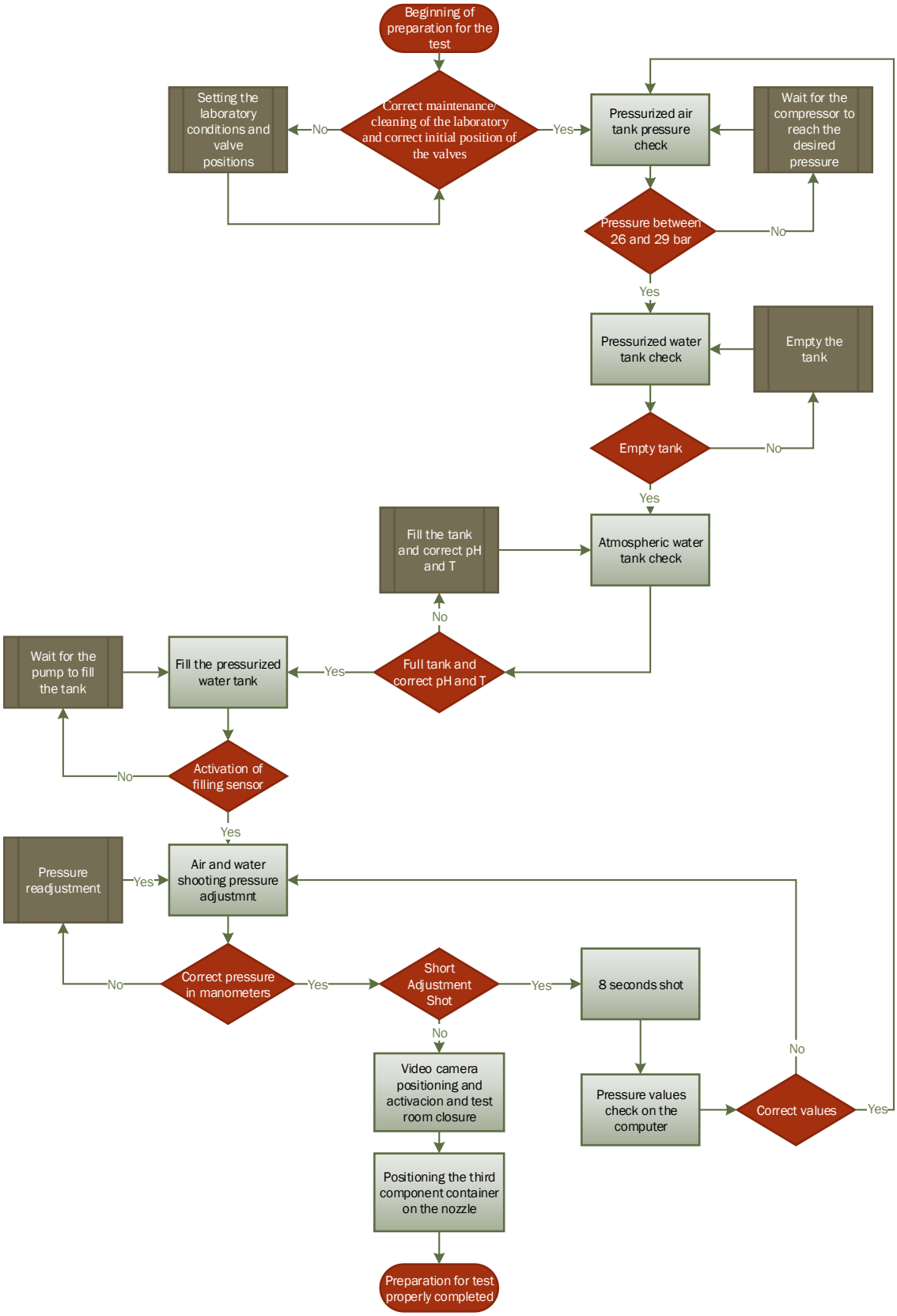

Figure 141: Diagram of the test procedure third component tests for nozzle B1:2 without third component pressure applicaction.

After this, the fog is generated by shooting the nozzle for 30 seconds at the pressures that have been established during the preparation for the test as shown in Figure 141. After this time, the test is considered complete and the room is opened. At the end of the test, the shooting pressure data are checked to ensure compliance with test conditions. Furthermore, test videos are reviewed to ensure that no irregularities occur during testing. Once it is verified that everything has happened as stipulated the test is taken as correct and water flow data is collected. Otherwise, the test is automatically discarded and repeated. Figure 142shows a diagram summarizing the test process.

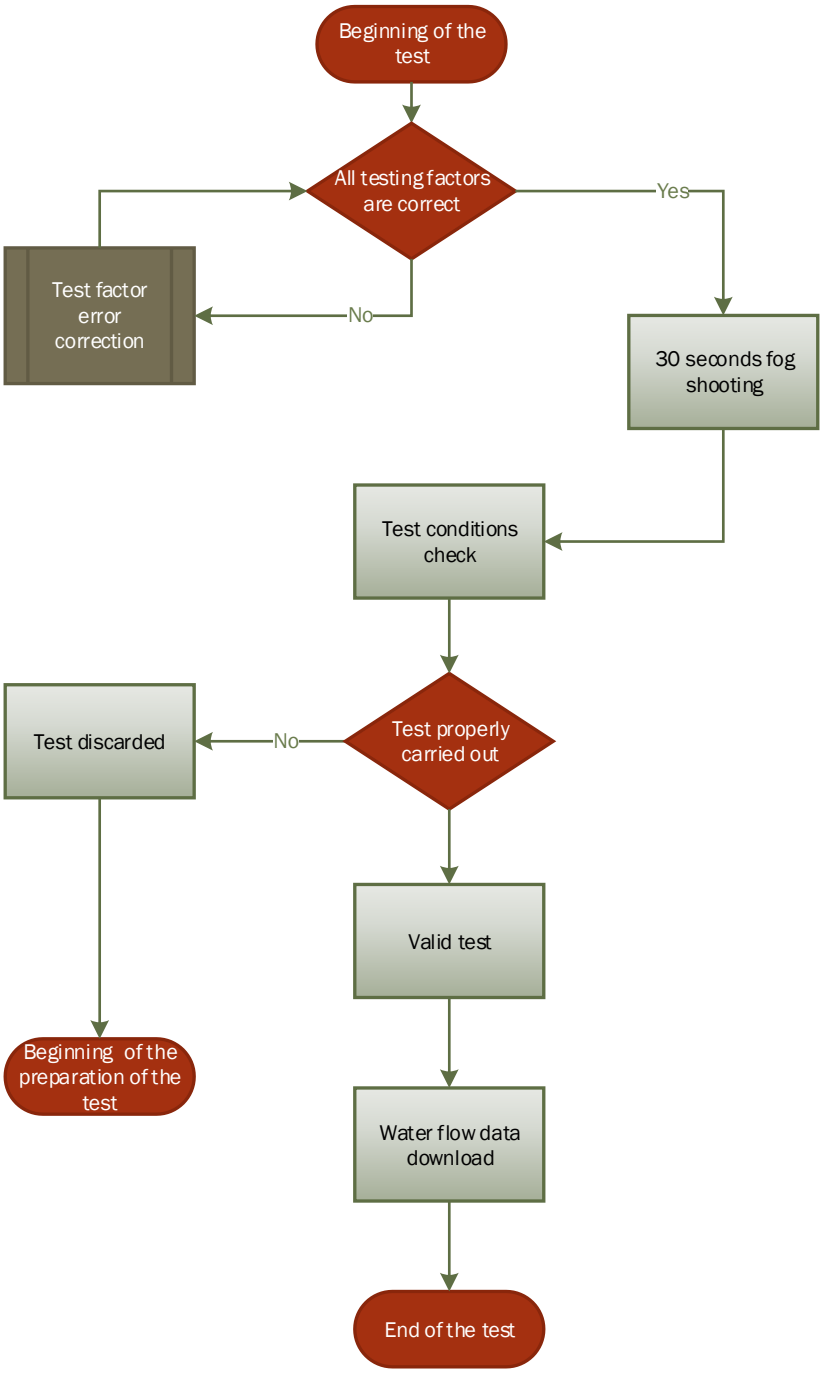

Figure 142: Diagram of the test procedure for third component tests for nozzle B1:2 without third component pressure applicaction.

4.5.2 Experimental results and Discussion

As previously mentioned, the shots taken in the execution of these tests will last 30 seconds. In this case and because of the results obtained, no numerical data are presented, but rather qualitative results by means of images. Once the tests have been carried out and the corresponding videos projected, it has been observed that the methyl orange stained water is expelled from one side of the container towards the outside without entering the nozzle (Figure 143 Figure 144).

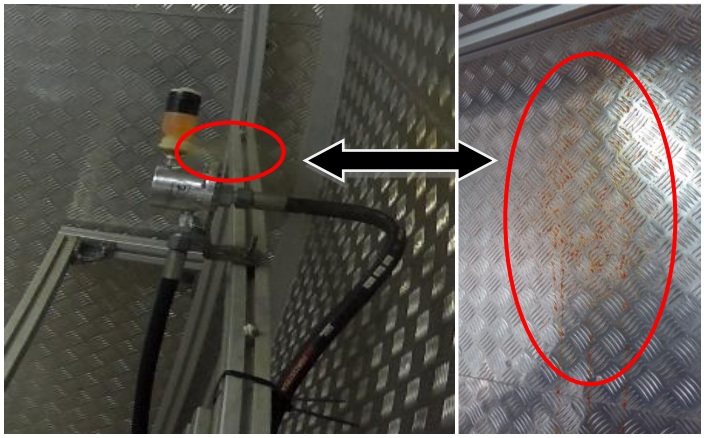

Figure 143: Ejection of the third component through the side opening of the designed container.

In addition, a more consistent test has been carried out on fog generation, leaving the entrance for the third component open, but without the placement of the container. Figure 144 shows how part of the fog flow deviates from its trajectory to exit through that orifice.

Figure 144: Some of the air and water flow generated inside the nozzle is expelled from the nozzle through the third component inlet.

Figure 145 shows how the entire volume of the third component used is ejected from the container during shooting.

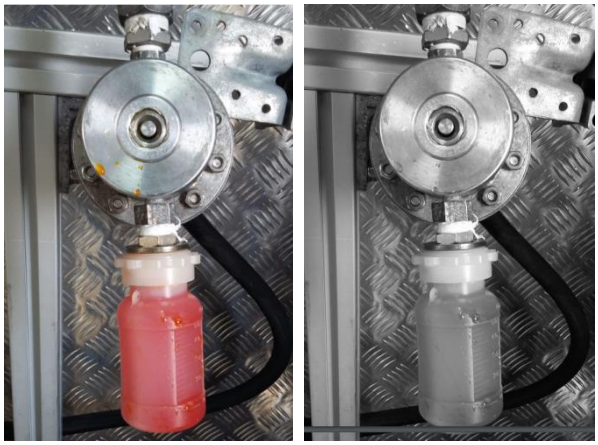

Figure 145: Volume of the third component in the container before and after the test in the worst-case scenario(ϕ= -90°).

Table 17 summarizes the results obtained for the flows of the third component during the tests.

Table 17: Third component flows obtained for B1:2 nozzle with no third component pressure application.

Nozzle model	P_{air} (bar)	P_{water} (bar)	P_{inlet} (bar)	φ (°)	Third component flow rate
B1:2	12	8	0	0	No
B1:2	12	8	0	90	No
B1:2	12	8	0	-90	No

It is observed how the third component cannot be ejected by the nozzle. The water and air pressures prevent the exit of the third component, even producing the inverse flow which, as can be seen in the images, is expelled towards the outside through the containers installed in the corresponding inlet.

Due to these results, it is necessary to study the case in which pressure is applied to the third component to force its ejection.

4.5.3 Conclusions

From the images obtained it can be concluded that:

- The simultaneous output of water and third component is not possible on the nozzle model B1:2 for the combination P_{air} = 12 bar and P_{water} = 8 bar without the application of a third componente pressure

- The pressure gradient generated at the inlet of the third component inlet is opposite to that expected in the design, instead of generating the suction of the third component, its expulsion is produced through the lateral orifice made in the container.

This makes it necessary to study the behaviour of this type of test by imposing a certain pressure on the third component to force it into the nozzle and expel it as part of the fog generated.

4.6 Introduction of the third component into the nozzle during fog generation with the application of pressure

The pressure combination chosen is P_{air} = 12 bar and P_{water} = 8 bar and its choice is the result of the analysis of the data obtained in the previous section of this chapter. As can be seen, this combination of pressures produces a fog that mostly generates drops of 5 and 10 μm, reaching percentages of approximately 60% and 35%, respectively. As can be deduced from the values obtained, it will be a dense fog due to the high number of droplets generated, but it will also last longer than other fogs because it has a higher number of droplets of 5 than 10 μm, as these drops have a lower sedimentation rate. It has been important in the choice of this combination of pressures that there are droplets of different sizes, as these will favor the capture and sweeping of particles of a wider range of sizes.

4.6.1 Experimental setup and procedure

Before performing each test the different parameters of the test room shall be established to ensure that these factors will not affect the fog generation process. In this way, the temperature and relative humidity of the room were set at 25 ºC and 95%, respectively. The composition of the fluid for the generation of the fog was limited to water, not being added any kind of neutralizing compound. Water tinted with methyl orange will be added at the entrance of the third component inlet to analyze the capacity of the nozzle to integrate a third component into the fog cone generated during the tests. The temperature and humidity of the test room, as well as the flow of water used in the generation of fog were monitored at all times during each test. For this porpuse, laboratory equipment (see section 3.2.2) was used during tests. In addition, a video camera recorded everything that happened inside the test room.

The temperature of the shooting water will be 12 ºC, while the pressures of air and water will be 12 bar and 8 bar, respectively. The third component pressure will vary according to the test.

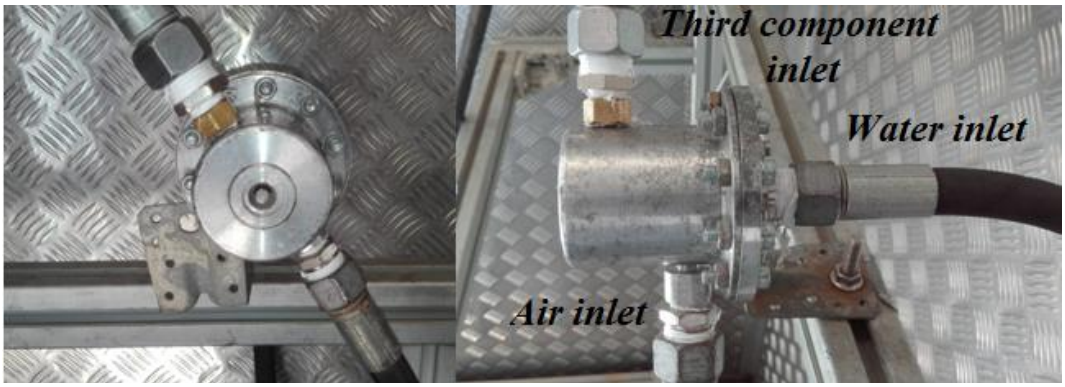

Figure 146: Assembly of the B1:2 nozzle with a third component inlet under pressure.

Once the factors have been defined, the working procedure used to carry out the tests is explained in detail. It should be noted that each test room has two pressurised outlets (one for water and one for air). Therefore, the introduction of the third component under pressure will be carried out by means of the pressure water outlet from the test room that is not being used. In this way, a 4 m long hose will be available for connection to the nozzle (Figure 146). The sliding door between the two test rooms must therefore remain open to allow this hose to pass through. Each test begins by ensuring the correct maintenance and cleaning of the different elements of the laboratory (see section 3.2.2), as well as the correct initial position of the pneumatic and manual ball valves. Then it is checked that the pressurized air tank is fully charged and that the pressurized water tank is empty. On the one hand, in the case of the pressurized air tank, it is checked that it is at a pressure of between 26 and 29 bar, as this is the maximum range provided by the compressor. This allows guaranteeing that the pressures that are subsequently imposed for fog generation are met. If this is not the case, the compressor will start up autonomously until it stops once the pressure range in the pressurized air tank defined above has been reached. On the other hand, to check the pressurized water tanks (both the one used for the shoting water and the one used for the introduction of the third component), the purge valves are opened to release any remaining pressure in the tank due to previous tests and then the ball valves are opened to allow the tanks to drain by gravity. Once completely empty, the purge and drain valves are closed. The next step is to check that the atmospheric water tanks are full and if necessary fill them with the hose connected to the water inlet. In addition, a pH test and temperature measurement is performed in each of the water tanks to ensure that the composition and temperature of the water used is the same for the entire test set. After completing the above steps the pressurized water tanks are filled with water from the atmospheric water tanks. To do this, the purge and fill valves are opened and the pumps are activated to allow the pressurized water tanks to fill to their maximum level (4.5 l). This maximum level is guaranteed by a sensor and an actuator that stops the pump once it has been reached. Once this process is completed the pump is switched off and the purge and fill valves are closed. For the particular case of the water tank for the introduction of the third component, prior to the closing of the purge valve, methyl orange is added to dye the water inside. This aims to facilitate a qualitative analysis at a visual level by observing the videos made during the tests. Once this is done, the ball valves installed inside the test room for the air and both water in Test Room 1 and 2 outlet are closed and the shooting pressures are adjusted. In the case of air, the air valve is opened allowing pressurized air to flow from the pressurized air tank through the air circuit. The shooting air pressure is adjusted by means of the manual regulating valve and the pressure manometer located at

the same point. Once properly adjusted, the air valve is closed and the air outlet ball valve is opened to release the remaining pressure in the ducts that reach the nozzle. In the case of water, the water pressure valves of both Test Rooms are opened to allow pressurized air to flow from the pressurized air tanks to the pressurized water tanks through the water circuits. The shooting water pressure are adjusted by means of both manual control valves and the pressure manometers located at the same point. Once correctly adjusted, the water outlet ball valves are opened to release the remaining pressure and to remove the residual water contained in the pipes leading to the nozzle. The air and water outlet ball valves will remain open until the next shot is fired. The next step is a short shot (approximately 8 seconds) to fill the water pipes of both water circuits with water without exhausting the pressurized water tank by simultaneously opening the air and water valves. In this way, it will be able to ensure that during the test the fog begins to be generated almost instantaneously without a significant delay from the opening of the shooting valves (air and water valves). This is of great importance due to the short test shooting times and the delays observed in fog generation of up to 5 seconds when the water circuit is empty. The air, water and water pressure valves are closed once the shot is finished and the computer in the Control Room is used to check that the air, water and third component shooting pressures obtained match with that established in the settings. Once this process has been completed, it is repeated from the beginning to leave the system ready to perform the test shot. At this point, the test room are closed and completely insulated. The video camera will have been placed and activated inside the test room immediately before the closure of the test room. It should be noted that the door seprating the two test rooms remains open during shoting in so that the the water stained with methyl orange will flow out of the water outlet in Test Room 2 into the third nozzle component inlet through both rooms using the suitable hose. Figure 147 shows adiagram summarizing the process of setting up the room for testing.

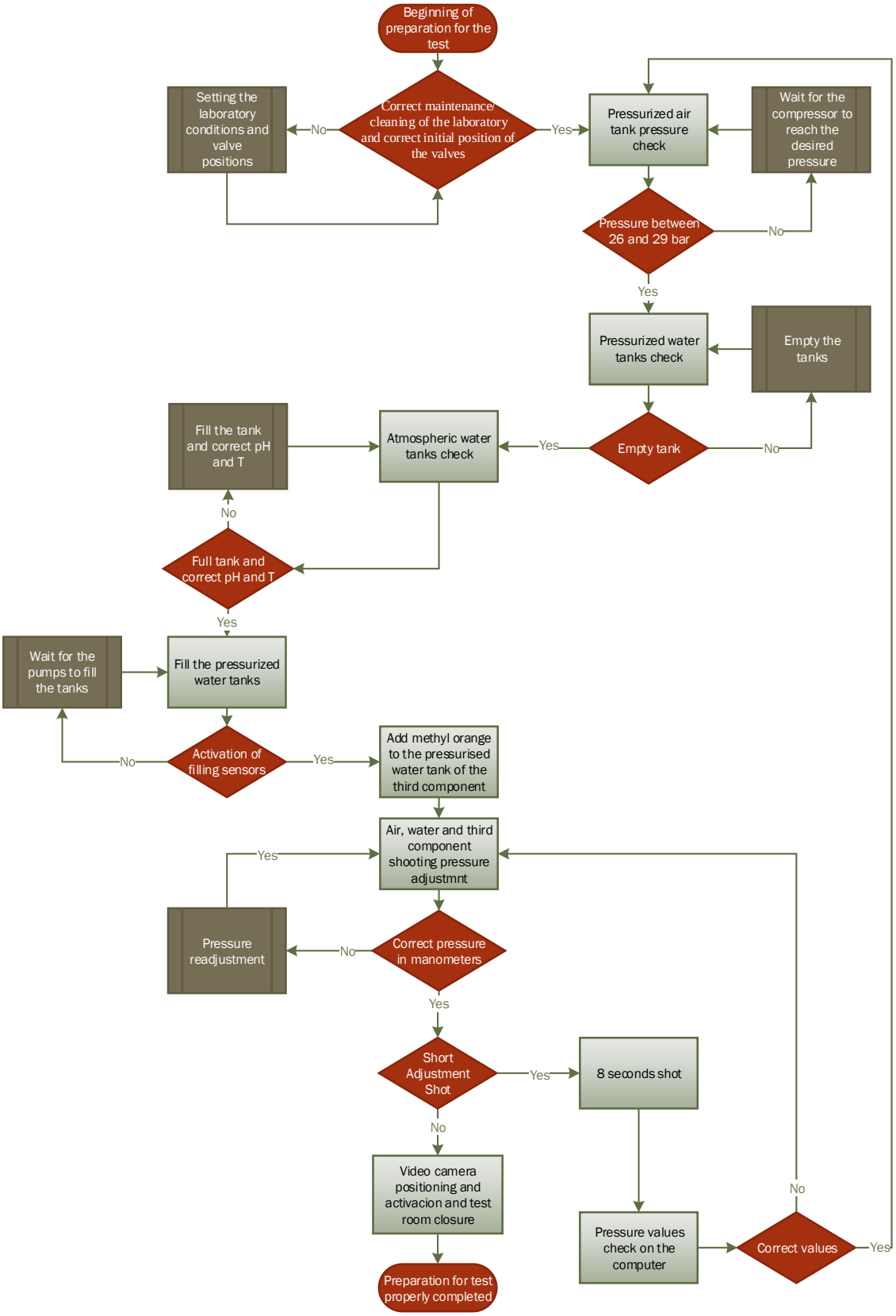

Figure 147: Diagram of the test procedure third component tests for nozzle B1:2 and different third component pressures.

As indicated above, once the video camera has been placed in the room, this is switched on and the test room is closed for perfect isolation from the outside of the laboratory. After this, the fog is generated by shooting the nozzle for 30 seconds at the pressures that have been established during the preparation for the test as shown in Figure 147. After this time, the test is considered complete and the room is opened. At the end of the test, the shooting water pressure data are checked to ensure compliance with test conditions. Furthermore, test videos are reviewed to ensure that no irregularities occur during testing. Once it is verified that everything has happened as stipulated the test is taken as correct and water flow data is collected. Otherwise, the test is automatically discarded and repeated. Figure 148 shows a diagram summarizing the test process.

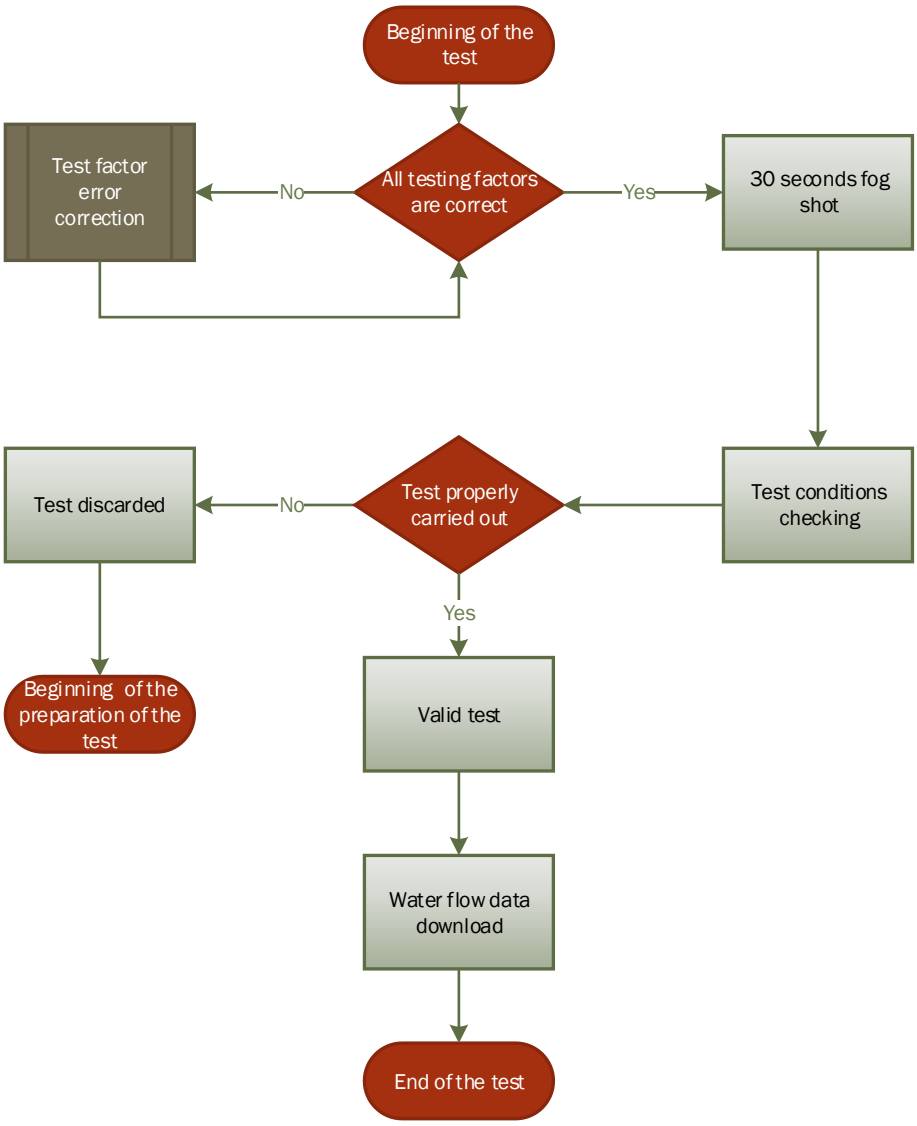

Figure 148: Diagram of the test procedure for third component tests for nozzle B1:2 and different third component pressures.

4.6.2 Experimental results and Discussion

As previously mentioned, the shots taken in the execution of these tests will last 30 seconds. The results obtained are presented below (Figure 149).The data presented are as follows:

- Nominal water pressure imposed prior to the test (P_{water})
- Nominal air pressure imposed prior to the test (P_{air})
- Nominal thrid component pressure imposed prior to the test (P_{inlet})
- Flow rate of water in liters per seconds collected in real time (Q_{water})
- Flow rate of third component in liters per seconds collected in real time (Q_{inlet})

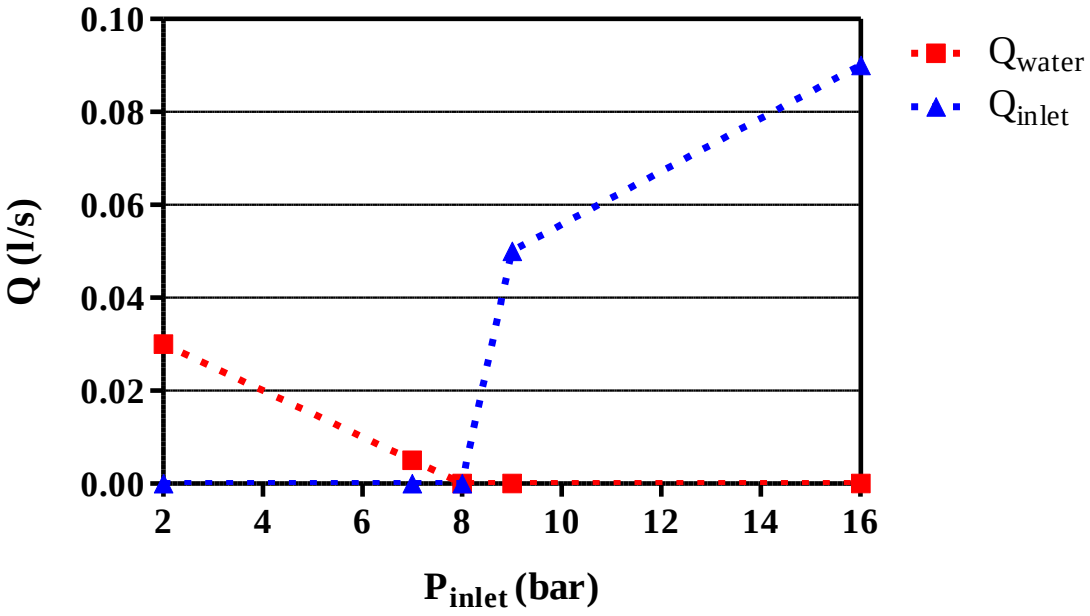

Figure 149: Water and third component flow rates for the B1:2 nozlle with a P_{air}=12bar and P_{water}=8bar combination.

Table 18 summarizes the results obtained for the flows of the third component during the tests.

Table 18: Third component flows obtained for B1:2 nozzle and different third component pressures.

Nozzle model	P_{air} (bar)	P_{water} (bar)	P_{inlet} (bar)	Third component flow rate (l/s)
B1:2	12	8	0	0
B1:2	12	8	2	0
B1:2	12	8	7	0
B1:2	12	8	8	0
B1:2	12	8	9	0.05
B1:2	12	8	16	0.09

It is observed in the graph how the water and third component cannot be ejected by the nozzle simultaneously. It will be the one whose pressure is greater the one that will be ejected, obtaining a flow greater than zero. When both have the same pressure applied, no flow is obtained in either case. When the pressure of one is greater than that of the other, the one that has greater pressure overcomes the resistance exerted by the other and, at the same time, that of the air, allowing its ejection. This leads us to think that the problem may be in the spatial position of the water inlets and third component in the nozzle, because they block each other, which does not happen with air, even if its pressure value is higher.

4.6.3 Conclusions

From the data and images obtained it can be concluded that:

- For third component shooting pressures below 8 bar, the third component flow rate is zero.
- For third component shooting pressures above 8 bar, the flow rate of the third component is greater than zero and increases as the set pressure increases.
- For a shooting pressure of 8 bar, both the water flow rate and the flow rate of the third component are zero.
- The simultaneous output of water and third component is not possible on the nozzle model B1:2 for the combination P_{air} = 12 bar and P_{water} = 8 bar.
- When the water pressure is higher than the pressure of the third component, part of the fog flow generated is introduced into the third component's duct, preventing it from entering the nozzle.

4.7 Validation of the computational fluid dynamics model

Below are some examples of comparison between the results obtained for nozzle B1:2 in the laboratory tests and the results provided by the numerical simulations of the nozzle. The objective of this section is, therefore, to determine if the results obtained by simulation are reliable. The results obtained in the simulations are provided by the project partner. The simulations carried out consist of two parts. The first part consists in the simulation of the whole flow field (Figure 150). Based on the results obtained, the new initial boundary conditions are established for the second part of the simulation. In this second part is in which the results relative of the fog cone are obtained (Figure 151).

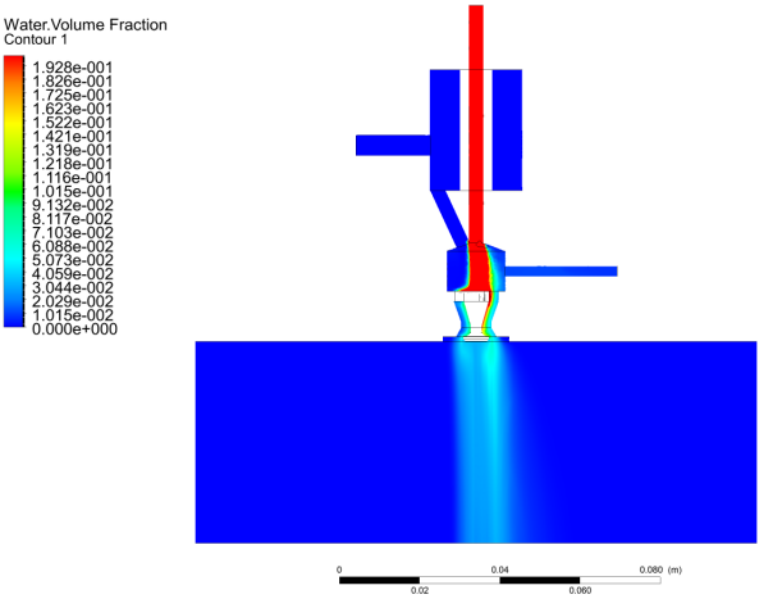

Figure 150: Whole flow field simulation result of water volume fraction.

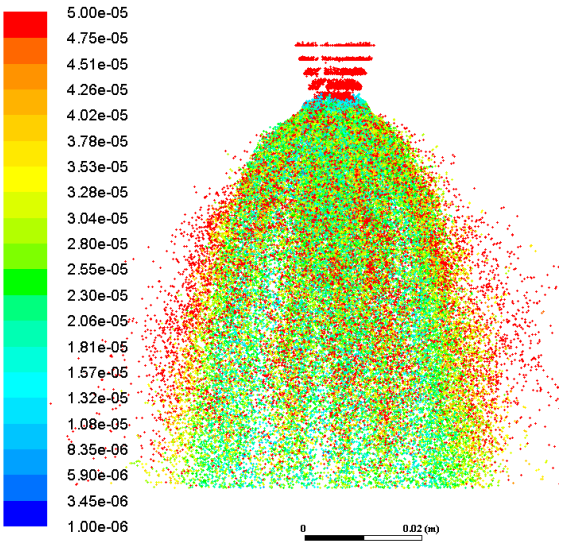

Figure 151: Example of the result of the cone and the droplet distribution for a simulation with a combination of pressures of Pair 6 bar; Pwater = 6bar.

4.7.1 Cone opening angle

Table 19 shows the cone opening angles for different combinations of air and water pressure.

Table 19: Cone opening angle comparisons between experimental and numerical results.

	IMAGES FROM EXPERIMENTS	IMAGES FROM SIMULATIONS
P_{air} = 2 bar ; P_{water} = 6 bar	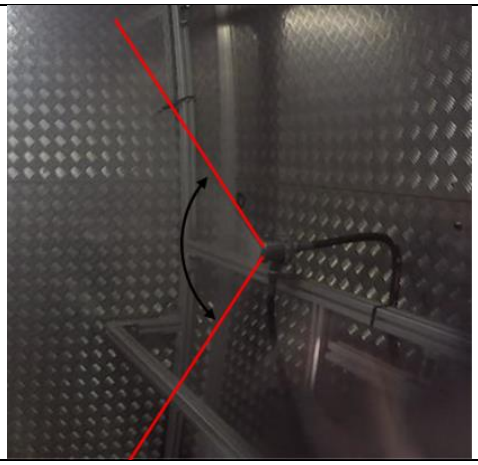	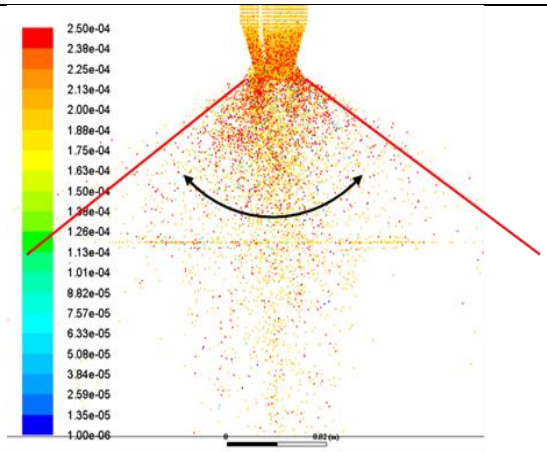
	113.8°	110.6°

P_{air}: = 4 bar ; P_{water} = 4 bar	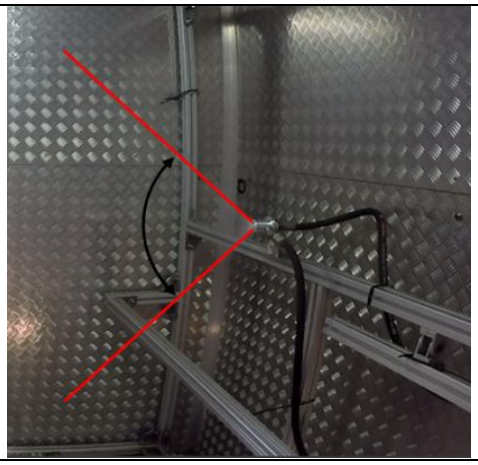	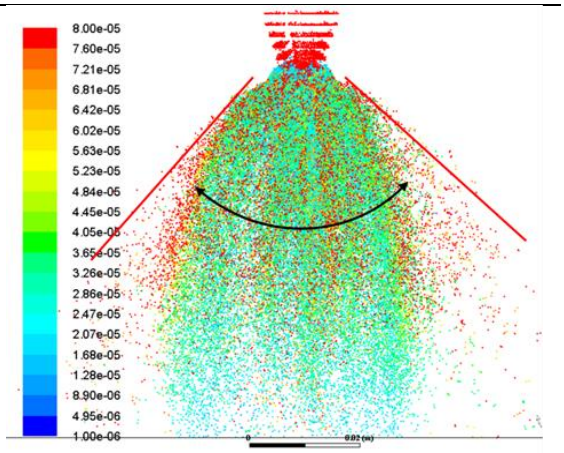
	90.4°	**90.0°**
P_{air} = 12 bar ; P_{water} = 8 bar	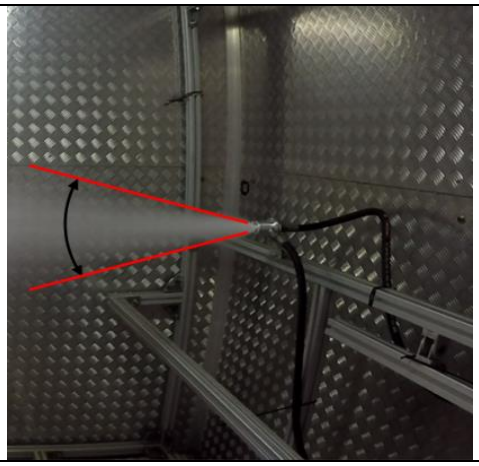	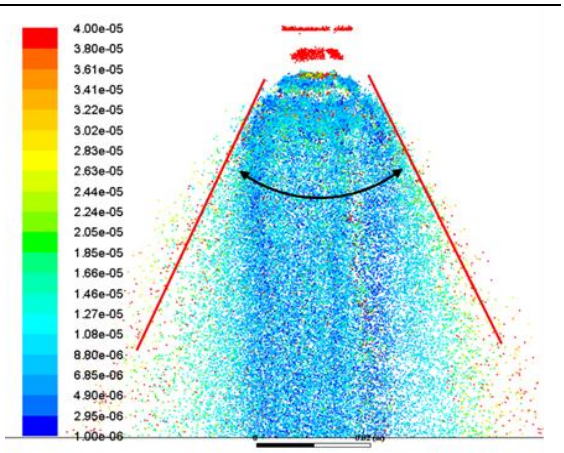
	32.6°	**50.1°**

4.7.2 Water flow rates

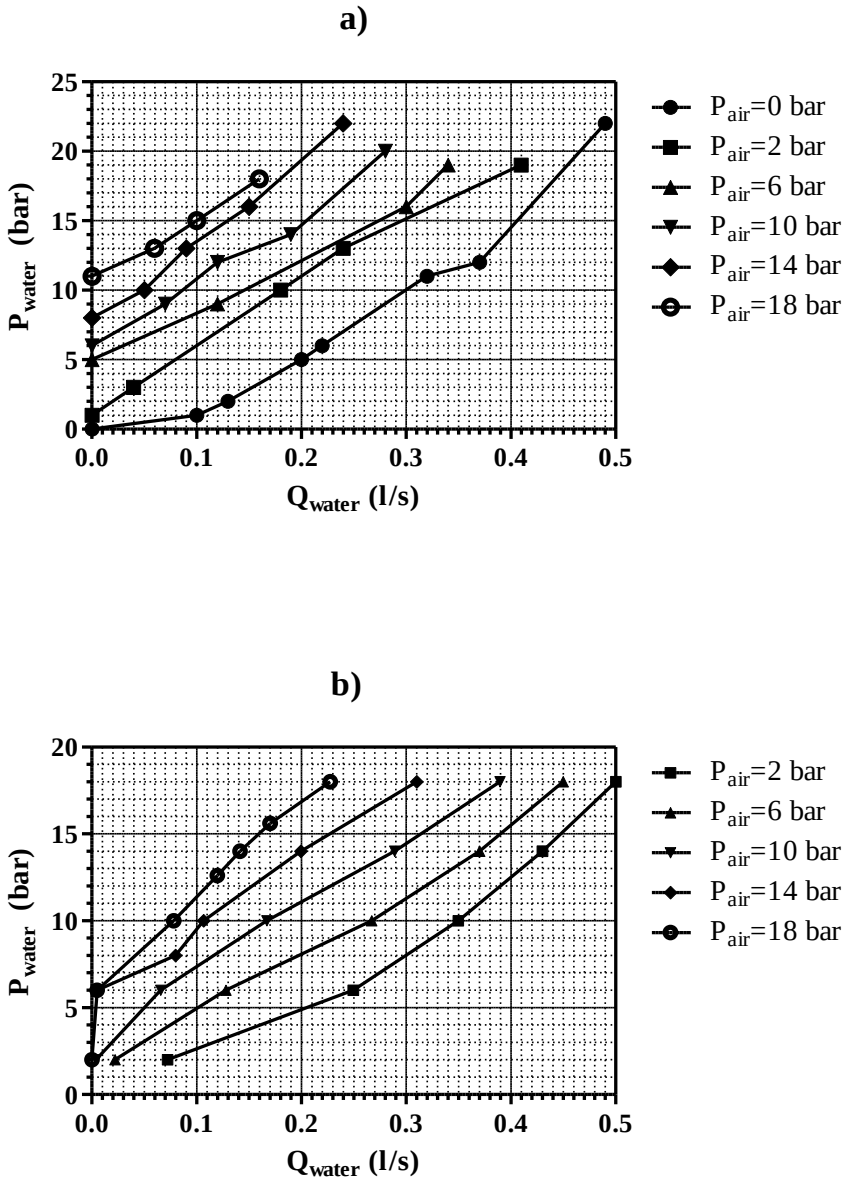

Figure 152: Flow rates results: a) Experimental results of water flow rates at different operating conditions; b) Computational result of water flow rates at different operating conditions.

4.7.3 Droplet distribution

On one hand, Table 20 shows the drop size distribution obtained experimentally for various combinations of water and air pressure with the B1:2 nozzle. These values are expressed in percentages. On the other hand, Table 21 shows the values obtained for the simulation of these same air and water pressure combinations.

Table 20: Experimental results of the droplet size distribution for various pressure combinations.

PERCENTAGE OF DROPLETS IN THE SIZE RANGE (%)							
P_{air} (bar)	**P_{water} (bar)**	**Particle size (µm)**					
		0.3	**0.5**	**1**	**2.5**	**5**	**10**
6	**6**	1.53	3.22	3.25	9.88	61.66	20.46
10	**6**	0.00	1.15	0.69	0.69	7.07	90.41
10	**10**	0.00	2.93	3.74	12.12	51.78	29.43
14	**8**	7.63	2.38	0.64	0.62	7.61	81.13
14	**10**	0.00	2.04	2.02	3.95	64.60	27.39
14	**14**	0.00	2.59	3.52	19.46	41.15	33.28

Table 21: Simulation results of the droplet size distribution for various pressure combinations.

PERCENTAGE OF DROPLETS IN THE SIZE RANGE (%)										
P_{air} (bar)	**P_{water} (bar)**	**Particle size (µm)**								
		0-0.3	**0.3-0.5**	**0.5-1**	**1-2**	**2-5**	**5-10**	**10-20**	**20-50**	**50-100**
6	**6**	0	0	0	0	1.09	41.91	44.29	12.48	0.24
10	**6**	0	0	0	0.62	29.90	44.29	24.35	0.84	0
10	**10**	0	0	0	0.01	1.21	38.23	46.47	13.97	0.127
14	**8**	0	0	0.02	2.90	44.10	44.13	8.53	0.33	0
14	**10**	0	0	0	0.98	28.33	46.80	23.02	0.86	0
14	**14**	0	0	0	0	3.30	38.65	46.14	11.83	0.09

Table 22 provides a comparison between the Sauter mean diameter (SMD) results obtained for the droplets numerically and experimentally.

Table 22: Comparisons between the experimental and numerical results.

RESULT COMPARISONS			
P_{air} (bar)	**P_{water} (bar)**	**Simulation results**	**Experimental results**
		SMD in measuring range (µm)	SMD in measuring range (µm)

6	**6**	7.05	5.43
10	**6**	6.61	9.42
10	**10**	7.05	5.89
14	**8**	6.38	8.55
14	**10**	6.61	6.10
14	**14**	7.00	5.92

4.7.4 Conclusions

From the data obtained in this section it can be seen that:

- There is a good agreement between numerical and experimental results of cone opening angles for the same combination of air and water pressures.

- There is a good agreement between the flows obtained experimentally and those obtained by simulation.

  T here is an evident agreement as well between the experimental and simulated distributions of drops. Particularly SMD in both cases remain similar –within 2 or 3 µm-.

Chapter 5

Analysis of the behaviour of the fog generated by the Counterfog® system

5.1 Introduction

The term fog generally refers to a suspension of droplets in a gas. However, from a meteorological point of view, the World Meteorogical Organization [WMO, 1992] defines fog as a suspension of water droplets of very small size, usually microscopic, in air, which reduces horizontal visibility on the earth's surface to less than 1 km. On the other hand, the terms mist or haze refer to visibility ranges from one to several kilometers.

In water droplet fogs, there is a strong relationship between the visibility of the fog, the number of droplets present per unit volume of air and the average droplet size. In this way, a dense fog with a visibility of approximately 100 m composed of droplets of sizes between 10 and 20 μm in diameter will contain between 0.1 and 0.2 gm^{-3} of water fog [Roach 1994].

Natural fog, considered as a form of condensed water present in the atmosphere, has a great influence on many different aspects of the environment such as the thermal

and radioactive balances of the atmosphere, air quality, local and global climate, flora and fauna, etc. [Pérez-Díaz et al. 2017].

In addition, it is important to keep in mind that the physical nature of fog and clouds is the same. They are therefore natural states of condensed water in the atmosphere. The difference between the two lies in the height at which they occur with respect to the earth's surface and in the size of the drop. While fog occurs in areas close to the earth's surface and is formed by droplets of micrometer size, clouds are produced at higher altitudes and the droplets that make them up reach diameters of up to several millimetres [Pérez-Díaz et al. 2017].

The nucleation process is responsible for the production of ultrafine particles, clouds and fog in the atmosphere. This process allows the condensation of water from the formation of droplet nuclei, which can be considered heterogeneous or homogeneous depending on the presence or absence of foreign agents in the formation of these nuclei [Nanev 2015].

For homogeneous nucleation to take place it is necessary to exceed either the threshold corresponding to the critical supersaturation of the water-vapor or the threshold corresponding to the critical supercooling [Pruppacher et al. 1997 and Haeffelin et al. 2016]. The particles thus formed may serve as cloud condensation nuclei (CCN) allowing the formation of droplets. The levels of supersaturation water-vapor necessary for homogeneous nucleation are much higher than those that can be found in the atmosphere, and the natural generation of nuclei through this process is not possible [Pruppacher et al. 1997 and Andreae et al. 2008]. However, under the presence of certain foreign agents the necessary supersaturation levels fall to attainable values in the atmosphere, facilitating the formation of droplet nuclei (heterogeneous nucleation).

Factors such as size, solute content, presence of surfactants, wettability and shape of insoluble particles, and presence of soluble gases are those that define the capacity of a particle to act as CNN before a certain level of water-vapor supersaturation. CCN originates in all the mechanisms that lead to the formation of atmospheric aerosols [Pérez-Díaz et al. 2017].

There is growing interest in the measurement, control and improvement of air quality. This is due to the direct relationship between the presence of solid particles in suspension and the increase in cardiovascular and respiratory diseases, as well as mortality in a large number of urban centres [Dockery et al. 1993; Pope et al. 1995 and WHO 2013]. Conducted studies estimate close to 6.4 million deaths per year due to this cause [Ezzati et al. 2002 and WHO 2002]. The World Health Organization (WHO) provides in its Air Quality Guidelines (AQG) detailed information on the adverse effects on human health when exposed to solid particles suspended in the air [WHO 2000].

PM suspended in the air is composed of a complex mixture of organic and inorganic substances. The explanation about the size distribution of PM was provided by Whitby (1972) making use of new instruments [Liu et al. 1974]. These particles can be classified into two groups according to their aerodynamic diameter: coarse and fine particles [Junji et al. 2013]. The first ones are those whose diameter reaches a value greater than 2.5 μm but a maximum of 10.0 μm ($PM_{10-2.5}$), while fine particles are considered to be those whose diameter reaches a maximum value of 2.5 μm ($PM_{2.5}$). The classification of particles according to their aerodynamic diameter is due to the size of these ones allows to predict its movement and deposition times. Its size is related to the chemical composition and the source of the particles and the aerodynamic diameter is directly related to the level of reach of these particles inside the human body. The particle size fractions suspended in air that are used as cut-off values are set at $PM_{2.5}$ and PM_{10}. This is due to the fact that experimental studies [Zhou and Cheng 2005] and simulations

[Rostami 2009] establish that particles with an aerodynamic diameter smaller than 10 μm can penetrate the organism without any resistance. PM_{10} can penetrate the respiratory system, reaching high respiratory tract and bronchi while $PM_{2.5}$ can penetrate in the respiratory system, reaching even the bronchioles and alveoli [Nel 2005].

Due to the above situation, the need to develop methods to effectively carry out the reduction of the concentration of contaminating solid particles in the ambient air is evidenced [Pérez-Díaz 2018.b, Martín-Pérez 2018]. Consequently, the design, development and set-up of the Counterfog® System [E.U. Patent No. EP17382293.3/22.05.17] has been carried out, consisting of the generation of fog by the ejection of water and air by means of a nozzle designed for this purpose [Pérez-Díaz 2018.a, Casarrubios 2018]. This fog can be of just water or contain a neutralizing compound. The droplets size of the fog can be changed depending on the water and air pressures that can be adjusted at will.

The following work aims to carry out an exhaustive analysis of the behaviour of the fog generated with the Counterfog® system. For this purpose, the variation of the data obtained in different positions for the same type of test will be studied.

5.2 Experimental setup and procedure

Before performing each test the different parameters of the test room shall be established to ensure that these factors will not affect the fog generation process. In this way, the temperature and relative humidity of the room were set at 25 ºC and 95%, respectively. The composition of the fluid for the generation of the fog was limited to water, not being added any kind of neutralizing compound. The temperature and humidity of the test room, as well as the flow of water used in the generation of fog were monitored at all times during each test.

The number and size of the water droplets was monitored by a particle counter (8306 Handheld Particle Counter, Particles Plus, Massachusetts, U.S.A.). Number of droplets per liter is measured between 0.3 μm and 10 μm. The height and inclination of this counter remained unchanged throughout all the tests performed, varying only the position and orientation of it as shown in Figure 153. This seeks a meaningful sample to characterize the fog generated in different parts of the test room that allows us to know if the fog thus generated has a homogeneous characteristic in space. In addition to the particle counter, laboratory equipment (see section 3.2.2) was used during tests. A video camera recorded everything that happened inside the test room.

Tests will be performed with the B1: 2 nozzle model. The temperature of the injected water will be 12 º C, while the pressures of air and water will be 12 bar and 8 bar, respectively. The pitch angle of the particle counter will be + 30º and its height, with respect to the ground level of the test room, of 0.65 m.

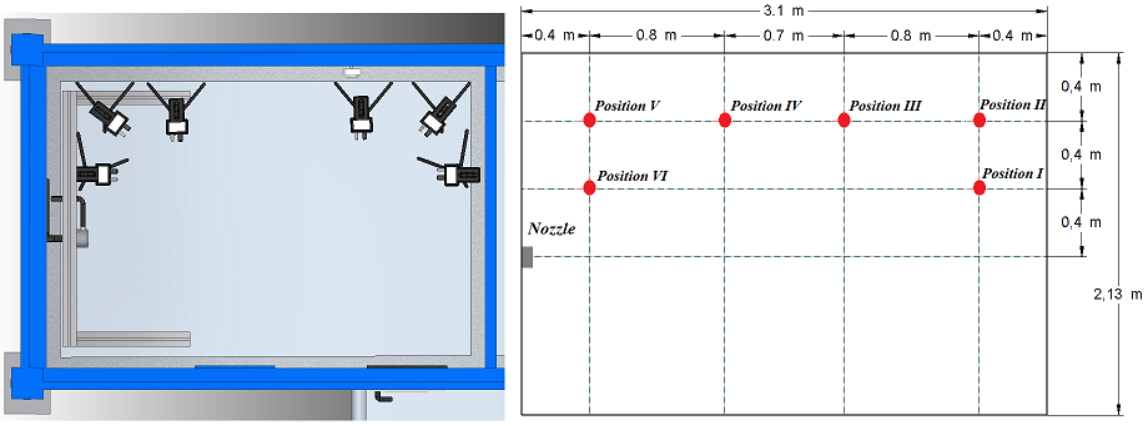

Figure 153: Different particle counter positions in fog homogeinity tests for nozzles B1:2.

Once the test factors has been defined, the working procedure used to carry out the tests is as follows. Each test begins by ensuring the correct state and cleaninless of the different elements of the laboratory (see section 3.2.2), as well as the correct initial position of the pneumatic and manual ball valves. Then the pressurized air tank is checked to be fully charged and that the pressurized water tank is empty. On the one hand, in the case of the pressurized air tank, it is checked that it is at a pressure of between 26 and 29 bar, as this is the maximum range provided by the compressor. This allows guaranteeing that the pressures that are subsequently imposed for fog generation are met. If this is not the case, the compressor will start up autonomously until it stops once the pressure range in the pressurized air tank defined above has been reached. On the other hand, to check the pressurized water tank, the purge valve is opened to release any remaining pressure inside due to previous tests. The ball valve is then opened to allow the tank to drain by gravity. Once completely empty, the purge and drain valves are closed. The next step is to check that the atmospheric water tank is full and if necessary fill it with the hose connected to the water inlet. In addition, a pH test and temperature measurement is performed to ensure that the composition and temperature of the water used is the same for the entire test set. After completing the above steps the pressurized water tank is filled with water from the atmospheric water tank. To do this, the purge and fill valves are opened and the pump is activated to allow the pressurized water tank to fill to its maximum level (4.5 l). This maximum level is guaranteed by a sensor and an actuator that stops the pump once it has been reached. Once this process is completed the pump is switched off and the purge and fill valves are closed. Once this is done, the ball valves installed inside the test room for the air and water outlet are closed and the water shooting pressures adjusted. In the case of air, and since the tests are carried out without the application of air, the air valve will remain closed at all times. The air outlet ball valve opens to release any remaining pressure in the ducts to the nozzle. In the case of water, the water pressure valve is opened to allow pressurized air to flow from the pressurized air tank to the pressurized water tanks through the water circuit. The nominal water pressure is adjusted by means of a manual control valve and a pressure manometer located at the same point. Once correctly adjusted, the water outlet ball valve is opened to release the remaining pressure and to remove the residual water contained in the pipes leading to the nozzle. The air and water outlet ball valves will remain open until the next shot is fired. The next step is a short shot (approximately 8 seconds) to fill the water pipes

of the water circuit with water without exhausting the pressurized water tank by opening the water valves. In this way, it will be able to ensure that during the test the fog begins to be generated almost instantaneously without a significant delay from the opening of the shooting valves (air and water valves). This is of great importance due to the short test shooting times and the delays observed in fog generation of up to 5 seconds when the water circuit is empty. The water and water pressure valves are closed once the shot is finished and the computer in the Control Room is used to check that the water shooting pressure obtained matches with that established in the settings. Once this process has been completed, it is repeated from the beginning to leave the system ready to perform the test shot. At this point, the test room is closed and completely insulated and the air inside it is renewed by activating the corresponding ventilation and air filtration system for 10 minutes.

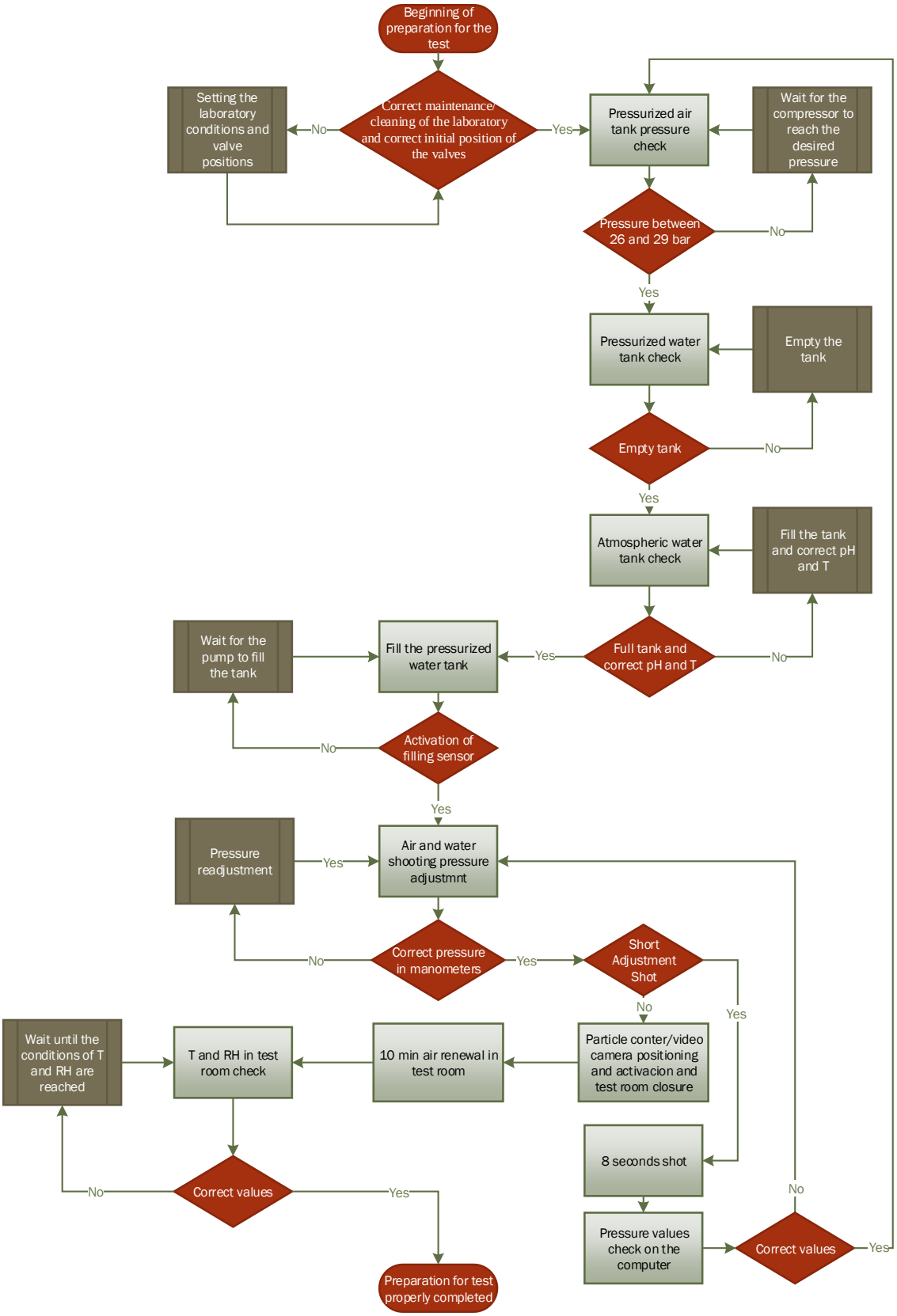

Figure 154: Diagram of the room preparation procedure for fog homogeinity tests for nozzle B1:2.

Finally, it is checked that the temperature of the room corresponds to that stipulated for the tests. In the same way, it is verified that the relative humidity in the room is also the desired one. It should be noted that this process is carried out automatically by the control system installed in the Control Room where the desired conditions to be provided by the heat pump and the chiller have been previously defined, thus guaranteeing compliance. The particle counter and video camera will have been placed and activated inside the room immediately prior to the closure of the test room. In the case of the particle counter, with the position, orientation and pitch angle corresponding to the test to be performed. Figure 154 shows a diagram summarizing the test room setup process.

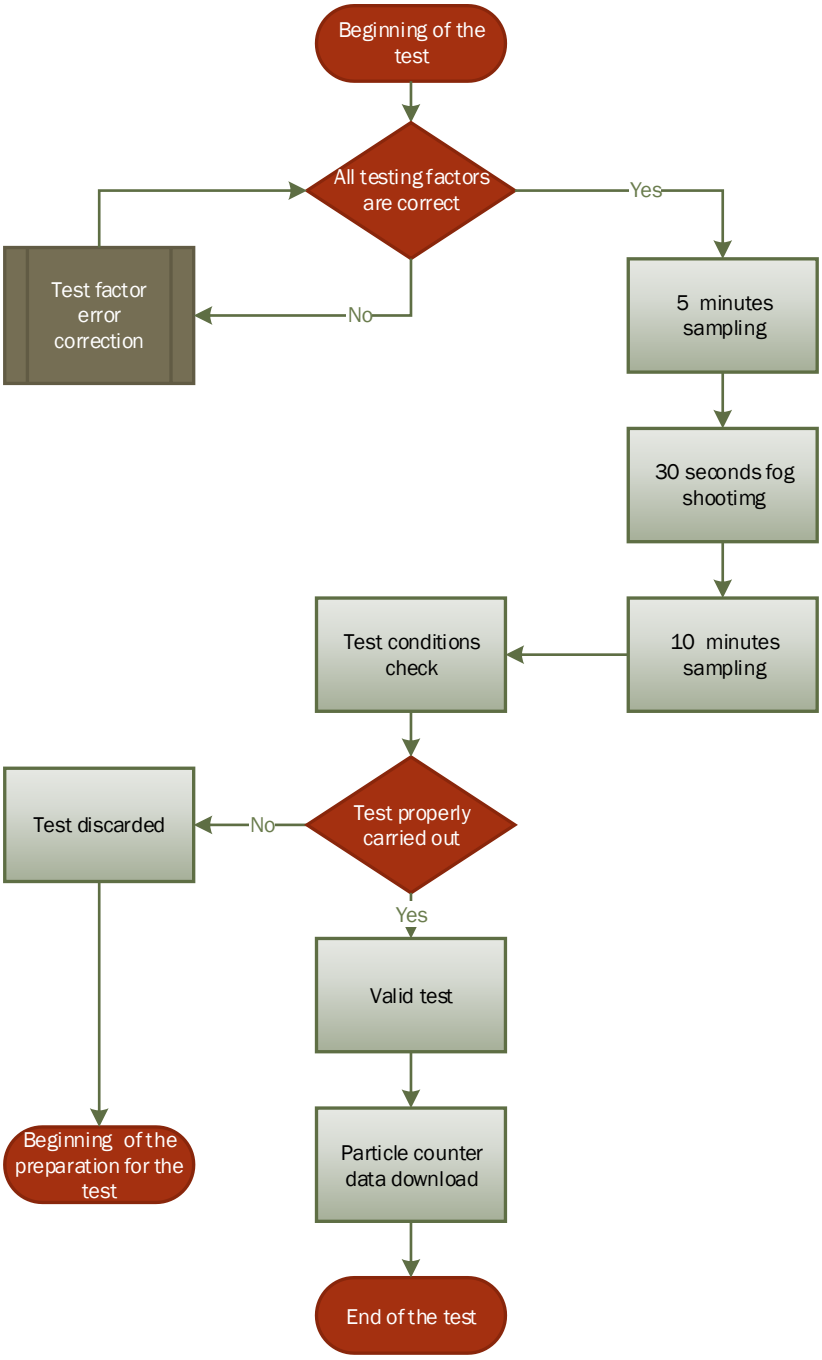

Figure 155: Diagram of the test procedure for fog homogeinity tests for nozzle B1:2.

Once the devices have been placed in the room and the correct configuration has been made, the particle counter and the video camera are switched on and the test room is closed for perfect isolation from the outside of the laboratory, as indicated above. The particle counter is maintained by taking 10 second samples every 20 seconds from then until the end of the test. The first stage of the test, once the humidity and temperature conditions in the room have been reached, consists of taking samples with the particle counter for a period of 5 minutes to establish the conditions prior to shooting in the test room, thus ensuring that the initial conditions of all tests are similar. After the specified time has elapsed, the fog is generated by shooting at the nozzle for 30 seconds at the air

and water pressures set during test preparation, as shown in Figure 154. Then it has to be waited for 10 minutes from the end of the shoot. During this time the particle counter continues to take samples. After this time, the test is considered complete and the room is opened and the particle counter and video camera are turned off. At the end of the test, the initial temperature and humidity data, as well as the shooting pressure data, are checked to ensure compliance with the test conditions. In addition, test videos are reviewed to ensure that no irregularities occur during testing.Once it is verified that everything has happened as stipulated, the test is taken as correct and the particle counter data is downloaded and processed. Otherwise, the test is automatically discarded and repeated. Figure 155 shows a diagram summarizing the test process.

5.3 Experimental results and Discussion

The density water droplets in air in the test room prior to activation of the Counterfog® system for each of the counter positions is shown in **Figure** 156. The average of the values corresponding to all the tests performed in which measurements were taken every minute from the start of the test (when the room was isolated and the test humidity and temperature conditions were reached) until the time of activation of the Counterfog® system are shown.

From the data obtained most of the droplets found corresponds to the size range 0.3 μm, followed by the 0.5 μm size droplets which are present in a smaller order of magnitude. Similarly, the 1.0 μm diameter droplets are also detected in number two orders of magnitude lower than those of 0.3 μm. Droplets corresponding to the rest of the size ranges are detected in a much smaller number, their presence not being significant for the results shown.

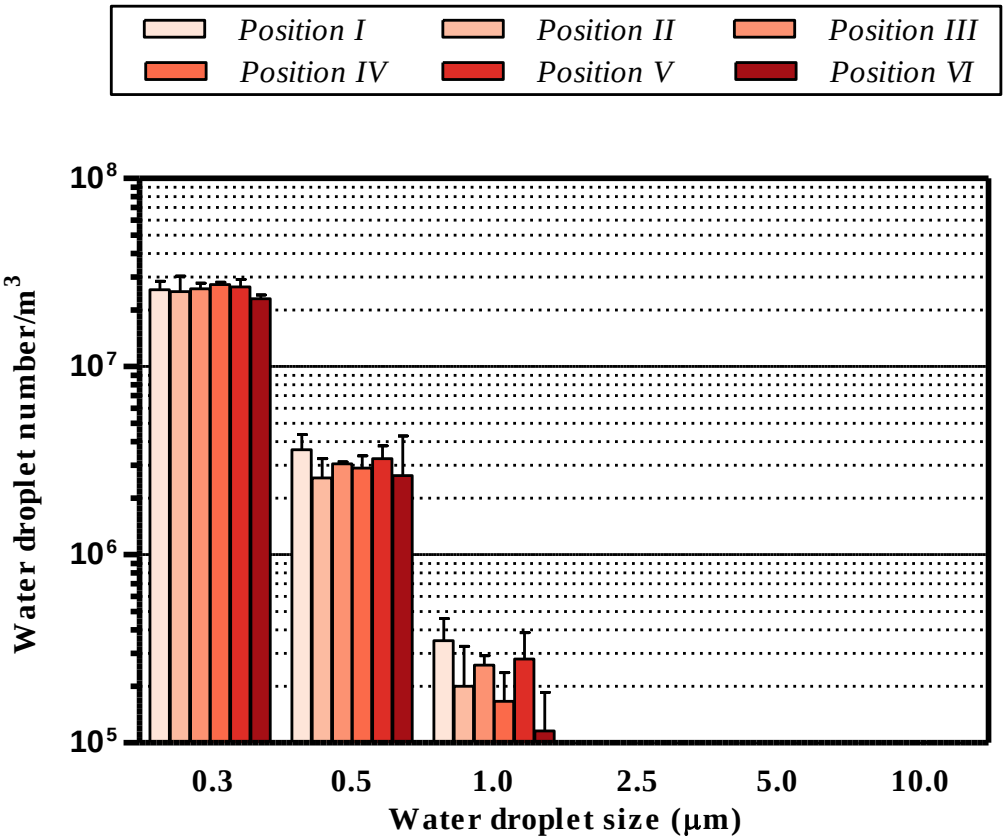

Figure 156: Background level of the number of water droplets per cubic meter of air inside the test room for each size range at each of the different spatial positions of the counter immediately prior to activation of the fog generating **Counterfog®** system

It is observed how the background values present in the room prior to the activation of the Counterfog® system follow a very similar pattern both as a function of time, since the deviation found in each measurement is small as a function of the position of the measurement point if the bars corresponding to each range of particle size are compared. As it is evident from Figure 156, the differences in the values obtained are greater in the case of size 1.0 μm droplets than in the case of size 0.5 μm droplets. Similarly, the differences are greater in the case of 0.5 μm than in the case of 0.3 μm droplets. This is due to the high values that are being handled which make that at higher degrees of magnitude, the deviations are relatively less relevant.

On the other hand, Figure 157 shows a graph for each measurement position in which the evolution of the number of droplets for each size range is observed. The measurements correspond to the values obtained for each minute after the operation of the fog generating Counterfog® system has ended up to a total of 10 minutes. Each graph shows the average of the values obtained for each sampling position for the same droplet size and the same instant. The deviations corresponding to these measures are also represented in the graphs.

Figure 157 shows how the evolution of the number of droplets for each size range has a similar qualitative behaviour for the set of all the positions. In this way, it can now be sensed with some certainty how the fog is reasonably homogeneously distributed over the entire surface of the test room.

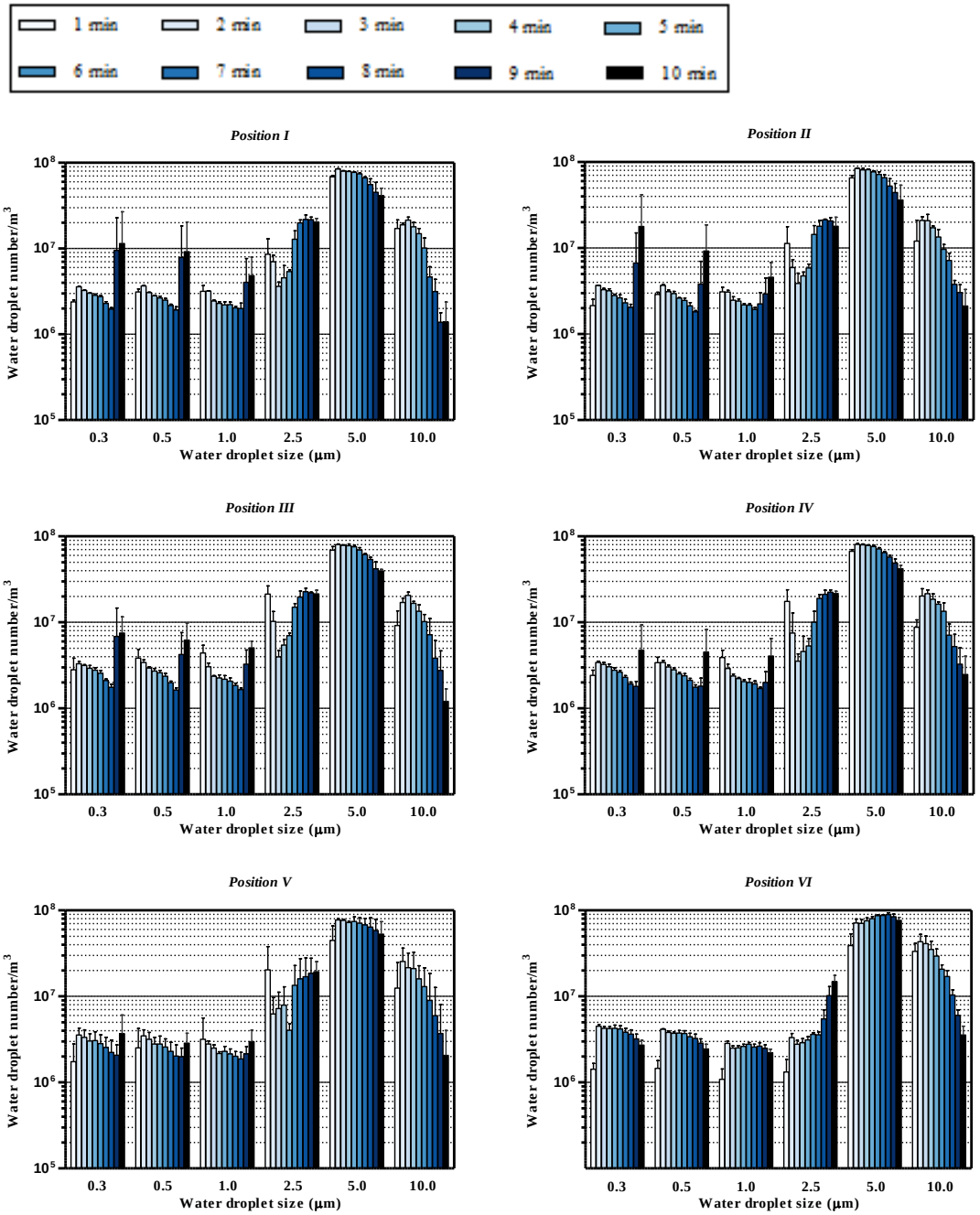

Figure 157: Number of water droplets per cubic metre of air inside the test room for each size range in each of the different spatial positions of the counter for each minute after the fog shot up to a total of 10 minutes

An individual analysis is now being carried out for each droplet size range in order to gain a better understanding of the behaviour of the fog generated by the Counterfog® system for the removing of contaminating particles in suspension.

For the droplet size ranges corresponding to the diameters 0.3, 0.5 and 1.0 µm it is found a similar evolution that is characterized by a continuous decrease in the number of droplets during the first 7 or 8 minutes of measurement until reaching a minimum, to then increase the number of droplets counted in the last two or three measurements abruptly.

Although, as indicated, this evolution is similar in the three cases, it should be noted that the initial state from which the test started, i.e. the droplet background accounted before the activation of the Counterfog® system, was very different in the three cases. While the initial number of 0.3 µm size droplets present in the test room was an order of magnitude above the first data recorded after activation of the Counterfog® system, the values corresponding to the size range of 1.0 µm were an order of magnitude below the values now obtained. On the other hand, in the case of 0.5 µm drops, the order of magnitude of both values is similar (Figure 156 and Figure 157). The fact that justifies this situation is due to the following rationale: while the generated fog has droplets of 1 µm in diameter, the particles of 0.5 and 0.3 µm are not generated by the fog. This clarifies why the number of droplets of 1 µm is significantly higher than the background and why the number of droplets of 0.5 µm does not have a significant variation. Due to the much larger size of the 5 and 10 µm droplets compared to the 0.3 µm droplets, the latter are swept and embedded by the former producing the decrease in the number seen in the graphs. Possible overlaps leading to a certain level of error on the part of the counter can be added to this fact.

On the other hand, in the case of the droplet range of 2.5 µm we also find a continuous decrease in the number of droplets over time before reaching a minimum and starting to increase the number afterwards. However, on this occasion this minimum occurs in the first 3 or 4 minutes of measurement to begin to grow during the remaining minutes.

Finally, the cases corresponding to the size ranges of 5.0 and 10.0 µm are observed. In both cases there is a continuous decrease in the number of drops over time, becoming evident as the slope of the 10.0 µm range is noticeably steeper. This is due to the fact that the settling velocity of the droplets is directly proportional to the square of its diameter, evidenced in a very clear way for these size ranges.

These data allow us to conclude that the Counterfog® system generates a fog composed of droplets of sizes greater than 1.0 µm, the most abundant being the droplets of range 5.0 µm, followed by those of size 2.5 and 10 µm that are presented in an magnitude of similar order. Finally, it is the 1.0 µm droplets that are generated in smaller numbers.

In addition, the phenomenon that justifies the abrupt growth of the number of droplets of size 0.3, 0.5, 1.0 and 2.5 µm is the surface evaporation produced in the droplets during their suspension time in the test room. Since the higher the surface/volume ratio, evaporation occurs at a higher rate, the smaller droplets will decrease their volume more rapidly, explaining why the growth is more pronounced for the 0.3 µm droplets than for the 0.5 µm droplets and also more pronounced for the 0.5 µm droplets than for the 1.0 µm droplets. In the case of droplets of size 2.5 µm this growth occurs earlier in time and also very pronounced due to the large number of droplets of size 5.0 µm that, although they do not evaporate as quickly as the smaller drops, this is offset by the much higher number in which they are present after the activation of the Counterfog® system.

Figure 158 is the average value of the number of droplets of all tests performed for all positions and for each droplet size range in its evolution over time after the Counterfog® system was applied for a total time of 10 min. As expected after the previous analysis, the profile of this graph is very similar to those obtained individually in the 6 positions of Figure 157. The deviations obtained are represented in the error bars of this graph showing a high degree of similarity between the different measurements made between the different tests and the different measurement points within the test room.

It is therefore possible to ensure with certainty that the characteristics of the fog generated under certain pre-determined conditions are maintained between tests, and it is possible to confirm the repeatability of the process, i.e. it is possible to reproduce a fog of similar characteristics by presetting the same test values.

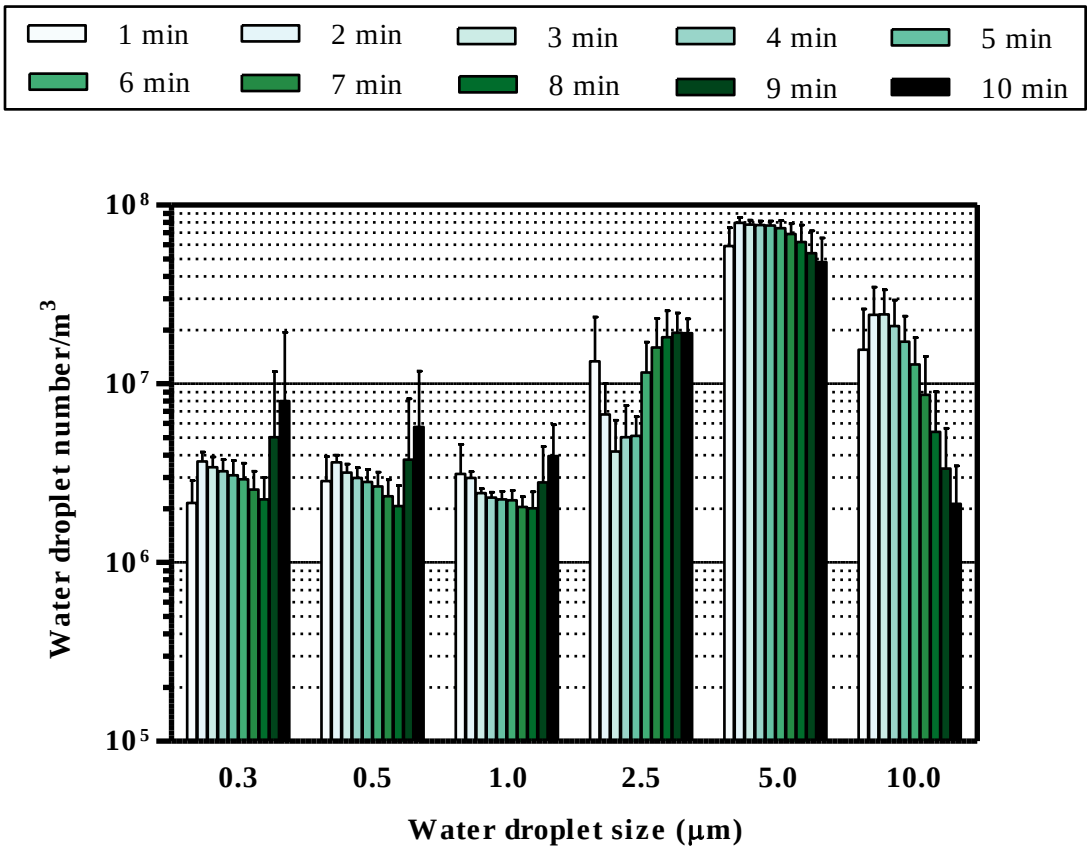

Figure 158: Mean and standard deviation of the number of water droplets per cubic meter of air inside the test room for each size range at the different spatial positions of the counter for each minute after the fog shot up to a total of 10 minutes.

But it is also possible to go further and ensure that not only the above is fulfilled, but also that the properties of the fog are similar at any point in the room for the same height of measurement. This means that the fog, one minute after the shot, is distributed evenly throughout the entire area of the test room, being able to guarantee its effectiveness in removing airborne particles at any point in the test room.

5.4 Conclusions

It has been demonstrated how the new Counterfog® system, conceived for the cleaning and decontamination of particulate matter suspended in air, can generate fogs with the same properties under the same shooting conditions, this is to say, the repeatability of the fogs generated by this system is guaranteed if the shooting conditions do not vary.

Furthermore, it can be gone a step further and ensure that, in the same shot and for

a given height and a given instant, the properties of the fog generated are homogeneous at all points inside the test room. This fact allows guaranteeing that the effectiveness of the system in indoor spaces does not depend on the position of the volume of air to clean for a given height. These very satisfactory results make the study in outdoor spaces a possible future way of developing the Counterfog® system. In this way, this technology could provide an unique and effective tool for cleaning air in cities, improving air quality and decreasing respiratory diseases among population in large cities. In this way, the path towards a healthier air environment for people is a little closer every day.

Chapter 6

Decontamination of Diesel particles from air by using the Counterfog® system

6.1 Introduction

There is a serious health risk associated with exposure to micron-sized solid particles in suspension [Dockery et al. 1993; Pope et al.1995; WHO2013]. Direct exposure includes direct inhalation from air or ingestion of those deposited on food [EEA 2017]. It is generally admitted that particles with a diameter lower than 10 μm (known as PM10) can penetrate the respiratory system, reaching high respiratory tract and bronchi while those under 2.5 μm can reach bronchioles and alveoli [Nel 2005]. The presence of solid particles floating in air is especially severe. It has been demonstrated that exhaust and non-exhaust traffic-related particles contribute almost equally to this problem [Grigoratos and Martini 2014]. Non-exhaust traffic particles are originated by brakes, clutches, tires, roads, and resuspended material. Exhaust particles are usually associated with the combustion process of Diesel engines and heating systems [Fenger and Tjell 2009; Lucking et al. 2011]. Natural mechanisms removing particles from the atmosphereare

known to be dry deposition or fall out and scavenging. The first one is produced by gravity driving solid particles down, while in the second phenomenon particles act as condensation nuclei to create water raindrops that eventually fall. These raindrops may supposedly wash out other particles and droplets as they fall [Allaby, 2003]. However, it is well-known that raindrops are not very effective removing micron-sized particles whichcan remain floatingin air for days [Greenfield 1957]. Thermal inversion in the atmosphere hinders the scattering of pollutant particles from urban areas to others as well [EEA 2012]. Recently, a new technology based on the interaction of fogs with the polluted air—called Counterfog®—has been proposed to reduce the concentration of air pollutants in large areas [Martín-Pérez et al. 2018; Pérez-Díaz et al. 2018; Casarrubios et al. 2018]. Using just water and compressed air Counterfog® creates a conic jet of fog composed of micron-sized droplets that are claimed to wash out particles from the surrounding air [Pérez-Díaz application EP 17382293]. Such effectiveness is based on the use of droplets of the size similar to those particles to remove by aggregation with the water droplets. Counterfog® uses just water and air maximizing environmental friendship. In the present work, the effectiveness of such a system to remove exhaust particles from air is tested in laboratory.

The aim of the work presented in this chapter is to measure the effectiveness of the Counterfog® system in removing diesel particles from the air.

6.2 Experimental setup and procedure

Before performing each test the different parameters of the test room shall be established to ensure that these factors will not affect the fog generation process. In this way, the temperature and relative humidity of the room were set at 25 ºC and 95%, respectively. The composition of the fluid for the generation of the fog was limited to water, not being added any kind of neutralizing compound. The temperature and humidity of the test room, as well as the flow of water used in the generation of fog were monitored at all times during each test.

The number and size of the water droplets was monitored by a particle counter (8306 Handheld Particle Counter, Particles Plus, Massachusetts, U.S.A.). Number of droplets per liter is measured between 0.3 µm and 10 µm. The height and inclination of this counter remained unchanged throughout all the tests performed. In addition to the particle counter, laboratory equipment (see section 3.2.2) was used during tests. A video camera recorded everything that happened inside the test room.

Tests will be performed with the B1: 2 nozzle model. The temperature of the shooting water will be 12 º C, while the pressures of air and water will be 12 bar and 8 bar, respectively. The pitch angle of the particle counter will be + 30º and its height, with respect to the ground level of the test room, of 0.65 m.

The performance of the tests requires the use of a Diesel engine whose characteristics are summarized in Table 23.

After the completion of each test, samples of the soil surface of the test room arecollected and subsequently analyzed by Scanning Electron Microscope, Energy-dispersive X-ray spectroscopy and •Laser diffraction particle analyser.

Table 23: Characteristics of Diesel Engine.

DIESEL ENGINE	
Motor	I4
Type	DW10ATED
Cycle	Four-stroke diesel engine
Cylinders	inline 4-cylinder
Calibre	85 mm
Stroke	88 mm
Cubic capacity	1997 cm^3
Compression ratio	18
Maximum power	109 HPW/ 4000 r.p.m.
Maximum torque	250 Nm/ 1750 r.p.m.
Specific consumption	6.6 l/ 100 km
Fiscal power	90 HPW

Once the test factors has been defined, the working method used to carry out the tests is explained in detail. Each test begins by ensuring the correct maintenance and cleaning of the different elements of the laboratory (see section 3.2.2), as well as the correct initial position of the pneumatic and manual ball valves. Then it is checked that the pressurized air tank is fully charged and that the pressurized water tank is empty. On the one hand, in the case of the pressurized air tank, it is checked that it is at a pressure of between 26 and 29 bar, as this is the maximum range provided by the compressor. This allows guaranteeing that the pressures that are subsequently imposed for fog generation are met. If this is not the case, the compressor will start up autonomously until it stops once the pressure range in the pressurized air tank defined above has been reached. On the other hand, to check the pressurized water tank, the purge valve is opened to release any remaining pressure inside due to previous tests. The ball valve is then opened to allow the tank to drain by gravity. Once completely empty, the purge and drain valves are closed. The next step is to check that the atmospheric water tank is full and if necessary fill it with the hose connected to the water inlet. In addition, a pH test and temperature measurement is performed to ensure that the composition and temperature of the water used is the same for the entire test set. After completing the above steps the pressurized water tank is filled with water from the atmospheric water tank. To do this, the purge and fill valves are opened and the pump is activated to allow the pressurized water tank to fill to its maximum level (4.5 l). This maximum level is guaranteed by a sensor and an actuator that stops the pump once it has been reached. Once this process is completed the pump is switched off and the purge and fill valves are closed. Once this is done, the ball valves installed inside the test room for the air and water outlet are closed and the water shooting pressures adjusted. In the case of air, and since the tests are carried out without the application of air, the air valve will remain closed at all times. The air outlet ball valve opens to release any remaining pressure in the ducts to the nozzle. In the case of water, the water pressure valve is opened to allow pressurized air to flow from the pressurized air tank to the pressurized water tanks through the water circuit. The shooting water pressure is adjusted by means of a manual control valve and a pressure manometer located at the same point. Once correctly adjusted, the water outlet ball valve is opened to release the remaining pressure and to remove the residual water contained in

the pipes leading to the nozzle. The air and water outlet ball valves will remain open until the next shot is fired. The next step is a short shot (approximately 8 seconds) to fill the water pipes of the water circuit with water without exhausting the pressurized water tank by opening the water valves. In this way, it will be able to ensure that during the test the fog begins to be generated almost instantaneously without a significant delay from the opening of the shooting valves (air and water valves). This is of great importance due to the short test shooting times and the delays observed in fog generation of up to 5 seconds when the water circuit is empty. The water and water pressure valves are closed once the shot is finished and the computer in the Control Room is used to check that the water shooting pressure obtained matches with that established in the settings. Once this process has been completed, it is repeated from the beginning to leave the system ready to perform the test shot. At this point, the test room is closed and completely insulated and the air inside it is renewed by activating the corresponding ventilation and air filtration system for 10 minutes. Finally, it is checked that the temperature of the room corresponds to that stipulated for the tests. In the same way, it is verified that the relative humidity in the room is also the desired one. It should be noted that this process is carried out automatically by the control system installed in the Control Room where the desired conditions to be provided by the heat pump and the chiller have been previously defined, thus guaranteeing compliance. The particle counter and video camera will have been placed and activated inside the room immediately prior to the closure of the test room. In the case of the particle counter, with the position, orientation and pitch angle corresponding to the test to be performed. Figure 159 shows a diagram summarizing the test room setup process.

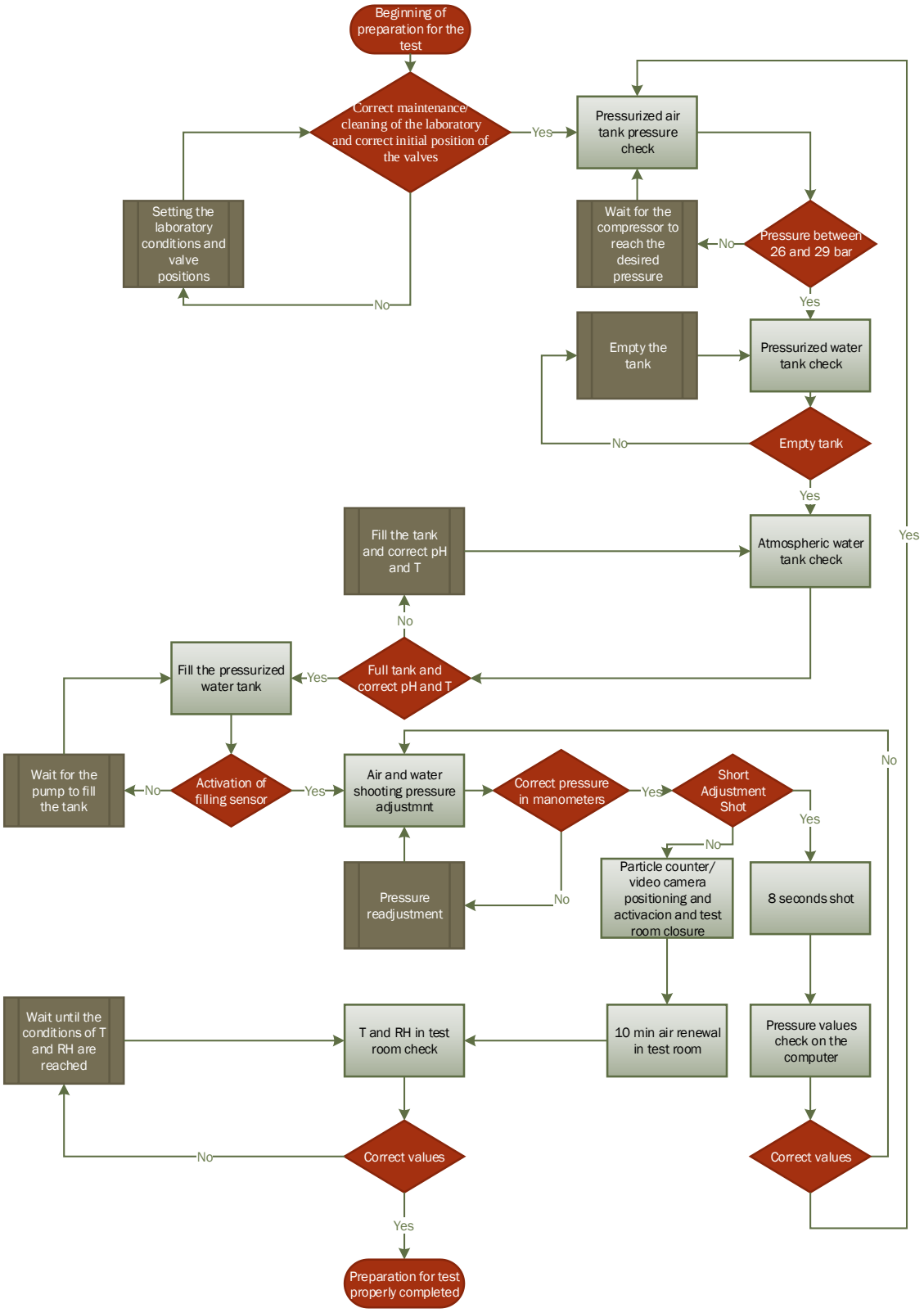

Figure 159: Diagram of the room preparation procedure for diesel tests for nozzle B1:2.

Once the devices has been placed in the room and the correct configuration has been made, the particle counter and the video camera are switched on and the test room is closed for perfect isolation from the outside of the laboratory as indicated above. The

particle counter is maintained by taking 10 second samples every 20 seconds from then until the end of the test.

Figure 160: Introduction of the gases resulting from the combustion of the four-stroke Diesel engine.

The first stage of the test, once the humidity and temperature conditions in the room have been reached, consists of taking samples with the particle counter for a period of 5 minutes to establish the conditions prior to shooting in the test room, thus ensuring that the initial conditions of all the tests are similar. Then, gases and solid particles generated in a four-stroke Diesel engine (Table 23) are conducted to the room during 5 minutes (Figure 160). Before proceeding to the decontamination of the air and after the perfect enclosing of the test room, few minutes are required (5 minutes) to ensure the homogeneity of the air in the laboratory. A natural deposition rate due to gravity and described by Stokes viscosity law is therefore determined with those data. After the specified time has elapsed, the fog is generated by shooting the nozzle for 30 seconds at the air and water pressures that have been established during the preparation for the test. Then 50 minutes have to been waited from the end of the shot. During this time the particle counter continues to take samples. After this time, the test is considered complete and the room is opened and the particle counter and video camera are turned off. The samples of residues generated after the application of the fog on the surface of the laboratory floor are then collected for subsequent analysis and characterization.

Figure 161: Safety equipment for laboratory staff during diesel tests.

At the end of the test, the initial temperature and humidity data as well as the shooting pressure data are checked to ensure compliance with test conditions. In addition, water flow data is collected to verify the repeatability of the test. Furthermore, test videos are reviewed to ensure that no irregularities occur during testing. Once it is verified that everything has happened as stipulated the test is taken as correct and the particles counter data is downloaded and processed. Otherwise, the test is automatically discarded and repeated. Figure 159 shows a diagram summarizing the test process. The tests are carried out with the relevant materials and safety measures that guarantee both the safety of the personnel and the non-contamination of the evidence obtained (Figure 161).

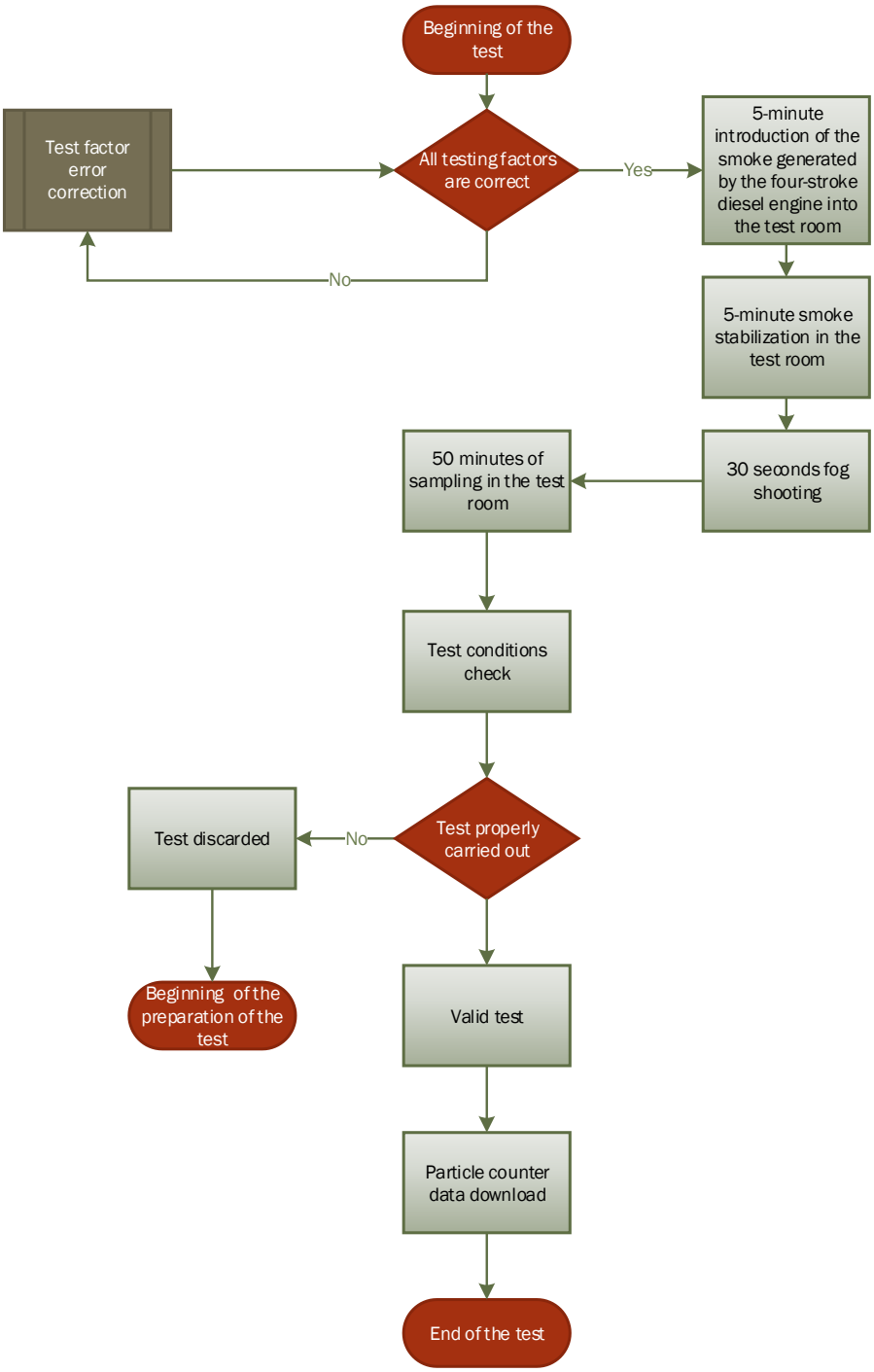

Figure 162: Diagram of the test procedure for diesel tests for nozzle B1:2.

6.3 Experimental results and Discussion

Samples were collected from the test room surface at the end of each test. The morphology of the samples was studied using Scanning Eelectron Microscope (SEM). In turn, a semi-quantitative composition analysis was performed using Energy Dispersive X-ray Analysis (EDXA). Finally, an analysis of the size distribution is carried out by means of a laser diffraction particle analyzer (see section 3.3). Figure 163 shows the black soot particles floating on water in a tray after 1 min actuation of Counterfog® system.

Figure 163: Black soot particles floating on water during a diesel test.

Figure 163 shows the time evolution of the number of particles corresponding to the size channels 2.5, 5 and 10 μm. The first of the bars indicates the initial number of particles in the room prior to the start of the introduction of the particles resulting from diesel combustion. The second bar indicates the number of particles in the room immediately after the 5 minute introduction of combustion particles. The third column shows the existing particles after 30 minutes from the application of the fog generated by the Counterfog® system. Finally, the last column corresponds to the theoretical number of particles that would be in the room air 30 minutes after the introduction of the diesel particles if the Counterfog® system had not been applied.

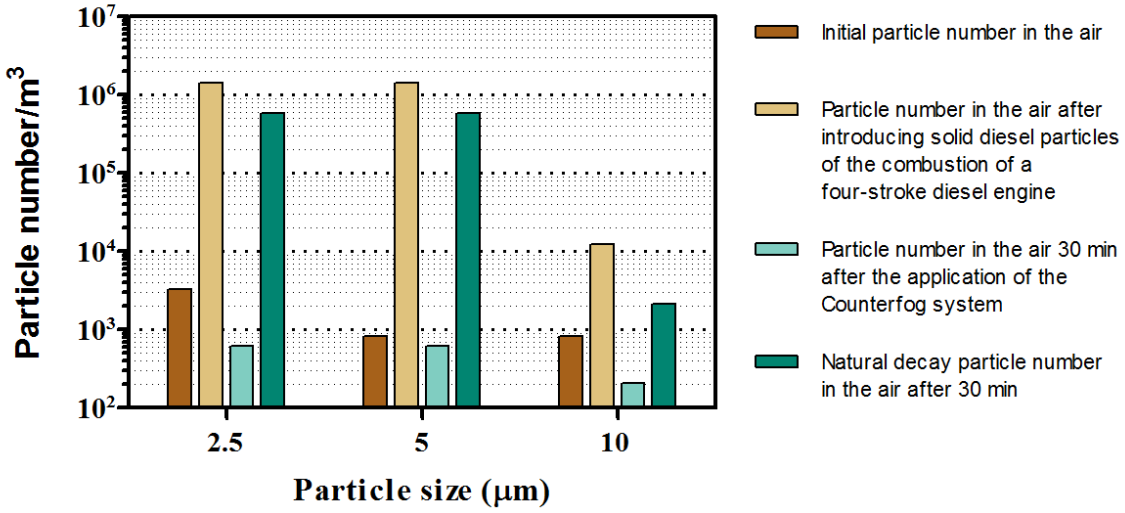

Figure 164: Number of particles per cubic meter of air for different particle sizes at different times of the diesel test.

After the test, samples with the water and the aggregated particles (Figure 165) deposited onto the floor were collected for analysis and characterization. Table 48 shows the particle reduction percentages for each size range 30 minutes after the introduction of the diesel combustion particles. The first column presents the results obtained in the case of application of the Counterfog® system, while the second column shows the percentage of reduction of these particles in the case of natural fall .

Figure 165: Residues deposited on the floor of the test room during the test.

Table 24: Percentage reduction of air-borne particles after 30 minutes.

PARTICLE SIZE	REDUCTION AFTER APPLICATION OF COUNTERFOG SYSTEM	NATURAL GRAVITATIONAL DECAY
2.5 µm	99.99 ± 1.10 %	10.80 ± 1.10 %
5.0 µm	99.96 ± 0.80 %	14.03 ± 0.80 %
10.0 µm	98.33 ± 0.40 %	75.22 ± 0.40 %

In Figure 165 is shown how the solid particles present in the air are deposited on the floor of the camera as a result of the fog. The dark grey colour of the residues gives the impression that these particles are hydrocarbon residues. This fact will be verified later by means of the analyses carried out on the samples taken. It is observed how the deposited solid particles tend to accumulate in certain regions of the surface and how the dimensions of the deposited residues are up to 40 cm allowing to assume the successful working of the Counterfog® system for this kind of situations. Figure 166 shows in detail some wastes analysed by SEM. The first three images correspond to images obtained by the secondary electron detector (SED) and have different magnification levels. These images allow to observe the topography of the sample, being able to observe agglomerates of particles of size superior to the 50 µm. The other three images were obtained by the method of detection of backscattered electrons (BSE). This method allows to observe the atomic weights of the different components of the sample, showing the elements in lighter colors the greater their weight.

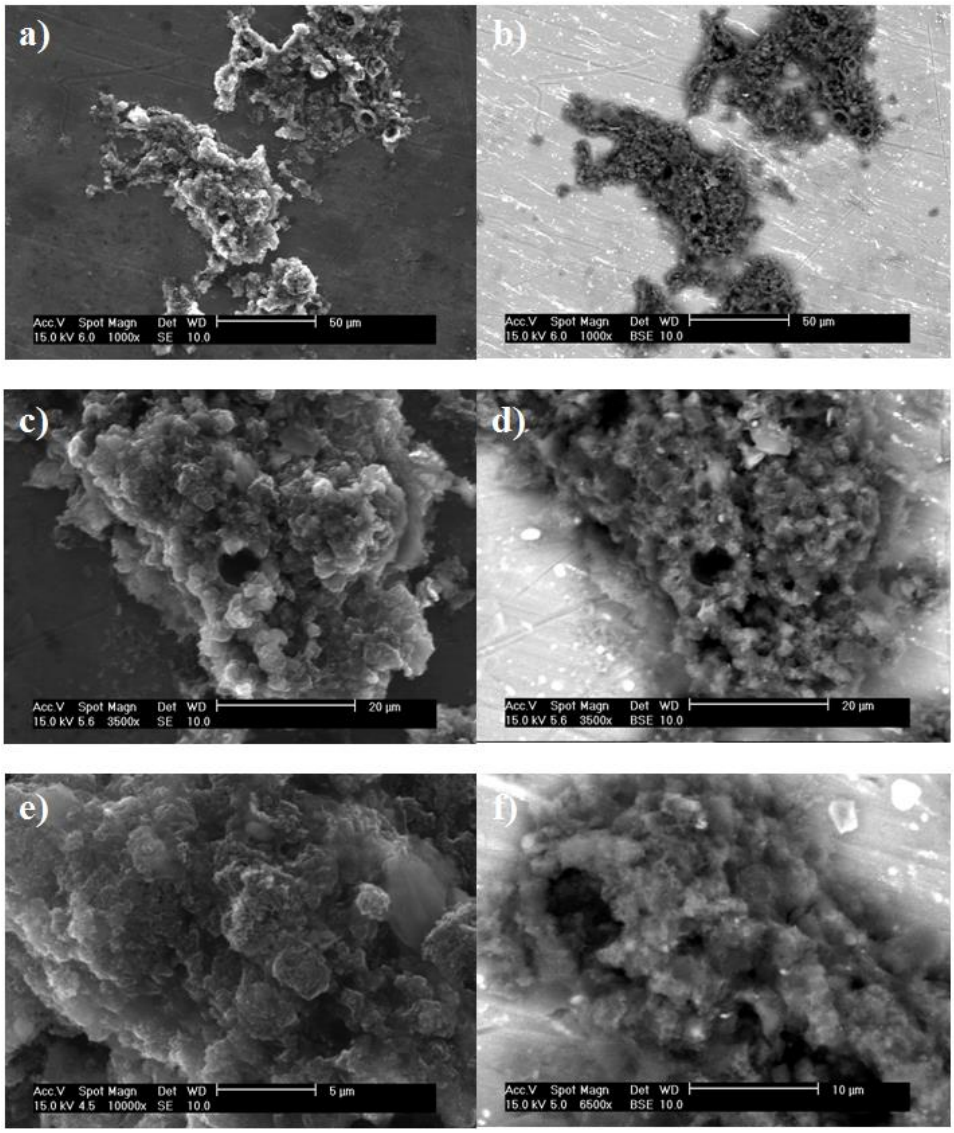

Figure 166: SEM images from the residues collected in water: (a) SED image taken at 1,000 magnifications; (b) SED image taken at 3,500 magnifications; (c) SED image taken at 10,000 magnifications; (d) BSE image taken at 1,000 magnifications; (e) BSE image taken at 3,500 magnifications; (f) BSE image taken at 6,500 magnifications.

The analysis performed with EDXA reveals that the main elements are carbon and oxygen (Table 25 and Figure 167), which corresponds to the expected composition of the diesel fuel combustion residue [Vogt et al., 2003; Wichmann, 2007].

Table 25: Semi-quantitative analysis of a sample with the residues obtained by EDXA.

ELEMENT	COMPOSITION	DEVIATION
C	67.9%	±6.14 %
O	20.105 %	±1.055 %
Si	3.945 %	±1.275 %
Fe	3.445 %	±2.035 %

ELEMENT	COMPOSITION	DEVIATION
Ca	1.735 %	±0.815 %
P	0.68 %	±0.25 %
Mg	0.63 %	±0.16 %
Na	0.565 %	±0.125 %
Cl	0.37 %	±0.16 %
S	0.34 %	±0.13 %
K	0.285 %	±0.135 %

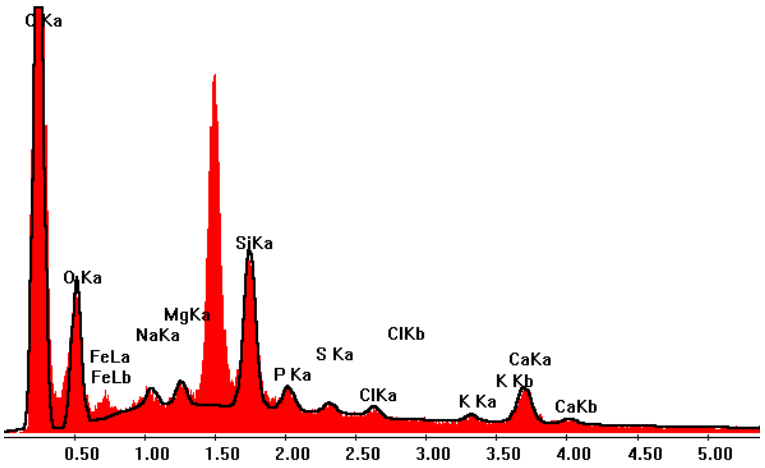

Figure 167: X-ray fluorescence lines detected in a sample analyzed by EDXA.

Nevertheless, the presence of a significant quantity of silicon what was not expected at the beginning of the study drove to a deeper study by SEM of the particles collected. In figure 5 some examples of these silicon particles are shown. As can be seen, those silicon particles confirmed by EDXA (Table 26 and Figure 168) are embedded in carbon agglomerations. Also, it is observed how the deposited particles are distributed in large agglomerations of more than 100 μm. On this occasion, the presence of numerous fibers of great length is observed and they are shown in detail in Figure 169.

Table 26: Semi-quantitative analysis of a sample with silicon residues obtained by EDXA.

ELEMENT	COMPOSITION	DEVIATION
O	36.47%	±4.56%
Si	31.995%	±4.935%
C	18.27%	±4.8%
Ca	5.07%	±1.63%
Cu	2.125%	±1.085%
Mg	1.61%	±0.13%
Zn	1.61%	±%0.84%
Al	1.305%	±0.175%
K	0.69%	±0.21%
Fe	0.6%	±0.28%

Cl	0.26%	±0.07%

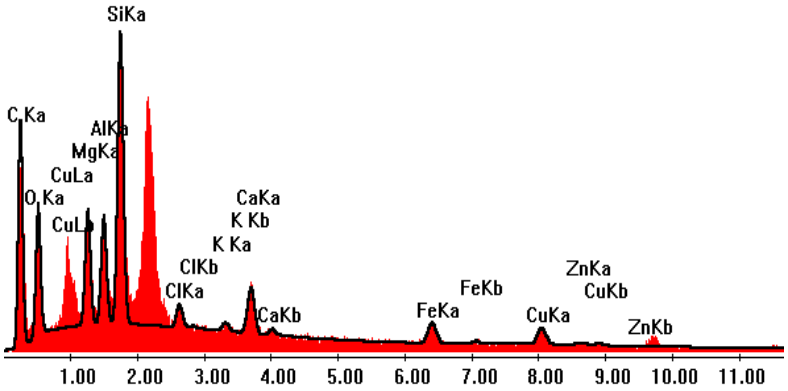

Figure 168: X-ray fluorescence lines detected in a sample with silicon residues analyzed by EDXA.

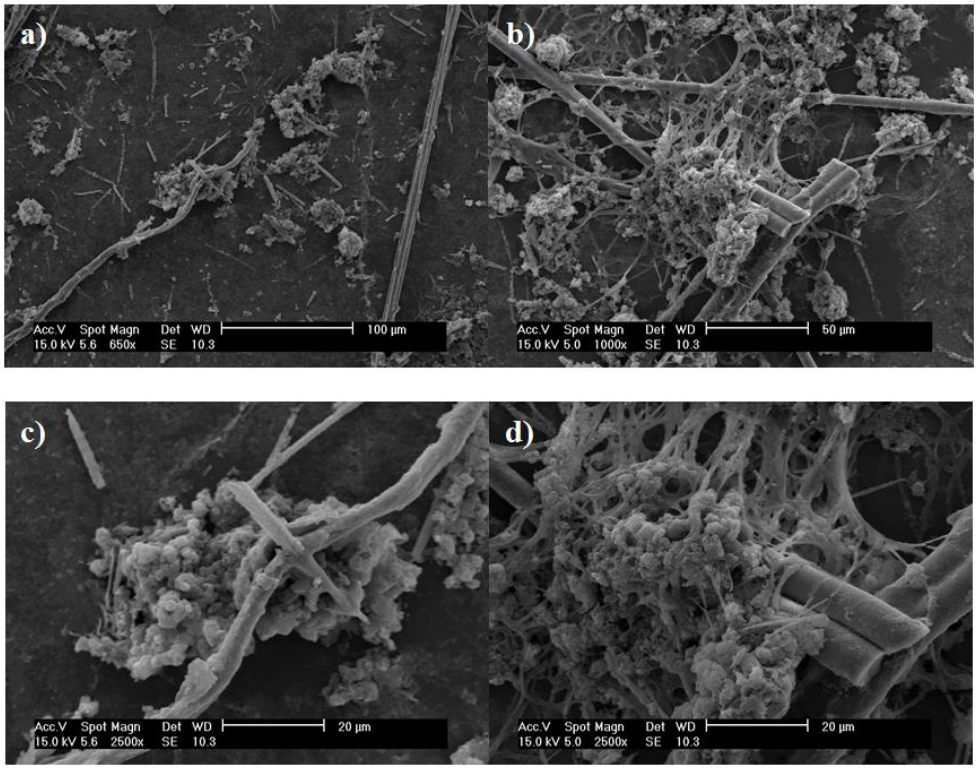

Figure 169: Images of examples of silicon residues deposited after the test takem by SEM: (a) SED image taken at 650 magnifications; (b) SED image taken at 1,000 magnifications; (c) SED image taken at 2,500 magnifications; (d) SED image taken at 2,500 magnifications.

In addition, an analysis of the particle size distribution of the different samples was performed using a laser diffraction particle size analyser as shown in Figure 170. The first graph shows the relative volumes for each particle size while the second graph shows the cumulative relative volume for each particle size.

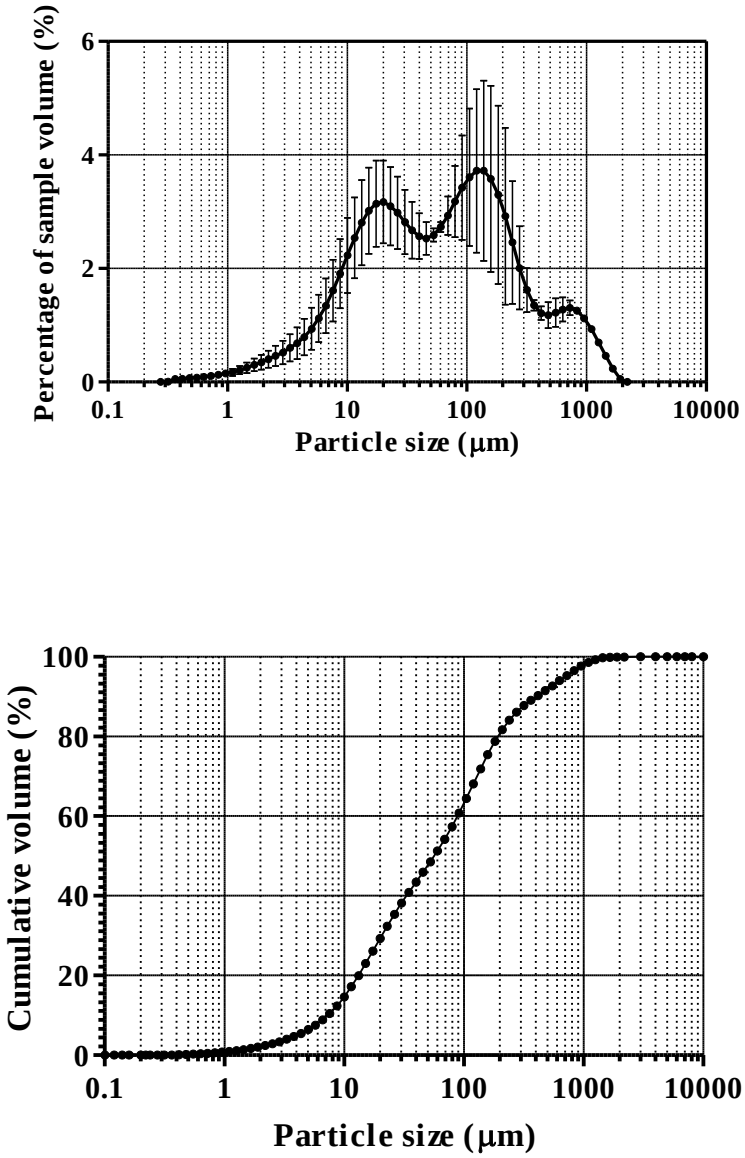

Figure 170: Sample analysis carried out by laser diffraction particle size analyser: (a) Mean and standard deviation distribution of relative volumes for each particle size. (b) Cumulative relative volume for each particle size.

Finally, the reduction percentages for each particle size 30 minutes after application of the Counterfog® system for each of the tests performed are shown in Table 27.

Table 27: Percentage of diesel particle reduction in each test after application of the **Counterfog®**. *system*

		PARTICLE SIZE (μm)		
		2.5	**5.0**	**10.0**
TEST	**I**	99.99% ± 1.1	99.96% ± 0.8	98.33% ± 0.4
	II	99,59% ± 1.1	99,49% ± 0.8	89,97% ± 0.4
	III	88,68% ± 1.1	91,00% ± 0.8	97,87% ± 0.4
	IV	98,96% ± 1.1	99,95% ± 0.8	88,75% ± 0.4
	V	94,86% ± 1.1	99,69% ± 0.8	99,99% ± 0.4
	VI	99,99% ± 1.1	98,62% ± 0.8	99,99% ± 0.4

6.4 Conclusions

- These silicon particles could be part of the diesel combustion residues or could be provided by the dust present in the atmosphere. The study of the composition of the commercial fuels shows that this silicon is not part of it. Further studies of the atmosphere should be done and they are now in process.

- Although the Figure 170.(a) trend is not a log-normal curve, it can be seen as the superposition of several log-normal curves. Three different peaks can be observed in all the samples analyzed. The first one is located between 5 μm and 20 μm what is confirmed by the SEM analysis shown above. The second and the third ones are located between 100 and 1000 μm. Although the particle size distribution is bigger than the described for emissions of Diesel engines by others authors [Bagley et al., 1998; Giechaskiel et al., 2009; Harris and Maricq, 2001], it can be explained by the fact that the emissions are not being measured but that the measurement is made on the basis of the waste collected. The particulate matter, in the removing process from the air by Counterfog®, tent to agglomerate in the water droplets generated in the fog and also in the pool that is generated after the activation of the system.

- The number of Diesel particles for 2.5, 5.0 and 10.0 μm decreases below the initial level after application of Counterfog®. This means that it washes out both the Diesel smoke particles as well as other particles that were already air-borne. The PM_{10} concentration of polluted air was 10,000 particles/m^3 approximately equivalent to 4.14μg/m^3 while the final concentration after actuation is of the order of 100 particles/m^3 which for PM_{10} corresponds to around 0.04 μg/m^3. That is, 4.10 μg/m3 have been removed from air.

- The results obtained (Table 27) indicate that the system allows to reduce the number of particles generated by the combustion of the Diesel in a percentage close to 100 % in the case of particles of sizes 2.5 μm, 5 μm and 10 μm diameter in a time not exceeding 30 minutes.

Chapter 7

Decontamination of biological agents from air by using the Counterfog® system

7.1 Introduction

Exposure to bioaerosols occurs through three routes: inhalation, dermal contact and ingestion, the first of which is the pathway that most frequently leads to adverse health effects [Ijaz et al., 2016]. Traditional methods of decontamination of biological agents use chemicals in a liquid or vaporized state. These methods have turned out to be highly toxic and carcinogenic [IARC, 2004]. Different tests with surrogates of biological agents have been carried out in the laboratory. The tests presented here make use of spores of *B. thurigiensis* CECT 4454 which is a surrogate of *B. anthracis* [Tufts et al., 2014].

7.2 Experimental setup and procedure

Before performing each test the different parameters of the test room shall be established to ensure that these factors will not affect the fog generation process. In this way, the temperature and relative humidity of the room were set at 25 ºC and 95%, respectively. The composition of the fluid for the generation of the fog was limited to water, not being added any kind of neutralizing compound. The temperature and humidity of the test room, as well as the flow of water used in the generation of fog were monitored at all times during each test.

The samples obtained were collected using a particle impactor (see section 3.3.1.4). In addition, laboratory equipment was specified (see section 3.2.2) during the tests. A video camera recorded everything that happened inside the test room.

Tests will be performed with the B1: 2 nozzle model. The temperature of the shooting water will be 12 º C, while the pressures of air and water will be 12 bar and 8 bar, respectively.

Biological agents are dispersed in the test room by a gavity spray gun (Figure 171). This has the advantage of being able to control the flow rate and air pressure as well as the opening cone for dust dispersion. The air pressure selected for the dispersion of these biological agents is 2 bar. The surrogate chosen is *B. thurigiensis* CECT 4454 and its density of spores in suspension will be 0.3 U of McFarland scale and serially diluted 10^{-2} in a volume of 20 ml.

.

Figure 171: Gravity spray gun used during biological tests.

The obtaining of the spores as well as the treatment and counting of the samples obtained after carrying out the tests is execute in the laboratories of the Faculty of Pharmacy of the University of Alcalá and they are accomplished by the staff of the Counterfog® project specialized in biological issues.

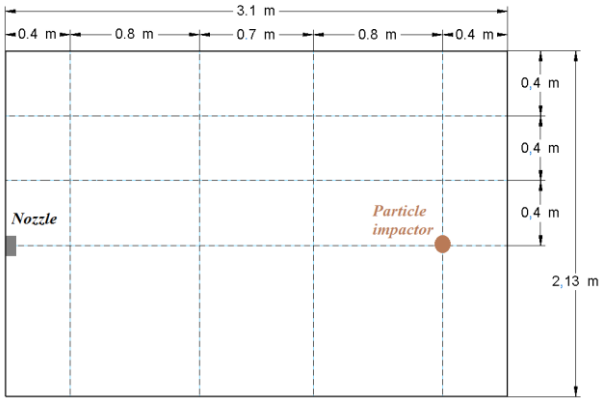

Figure 172: Position of the particle impactor in the test room during the biolocical tests.

Once the set of factors to be taken into account during the tests has been defined, the working procedure used to carry out the tests is explained in detail. Each test begins by ensuring the correct maintenance and cleaning of the different elements of the laboratory (see section 3.2.2), as well as the correct initial position of the pneumatic and manual ball valves. Then it is checked that the pressurized air tank is fully charged and that the pressurized water tank is empty. On the one hand, in the case of the pressurized air tank, it is checked that it is at a pressure of between 26 and 29 bar, as this is the maximum range provided by the compressor. This allows to guarantee that the pressures that are subsequently imposed for fog generation are met. If this is not the case, the compressor will start up autonomously until it stops once the pressure range in the pressurized air tank defined above has been reached. On the other hand, to check the pressurized water tank, the purge valve is opened to release any remaining pressure inside due to previous tests. The ball valve is then opened to allow the tank to drain by gravity. Once completely empty, the purge and drain valves are closed. The next step is to check that the atmospheric water tank is full and if necessary fill it with the hose connected to the water inlet. In addition, a pH test and temperature measurement is performed to ensure that the composition and temperature of the water used is the same for the entire test set. After completing the above steps the pressurized water tank is filled with water from the atmospheric water tank. To do this, the purge and fill valves are opened and the pump is activated to allow the pressurized water tank to fill to its maximum level (4.5 l). This maximum level is guaranteed by a sensor and an actuator that stops the pump once it has been reached. Once this process is completed the pump is switched off and the purge and fill valves are closed. Once this is done, the ball valves installed inside the test room for the air and water outlet are closed and the water shooting pressures adjusted. In the case of air, and since the tests are carried out without the application of air, the air valve will remain closed at all times. The air outlet ball valve opens to release any remaining pressure in the ducts to the nozzle. In the case of water, the water pressure valve is opened to allow pressurized air to flow from the pressurized air tank to the pressurized water tanks through the water circuit. The shooting water pressure is adjusted by means of a manual control valve and a pressure manometer located at the same point. Once correctly adjusted, the water outlet ball valve is opened to release the remaining pressure and to remove the residual water contained in the pipes leading to the nozzle. The air and water outlet ball valves will remain open until the next shot is fired. The gravity spray gun, which will be shot manually from the adjacent test room, is also adjusted to its set pressure and cone opening.The next step is a short shot (approximately 8 seconds) to fill

the water pipes of the water circuit with water without exhausting the pressurized water tank by opening the water valves. In this way, it will be able to ensure that during the test the fog begins to be generated almost instantaneously without a significant delay from the opening of the shooting valves (air and water valves). This is of great importance due to the short test shooting times and the delays observed in fog generation of up to 5 seconds when the water circuit is empty. The water and water pressure valves are closed once the shot is finished and the computer in the Control Room is used to check that the water shooting pressure obtained matches with that established in the settings. Once this process has been completed, it is repeated from the beginning to leave the system ready to perform the test shot. At this point, the different surfaces of the test room are covered (Figure 173) to avoid any possible spores escaping to the outside of the laboratory and to easily eliminate any type of residue generated during the test at the end of it. In addition, since the door between the rooms remains open in order to disperse the spores from the other test room, the gap between the two rooms is completely covered, with a small opening through which the spray gun is introduced . This opening has a cover that allows it to be completely closed and opened at the discretion of the laboratory staff. This opening is also used to introduce and remove the particle impactor for the change of the petri dishes that are necessary to introduce for the measurements. Afer that, the test rooms is closed and completely insulated and the air inside it is renewed by activating the corresponding ventilation and air filtration system for 10 minutes.

Figure 173: Surface coverage and preparation of the test room for the biological tests.

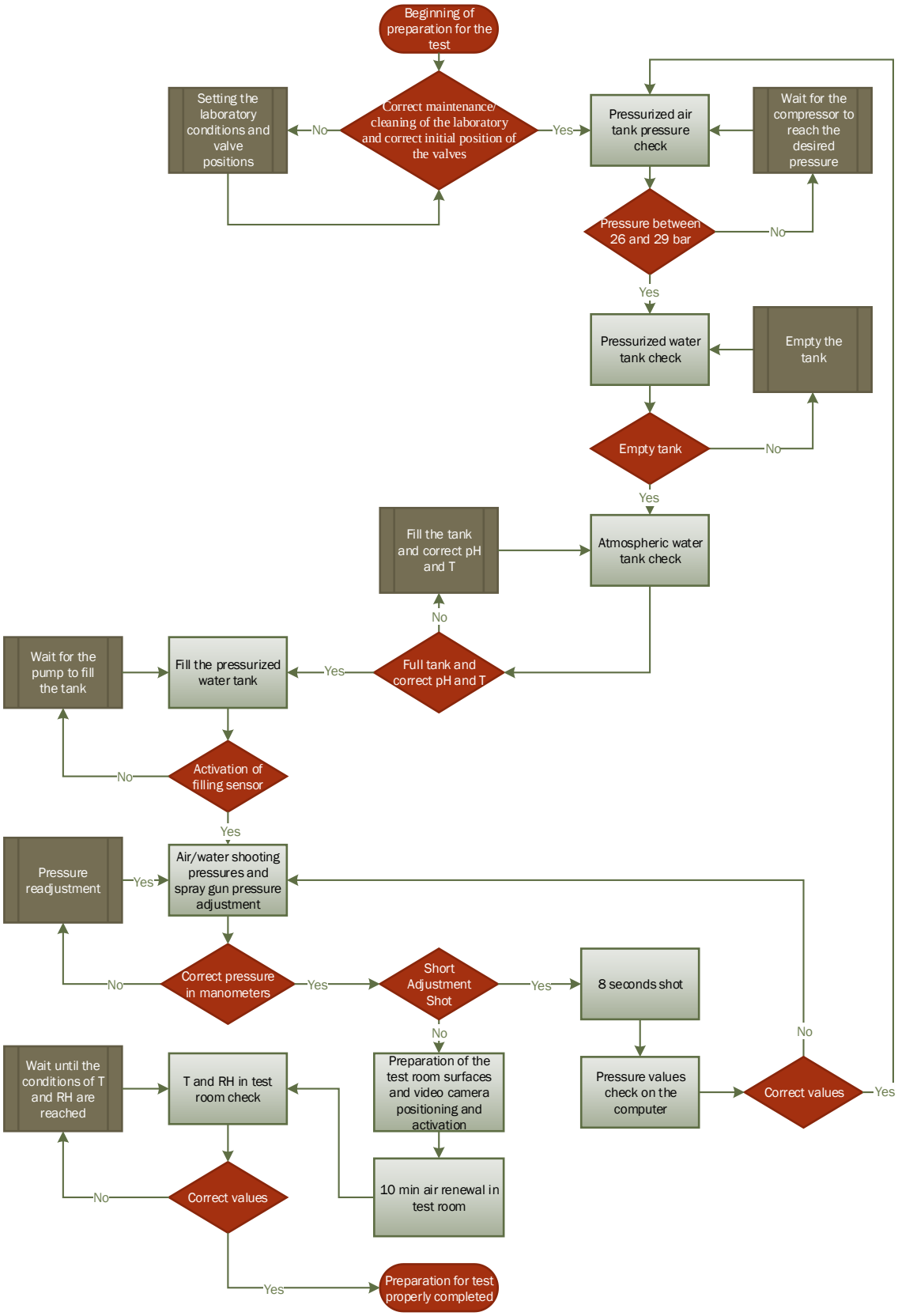

Figure 174: Diagram of the room preparation procedure for biological tests for nozzle B1:2.

Finally, it is checked that the temperature of the room corresponds to that stipulated for the tests. In the same way, it is verified that the relative humidity in the room is also the desired one. It should be noted that this process is carried out automatically by the control system installed in the Control Room where the desired conditions to be provided by the heat pump and the chiller have been previously defined, thus guaranteeing compliance. The video camera will have been placed and activated inside the room immediately prior to the closure of the test room. Figure 174 shows a diagram summarizing the test room setup process. Once the humidity and temperature conditions in the room have been reached, the suspension of spores is released in the air of the test room and after 2 min of the releasing the Counterfog® system is activated during 30 s in different assays. At different times since the dispersion of spores (1, 3, 7, 10, 15 and 20 min) a sample of 50 l of air is taken by the particle impactor. In addition, natural spore decay tests are also carried out, i.e. without the application of fog on which different 50 l air samples are taken by the particle impactor at different times (1, 3, 7, 10, 15, 20, 30, 40, 50 and 60 min). After this time, the test is considered complete and the room is properly disinfected to ensure that no spores escape to the outside. Then the room is opened and the video camera is turned off. At the end of the test, the initial temperature and humidity data, as well as the shooting pressure data, are checked to ensure compliance with the test conditions. In addition, test videos are reviewed to ensure that no irregularities occur during testing. Once it is verified that everything has happened as stipulated, the test is taken as correct. Otherwise, the test is automatically discarded and repeated. Figure 176 shows a diagram summarizing the test process. The Petri dishes obtained are incubated and counted in the laboratories of the Faculty of Pharmacy of the University of Alcalá by the staff of the Counterfog® project specialized in biological issues.

Figure 175: Safety equipment for laboratory staff during biological tests.

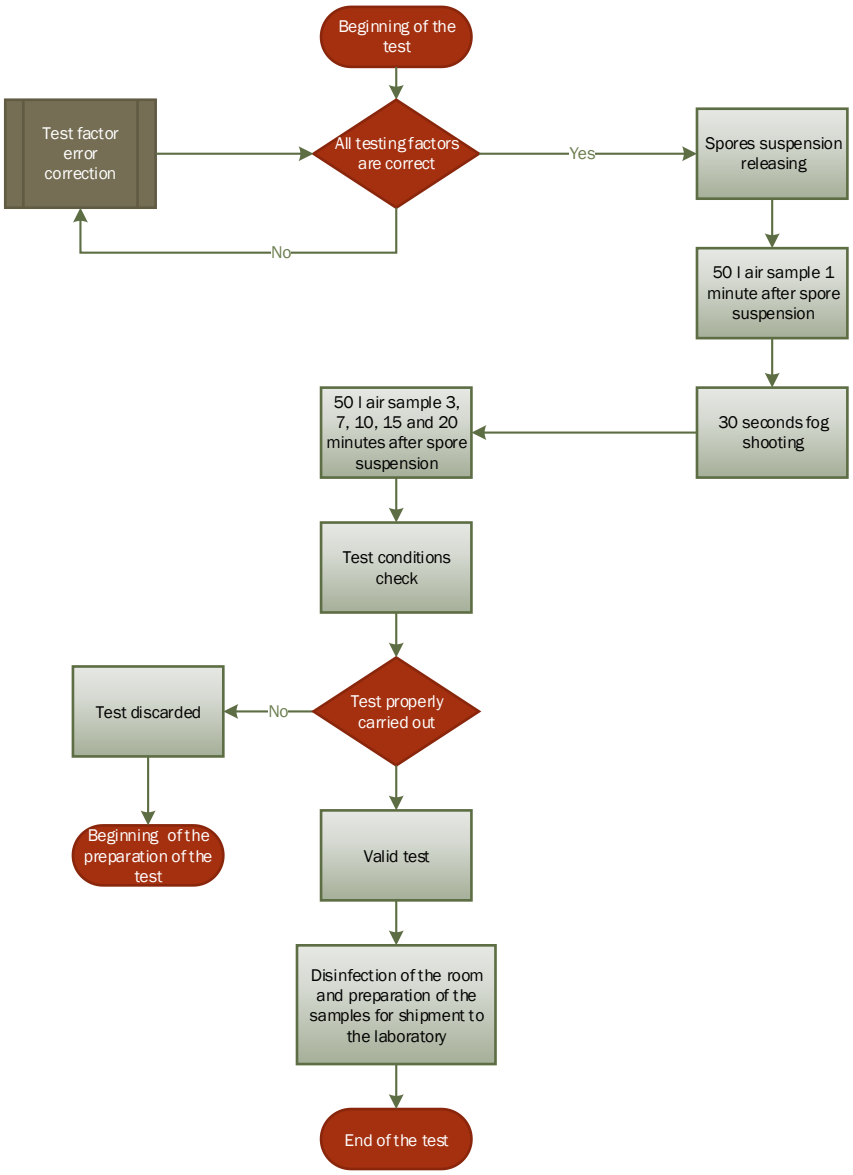

Figure 176: Diagram of the test procedure for biological tests for nozzle B1:2.

The tests are carried out with the relevant materials and safety measures that guarantee both the safety of the personnel and the non-contamination of the evidence obtained (Figure 175).

7.3 Experimental results and Discussion

To calculate the efficacy of the air contamination and decon-tamination, the number of viable spores counted in each time was compared with the number of viable spores extracted immediately after the releasing of the spores. In order to know the natural

reduc-tion of the spores in the air, the log reduction was calculated using the following equation:

$$Log\ Reduction\ =\ log\ (N/N')$$

where *N* is the mean number of viable organisms recovered from the samples at different times or samples subjected to Counterfog® system, and *N'* is the number of viable organisms recovered immediately after the dispersion of the spores or before decontamination. For plates where viable organisms were not detected, the efficacy was calculated as the log of the mean number of viable organisms recovered from the plates took before the decontamination. Using the calculated log reduction for each test, the mean (±*SD*) log reduction was calculated. Also, the reduction percentage was calculated for each of the samples by comparing the number of colonies in the first sample with the number of colonies in the rest of the samples.
Table 28 shows the results obtained in the tests in which the Counterfog® system has not been applied. Figure 177 shows in images the temporal evolution of the spores in the air of the room.

Table 28: Contamination efficacy of Bacillus thurigiensis spores in the air in biological tests without fog application. Values are expressed as mean ± SD from triplicates of three different experiments.

	Time of sampling after the release of the spores (min)	**Total of spores recovered without fog (CFU/m^3)**	**Log reduction**	**% Reduction**
Sample 1	1	3.56E+03 ± 1.47E+03	NA	NA
Sample 2	3	3.81E+03 ± 1.65E+03	-0.030	-7.12
Sample 3	7	2.83E+03 ± 1.35E+03	0.100	20.60
Sample 4	10	2.23E+03 ± 9.09E+02	0.202	37.27
Sample 5	15	1.63E+03 ± 8.93E+02	0.338	54.12
Sample 6	20	1.33E+03 ± 5.46E+02	0.426	62.55
Sample 7	30	9.73E+02 ± 6.29E+02	0.563	72.66
Sample 8	40	6.00E+02 ± 2.99E+02	0.773	83.15
Sample 9	50	4.93E+02 ± 3.03E+02	0.858	86.14
Sample 10	60	3.87E+02 ± 2.08E+02	0.964	89.14

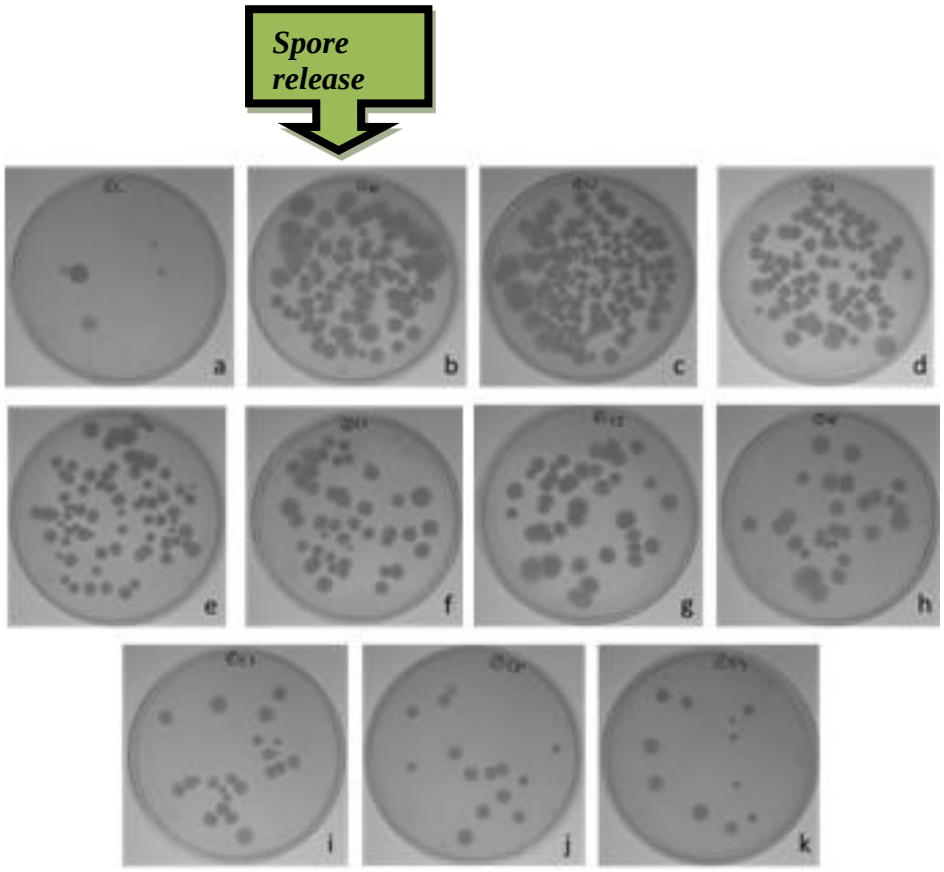

Figure 177: Impact air sampler plates obtained from the air of the room where the spores have been disseminated with the gravity spray gun in a biological test without fog application: **a)** Control; **b)** Sample 1: taken 1 min after the releasing of spores; **c)** Sample 2: taken 3 min after the releasing of spores; **d)** Sample 3: taken 7 min after the releasing of spores; **e)** Sample 4: taken 10 min after the releasing of spores; **f)** Sample 5: taken 15 min after the releasing of spores; **g)** Sample 6: taken 20 min after the releasing of spores; **h)** Sample 7: taken 30 min after the releasing of spores; **i)** Sample 8: taken 40 min after the releasing of spores; **j)** Sample 9: taken 50 min after the releasing of spores and **k)** Sample 10: taken 60 min after the releasing of spores.

Table 29 shows the results obtained in the tests in which the Counterfog® system has not been applied. Figure 178 shows in images the temporal evolution of the spores in the air of the room.

Table 29: Contamination efficacy of Bacillus thurigiensis spores in the air in biological tests with fog application. Values are expressed as mean ± SD from triplicates of three different experiments.

	Time of sampling after the release of the spores (min)	**Total of spores recovered with 30 s of fog (CFU/m^3)**	**Log reduction with 30 s of fog**	**% Reduction with 30 s of fog**
Sample 1	1	8.67E+03 ± 6.13E+03	NA	NA
Sample 2	3	3.07E+02 ± 2.17E+02	1.451	96.46
Sample 3	7	1.33E+02 ± 9.40E+01	1.814	98.47

Sample 4	10	9.33E+01 ± 6.60E+01	1.968	98.92
Sample 5	15	8.00E+01 ± 5.66E+01	2.035	99.08
Sample 6	20	6.67E+01 ± 4.72E+01	2.114	99.23

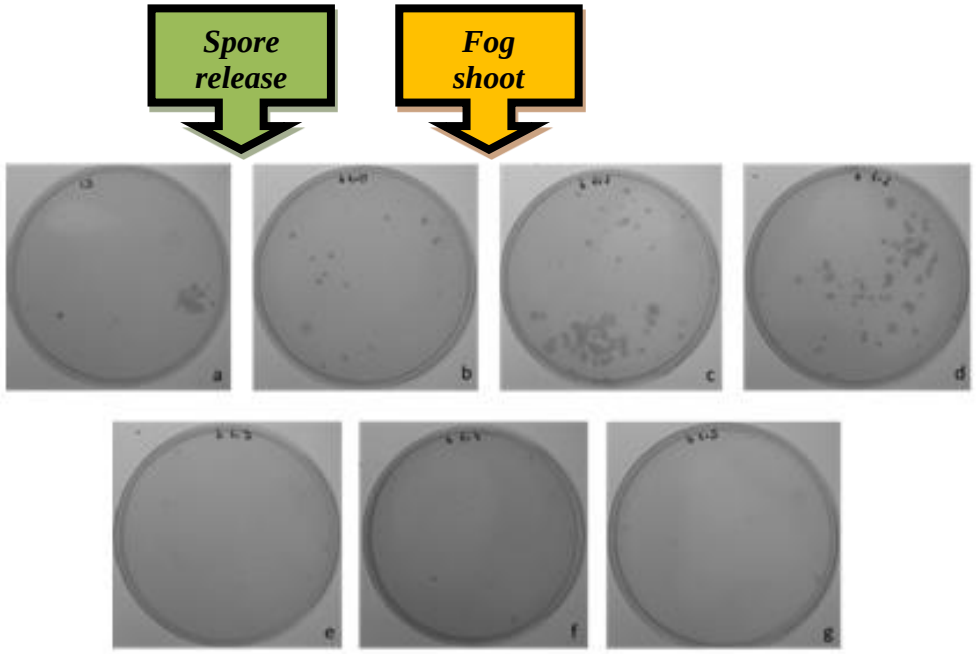

Figure 178: Impact air sampler plates obtained from the air of the room where the spores have been disseminated with the gravity spray gun in a biological test with fog application: **a)** Control; **b)** Sample 1: taken 1 min after the releasing of spores; **c)** Sample 2: taken 3 min after the releasing of spores; **d)** Sample 3: taken 7 min after the releasing of spores; **e)** Sample 4: taken 10 min after the releasing of spores; **f)** Sample 5: taken 15 min after the releasing of spores and **g)** Sample 6: taken 20 min after the releasing of spores.

Figure 179 graphically shows the time comparison of the number of spores recovered during sampling for the two types of tests performed, i.e., those in which the Counterfog® system was applied and those in which it was not.

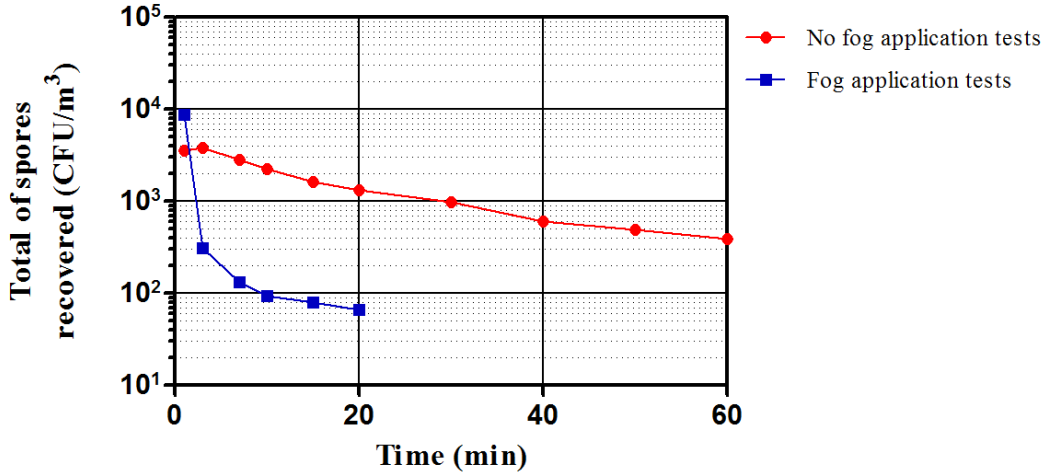

Figure 179: Mean of total of spores recovered over time for biological test with without Counterfog® system application

Similarly, **Figure 180** shows the percentages of reduction of test types in their evolution over time.

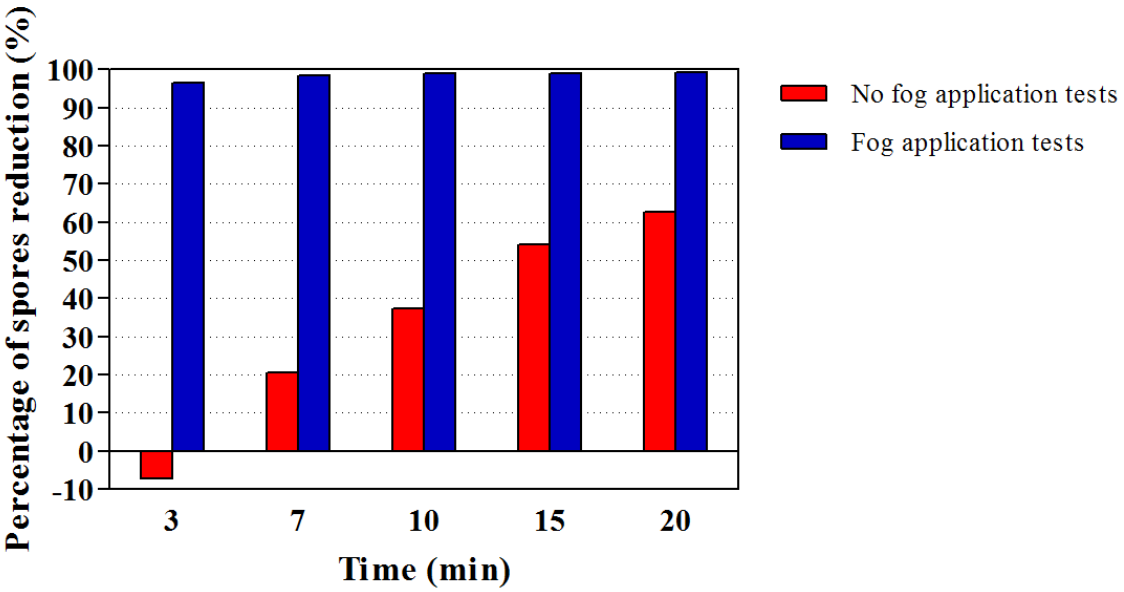

Figure 180: Reduction percentage of total of spores recovered over time for biological test with and without Counterfog® system application.

7.4 Conclusions

- The number of spores collected in the case of non-application of fog is higher than the value obtained when the system has been applied, even though the initial number dispersed in the room is higher in the second case.

- 20 minutes after the spores have been dispersed, the number obtained in the case of non-application of fog is two orders of magnitude higher than the value obtained in the case of application of the Counterfog® system.

- After one hour of measurements, the spore values obtained in the case of non-application of fog are still one order of magnitude higher than those obtained in the case of application of the Counterfog® system 20 minutes after spore dispersion.

- The spore reduction percentages after mist application reach values above 90% within just a few minutes of fog application, reaching almost 100% spore reduction values in less than 10 minutes. However, even after 20 minutes from spore dispersion, reduction rates of less than 65% are obtained when the Counetrfog system is not applied.

Chapter 8

Decontamination of chemical agents from air by using the Counterfog® system

8.1 Introduction

This chapter presents the study conducted for assessing the effectiveness of the Counterfog® system to counteract the effects of a potential dispersion of chemical warfare agents (CWA). The aim of the work was to achieve a complete decontamination of the scenario, combining in the same process a physical decontamination and a chemical decontamination through the use of fog and nanomaterials (NMs): TiO2 and TiO2-Al2O3.

To achieve these objectives a comprehensive experimental procedure was developed. This research includes a physicochemical characterization of the nanomaterials tested in order to evaluate the interaction of NMs and CWA surrogates selected and of these with fog.

Health hazards can be avoided by decontamination of Chemical Warfare Agent (CWA). Literature classifies decontamination of CWA by mechanical, physical, and chemical methods. Dilution, washing operations, adsorption procedures, evaporation,

reverse-osmosis and ultra-filtration come under physical decontamination methods. Chemical decontamination includes reactive compounds which take part in either hydrolysis or elimination or oxidation reactions with enhanced rates to neutralize these completely into non-toxic products.

The currently fielded chemical decontamination methods use compounds that cause corrosion to metal surfaces after prolonged contact and soften, removes paint. Owing to this reason, a need exists for developing a versatile CWA decontamination solution which is non-corrosive, non-toxic, non-flammable, and environmentally safe.

Recently, it has been found that nanosized metal oxides of MgO, Al_2O_3, TiO_2 (among others) are capable of performing both physical decontamination owing to their high specific surface area and/or chemical decontamination due to its potential reactivity (i.e., site density) toward warfare agents.

8.2 Experimental setup and procedure

In order to define the set-up parameters and conditions to perform the experiments and assess the ability of the proposed design, the following steps were established:

- Assessment and selection of surrogate materials (i.e. simulating chemical agents) to be used in the experiments
- Physicochemical characterization of solid additives (NMS): Specific surface area, particle size distribution, chemical composition and site density.
- Establishment of a procedure to disperse "homogeneously" the selected surrogates in the experimental area.
- Measure of Surrogates Time Of Flight (TOF) as a key parameter for determining the system efficiency on cleaning the dispersed NMs.
- Study of parameters and variables that should have any influence on fog - surrogate interaction. The neutralization/cleaning capacity of the fog will depend to a great extent on the interaction surface between the fog droplets and the agent. It is expected that any amendment increasing the extent of the contact surface between both would result in an improvement of the results.

8.2.1 Assesment, selection and dispersion of the surrogates

Due to the toxicity and restrictions to the use of CWA, to analyse their behaviour the so-called "surrogates, simulants or mimics" are used. The expectation is that, if a surrogate resembles an agent in molecular structure or physicochemical properties then the simulant's performance may offer guidance for handling the CWA. In this way, an ideal surrogate agent would mimic all relevant chemical and physical properties of the agent without its associated toxicological properties. Although a number of compounds have been used as CWA surrogates, no individual compound is ideal because a single simulant cannot satisfactorily represent all environmental fate properties of a given CWA. Thus, a number of different chemicals have been used as CWA simulants depending on the

physical-chemical property of interest, such as, hydrolysis, sorption, bioavailability and volatilization.

In the context of the Counterfog® project, the selection of chemical surrogates was done by experts in the Advisory Board, the Defence Ministry of Spain and the consortium itself according to the proposed objectives.

Sets of agents were selected as the most important and their corresponding surrogates usually accepted in North Atlantic Treaty Organization (NATO) (Table 30).

Table 30: Physicochemical properties of CWA and its potential surrogates

Agent Name	Abbrev.	Molecular Weight (g/mol)	KHº	Boiling Point (ºC)	Pv (mm Hg)	S (mg/l)
Taburn (C5H5N2O2P)	**GA**	**162**	**6.5×10^{-7}**	**248**	**0.057**	**7.2×10^{4}**
Sarin (C4H10FO2P)	**GB**	**140**	**3.8×10^{-4}**	**158**	**2.1**	**1.0×10^{6}**
Soman (C7H16FO2P)	**GC**	**182**	**1.9×10^{-4}**	**198**	**0.4**	**2.1×10^{4}**
Diisopropyl methylphosphonate	DIMP	180	1.8×10^{-3}	121	0.277	1.5×10^{3}
Dimethyl methylphosphonate	DMMP	124	5.3×10^{-5}	181	0.96	1.0×10^{6}
Dypropyleneglycol monomethyl ether	**DPGME**	**148**	**4.7×10^{-8}**	**188**	**0.55**	**1.0×10^{6}**
Disiopropyl fluorophosphates	DFP	184	5.3	183	0.58	1.5×10^{4}
Triethyl Phosphate	**TEP**	**182**	**6.1×10^{-5}**	**215**	**0.39**	**5×10^{5}**
Sulfurd Mustard (C4H8Cl2S)	**HD**	**159**	**9.8×10^{-4}**	**218**	**0.11**	**684**
2-chloroethyl ehtyl sulfide	CEES	125	1.5×10^{-2}	157	3.4	1,062
2-chloroethyl phenyl sulfide	CEPS	173	3.0×10^{-3}	257	1.9×10^{-2}	84
Methyl 2-hydroxybenzoate	MS	152	4.0×10^{-3}	223	0.04	700
VX (C11H26NO2PS)	VX	267	1.4×10^{-7}	292	7×10^{-4}	3×10^{4}
o,o-dimethyl phosphorodithioate	Malathion	330	2.0×10^{-7}	156	3.4×10^{-6}	143
o,o-diethyl-o,p-nitrophenyl thiophosphate	Parathion	291	$1.8\text{x}10^{-5}$	375	6.7	11

Since the group of G-Agents comprises several compounds with different physicochemical characteristics, to perform the study two surrogates were selected: Triethyl phosphate (TEP) having a core molecular structure similar to these agents with the P-O functional group and Dypropyleneglycol monomethyl ether (DPGME) whose physical parameters allows to cover the range of boiling point, KH and solubility.

Finally, according to the hydrolysis, it could be evaluated the hydrolysis reaction of G-agents. There are a lot of potential simulants for Taburn (GA), Sarin (GB) and Soman (GD) that have similar molecular structures including TEP.

Regarding Distilled Mustard (HD), Methyl 2-hydroxybenzoate or Methyl Salicylate (MS) has boiling point, KH and solubility very close to the target compound. Although the chemical functionality (sulphur-ethyl-chlorine) of the other two surrogates, 2-chloroethyl phenyl sulphide (CEPS) and 2-chloroethyl ethyl sulphide (CEES) is similar to mustard gas, its high toxicity did not permit their use during tests. MS and HD show similar skin absorption characteristics.

The method of dispersion established was the generation of the vapour. To do this, the same basic protocol was used for all experiments with minimal noted procedural differences. Before the start of experiment the Counterfog®-Lab was closed and its walls and ceiling were heated until 25 ºC to prevent condensation of vapours on them.

The surrogates were evaporated by means of porcelain capsule located onto a hotplate (180 - 240 °C) at 1.2 m height in the centre of the laboratory. The evaporation device was placed in height because vapours of studied compounds are denser than air (relative density MS: 5.24, TEP: 6.28, DPGME: 5.14), so that once generated these will tend to fall to the ground. 5-10 ml of product was evaporated in each experiment. According to tests done prior to the experiment, after 10 min of heating the product evaporated.

8.2.2 Characterization of the nanomaterials

Another option to liquid decontamination media is the use of nanomaterials (NMs). Due to large surface area, NMs have enhanced capacity to strongly adsorb CWA. Once trapped in pores of sorbent, their drag by fog increasing the efficiency and accelerates the time necessary to remove the agent from the atmosphere. Moreover, CWA trapped in MNs undergo reactions, facilitated by reactive sites integrated in NMs, which could neutralize hazardous properties rendering the agent non-toxic.

Due to their high surface area, large number of highly reactive edges, corner defects sites, unusual lattice planes and high surface to volume ratio, nanocrystalline metal oxides possess enhanced reactive properties towards CWA. Thus NMs of metal oxides (Al_2O3, TiO_2) will be used for decontamination tests.

As mentioned above, the properties of nanomaterials depend largely on its surface area, which in turn determines the number of active sites and the interactions with other substances. Surface area is related to particle size, particle morphology and porosity. So, in order to assess the possible interactions of NMs and CWA surrogates, these parameters in the samples used for tests were studied.

Since the methodology to be applied contemplates the use of nanomaterials and fog, another point to consider is the interaction of dispersed nanomaterials with the fog and its ability to deposit them. For this purpose two set of experiments were performed for dispersing:

- The particulate material alone and following their evolution in the Lab atmosphere over a period of time
- The nanomaterial and a few minutes later shooting the fog observing the evolution of the material in these conditions.

To carry out these studies the number of particles in the lab was monitored by means a particle counter (see section 3.2.2).

8.2.3 Procedure details

The overall process implies the dispersion of surrogates, the dispersion of nanomaterials and the fog generation for dragging the nanomaterials with the adsorbed surrogates or sub products generated. The sampling procedure was planned according to the next diagram (Figure 181):

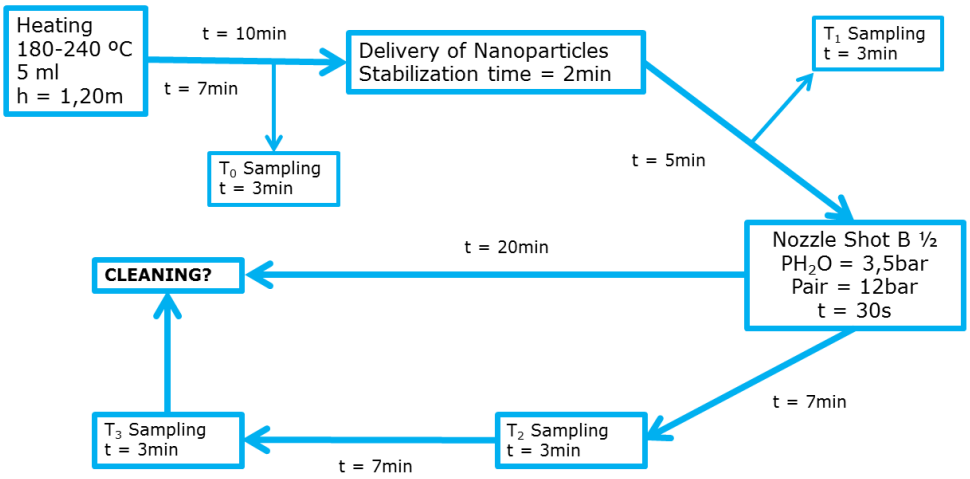

Figure 181: Sampling process decontamination test.

To perform the tests, 5 ml of the chemical surrogate sample (MS, DPGME and TEP) were heated on a hotplate and allowed the time needed for it to diffuse into the atmosphere of the test room. After a lapse of 7 min, the first sampling ($\mathbf{T_0}$) was taken using the extraction pump located outside the test room, which bubbled gas into a vessel containing ethanol. Then a balloon containing 2 g of nanoparticles was burst and allowed to elapse a time of 2 min so the cloud of nanomaterial created was stabilized. Then, a sampling was taken, also in a vessel containing ethanol, to monitor how nanoparticles behave against chemical and whether there was any neutralization of molecules ($\mathbf{T_1}$). Once the nanoparticles are stabilized, after 5 min, a fog, containing 1% diluted isopropanol was shot during 30 seconds. 2 more sampling at intervals of 10 min ($\mathbf{T_2}$ and $\mathbf{T_3}$) were taken.

The sampling system used during the tests was the uptake of the simulator in suitable solvent by means of a bubbler as it allows the analysis of the sample without pre-treatment.

8.3 Experimental results and Discussion

8.3.1 Interaction between fog and nanomaterials

In order to explore and quantify the interaction between fog and nanomaterial, a set-up of trials was performed for this study. The experiment procedure consists on dispersing only the nanomaterial in the following way: a balloon containing ≈ 2 g of nanomaterial (TiO_2 or TiO_2-Al_2O_3) was burst with a 2 bar air pressure line and the evolution of particle dispersion in air was monitored.

The tests were repeated at least 5 times for each compound in order to have an experimental confidence in the results presented in this paragraph.

Representative results for each one of the tested nanomaterial are shown below (**Figure** 182 and Figure 183) for discussion.

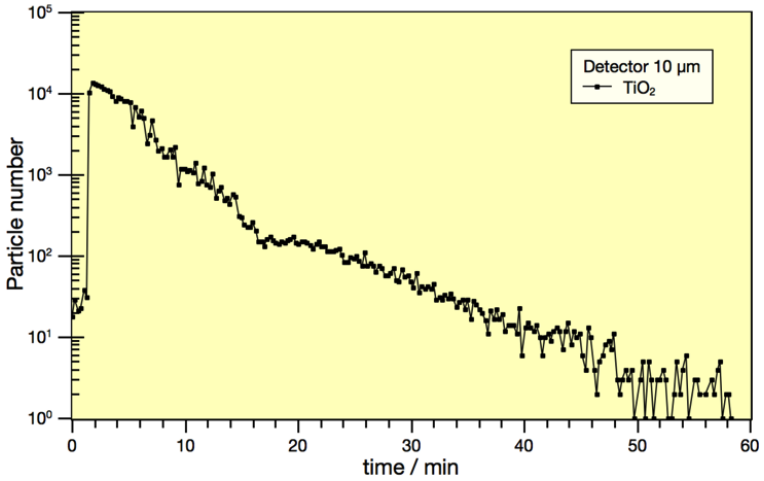

Figure 182: Evolution in time of TiO2 nanoparticles suspended on atmosphere.

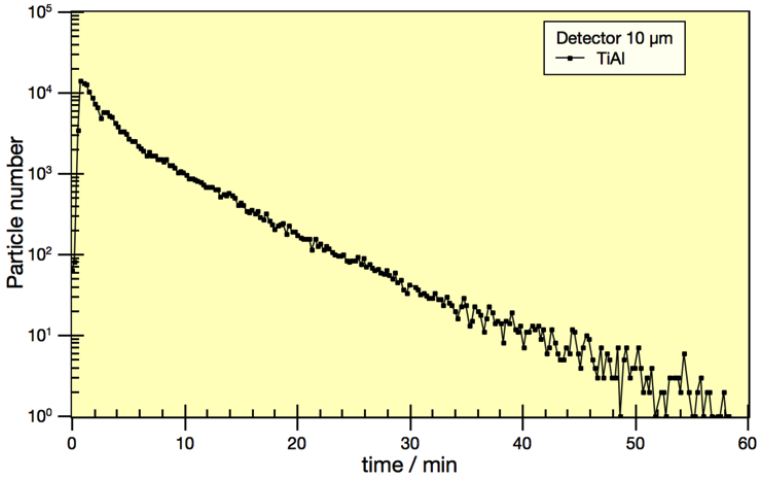

Figure 183: Evolution in time of TiO2-Al2O3 nanoparticles suspended on atmosphere.

Since the overall process of decontamination implies the use of a fog for dragging the nanomaterials with the adsorbed surrogates, it is necessary to determine the ability of

the fog (nozzle B1:2 to 4 bar water and 12 bar air) to drag the particulate metal oxides. So, the tests were repeated with the same nanoparticles but shooting the fog after 2 min having dispersed the nanomaterial. The same monitoring as in the previous case was carried out to thereby determine the number of particles that remain suspended in function of time and check the effect of fog (Figure 184 and **Figure** 185). The addition of 1 % isopropanol as an additive has been used in the actual experiments.

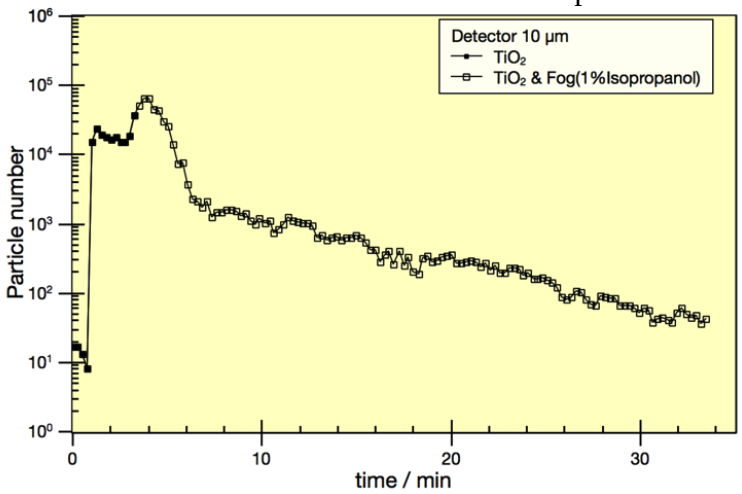

Figure 184 : Interaction between TiO_2 nanomaterial - fine droplet fog (P_{water} = 3.5 bar, P_{air} = 12 bar; 1 % isopropanol for B 1:2 nozzle).

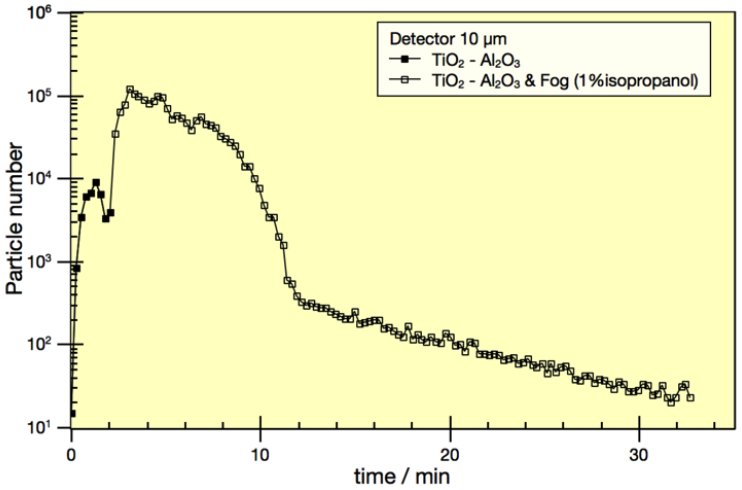

Figure 185: Interaction between TiO_2 - Al_2O_3 nanomaterial - fine droplet fog (P_{water} = 3.5 bar, P_{air} = 12 bar; 1 % isopropanol for B 1:2 nozzle).

As can be observed, nanoparticles remain long time suspended on the laboratory atmosphere, but as soon as the fog is dispersed in the Lab, the concentration decreases really faster. In this sense, the mixture of oxides (TiO_2 -Al_2O_3) shows the quickest interaction. This may be due to several factors among which the differences properties of the nanomaterials (i.e., specific surface area, roughness, particle size distribution, site density, increased polarity, etc.), which facilitates interaction with fog and chemical agent.

8.3.2 MS quantification

In Figure 186 and Figure 187 can be observed the evolution of the concentration of salicylate along the experiment for each nanomaterial tested (TiO_2 and TiO_2 - Al_2O_3, respectively). As can be seen in the graphs, the nanoparticles used decrease the concentration of the contaminant after 2 min of being dispersed. At the end of the test, the fog has dragged and deposited all the contaminant observed similar to the previous target values done.

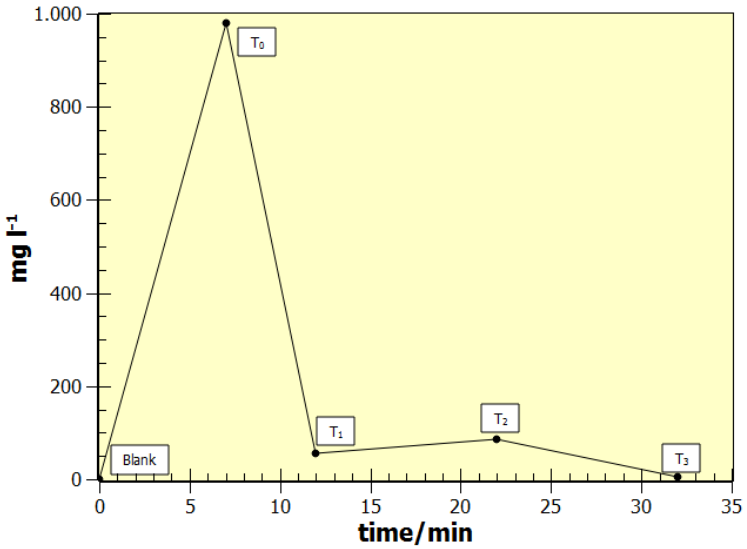

Figure 186: Evolution of the MS concentration versus different times by using nanoparticles and fog (P_{water} = 3.5 bar, P_{air} = 12 bar for B 1:2 nozzle) with 1% isopropanol. Where T_0 applies for MS dispersion; T_1 for nanoparticles action; T_2 to 7 min after fog shooting and T_3 to the end of the test. Particles of TiO_2.

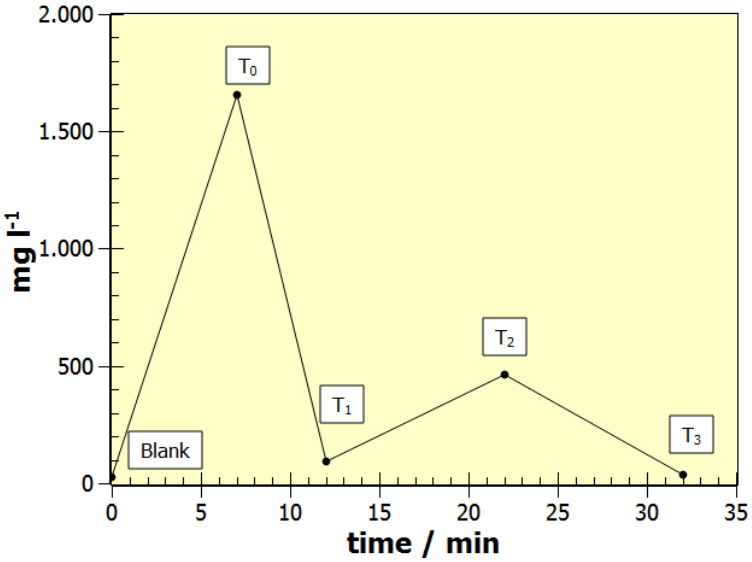

Figure 187: Evolution of the MS concentration versus different times by using nanoparticles and fog (P_{water} = 3.5 bar, P_{air} = 12 bar for B 1:2 nozzle) with 1% isopropanol. Where T_0 applies for MS dispersion; T_1 for nanoparticles action; T_2 to 7 min after fog shooting and T_3 to the end of the test. Particles of TiO_2-Al2O_3.

On the other hand, the evolution of nanomaterial particles, both TiO_2 and TiO_2-Al_2O_3, in the laboratory atmosphere during the process, apparently shows that when the MS is no longer in the laboratory environment, there are still a significant number of nanomaterial particles in suspension (Figure 188). The explanation for this fact would be that the salicylate is adsorbed to the metal oxide through the phenolic group, which would hinder the formation of colour complex. On the other hand, according to these results, at the end of the experiment the nanoparticles have not completely disappeared from the lab atmosphere. This fog does not seem to be effective to quickly collapse them, reason why it would be necessary either to increase the time or to use another type of fog like for example a mixed fog.

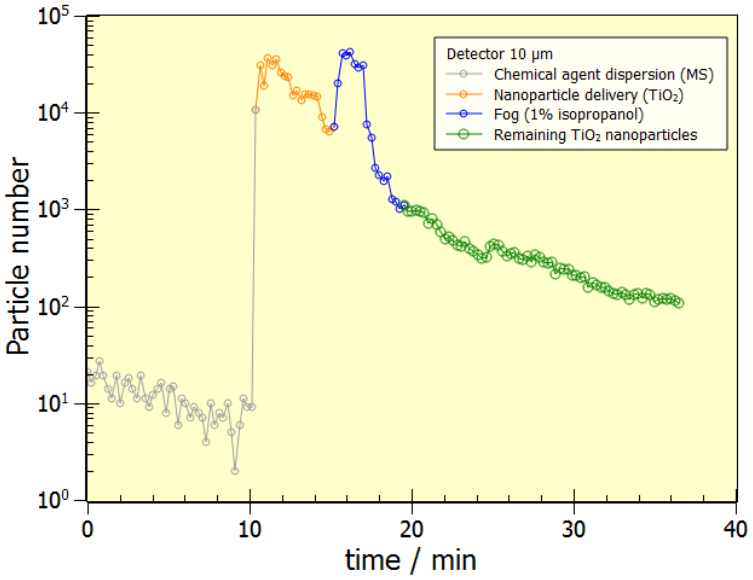

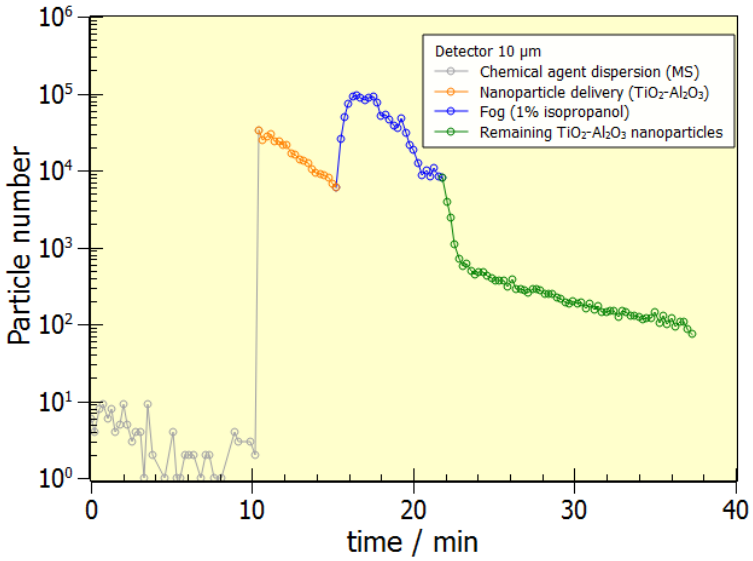

Figure 188: Evolution of particles in the test room with MS, nanoparticles (TiO_2 and TiO_2-Al_2O_3, respectively) and fog (P_{water} = 3.5 bar and P_{air} = 12 bar for B 1:2 nozzle) with 1% isopropanol.

8.3.3 DPGME quantification

The evolution of this surrogate in the experiment is displayed in Figure 189 and Figure 190 showing behaviour similar to the MS. Thus, the DPGME concentration measured in the laboratory environment following the dispersion of nanoparticles of TiO_2 and TiO_2-Al_2O_3 is negligible, just like after shooting the fog.

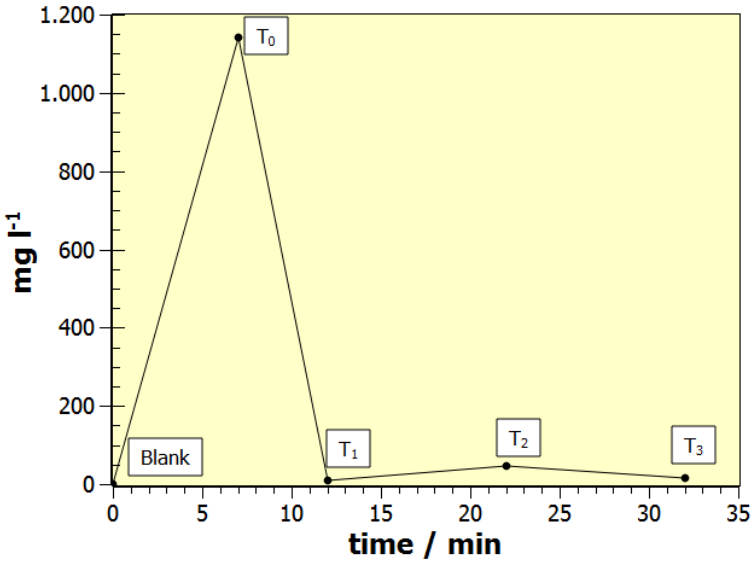

Figure 189: Evolution over time of the DPGME concentration by using TiO_2 nanoparticles and fog (P_{H2O} = 3.5 bar and P_{air} = 12 bar for B ½ nozzle) with 1% isopropanol. Where T_0 applies for DPGME dispersion; T_1 for nanoparticles action; T_2 to 7 min after fog shooting and T_3 to the end of the test.

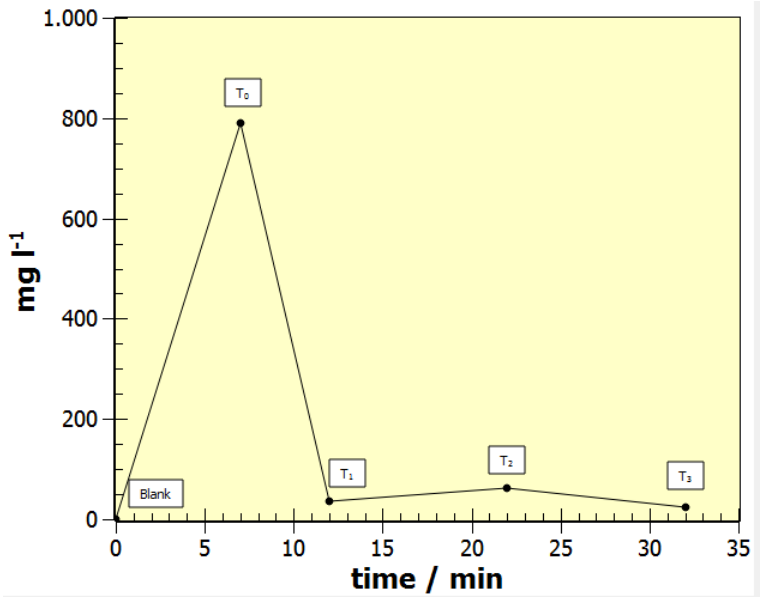

Figure 190: Evolution over time of the DPGME concentration by using TiO_2-Al_2O_3 nanoparticles and fog (P_{H2O} = 3.5 bar and P_{air} = 12 bar for B ½ nozzle) with 1% isopropanol. Where T_0 applies

for DPGME dispersion; T_1 for nanoparticles action; T_2 to 7 min after fog shooting and T_3 to the end of the test.

Concerning the evolution of nanoparticles in this interval (Figure 191) the highest amount corresponds to the fall of surrogate in the lab atmosphere. This fact seems to indicate the effectiveness of its adsorption to the nanomaterial. As in previous graphics corresponding to the MS, it is shown a gradual decay of the remaining nanoparticles still suspended in the atmosphere of the test room.

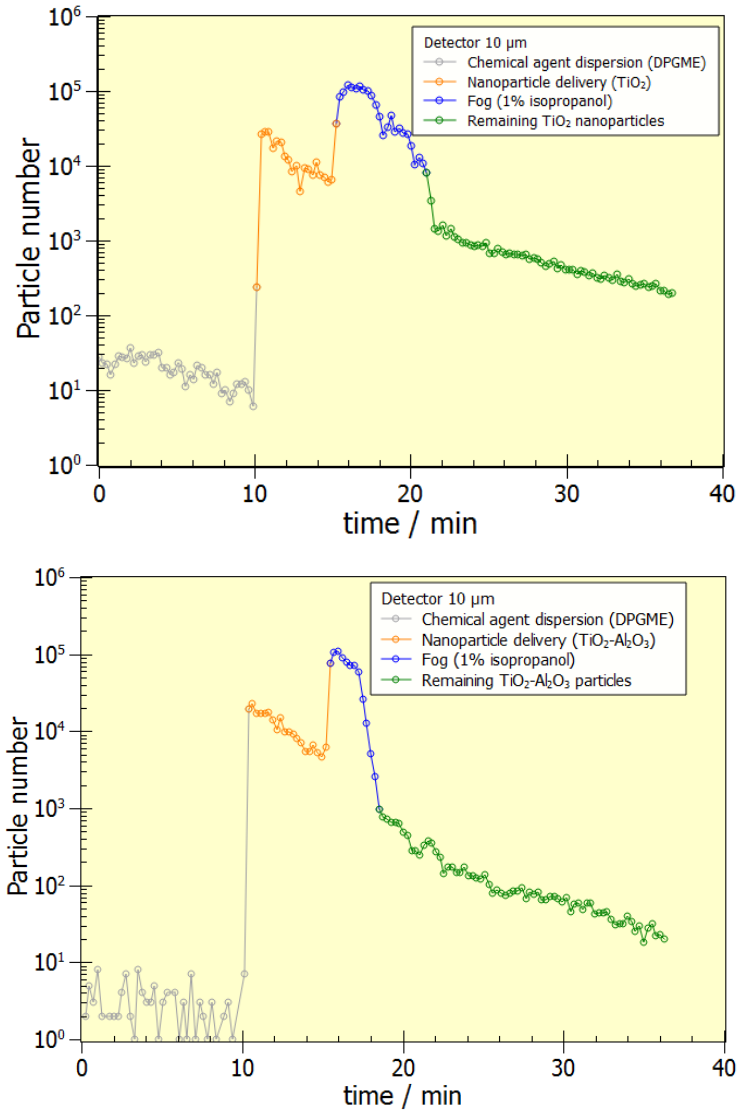

Figure 191: Evolution of particles in the test room with DPGME, nanoparticles (TiO_2 and TiO_2-Al_2O_3, and fog (P_{water} = 3.5 bar and P_{air} = 12 bar for B 1:2 nozzle) with 1% isopropanol.

8.3.4 TEP quantification

The evolution of the concentration of triethyl phosphate (TEP) follows the same pattern as the previous surrogates as may be seen in Figure 192 and Figure 193. In general, the behavior of nanoparticles is repeated throughout the experiment (Figure 194).

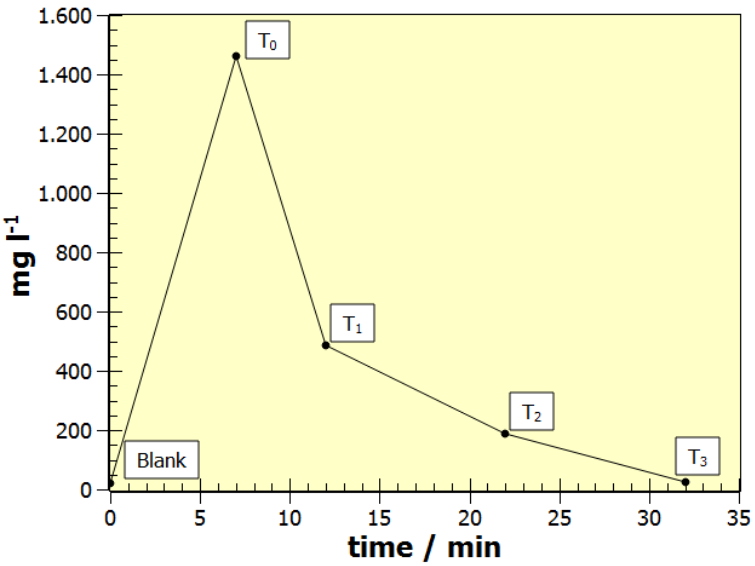

Figure 192: Evolution of the TEP concentration versus time by using TiO_2 nanoparticles and fog (P_{water} = 3.5 bar and P_{air} = 12 bar for B 1:2 nozzle) with 1% isopropanol. Where T_0 applies for TEP dispersion; T_1 for TiO_2 action; T_2 to 7 min after fog and t_3 to the end of the test.

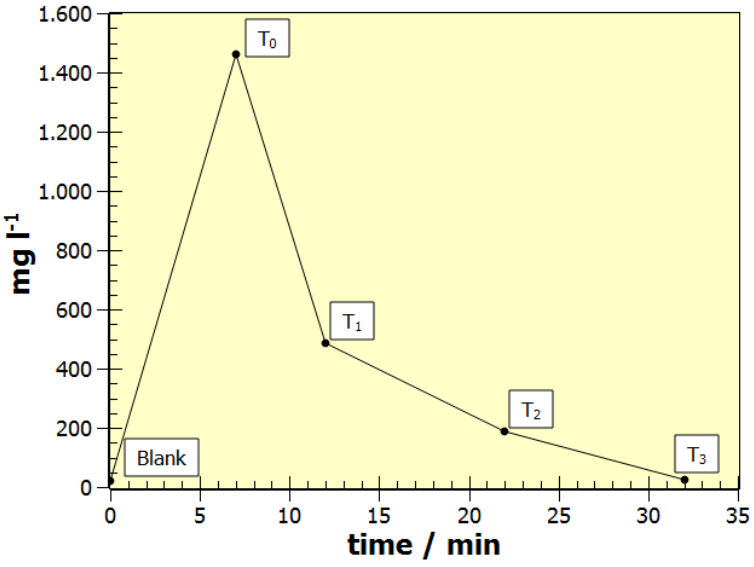

Figure 193: Evolution of the TEP concentration versus time by using TiO_2-Al_2O_3 nanoparticles and fog (P_{water} = 3.5 bar and P_{air} = 12 bar for B 1:2 nozzle) with 1% isopropanol. Where T_0 applies for TEP dispersion; T_1 for nanoparticles action; T_2 to 7 min after fog shooting and T_3 to the end of the test.

Although the rate of fall of the nanoparticles by the action of the fog is smaller, at the end of the test they have almost disappeared from the atmosphere of the laboratory.

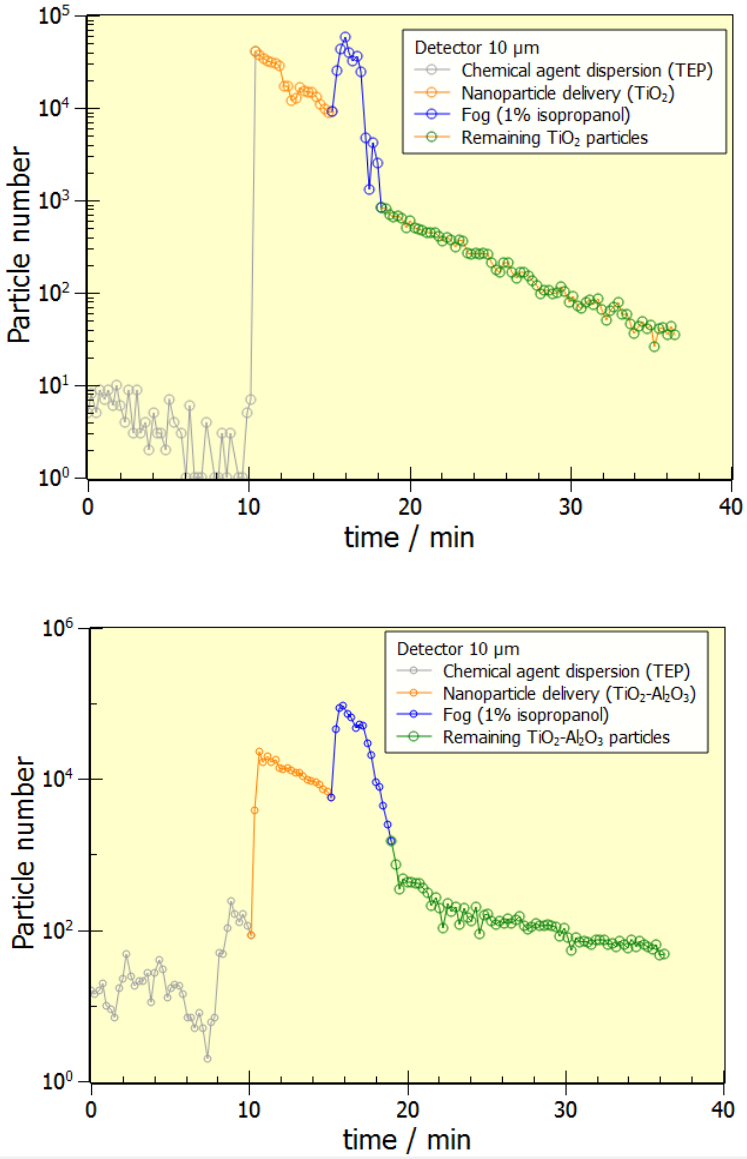

Figure 194: Measure of particles during the tests. Fog (P_{water} = 3.5 bar and P_{air} = 12 bar for B 1:2 nozzle) with 1% isopropanol. Nanoparticles of TiO_2 and TiO_2-Al_2O_3, respectively

8.3.5 Comparative analysis

At this point it is highlighted a significant difference between the effectiveness of cleaning the test room atmosphere through the Counterfog® system method adding TiO_2 and TiO_2-Al_2O_3 nanoparticles b a mechanical mean versus evolution of the chemical warfare agent surrogate in the case where no cleaning means is being used.

In the graphics of the Figure 195, Figure 196 and Figure 197, it is shown the evolution of the CWA surrogates concentration in laboratory atmosphere in three test conditions: two combinations of nanoparticles with fog and without the use of no cleaning means (nanoparticles and/or fog). For the three surrogates, it can be appreciated that without the use of a countermeasure their concentration does not decrease during the

experiment. As it is observed, the synergic effect of dispersed nanomaterials (individually or together) and fog collaborate to improve the cleaning of the test room atmosphere.

The data for MS agree with qualitative results of previous batch experiments for nanoparticles. Thus, after the initial adsorption of the CWA in the nanomaterial (T_1), the competition between the agent and H_2O molecules for sorption sites releases some surrogate molecules, causing a punctual increase of concentration (T_2). The final decrease in concentration may be due to both resorptions at the surface of the nanomaterial and to hydrolytic activity of water. This effect is more pronounced with the mixture of NMs, so its seems to be due to aluminium oxide mainly. The same explanation can be given to the evolution of DPGME and TEP.

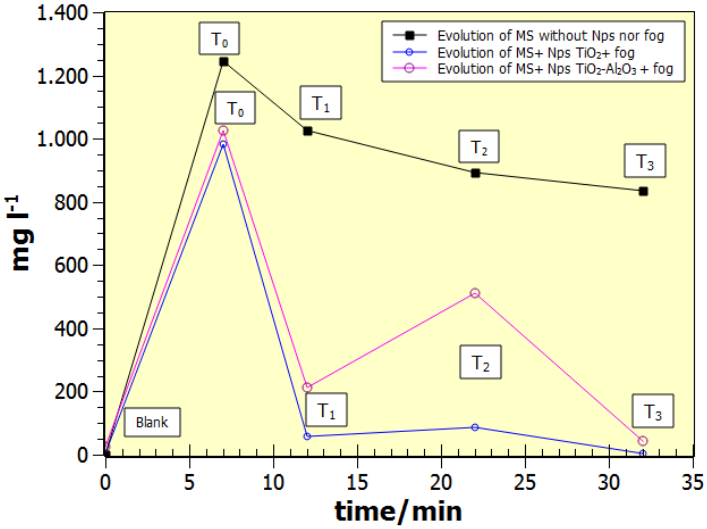

Figure 195: Evolution of the MS concentration.

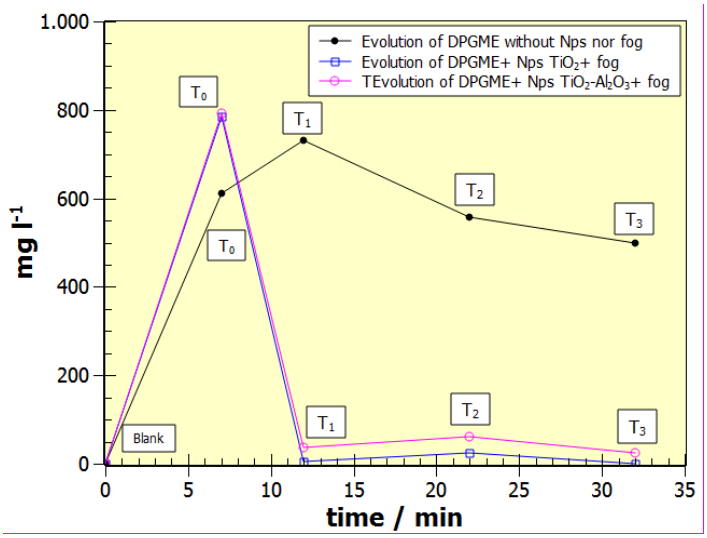

Figure 196: Evolution of the DPGME concentration.

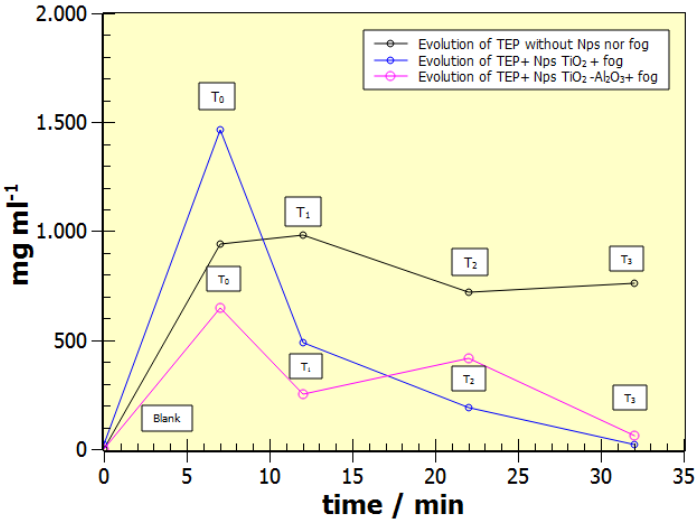

Figure 197: Evolution of the TEP concentration without nanoparticles and fog versus evolution of TEP with TiO_2 and fog and TiO_2-Al_2O_3 and fog.

During the last years, great advances of the technologies for decontamination surfaces have been done. Whereas, there are a few systems which are focused-on air decontamination. Hence, the use of harmless products which can be used in a wide range of scenarios in presence of persons is needed. The advantage of Counterfog® is that if the decontamination is done only with water or water with 1 % of isopropanol (which is not toxic for human being), the chemicals agents are removed from the air. But, if nanoparticles are added to the fog, these nanoparticles are able to interact with the surrogates tested and neutralizing them. So, the product formed and deposited on the surfaces of the room is not toxic.

8.4 Conclusions

- The fog applied to entrain the CWA was generated with the nozzle B 1:2 and pressures of water and air capable of generating a dispersion of fine droplets which takes about 20 minutes to be deposited. Likewise, isopropanol was added (1% concentration) to increase its effectiveness.

- The use of nanomaterials in the process has pursued a dual objective:

  - Remove from the laboratory atmosphere the dispersed compounds taking advantage of its high adsorption capacity and,
  - Decontaminate, i.e. convert toxic agents in by products with less or no toxicity due to its chemical reactivity

  Since these properties depend largely on the surface area and active sites available, the nanomaterials used in this work, TiO2 and TiO2-Al2O3 have been physicochemical characterized. Finally, based on the results obtained, their

behaviour has been related to these characteristics. Thus, although, TiO2-Al2O3 has high surface area than TiO2, it exhibited slightly lower removal efficiency. In terms of physical adsorption this suggests that its effective surface area, i.e. the number of available active sites, is lower.

- The proposed cleaning procedure involves three agents: fog, CWA and nanomaterials, so the interaction between them has been studied, concluding that:

  - The fog can effectively clean the CWA surrogates and nanomaterials if both are individually dispersed in the laboratory. In the case of nanopowders the dwell time in suspension is halved, being greater this effect with TiO_2-Al_2O_3
  - Nanomaterial effectiveness for decontaminating decreases if it is in aqueous suspension, reason why its dispersion has been made as dry powder after the release of CWA surrogate and before shooting the fog.
  - The efficiency of the fog to drag the surrogate-nanomaterial adsorbate decreases indicating a change in the interaction with respect to separate compounds.

Chapter 9

Conclusions

In this chapter the main conclusions obtained during the execution of this work are presented. These conclusions will be summarized in Section 9.1. Considering the performed investigations, the main lines of research that remain open and future lines of research will be described in Section 9.2. Finally, a list of published work produced during this thesis is presented in Section 9.3.

9.1 Summary of conclusions

After a first characterization of the nozzle models B1:2 and F1:2, designed during the course of the Counterfog®® project, the following conclusions were obtained:

- As expected, the cone generated by the B1:2 nozzle is a hollow cone while the one generated by the F1:2 nozzle is a solid cone.

- For the same air pressure, the water flow rate increases with increasing water pressure for both nozzles.

- For the same air pressure, the opening angle of the cone increases with increasing water pressure for both nozzles.

- Water flow rates obtained for the B1:2 nozzle are higher than those obtained for the F1:2 nozzle for air pressure below 10 bar; while water flrow rates ofr F1:2 are larger than those of B1:" for air pressure above 10 bar.

- For the same air and water pressure combination, cone opening angles for B1:2 nozzle are larger than those obtained for the F1:2 nozzle.

- For constant water pressure, the lower the air pressure is, the larger cone opening angle for both nozzle models.

- Both nozzle models can generate fog with water flows as low as 0.01 l/s.

- For similar air and water pressure combinations, the fog obtained for the B1:2 nozzle is denser and remains longer than that obtained for the F1:2 nozzle.

The above conclusions led to the choice of model B1:2 as the nozzle to be used for the different decontamination tests exposed throughout this doctoral thesis. For this purpose, a more detailed characterization was carried out with this nozzle model. The conclusions obtained are the following:

- The larger the water pressure is supplied the larger the water flow rate.

- The application of air pressure narrows the cone and reduceds the water flow.

- The water flow approaches asymptotically to a maximum value when water pressure grows.

- The generation of droplets is mainly of sizes 2.5, 5 and 10 μm.

- For the same air pressure, it is observed that the production of 5 and 10 μm droplets increases as the water pressure supply is increased up to a maximum and finally decreases.

- Fog density, remaining time and particle size have been characterized as a function of air and water pressure.

- For third component supply pressure below 8 bar, the third component flow rate is zero.

- For third component shooting pressures above 8 bar, the flow rate of the third component is greater than zero and increases as the third component pressure increases.

- For a water pressure of 8 bar, both water flow rate and third component flow rate are zero.

- When the water pressure is higher than the pressure of the third componentit prevents the third component entering the nozzle.

- There is a good agreement between numerical and experimental results of cone opening angles for the same combination of air and water pressures.

- There is a good agreement between the flows obtained experimentally and those obtained by simulation.
- There is an evident agreement as well between the experimental and simulated distributions of drops. Particularly SMD in both cases remain similar –within 2 or 3 μm-.

After carrying out a series of tests aimed at characterising the behaviour of the fog generated, the following conclusions were reached:

- It has been demonstrated how the new Counterfog® system, conceived for the cleaning and decontamination of particulate matter suspended in air, can generate fogs with the same properties under the same conditions, this is to say, the repeatability of the fogs generated by this system is guaranteed if the activation conditions are not changed.

- It can be ensured that, in the same shot and for a given height and a given time, the properties of the fog generated are homogeneous at all points inside the test room. This fact allows to guarantee that the effectiveness of the system in indoor spaces does not depend on the position of the volume of air to clean for a given height.

The main conclusions obtained after the tests for the decontamination of Diesel particles are:

- Particulate matter, in the removing process from the air by Counterfog®, tend to agglomerate tothe water droplets generated in the fog and also in the pool that is generated after the activation of the system.

- The number of Diesel particles for 2.5, 5.0 and 10.0 μm decreases below the initial level after application of Counterfog®. This means that it washes out both the Diesel smoke particles as well as other particles that were already air-borne.

- The system allows to reduce the number of particles generated by the combustion of the Diesel in several orders of magnitude in the case of particles of sizes 2.5 μm, 5 μm and 10 μm diameter in a time not exceeding 30 minutes.

The main conclusions obtained after the tests for the decontamination of biological agents are:

- The number of Bacillum turighiensis bacteria and spores in air is reduced in 2 to 4 orders of magnitude after applying Counterfog@ between 15s and 1 min in the laboratory.

- One hourlater, the spore values obtained in the case of non-application of fog are still one order of magnitude higher than those obtained in the case of application of the Counterfog® system 20 minutes after spore dispersion.

- The spore reduction percentages after mist application reach values above 90% within just a few minutes of fog application, reaching almost 100% spore reduction values in less than 10 minutes. However, even after 20 minutes from spore dispersion, reduction rates of less than 65% are obtained when the Counetrfog® system is not applied.

Finally, for the case of chemical agents in the air, the proposed cleaning procedure involves three agents: fog, CWA and nanomaterials, so the interaction between them were studied. The main conclusions obtained after the tests for the decontamination of biological agents are:

- Although, TiO2-Al2O3 have larger surface area than TiO2 particles,those exhibited slightly lower removal efficiency than these. In terms of physical adsorption this suggests that their effective surface area, i.e. the number of available active sites, is lower.

- The fog can effectively clean the CWA surrogates and nanomaterials if both are individually dispersed in the laboratory. In the case of nanopowders the dwell time in suspension is halved, being greater this effect with TiO_2-$Al2O_3$.

9.2 Future research lines

Many challenges remain in the field of CBRN agent decontamination.. Taking into account the research carried out in this thesis, the following lines of future research are listed below, some of which are currently in progress:

- The very satisfactory results obtained make the study in outdoor spaces a possible future way of developing the Counterfog® system. In this way, this technology could provide a unique and effective tool for cleaning air in cities, improving air quality and decreasing respiratory diseases among population in large cities. In this way, the path towards a healthier air environment for people is a little closer every day.

- Study of the efficiency of the Counterfog® system for the decontamination of surfaces contaminated by CBRN agents, as well as by suspended particles such as residues from the combustion processes of diesel engines.

- Improvements in the design of the nozzle such as an adjustment of the angle of introduction of the third component that allows its entry without the application of external pressure, that is, be sucked naturally by the main flow of the nozzle, composed of air and water.

9.3 List of publications

Alist of publications is shown belowas well as awards obtained during the course of candidature for the degree.

- **Publications:**

  J.L. Pérez-Díaz, F.J. Llerena-Aguilar, T. Martín-Pérez, J.Sánchez García Casarrubios, E. Ruiz Navas, I.Valiente-Blanco (2019). Decontamination of Diesel particles from air by using the Counterfog system. Air Quality, Atmosphere & Health. March 2019. 12 (3): 305-310 https://doi.org/10.1007/s11869-018-00656-7

  - T. Martín-Pérez, F.J. Llerena-Aguilar, J.Pérez-Serrano, J.L. Copa-Patiño, J. Solivieri de Carranza, J.M. Orellana-Muriana, J.L. Pérez-Díaz. Eco- friendly air decontamination of biological warfare agents using "Counterfog" system. 1st Scientific International Conference on CBRNE SICC 2017 Proceedings. ISBN: 978-3-319-91791-7

  - J.Sánchez-García-Casarrubios, F.J. Llerena-Aguilar, J.L. Pérez-Díaz. Fog Dynamics. 1st Scientific International Conference on CBRNE SICC 2017 Proceedings. ISBN: 978-3-319-91791-7

- Counterfog® **Project Patents:**

  - Atomizing nozzle, José Luis Pérez-Díaz, Javier Quiñones Díez, Yi Qin, Yankang Tian, Wolfgang Hornig. application Nº EP17382233.9 /28.04.2017 of European Patent Office

  - Method for Eliminating Particles Floating in Air, José Luis Pérez-Díaz, application Nº EP17382293.3/22.05.17 of European Patent Office.

  - A method for determining the threshold ablation of solid materials, Ognyan Ivanov, Valentin Mihailov, Stefan Karatodorov, José Luis Pérez-Díaz, application № 112446 / 24.01.2017 of the Patent Office of the Republic of Bulgaria.

  - Contactless detection of phase transition in liquid crystal state by means of laser induced surface photo charge effect through measurement of one electrical signal, Ognyan Ivanov, Haritun Naradikian, José Luis Pérez-Díaz, application № 112488 / 13.04.2017 of the Patent Office of the Republic of Bulgaria.

- Counterfog® **Project Awards:**

  - First prize in the category: Promotion and dissemination of science by the University of Alcalá.

  - Bulgarian Industrial Association Award.

  - First prize in the category: Most Significant Applied Scientific

  - Achievements of the Bulgarian Academy of Science.

  - Accésit in the Madrid+D awards. Categoría de empresas e ideas de base tecnológica.

  - First prize in the First international CBRN Scientific Conference (SICC 2017) for the poster 'Fog Dynamics'.

Glossary

APHEA	Air Pollution and Health: a European Approach
AQG	Air Quality Guidelines
BS	Black Smoke indicator
BSE	Backscattered-Eelectron Detector
BSE	Backscattered electrons
CBRN	Chemical, biological, radiological and nuclear
CCN	Cloud Condensation Nuclei
CEES	2-chloroethyl ethyl sulphide
CEPS	2-chloroethyl phenyl sulphide
CIEMAT	Centre for Energy, Environmental and TechnologicalResearch
CWA	Chemical Warfare Agents
DPGME	Dypropyleneglycol ponomethyl
EDXA	Energy Dispersive X-ray Analysis
EDXS	Enery-dispersive X-ray spectroscopy
EPA	Environmental Protection Agency

EU	European Union
GA	Taburn gas
GB	Sarin gas
GC	Soman gas
HEI	Health Effects Institute
HM	Distilled Mustard
INP	Ice Nucleating Particles
ISO	International Organization for Standardization
KH	Henry's Law constant
MS	Methyl Salicylate
NATO	North Atlantic Treaty Organization
NMs	Nanomaterials
PLS	Polystyrene latex spheres
PM	Particulate matter
REBT	Electrotechnical Regulations for Low Voltage
RH	Relative Humidity
SD	Standard Deviation
SE	Transmitted electrons
SED	Secondary-Electron Detector
SEM	Scanning Electron Microscopy
TEP	Triethyl phosphate
TOF	Time Of Flight
VOCs	Volatile organic compounds
WHO	World Health Organization
WMO	World Meteorogical Organization

Bibliography

[Abbey et al., 1999] Abbey D.E. et al (1999). Long-term inhalable particles and other air pollutants related to mortality in nonsmokers. Am J Respir Crit Care Med 1999 Feb.; 159(2): 373–382

[Allaby, 2003] Allaby M (2003) Fog, smog and poisoned rain. Facts on File, Inc., New York Bagley

[Andreae et al. 2008] Andreae, M.O. and Rosenfeld, D. (2008). Aerosol-cloud-precipitation interactions. Part 1. The nature and sources of cloud-active aerosols. Earth-Sci. Rev. 2008; 89: 13–41.

[Andronache et al., 2006] Andronache, C., Grönholm, T., Laakso, L., Phillips, V., and Ven¨al¨ainen, A.: Scavenging of ultrafine particles by rainfall at a boreal site: observations and model estimations, Atmos. Chem. Phys., 6, 4739–4754, doi:10.5194/acp-6-4739-2006, 2006.

[Andronache, 2004] Diffusion and electric charge contributions to below-cloud wet removal of atmospheric ultra-fine aerosol particles. Journal of Aerosol Science, 2004. 35(12): 1467-1482

[ANSYS, 2016] "ANSYS," vol. 17.0, ed: ANSYS Inc, 2016.

[APHEIS, 2004] Air Pollution and Health: a European Information System (APHEIS) (2004). Health Impact Assessment of Air Pollution and Communication Strategy. Third-Year Repor 2002-2003t. Paris: Institut de Veille Sanitaire, 2004 Jul

[Arnon, 2001] Arnon S.S. (2001). Botulinum Toxin as a Biological WeaponMedical and Public Health Management. JAMA. 2001; 285(8): 1059-1070

[Atkinson et al., 2001] Atkinson .R.W. et al. (2001). Acute Effects of Particulate Air Pollution on Respiratory Admissions Results from APHEA 2 Project. American Journal of Respiratory and Critical Care Medicine. 2001 Nov.; 164(10): 1860-1866.

[Bae et al., 2009] Bae, S. Y., Jung, C. H., and Kim, Y. P.: Relative contributions of individual phoretic effect in the below-cloud scavenging process, J.Aero. Sci., 40, 621 – 632, doi:10.1016/j.jaerosci.2009.03.003, 2009.

[Bagley et al., 1998] Bagley S T, Gratz L D, Johnson J H and McDonald J F 1998. Effects of an oxidation catalytic converter and a biodiesel fuel on the chemical, mutagenic, and particle size characteristics of emissions from a diesel engine Environ. Sci. Technol. 32 1183-1191

[Beard and Grover, 1974] Beard, K.V. and Grover, S.N. (1974). Numerical collision efficiencies for small raindrops colliding with micron size particles. J. Atmos. Sci. 1974; 31: 1595-1603

[Beard, 1974] Beard, K.V. (1974). Experimental and numerical collision efficiencies for submicron particles scavenged by small raindrops. J. Atmos. Sci. 1974; 31: 1595-1603

[Beeson, Abbey and Knutsen, 1998] Beeson W.L. , Abbey D.E. and Knutsen S.F. (1998). Long-term concentrations of ambient air pollutants and incidence lung cancer in California adults: results from the AHSMOG study. Advestist Health Study on Smog. Environ Health Perspect 1998 Dec.; 106(12): 813–823

[Bell and Davis, 2001] Bell M.L. and Davis D. L. (2001). Reassessment of the Lethal London Fog of 1952: Novel Indicators of Acute and Chronic Consequences of Acute Exposure to Air Pollution. Environmental Health Perspectives. 2001, 109(3), 389-394

[Belyaev and Levin. 1972] Belyaev and Levin. 1972. “Investigation of aerosol aspiration by photographing particle tracks under flash illumination”. Journal of Aerosol Science, 3, pp127-140.

[Bennett, 2007] Bennett, D (2007).Terrorists and Unconventional Weapons: Is the Threat Real?. Low Intensity Conflict & Law Enforcement 2007 Jan.; 12(1): 20-50

[Beresnev and Chernyak, 1995] S. Beresnev, V. Chernyak. Thermophoresis of a spherical particle in a rarefied gas: numerical analysis based on the model kinetic equations Phys. Fluids, 7 (1995), pp. 1743-1756

[Bernstein, 2004] Bernstein, J. (ed.) 2004. Health effects of air pollution. Journal of Allergy and Clinical Immunology. 2004 Nov. ; 114(5): 1116–1123

[Bradley et al., 1958] Bradley, W.H. et al. (1958). The London Fog of December 2nd-5th, 1957. Monthly Bull. Ministry of Health & Pub. Health Lab. Service (directed by Med. Res. Council), 1958; 17: 156-66

[Braun-Fahrlander et al., 1992] Braun-Fahrlander, C. et al. (1992). Air pollution and respiratory symptoms in preschool children. Am Rev Respir Dis 1992 Jan.; 145(1): 42–47

[Brunekreef, 1997] Brunekreef B. (1997). Air pollution and life expectancy: Is there a relation?. Occup Environ Med 1997 Nov.; 54(11): 781–784

[Buttner et al., 2004] Buttner, M. P., Cruz, P., Stetzenbach, L. D., Klima-Comba, A. K., Stevens, V. L., & Cronin, T. D. (2004). Determination of the efficacy of two building decontamination strategies by surface sampling with culture and quantitative PCR analysis. Applied and Environmental Microbiology; 70(8): 4740-4747.

[Calvert, 1984] Calvert, S. (1984). Particle control by scrubbing. In: S. Calvert, & H.M. Englund (Eds.), Handbook of air pollution technology (pp. 215–248). New York: Wiley.

[Cao et al., 2012] Cao, J.J., Shen, Z.X., Chow, J.C., Lee, S.C., Watson, J.G., Tie, X.X., Ho, K.F., Wang, G.H. and Han, Y.M. (2012). Winter and Summer PM2.5 Chemical Compositions in 14 Chinese cities. J. Air Waste Manage. Assoc. 62: 1214–1226, doi: 10.1080/10962247.2012.701193.

[Cao et al., 2013] Cao J. et al (2013). Evolution of PM2.5 Measurements and Standards in the U.S. and Future Perspectives for China. Aerosol and Air Quality Research 2013; 13: 1197–1211

[Casarrubios, 2018] Casarrubios JSG, Llerena-Aguilar FJ, Pérez-Díaz JL (2018) Fog dynamics. In: Malizia A, D'Arienzo M (eds) Enhancing CBRNE safety & security: proceedings of the SICC 2017 conference. Springer, Cham.

[Chate and Kamra, 1997] Chate, D.M. and Kamra, A.K. (1997). Collection efficiencies of large water drops collecting aerosol particles of various densities. Atmospheric Environment 1997; 31(11): 1631-1635

[Chate and Pranesha, 2004] Chate, D. and Pranesha, T.: Field studies of scavenging of aerosols by rain events, J. Aero. Sci., 35, 695 – 706, doi:10.1016/j.jaerosci.2003.09.007, 2004.

[Chernyak et al., 2001] V.G. Chernyak, S.A. Starikov, S.A. BeresnevDiffusiophoresis of an aerosol particle in a binary gas mixture J. Appl. Mech. Tech. Phys., 42 (2001), pp. 445-454

[COMEAP, 2006] Commitee on the Medical Effects of Air Pollutants (COMEAP) (2006).Cardiovascular Disease and Air Pollution: a report by the committee on the medical effects of air pollution

[Committee of the Environmental and Occupational Health Assembly of the American Thoracic Society, 1996] Committee of the Environmental and Occupational Health Assembly of the American Thoracic Society (1996). Health effects of outdoor air pollution. Am J Respir Crit Care Med 1996 Jan; 153(1): 3-50 and 477-98

[Cornish, 2007] Cornish P. (2007). THE CBRN SYSTEM Assessing the threat of terrorist use of chemical, biological, radiological and nuclear weapons in the United Kingdom. An international Security Programme Rport. Chatam House (The Royal Institute of International Affairs 2007 Feb.

[Croft et al., 2010] Croft, B., Lohmann, U., Martin, R. V., Stier, P., Wurzler, S., Feichter, J., Hoose, C., Heikkil¨a, U., van Donkelaar, A., and Ferrachat, S.: Influences of in-cloud aerosol scavenging parameterizations on aerosol concentrations and wet

deposition in ECHAM5-HAM, Atmos. Chem. Phys., 10, 1511– 1543, doi:10.5194/acp-10-1511-2010, 2010.

[Cunha, 2002] Cunha B.A. (rev) (2002). Anthrax, tularemia, plague, ebola or smallpox as agents of bioterrorism: recognition in the emergency room. Clin Microbiol Infect 2002; 8: 489–503

[D1.1, 2014] "D 1.1 First model of the nozzle," University of Strathclyde 2014.

[D1.2, 2014] "D 1.2: Detailed mechanical 3D model of nozzle," University of Strathclyde 2014.

[D1.4, 2015] "D 1.4 Nozzle redesign," University of Strathclyde 2015.

[Davenport and Peters, 1978] Davenport, H. and Peters, L. K.: Field studies of atmospheric particulate concentration changes during precipitation, Atmos. Env., 12, 997–1008, doi:10.1016/0004-6981(78)90344-X, 1978. doi:10.5194/acp-10-5685-2010, 2010.

[Dennis, Lewis and Matteson, 1975] Dennis, R.M., Lewis, L. and Matteson, M.J. (1975). The collection of aerosold by charged water droplets. Paper presented at the 25th Conf. Canadian Society for Chemical Engineering, Montreal 1975 August.

[Dockery et al., 1993] Dockery, D.W. et al. (1993). An association between air pollution and mortality in six U.S. cities. N Engl J Med 1993 Dec.; 329: 1753-1759

[DWD, 2018] DWD, 2018 Deutscher Wetterdienst (https://www.dwd.de)

[E.U. Patent No. EP17382293.3/22.05.17] Pérez-Díaz, J.L. Method for Eliminating Particles Floating in Air. *A*pplication No. EP17382293.3/22.05.17 of European Patent Office

[EEA, 2012] European Environment Agency (EEA). 2012. Climate change, impacts and vulnerability in Europe 2012. ISSN 1725-9177 Report No 12/2012

[EEA, 2016] European Environment Agency (EEA) (2016). Air quality in Europe. ISSN 1977-8449 Report No 28/2016

[EEA, 2017] European Environment Agency (EEA) 2017 Air quality in Europe ISSN 1725-9177 Report No 13/2017

[Eliseo et al., 2008] Eliseo, T. et al. (2008). Terror Australis 2004: preparedness of Australian hospitals for disasters and incidents involving chemical, biological and radiological agents. Terror Australis 2004: preparedness of Australian hospitals for disasters and incidents involving chemical, biological and radiological agents 2008 Jun.; 10(2): 125-136

[Ezzati and Kammen, 2002] Ezzati, M. and Kammen D. (2002). The health impacts of exposure to indoor air pollution from solid fuels in developing countries: knowledge,

gaps, and data needs. Environmental Health Perspectives. 2002 Nov; 110(11): 1057-1068

[Ezzati et al., 2002] Ezzati, M. et al. (2002). Selected major risk factors and global and regional burden of disease. Lancet. 2002; 360: 1203-1209

[Facy, 1958] Facy, 1958 L. FacyMechanisms of capture of aerosol particles in the process of condensation–evaporation C. R. Acad. Bulg. Sci., 246 (1958), pp. 3161-3164

[Fenger and Tjell 2009] FengerJ,TjellJC(2009)Airpollution-from local to a global perspective. RCS Publishing Polyteknisk, Forlag Giechaskiel B , Alföldy B, Drossinos Y (2009). Ametric for health effects studies of diesel exhaust particles. J Aerosol Sci 40:639–651

[Fennelly, 1975] Fennelly, P. (1975). Primary and secondary particulates as pollutants. A Literature Review. Journal of the Air Pollution Control Association, 25:7, 697-704.

[Gamble, 1996] Gamble, J.F. and Lewis, R.J. (1996) "Health and respirable particulate matter (PM10) air pollution: A causal or a statistical association," Environ. Health Perspect. 1996 Aug.; 104(8), 838–850.

[Gamble, 1998] Gamble, J.F. (1998). "PM2.5 and mortality in long-term prospective cohort studies: Cause-effect or statistical associations?" Environ. Health Perspect. 1998 Sep.; 106(9): 535–549.

[Geoghegan and Tong, 2006] Geoghegan , J. and Tong, J.L. (2006). Chemical warfare agents. Continuing Education in Anaesthesia Critical Care & Pain 2006 Dec.; 6(6): 230-234

[Giechaskiel et al., 2009] Giechaskiel B, Alföldy B and Drossinos Y 2009 A metric for health effects studies of diesel exhaust particles J. Aerosol. Sci. 40 639-651

[Goldberg et al., 2001] Goldberg, M.S. et al. (2001). Associations between daily cause-specific mortality and concentrations of ground level ozone in Montreal, Quebec. Am J Epidemiol 2001; 154: 817-826

[Goldberg et al., 2001] Goldberg, M.S. et al. (2001). Identification of persons with cardiorespiratory conditions who are at risk of dying from the acute effects of ambient air particles. Environmental Health Perspectectives 2001 Aug.; 109(4): 487-494

[Gouveia et al., 2000] Gouveia, N. et al. (2000). Time-series analysis of air pollution and mortality: effects by cause, age and socioeconomic status. J Epidemiol Community Health 2000; 54: 750–755

[Grainger, 2017] Grainger, R.G. (2017). Some Useful Formulae for Aerosol Size Distributions and Optical Properties

[Greenfield, 1957] Greenfield, S. M.: Rain scavenging of radioactive particulate matter from the atmopshere, J. Meteor., 14, 115–125, doi:10.1175/1520-0469(1957)014h0115:RSORPMi2.0.CO;2, 1957.

[Grigoratos and Martini 2014] Grigoratos T, Martini G (2014) Brake wear particle emissions: a review. Environ Sci Pollut Res 22(4):2491–2504

[Grover at al., 1977] Grover, S.N., Pruppacher, H.R. and Hamelec, A.R. (1977). A numerical determination of the efficiency with which spherical aerosol particles collide with spherical water drops in air due to hydrodynamic-, phoretic-, and electrical forces. J. Atmos. Sci., 34: 1655-1663.

[Haeffelin et al. 2016] Haeffelin, M.; Laffineur, Q.; Bravo-Aranda, J.A.; Drouin, M.A.; Casquero-Vera, J.A.; Dupont, J.C.; De Backer, H. (2016). Radiation fog formation alerts using attenuated backscatter power from automatic lidars and ceilometers. Atmos. Meas. Tech. 2016; 9: 5347–5365.

[Hangal and Willeke, 1990] Hangal, S. and Willeke, K. 1990. "Overall efficiency of tubular inlets sampling at 0-90 degrees from horizontal aerosol flows". Atmospheric Environment, 24A(9), pp2379-86.

[Harris and Maricq, 2001] Harris S J and Maricq M M 2001 Signature size distributions for diesel and gasoline engine exhaust particulate matter J. Aerosol. Sci. 32 749-764

[Hinds, 1982] Hinds, W.C. 1982. "Aerosol Technology. Properties, Behavior, and Measurement of Airborne Particles". John Wiley & Sons. New York, Chichester, Brisbane, Toronto, Singapur.

[Hinds, 1999] Hinds, W.C. 1999. "Aerosol Technology. Properties, Behavior, and Measurement of Airborne Particles". John Wiley & Sons. New York, Chichester, Weinheim, Brisbane, Singapore, Toronto.

[Holownia et al., 2008] Holownia, D., Kwiatkowska, I., and Hupka, J.: An investigation on wetting of porous materials., Physicochemical Problems of Mineral Processing, 42, 251–262, 2008.

[Horak et al., 2002] Horak F. et al. (2002). Particulate matter and lung function growth in children: a 3-yr follow-up study in Austrian schoolchildren. Eur Respir J 2002; 19: 838–845

[IARC, 2004] International Agency for Research on Cancer. (2004). IARC classifies formaldehyde as carcinogenic to humans. http://monographs.iarc.fr/ENG/Monographs/vol88/index.php

[IARC, 2013] International Agency for research on Cancer (IARC) (2013). Press release Nº221. http://www.iarc.fr/en/media-centre/pr/2013/pdfs/pr221_E.pdf

[Ijaz et al., 2016] Ijaz, M. K., Zargar, B., Wright, K. E., Rubino, J. R., & Sat-tar, S. A. (2016). Generic aspects of the airborne spread of human pathogens indoors and emerging air decontamination technologies. American journal of infection control, 44(9): 109-120.

[Jaenicke, 1978] Jaenicke, R. (1978). Über die Dynamik atmosphärischer Aitkenteilchen, Berichte der Bunsengesellschaft für physikalische Chemie,. 82(11), 1198-1202, https://doi.org/10.1002/bbpc.19780821126.

[Jennings, 1988] Jennings, S.C. (1988). The mean free path in air. Journal of Aerosol Science, 19 (2), 159–166.

[Jung and Lee, 1998] Jung, C. H., & Lee, K. W. (1998). Filtration of fine particles by multiple liquid drop and gas bubble systems. Aerosol Science and Technology, 29, 389–401.

[Jung, Kim, and Lee, 2002] Jung, C. H., Kim, Y. P., & Lee, K. W. (2002). Analytic solution for polydispersed aerosol dynamics by a wet removal process. Journal of Aerosol Science, 33, 753–767.

[Junji et al. 2013] Junji Cao1, Judith C. Chow, Frank S.C. Lee, John G. Watson. Evolution of $PM_{2.5}$ Measurements and Standards in the U.S. and Future Perspectives for China. Aerosol and Air Quality Research, 13: 1197-1211

[Kampa and Castanas, 2007] Kampa, M. and Castanas, E. (2007). Human health effects of air pollution. Environmental Pollution. 2008 Jan. ; 151:2, 362-367

[Kampa and Castanas, 2008] Kampa M. and Castanas E. (2008). Human health effects of air pollution. Environmental Pollution 2008 Jan.; 151(2): 362-367

[Katsouyanni et al., 1997] Katsouyanni K.et al. (1997). Short-term effects of ambient sulphur dioxide and particulate matter on mortality in 12 European cities: results from time series data from the APHEA project. BMJ 1997; 314: 1658–1663

[Katsouyanni et al., 2001] Katsouyanni K., et al.(2001). Confounding and effect modification in the short-term effects of ambient particles on total mortality: Results from 29 European cities within the APHEA2 Project. Epidemiology 2001 Sep.; 12(5): 521–531

[Katsouyanni et al., 2001] Katsouyanni, K. et al. (2001). Confounding and Effect Modification in the Short-Term Effects of Ambient Particles on Total Mortality: Results from 29 European Cities within the APHEA2 Project. Epidemiology. 2001 Sep.; 12(5): 521-531

[Katsouyanni, 2003] Katsouyanni, K. (2003). Ambient air pollution and health. British Medical Bulletin, 2003 Dec. ; 68:1, 143–156

[Khatery et al., 2003] Khatery, S. et al (2003). Incidence of Lung, Eye, and Skin Lesions as Late Complications in 34,000 Iranians With Wartime Exposure to Mustard Agent. Journal of Occupational and Environmental Medicine 2003 Nov.; 45(11): 1136-1143

[Koburger et al., 2011] Koburger, T., Below, H., Dornquast, T., & Kramer, A. (2011). Decontamination of room air and adjoining wall sur-faces by nebulizing hydrogen peroxide. GMS Kranken-haushygiene interdis

[Kollel, 2003] Kollel, D. (2003).Canadian emergency department preparedness for a nuclear, biological or chemical event. Canadian Journal of Emergency Medicine 2003 Jan.; 5(1): 18-26

[Kulkarni et al., 2011] Kulkarni, P., Baron, P., andWilleke, K.: Aerosol Measurement: Principles, Techniques, and Applications, Wiley, URL https://books.google.ch/books?id=ETvXooNW4-EC, 2011.

[Künzli et al., 2000] Künzli N. et al. (2000). Public-health impact of outdoor and traffic-related air pollution: a European assessment. The Lancet 2000 Sep.; 356(9232): 795-801

[Laakso et al., 2003] Laakso, L., Groenholm, T., Rannik, U., Kosmale, M., Fiedler, V., Vehkamaeki, H., and Kulmala, M.: Ultrafine particle scavenging coefficients calculated from 6 years field measurements, Atmospheric Environment, 37, 3605 – 3613, doi:10.1016/S1352-2310(03)00326-1, 2003.

[Ladino et al. 2011a] Ladino, L., Stetzer, O., Hattendorf, B., Guenther, D., Croft, B., and Lohmann, U.: Experimental Study of Collection Efficiencies between Submicron Aerosols and Cloud Droplets, J. Atmos. Sci., 68, 1853–1864, doi:10.1175/JAS-D-11-012.1, 2011a.

[Ladino et al., 2013] Ladino Moreno, L. A., Stetzer, O., and Lohmann, U.: Contact freezing: a review of experimental studies, Atmos. Chem. Phys., 13, 9745–9769, doi:10.5194/acp-13-9745-2013, 2013.

[Ladino, 2011] Ladino, L.: Experiemntal study on collection efficiency and conatact freezing of aerosols in a new collision chamber, Ph.D. thesis, ETH, Zürich, Switzerland, 2011.

[Lay, Dayan and Kerker, 1977] Lay, K.Y , Dayan, N. and Kerker, M. (1977). Scavenging of Aerosol Particles by a Falling Water Drop. Air. J. Atmos. Sci. 1977; 35: 674-682

[Lee, 2003] Lee, E.C. (2003).Clinical Manifestations of Sarin Nerve Gas Exposure. JAMA 2003 Aug.: 290(5): 659-662

[Leong et al., 1982] Leong, K. H., Beard, K. V., and Ochs, H. T.: Laboratory Measurements of Particle Capture by Evaporating Cloud Drops, J. Atmos. Sci., 39, 1130–1140, doi:10.1175/1520-0469(1982)039h1130:LMOPCBi2.0.CO;2, 1982.

[Liu et al. 1974] Liu, B.Y.H., Whitby, K.T. and Pui, D.Y.H. (1974). A Portable Electrical Analyzer for Size Distribution Measurement of Submicron Aerosols. J. Air Pollut. Contr. Assoc. 24: 1067–1072.

[Liu et al., 1989] Liu, Zhang y Kuehn. 1989. “A numerical study of inertial errors in anisokinetic sampling”. Journal of Aerosol Science, 20(3), pp367-380.

[Lohman et al., 2016] Lohmann, U., Lüönd, F. and Fabian, M.: An introduction to clouds: from the microscale to climate, Cambridge University Press, 2016.

[Lucking et al. 2011] Lucking A. J. , Lundbäck M., Barath S.L., Mills N.L., Sidhu M.K., Langrish J.P., Boon N.A., Pourazar J., Badimon J.J., Gerlofs-Nijland M.E., Cassee F.R., Boman C, Donaldson K, Sandstrom T, Newby D.E., Blomberg A (2011) Particle traps prevent adverse vascular and prothrombotic effects of diesel engine

exhaust inhalation in men. Circulation 123: 1721–1728. https://doi.org/10.1161/CIRCULATIONAHA.110. 987263

[Maria and Russell, 2005] Maria, S. F. and Russell, L. M.: Organic and Inorganic Aerosol Below-Cloud Scavenging by Suburban New Jersey Precipitation, Environmental Science & Technology, 39, 4793–4800, doi: 10.1021/es0491679, pMID: 16053076, 2005.

[Martín-Pérez 2018] Martín-Pérez T, Llerena-Aguilar FJ, Pérez-Serrano J, Copa-Patiño JL, de Carranza JS, Orellana-Muriana JM, Pérez-Díaz JL (2018) Ecofriendly air decontamination of biological warfare agents using Counterfog® system. In: Malizia A, D'Arienzo M (eds) Enhancing CBRNE safety & security: proceedings of the SICC 2017 conference. Springer, Cham

[McConnel et al., 2002] McConnel,l R. et al. (2002). Asthma in exercising children exposed to ozone: a cohort study. Lancet 2002 Mar.; 359(9309): 386–391

[McDonnell et al., 1999] McDonnell, W.F. et al (1999). Long-term ambient ozone concentration and the incidence of asthma in nonsmoking adults: the Ahsmog Study. Environ Res 1999 Jan.; 80: 110–121

[Myers and Maynard, 2005] Myers, I. and Maynard R.L. (2005). Polluted air- outdoors and indoors. Occupational Medicine. 2005; 55: 432-438

[Nagare et al., 2015] Nagare, B. et al. (2015). Comparison of measured and calculated collision efficiencies at low temperatures. Atmos. Chem. Phys., 15, 13759–13776, 2015.

[Nagare, 2016] Nagare, B. (2016). Experimental study on collision efficiency and contact freezing. ETH Zürich. Research Collection. https://doi.org/10.3929/ethz-a-010669812

[Nanev 2015] Nanev, C. (2015). Theory of nucleation. In Handbook of Crystal Growth (Fundamentals: Thermodynamics and Kinetics), 2nd ed.; Nishinaga, T., Ed.; Elsevier: Amsterdam, The Netherlands; 315–358

[Nel, 2005] Nel A. (2005). Air Pollution-Related Ilness: Effects of Particles. Science 2005 May.; 308(5723): 804-806

[Nemery and Nemmar, 2001] Nemery B, Hoet PH, Nemmar A. The Meuse Valley fog of 1930: an air pollution disaster. Lancet. 2001 Mar 3;357(9257):704–708.

[Okazaki et al., 1987] Okazaki, K.R.; Wienwe, W. y Willeke, K. 1987. “The combined effect of aspiration y transmission on aerosol accuracy for horizontal isoaxial sampling”. Atmospheric. Environment, 21(5), pp1181-1185.

[Omer and Ashgriz, 2011] Omer, K. and Ashgriz, N. "Spray Nozzles," in Handbook of Atomization and Sprays, ed: Springer, 2011.

[Park et al. 2005] Park, S., Jung, C., Jung, K., Lee, B., and Lee, K.: Wet scrubbing of polydisperse aerosols by freely falling droplets, Journal of Aerosol Science, 36, 1444 – 1458, doi:10.1016/j.jaerosci.2005.03.012, 2005.

[Pérez-Díaz 2018.a] Pérez-Díaz JL, Qin Y, Ivanov O, Quiñones J, Stengl V, Nylander K, Hornig W, Álvarez J, Ruiz-Navas EM, Manzanec K (2018.a) Fast response CBRN high-scale decontamination system: COUNTERFOG. In: Malizia A, D'Arienzo M (eds) Enhancing CBRNE safety & security: proceedings of the SICC 2017 conference. Springer, Cham

[Pérez-Díaz 2018.b] Pérez-Díaz, J.L., Llerena-Aguilar, F.J. Martín-Pérez, T., Sánchez-García-Casarrubios, J. and Ruiz-Navas, E. (2018.b). Decontamination of Diesel particles from air by using the Counterfog® system. Air Quality, Atmosphere & Health, 12 (63): 1-6

[Pérez-Díaz et al. 2018] Pérez-Díaz J.L., Qin Y., Ivanov O., Quiñones J., Stengl V., Nylander K., Hornig W., Álvarez J., Ruiz-Navas E.M., Manzanec K. (2018). Fast response CBRN high-scale decontamination system: COUNTERFOG. In: Malizia A, D'Arienzo M (eds) Enhancing CBRNE safety & security: proceedings of the SICC 2017 conference. Springer, Cham

[Pérez-Díaz et al., 2013] Pérez-Díaz, J.L et al. (2013). Method for Modifying the Surface Tension in Liquid-Air Interfaces. ES Patent P201132074, 24 July 2013.

[Pérez-Díaz et al., 2017] Pérez-Díaz, J.L. et al. (2017). Fogs: Physical Basis, Characteristic Properties, and Impacts on the Environment and Human Health. Water, 9 (10): 807-827

[PNR, 2007] PNR. (CTG SH 07 EU). Spray Engineering Handbook. https://docplayer.net/23948198-Spray-engineering-handbook-ctg-sh-07-eu.html
[Pope et al., 1995] Pope, C.A. et al. (1995). Particulate air pollution as a predictor of mortality in a prospective study of U.S. adults. Am J Respir Crit Care Med 1955; 151: 669-674.

[Pope et al., 2002] Pope CA. 3rd et al. Lung Cancer, Cardiopulmonary Mortality, and Long-term Exposure to Fine Particulate Air Pollution. JAMA. 2002 Mar.; 287(9): 1132-1141

[Pope, 2000] Pope CA., 3rd Epidemiology of fine particulate air pollution and human health: biologic mechanisms and who's at risk? Environ Health Perspect. 2000 Aug;108 (Suppl 4): 713–723.

[Pramod, et al. 2011] Pramod, K. et al . 2011. Aerosol Meausrement. Principles, Techniques, and Apllications. Third Edition.

[Pruppacher and Klett, 1997] Pruppacher, H. R. and Klett, J. D.: Microphysics of Clouds and Precipitation., Kluwer : Dordrecht, The Netherlands, 1997.

[Quincey, 2007] Quincey, P. (2007). A relationship between Black Smoke Index and Black Carbon concentration. Atmospheric Environment 2007; 47: 7964-7968

[Radke et al., 1980] Radke, L. F., Hobbs, P. V., and Eltgroth, M. W.: Scavenging of Aerosol Particles by Precipitation, J. Appl. Meteor., 19, 715–722, doi:10.1175/1520-0450(1980)019h0715:SOAPBPi2.0.CO;2, 1980.

[Rijnders et al., 2001] Rijnders, E. et al. (2001). Personal and outdoor nitrogen dioxide concentrations in relation to degree of urbanization and traffic density. Environ Health Perspect 2001 Jun.: 109(3): 411-417.

[Roach 1994] Roach, W.T. (1994). Back to basics: Fog: Part 1-Definitions and basic physics. Weather. Royal Meteorolical Society, 49 (12): 411-415

[Rostami, 2009] Rostami, A.A. (2009). Computational Modeling of Aerosol Deposition in Respiratory Tract: A Review. Inhalation Toxicol. 21: 262–290.

[Rotz et al., 2002] Rotz, L.D. et al. (2002). Public Health Assessment of Potential Biological Terrorism Agents. Emerging Infectious Diseases 2002 Feb.; 8(2): 225-230

[Ruppin, 1979] Ruppin, L. (1979). Mie theory with spatial dispersion. Optics Communications, 30 (3): 390-382

[Samet, Zeger and Dominici 2000] Samet J., Zeger S.L. and Dominici, F. (2000). The National Morbidity, Mortality and Air Pollution Study. Part II Results. Health Effects Institute Report no 94, Part II 2000 Jun.

[Sartor, 1954] Sartor, D. (1954). A laboratory investigation of collision efficiencies, coalescence and electrical charging simulated cloud droplets. J. Meteor.1854 Apr.; 11: 91-103

[Schmitt and Waldmann, 1960] Schmitt and Waldmann, 1960 K.H. Schmitt, L. WaldmannUntersuchungen an Schwebstoffteilchen in diffundierendem Gasen Z. Naturforsch., 15A (1960), pp. 843-851

[Schmitt, 1961] Schmitt, 1961 K.H. SchmittUntersuchungen an Schwebstoffteilchen in diffundierendem. Wasserdampf Z. Naturforsch., 16a (1961), pp. 144-149

[Schroth, 1996] Schroth, T., 1996. New HEPA/ULPA filters for clean-room technology. Filtration & Separation. 33 (3)- 245-250.

[Schwartz, 1999] Schwartz J.(1999). Air pollution and hospital admissions for heart disease in eight U.S. counties. Epidemiology 1999 Jan.; 10(1): 17–22

[Seinfeld and Pandis, 2006] Seinfeld, J. H. and Pandis, S. N.: Atmospheric Chemistry and Physics: From Air Pollution to Climate Change:, John Wiley & Sons, Inc., 2006.

[Seinfeld and Pandis, 2012] Seinfeld, J. H. and Pandis, S. N.: Atmospheric chemistry and physics: from air pollution to climate change, John Wiley & Sons, 2012.

[Sexton, Spengler and Treitman, 1984] Sexton, K.; Spengler, J.D. and Treitman, R.D. (1984) “Personal exposure to respirable particles: A case study in Waterbury, Vermont,” Atmos. Environ. 1984; 18(7): 1385–1398

[Sidell and Borak, 1992] Sidell F.R. and Borak, J. (1992), Chemical warfare agents: II. nerve agents. Annals of Emergency Medicine 1992 Jul.; 21(7): 865-871

[Slinn and Hales, 1971] Slinn, W. G. N. and Hales, J. M.: A Reevaluation of the Role of Thermophoresis as a Mechanism of In- and Below-Cloud Scavenging, J. Atmos. Sci., 28, 1465–1471, doi:10.1175/1520-0469(1971) 028h1465:AROTROi2.0.CO;2, 1971.

[Slinn, 1983] Slinn, W. G. N.: Precipitation scavenging, in: Atmospheric Sciences and Power Production, chap. 11, Division of Biomedical Environmental Research,U.S. Department of Energy, Washington DC, USA, 1983.

[Stefan, 1881] Stefan, 1881 J. StefanÜber die Verdampfung aus einem kreisförming oder elliptisch begrenzten Becken Wien. Ber., 83 (1881), pp. 943-949

[Sunyer, 1991] Sunyer J. et al. (1991). Air pollution and emergency room admissions for chronic obstructive pulmonary diseases. Am J Epidemiol 1991; 134: 277–86

[Talbot et al., 1980] Talbot, R.K. Cheng, R.W. Schefer, D.R. Willis. Thermophoresis of particles in a heated boundary layer J. Fluid Mech., 101 (1980), pp. 737-758

[Thatcher and Layton, 1995] Thatcher, T.L.; Layton, D.W. (1995) "Deposition, resuspension, and penetration of particles within a residence," Atmos. Environ. 1995, 29, 14871497.

[Tinsley and Leddon, 2013] Tinsley, B. A. and Leddon, D. B.: Charge modulation of scavenging in clouds: Extension of Monte Carlo simulations and initial parameterization, J. Geophys. Res. Atmos., 118, 8612–8624, doi: 10.1002/jgrd.50618, 2013.

[Tinsley et al., 2001] Tinsley, B. A. et al. (2001). Electroscavenging in clouds with broad droplet size distributions and weak electrification. Atmospheric Research. 59-60: 115-13.

[Tinsley et al., 2006a] Tinsley, B. A., Zhou, L., and Plemmons, A.: Changes in scavenging of particles by droplets due to weak electrification in clouds, Atmospheric Research, 79, 266 – 295, doi:10.1016/j.atmosres.2005.06.004, 2006a.

[Tinsley et al., 2006b] Tinsley, B. A., Zhou, L., and Plemmons, A.: Changes in scavenging of particles by droplets due to weak electrification in clouds, Atmospheric Research, 79, 266–295, doi:10.1016/j.atmosres.2005. 06.004, 2006b.

[Tinsley, 2010] Tinsley, B. A.: Electric charge modulation of aerosol scavenging in clouds: Rate coefficients with Monte Carlo simulation of diffusion, J. Geophys. Res. Atmos., 115, doi:10.1029/2010JD014580, 2010.

[Touloumi et al., 1997] Touloumi G. et al. (1997). Short-term effects of ambient oxidant exposure on mortality: a combined analysis within the APHEA project. Am J Epidemiol 1997 Jul.; 146(2): 177–185

[Touloumi, Samoli and Katsouyanni, 1996] Touloumi G., Samoli E. and Katsouyanni K (1996). Daily mortality and 'winter type' air pollution in Athens, Greece—a time-

series analysis within the APHEA project. J Epidemiol Common Health 1996; 50(1): 47–51

[Tripathi and Harrios, 2002] Tripathi, S.N. and Harrios, R.G. (2002). Enhancemente of contact nucleation by scavenging of charged aerosol particles. Atmospheric Research 2002 May.; 62(1-2): 57-70.

[Tufts et al., 2014] Tufts. JA et al. (2014).Bacillus thuringiensis as a surrogate for Bacillus anthracis in aerosol research. World Journal of Microbiology and Biotechnology. 24(5): 1453-1461

[UECD, 2002] EUROPEAN UNION. Directive 2002/3/EC of the European Parliament and of the Council of 12 February 2002. Relating to ozone in ambient air, 1999.

[UECD, 2008] EUROPEAN UNION. Directive 2008/50/EC of the European Parliament and of the Council of 21 May 2008. On ambient air quality and cleaner for Europe, 2008.

[Vincent, 1989] Vincent, J.H. 1989. "Aerosol sampling. Science and Practice". John Wiley & Sons. Chichester - New York - Brisbane - Toronto - Singapore.

[Vogt et al., 2003] Vogt R, Kirchner U, Scheer V, Hinz K P, Trimborn A and Spengler B 2003. Identification of diesel exhaust particles at an Autobahn, urban and rural location using single-particle mass spectrometry J. Aerosol. Sci. 34 319-337

[Wagner, 2012] Wagner G. W., Peterson G. W., and Mahle J. J. (2012). Effect of adsorbed water and surface hydroxyls on the hydrolysis of VX, GD, and HD on Titania Materials: The development of self-decontaminating paints. Ind.Eng.Chem.Res, vol. 51, p. 35983603, 2012.

[Waldmann, 1959] L. Waldmann (1959). Über die Kraft eines inhomogenen Gases auf kleine suspendierte Kugeln. Zeitschrift für Naturforschung, 14(7): 589-599

[Wang and Pruppacher, 1977] Wang, P. K. and Pruppacher, H. R.: An Experimental Determination of the Efficiency with Which Aerosol Particles are Collected byWater Drops in Subsaturated Air, J. Atmos. Sci., 34, 1664–1669, doi:10.1175/1520-0469(1977)034h1664:AEDOTEi2.0.CO;2, 1977.

[Wang et al., 1978] Wang, P. K., Grover, S. N., and Pruppacher, H. R.: On the Effect of Electric Charges on the Scavenging of Aerosol Particles by Clouds and Small Raindrops, J. Atmos. Sci., 35, 1735–1743, doi: 10.1175/1520-0469(1978)035h1735:OTEOECi2.0.CO;2, 1978.

[Wang et al., 2010] Wang, X., Zhang, L., and Moran, M. D.: Uncertainty assessment of current size-resolved parameterizations for below-cloud particle scavenging by rain, Atmos. Chem. Phys., 10, 5685–5705.

[Watson, Chow and Pace, 2000] Watson, J.G., Chow, J.C. and Pace, T.G. (2000). Fugitive Dust Emissions. Air Pollution Engineering Manual, Second Edition, Davis, W.T. (Ed.), John Wiley & Sons, Inc., New York, p. 117–135

[Wen, 1996] Wen, C.C. 1996. The Fundamentals of Aerosol Dynamics. World Scientific. Singapore-New Jersey-London-Hong Kong.

[Went, 1966] Went, F. W. (1966). On the nature of Aitken condensation nuclei. Tellus 1966; 18(2-3): 549-556

[Whitby 1972] Whitby, K.T., Husar, R.B., Liu, B.Y.H. (1972). The Aerosol Size Distribution of Los Angeles Smog. J. Colloid Interface Sci. 39: 177–204

[Whitby, 1978] Whitby, K. T., The physical characteristics of sulfur aerosols, Atmos. Environ., 12, 135-159, 1978.

[WHO, 2000] WHO Air Quality Guidelines for Europe, Second edition. Copenhagen, WHO Regional Office for Europe, 2000 (WHO Regional Publications, European Series, No 91).

[WHO, 2002] WHO, The World Health Report 2002. Reducing Risks, Promoting Healthy life. Geneva, World Health Organization, 2002. pp-67-73

[WHO, 2006] WHO, 2006, Air Quality Guidelines: Global update 2005. Particulate matter, ozone, nitrogen dioxide and sulphur dioxide, World Health Organization, Regional Office for Europe, Copenhagen.

[WHO, 2013] World Health Organization (WHO) 2013 Health effects of particulate matter Convention on Long-Range Transboundary Air Pollution ISBN 978 92 890 00017

[Wichmann, 2007] Wichmann H E. 2007. Disel Exhaust Particles Inhal. Toxicol.19 241-244

[Wilson and Suh, 1997] Wilson, W.E. and Suh, H.H (1997). "Fine and coarse particles: Concentration relationships relevant to epidemiological studies," J Air & Waste Manage. Assoc. 1997; 47(12): 1238–1249.

[WMO, 1992] WMO (1992). International Meteorological Vocabulary. Secretariat of the World Meteorological Organization, Geneva, Switzerland. WMO Publication 182

[Yamamoto and Ishihara, 1988] Yamamoto and Ishihara, 1988 K. Yamamoto, Y. IshiharaThermophoresis of a spherical particle in a rarefied gas of a transition regime Phys. Fluids, 31 (1988), pp. 3618-3624

[Zhou and Cheng, 2005] Zhou, Y. and Cheng, Y.S. (2005). Particle Deposition in a Cast of Human Tracheobronchial Airways. Aerosol Sci. Technol. 39: 492–500.

Annex A

- **Test I**

NOZZLE	Model	B
	Scale	1:2
AIR PRESSURE		4.5 bar
WATER PRESSURE		1.5 bar

Stabilized cone of nozzle B1:2 for a P_{air}= 4.5 bar and P_{water}= 1.5 bar combination and cone opening angle.

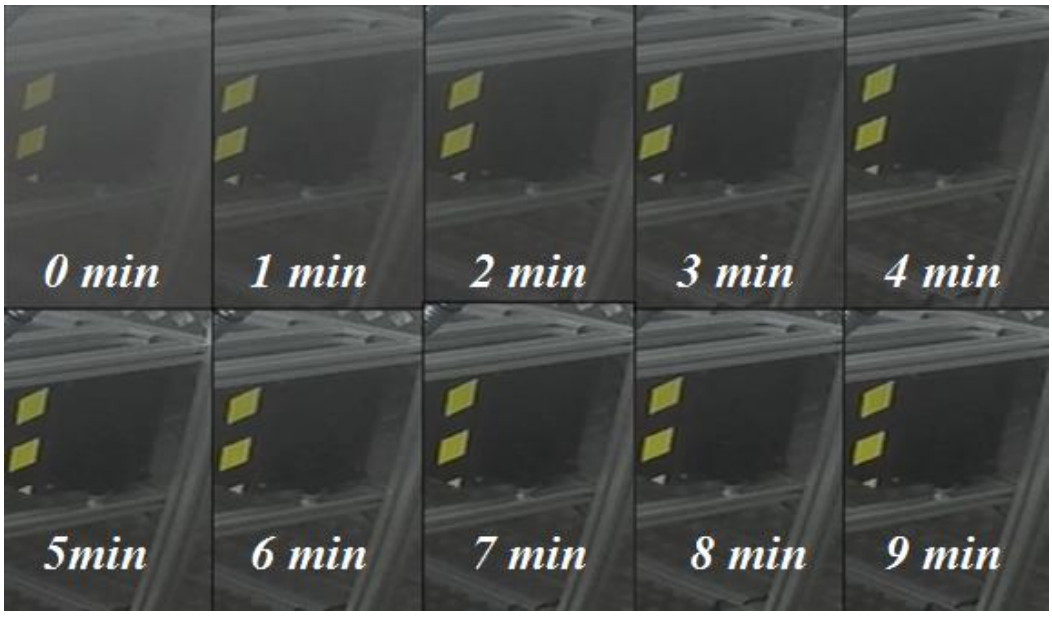

Time evolution of the fog generated with the B1:2 nozzle for a combination of P_{air}= 4.5 bar and P_{water}= 1.5 bar. The images show the concentration of fog in the room every minute since the shot was taken.

The pressurized water tank, with a capacity of 4.5 l of water, is not emptied during shooting. The maximun water flow rate obtained is lower than the sensitivity offered by the flowmeters installed in the laboratory. Therefore, it has not been possible to obtain a numerical flow rate value. Figures show the cone stabilized during the shooting and the evolution of the fog with the time elapsed after the shot.

- **Test II**

NOZZLE	Model	B
	Scale	1:2
AIR PRESSURE		5 bar
WATER PRESSURE		5 bar

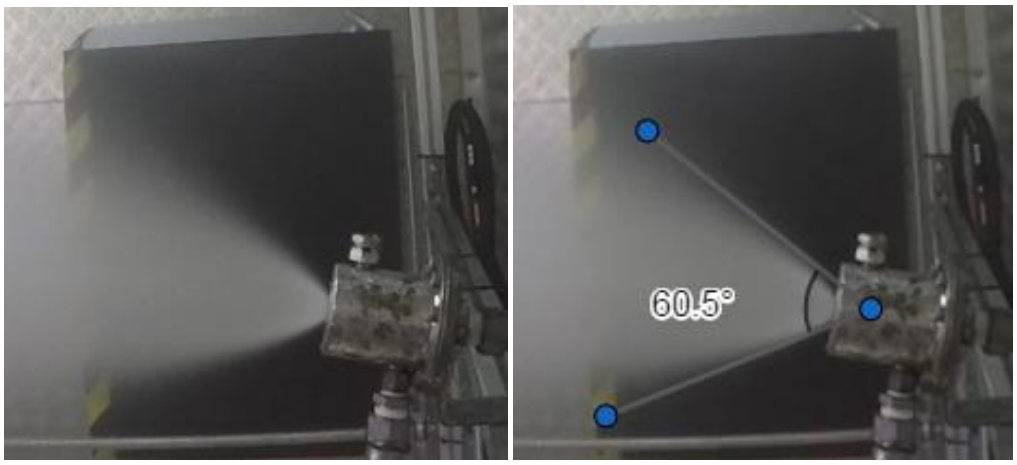

Stabilized cone of nozzle B1:2 for a P_{air}= 5 bar and P_{water}= 5 bar combination and cone opening angle.

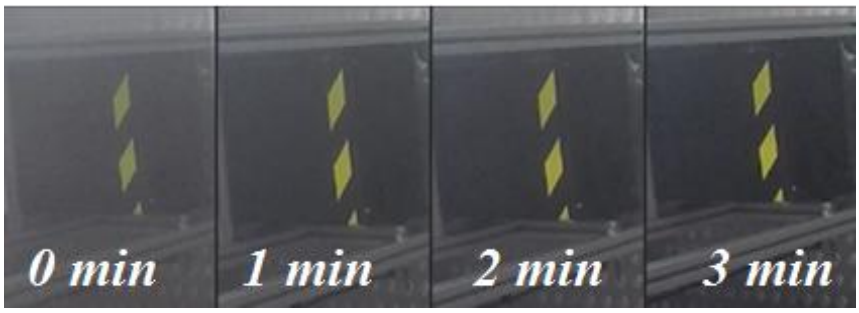

Time evolution of the fog generated with the B1:2 nozzle for a combination of P_{air}= 5 bar and P_{water}= 5 bar. The images show the concentration of fog in the room every minute since the shot was taken.

The pressurized water tank, with a capacity of 4.5 l of water, is not emptied during shooting. The water maximum flow rate obtained is 0.13 l/s. Figures show the cone stabilized during the shooting and the evolution of the fog with the time elapsed after the shot.

- **Test III**

NOZZLE	Model	B
	Scale	1:2
AIR PRESSURE		5 bar
WATER PRESSURE		10 bar

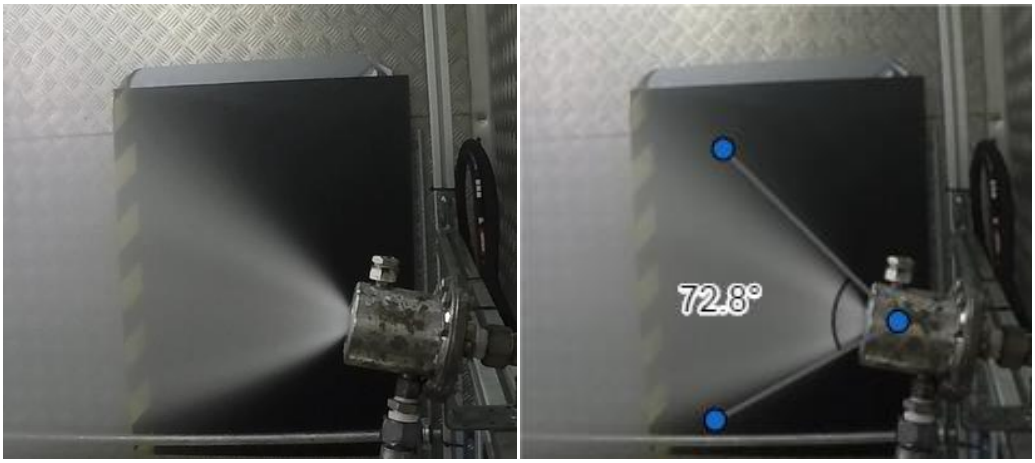

Stabilized cone of nozzle B1:2 for a P_{air}= 5 bar and P_{water}= 10 bar combination and cone opening angle.

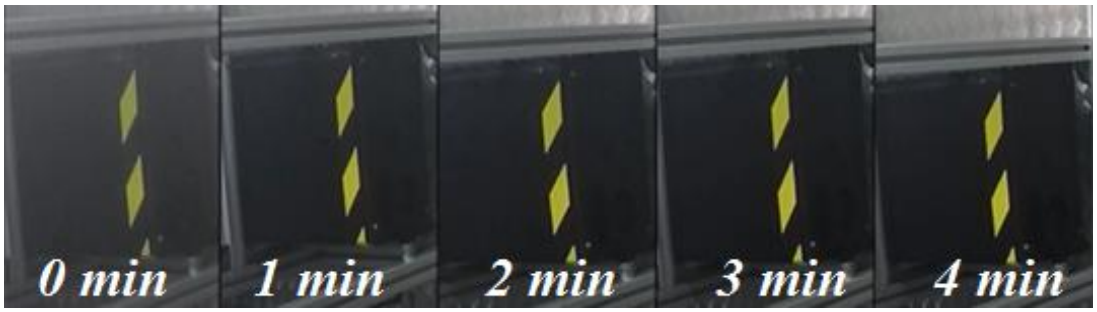

Time evolution of the fog generated with the B1:2 nozzle for a combination of P_{air}= 5 bar and P_{water}= 10 bar. The images show the concentration of fog in the room every minute since the shot was taken.

The pressurized water tank, with a capacity of 4.5 l of water, is emptied during shooting. The water flow rate obtained is 0.23 l/s. Figure show the cone stabilized during the shooting and the evolution of the fog with the time elapsed after the shot.

- **Test IV**

NOZZLE	Model	B
	Scale	1:2
AIR PRESSURE		5 bar
WATER PRESSURE		15 bar

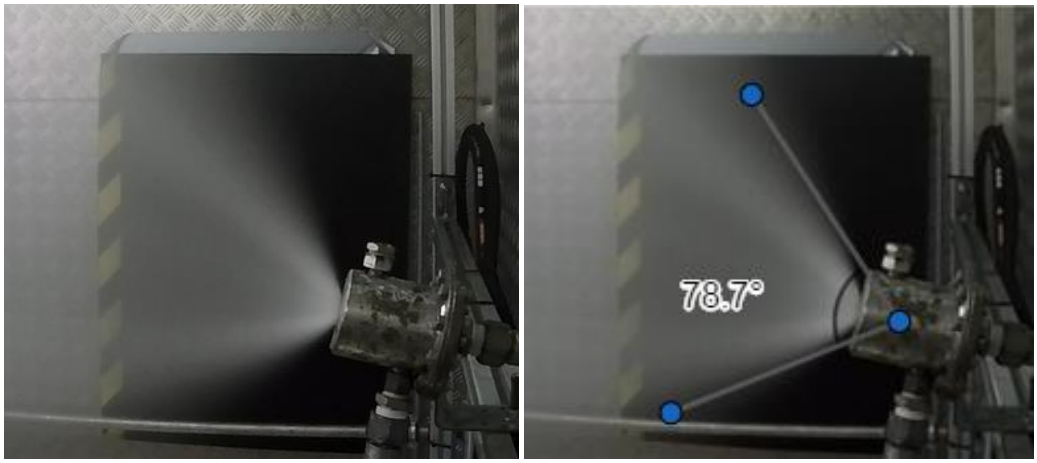

Stabilized cone of nozzle B1:2 for a P_{air}= 5 bar and P_{water}= 15 bar combination and cone opening angle.

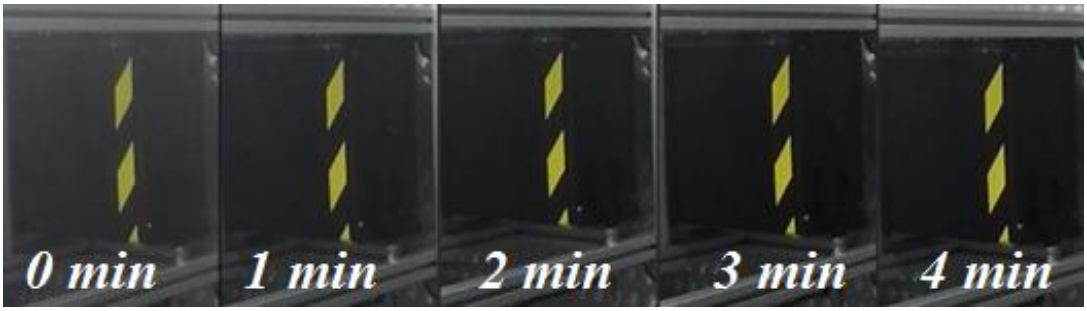

Time evolution of the fog generated with the B1:2 nozzle for a combination of P_{air}= 5 bar and P_{water}= 15 bar. The images show the concentration of fog in the room every minute since the shot was taken.

The pressurized water tank, with a capacity of 4.5 l of water, is emptied during shooting. The water flow rate obtained is 0.30 l/s. Figures show the cone stabilized during the shooting and the evolution of the fog with the time elapsed after the shot.

- **Test V**

NOZZLE	Model	B
	Scale	1:2
AIR PRESSURE		5 bar
WATER PRESSURE		20 bar

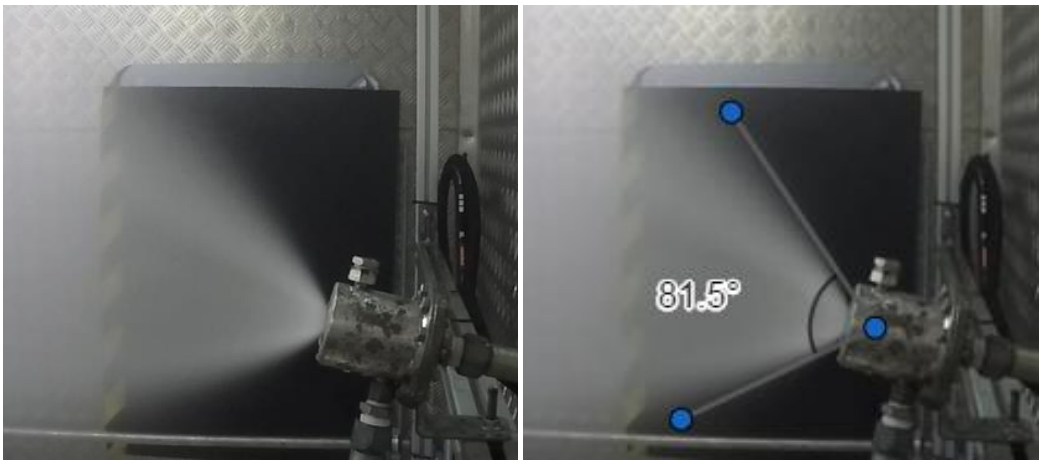

Stabilized cone of nozzle B1:2 for a P_{air}= 5 bar and P_{water}= 20 bar combination and cone opening angle.

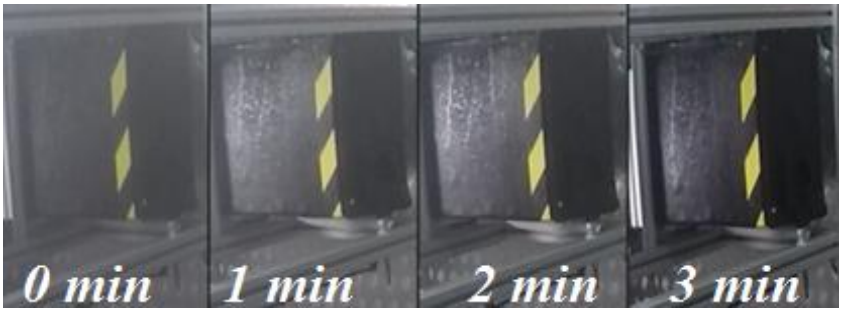

Time evolution of the fog generated with the B1:2 nozzle for a combination of P_{air}= 5 bar and P_{water}= 20 bar. The images show the concentration of fog in the room every minute since the shot was taken.

The pressurized water tank, with a capacity of 4.5 l of water, is emptied during shooting. The water flow rate obtained is 0.33 l/s. Figures show the cone stabilized during the shooting and the evolution of the fog with the time elapsed after the shot.

- **Test VI**

NOZZLE	Model	B
	Scale	1:2
AIR PRESSURE		5 bar
WATER PRESSURE		25 bar

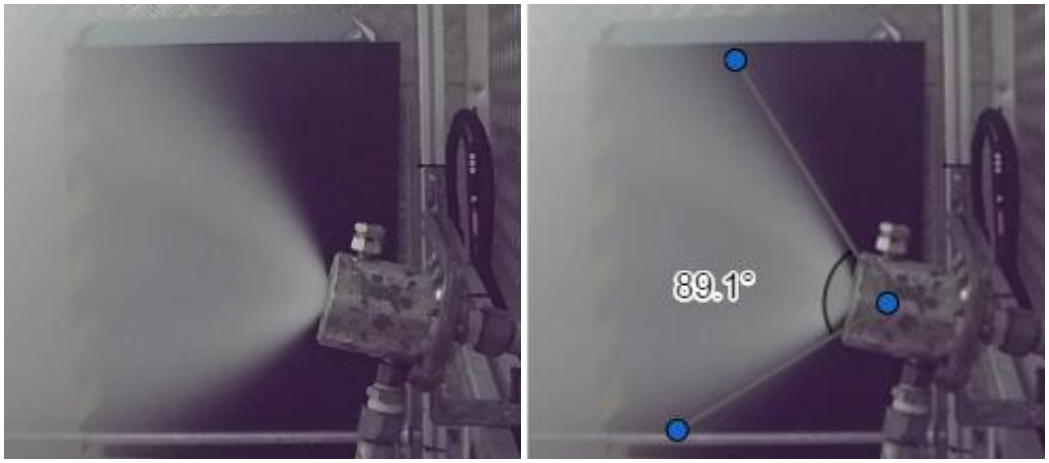

Stabilized cone of nozzle B1:2 for a P_{air}= 5 bar and P_{water}= 25 bar combination and cone opening angle.

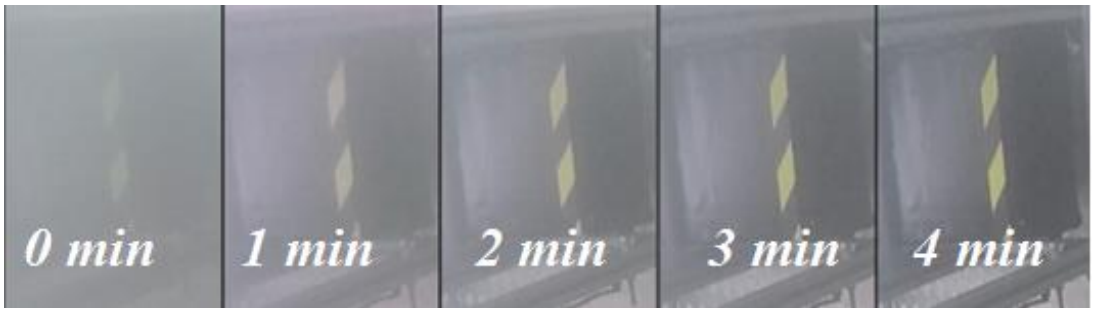

Time evolution of the fog generated with the B1:2 nozzle for a combination of P_{air}= 5 bar and P_{water}= 25 bar. The images show the concentration of fog in the room every minute since the shot was taken.

The pressurized water tank, with a capacity of 4.5 l of water, is emptied during shooting. The water flow rate obtained is 0.36 l/s. Figures show the cone stabilized during the shooting and the evolution of the fog with the time elapsed after the shot.

- **Test VII**

NOZZLE	Model	B
	Scale	1:2
AIR PRESSURE		6 bar
WATER PRESSURE		1.5 bar

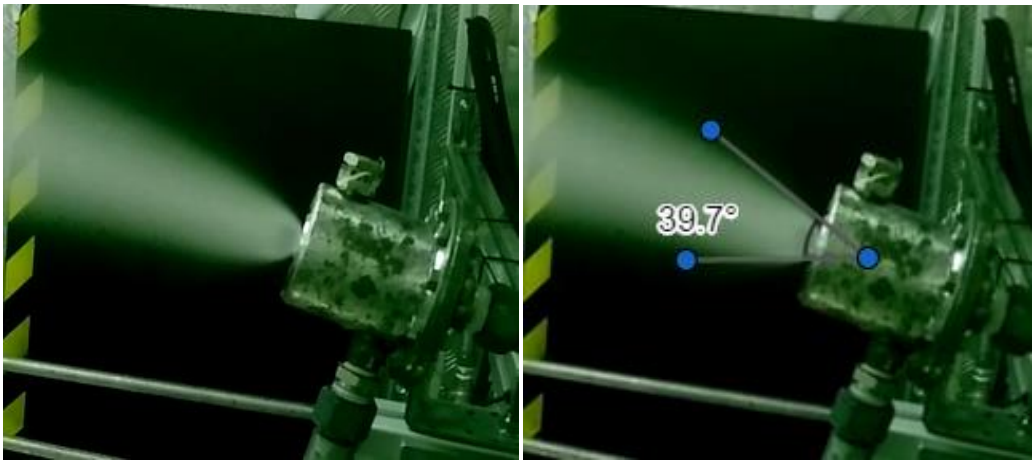

Stabilized cone of nozzle B1:2 for a P_{air}= 6 bar and P_{water}= 1.5 bar combination and cone opening angle.

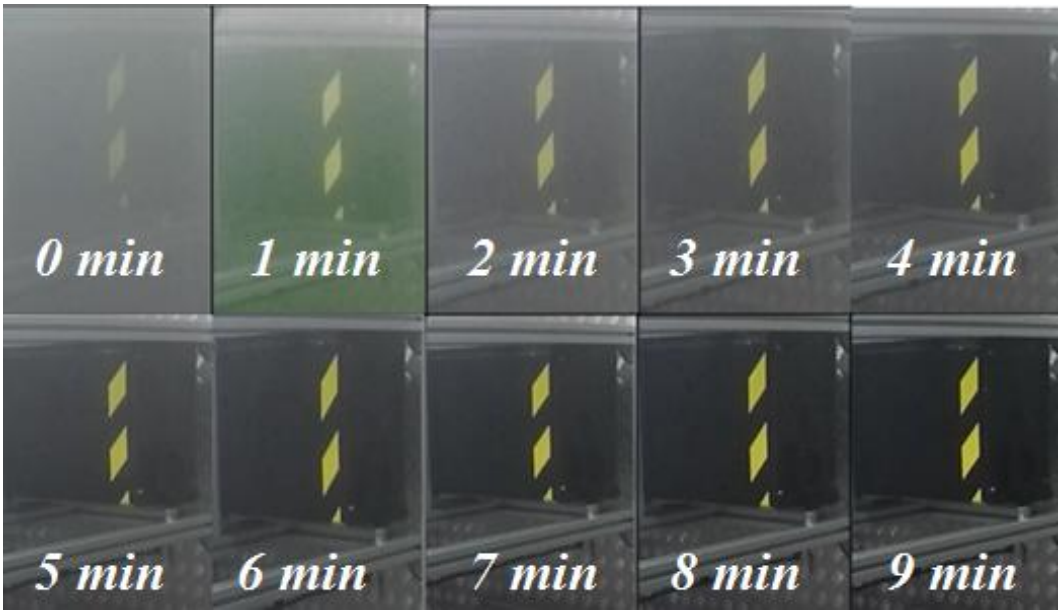

Time evolution of the fog generated with the B1:2 nozzle for a combination of P_{air}= 6 bar and P_{water}= 1.5 bar. The images show the concentration of fog in the room every minute since the shot was taken.

The pressurized water tank, with a capacity of 4.5 l of water, is not emptied during shooting. The flow maximun water flow rate obtained is lower than the sensitivity offered by the flow meters installed in the laboratory. Therefore, it has not been possible to obtain a numerical flow rate value. Figures show the cone stabilized during the shooting and the evolution of the fog with the time elapsed after the shot.

- **Test VIII**

NOZZLE	Model	B
	Scale	1:2
AIR PRESSURE		7 bar
WATER PRESSURE		1.5 bar

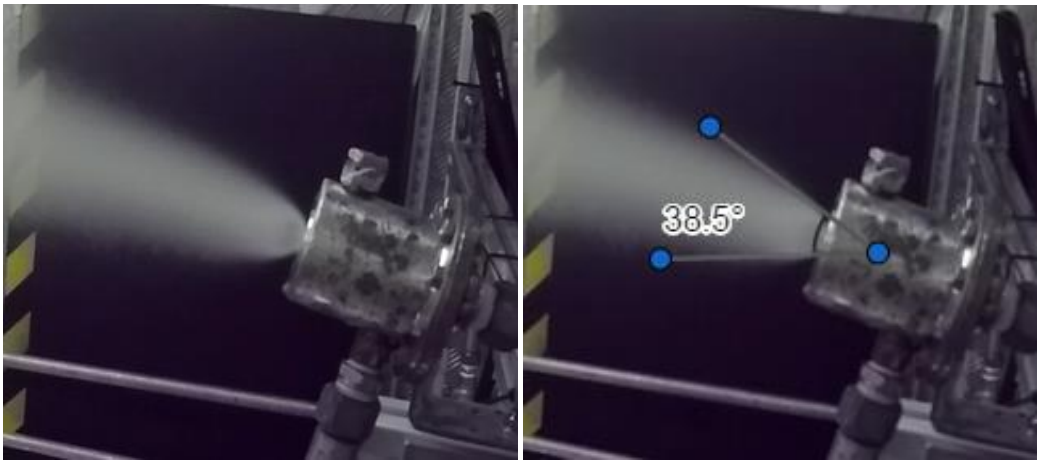

Stabilized cone of nozzle B1:2 for a P_{air}= 7 bar and P_{water}= 1.5 bar combination and cone opening angle.

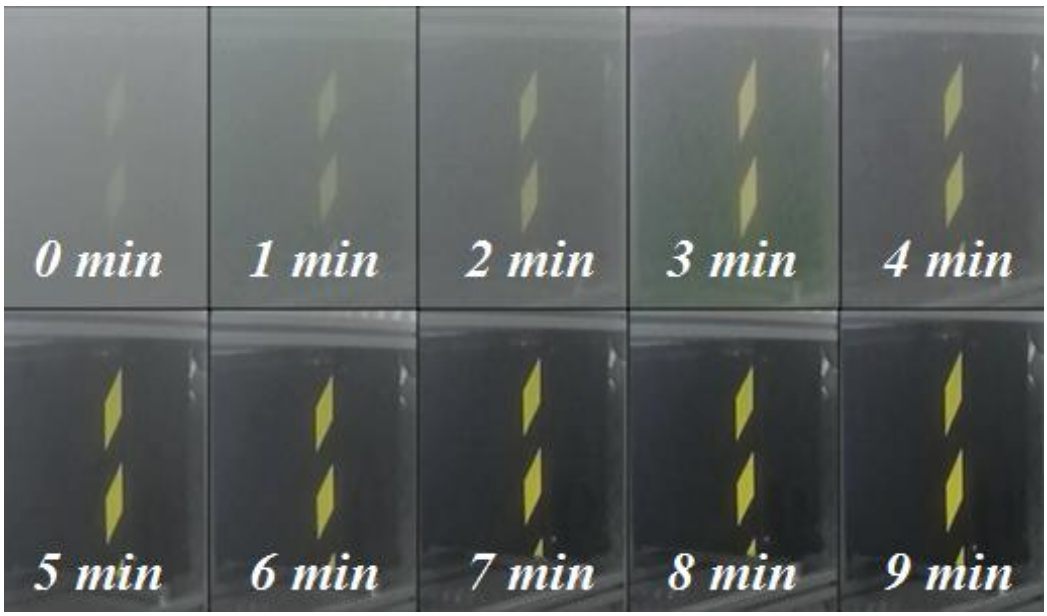

Time evolution of the fog generated with the B1:2 nozzle for a combination of P_{air}= 7 bar and P_{water}= 1.5 bar. The images show the concentration of fog in the room every minute since the shot was taken.

The pressurized water tank, with a capacity of 4.5 l of water, is not emptied during shooting. The flow maximun water flow rate obtained is lower than the sensitivity offered by the flow meters installed in the laboratory. Therefore, it has not been possible to obtain a numerical flow rate value. Figures show the cone stabilized during the shooting and the evolution of the fog with the time elapsed after the shot.

- **Test IX**

NOZZLE	Model	B
	Scale	1:2
AIR PRESSURE		8 bar
WATER PRESSURE		1.5 bar

Stabilized cone of nozzle B1:2 for a P_{air}= 8 bar and P_{water}= 1.5 bar combination and cone opening angle.

Time evolution of the fog generated with the B1:2 nozzle for a combination of P_{air}= 8 bar and P_{water}= 1.5 bar. The images show the concentration of fog in the room every minute since the shot was taken.

The pressurized water tank, with a capacity of 4.5 l of water, is not emptied during shooting. The flow maximun water flow rate obtained is lower than the sensitivity offered by the flow meters installed in the laboratory. Therefore, it has not been possible to obtain a numerical flow rate value. Figures show the cone stabilized during the shooting and the evolution of the fog with the time elapsed after the shot.

- **Test X**

NOZZLE	Model	B
	Scale	1:2
AIR PRESSURE		9 bar
WATER PRESSURE		1.5 bar

Stabilized cone of nozzle B1:2 for a P_{air}= 9 bar and P_{water}= 1.5 bar combination and cone opening angle.

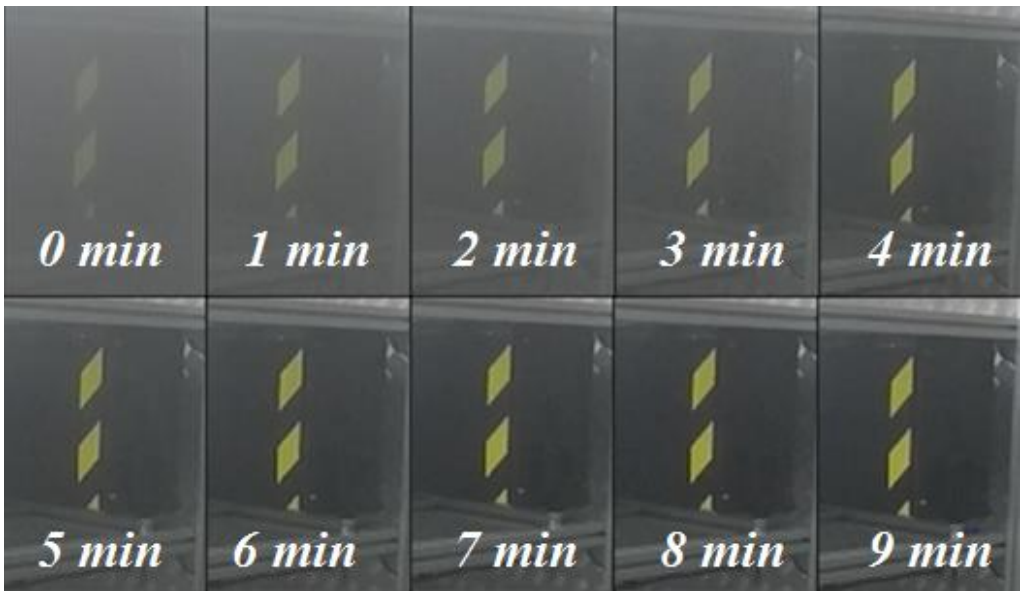

Time evolution of the fog generated with the B1:2 nozzle for a combination of P_{air}= 9 bar and P_{water}= 1.5 bar. The images show the concentration of fog in the room every minute since the shot was taken.

The pressurized water tank, with a capacity of 4.5 l of water, is not emptied during shooting. The flow maximun water flow rate obtained is lower than the sensitivity offered by the flow meters installed in the laboratory. Therefore, it has not been possible to obtain a numerical flow rate value. Figures show the cone stabilized during the shooting and the evolution of the fog with the time elapsed after the shot.

- **Test XI**

NOZZLE	Model	B
	Scale	1:2
AIR PRESSURE		10 bar
WATER PRESSURE		1.5 bar

No fog is generated for the chosen pressure combination.

- **Test XII**

NOZZLE	Model	B
	Scale	1:2
AIR PRESSURE		10 bar
WATER PRESSURE		5 bar

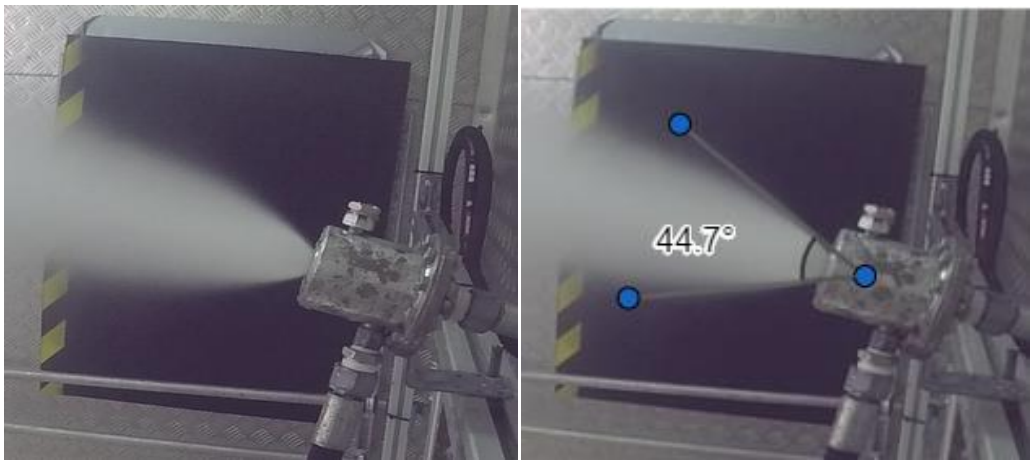

Stabilized cone of nozzle B1:2 for a P_{air}= 10 bar and P_{water}= 5 bar combination and cone opening angle.

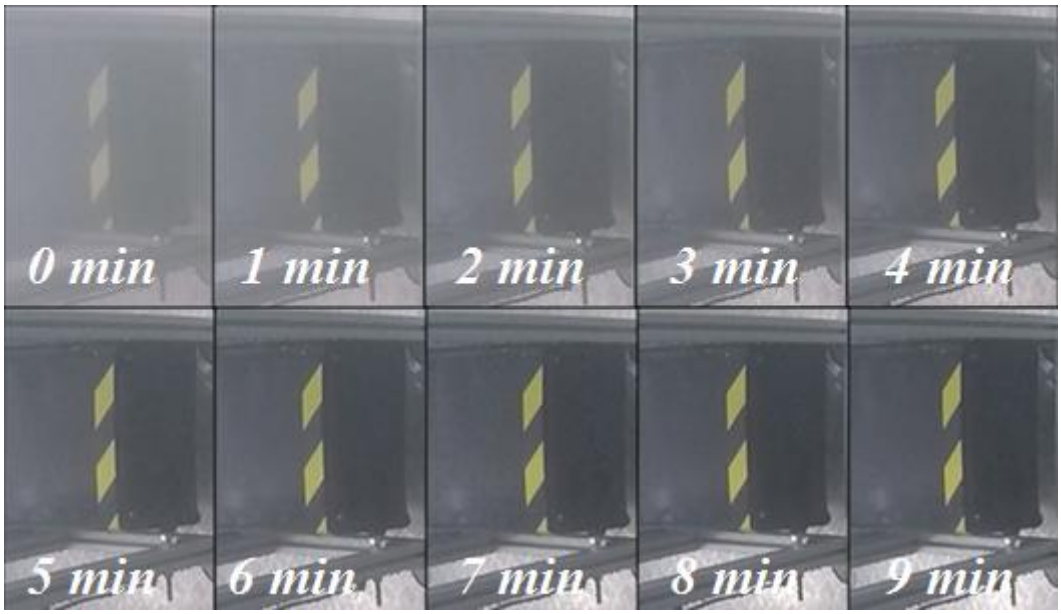

Time evolution of the fog generated with the B1:2 nozzle for a combination of P_{air}= 10 bar and P_{water}= 5 bar. The images show the concentration of fog in the room every minute since the shot was taken.

The pressurized water tank, with a capacity of 4.5 l of water, is not emptied during shooting. The water maximum flow rate obtained is 0.0425 l/s. Figures show the cone stabilized during the shooting and the evolution of the fog with the time elapsed after the shot.

- **Test XIII**

NOZZLE	Model	B
	Scale	1:2
AIR PRESSURE		10 bar
WATER PRESSURE		10 bar

Stabilized cone of nozzle B1:2 for a P_{air}= 10 bar and P_{water}= 10 bar combination and cone opening angle.

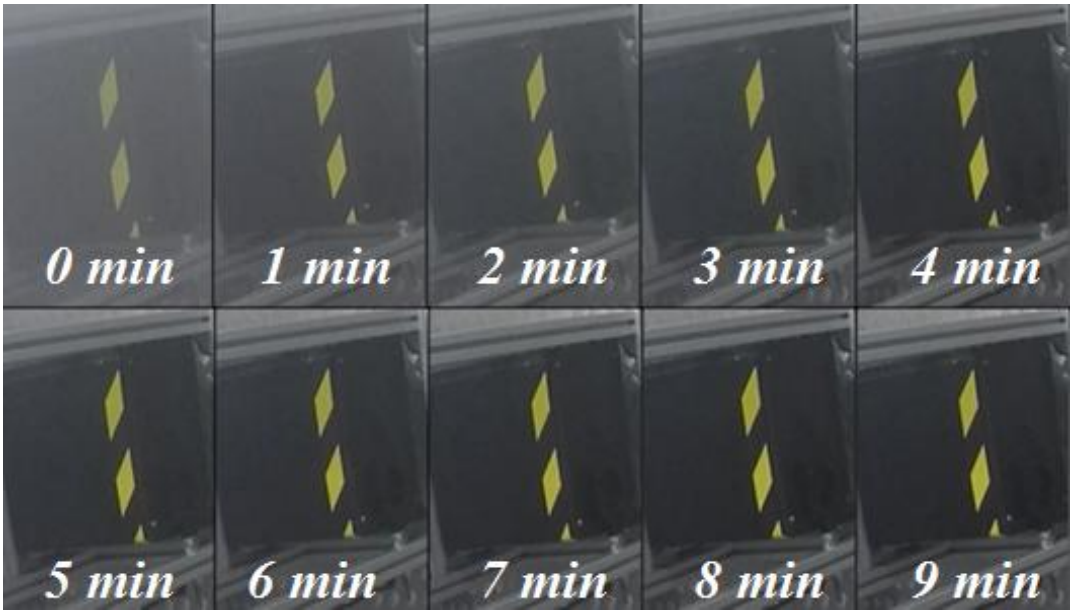

Time evolution of the fog generated with the B1:2 nozzle for a combination of P_{air}= 10 bar and P_{water}= 10 bar. The images show the concentration of fog in the room every minute since the shot was taken.

The pressurized water tank, with a capacity of 4.5 l of water, is not emptied during shooting. The water maximum flow rate obtained is 0.16 l/s. Figures show the cone stabilized during the shooting and the evolution of the fog with the time elapsed after the shot.

- **Test XIV**

NOZZLE	Model	B
	Scale	1:2
AIR PRESSURE		10 bar
WATER PRESSURE		15 bar

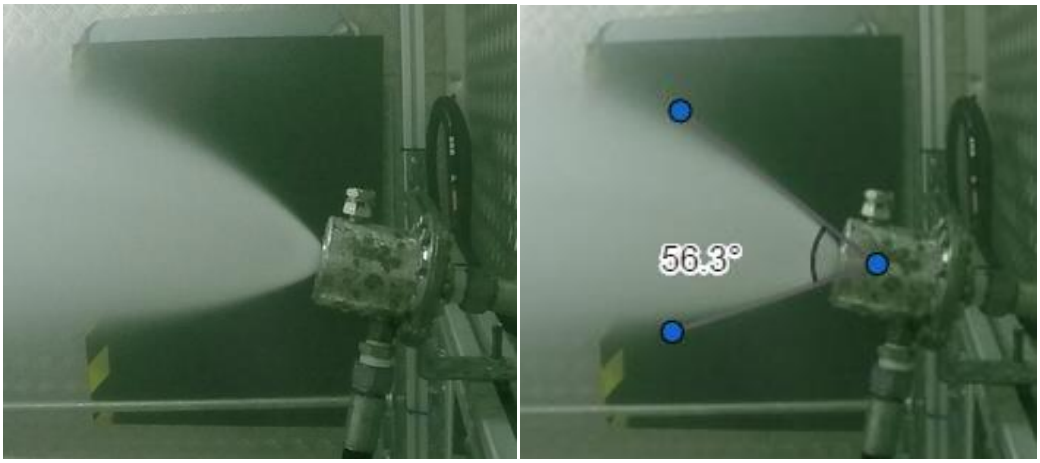

Stabilized cone of nozzle B1:2 for a P_{air}= 10 bar and P_{water}= 15 bar combination and cone opening angle.

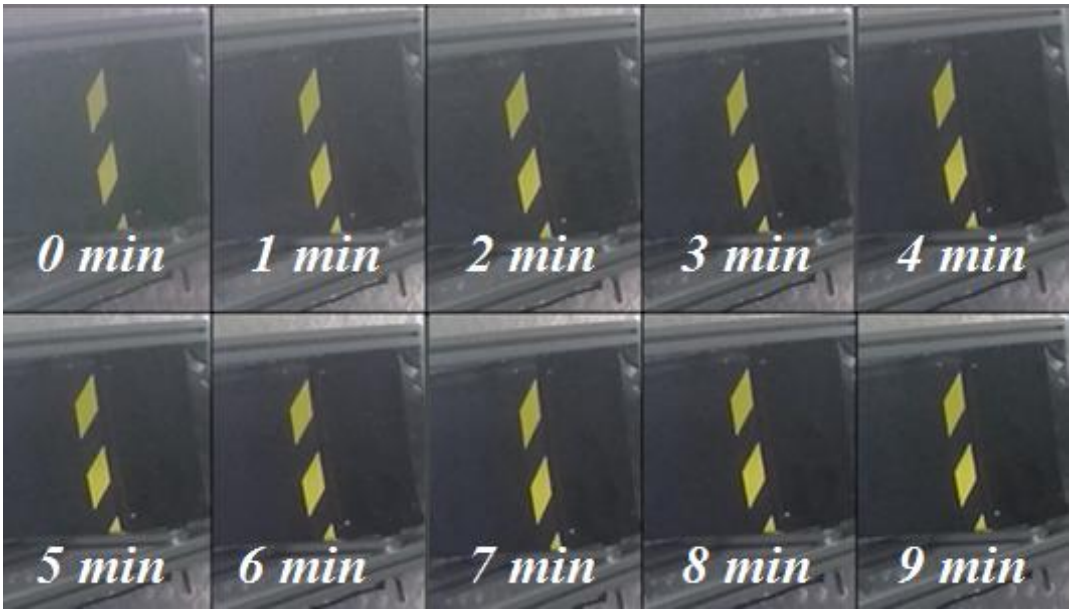

Time evolution of the fog generated with the B1:2 nozzle for a combination of P_{air}= 10 bar and P_{water}= 15 bar. The images show the concentration of fog in the room every minute since the shot was taken.

The pressurized water tank, with a capacity of 4.5 l of water, is emptied during shooting. The water flow rate obtained is 0.24 l/s. Figures show the cone stabilized during the shooting and s the evolution of the fog with the time elapsed after the shot.

- **Test XV**

NOZZLE	Model	B
	Scale	1:2
AIR PRESSURE		10 bar
WATER PRESSURE		20 bar

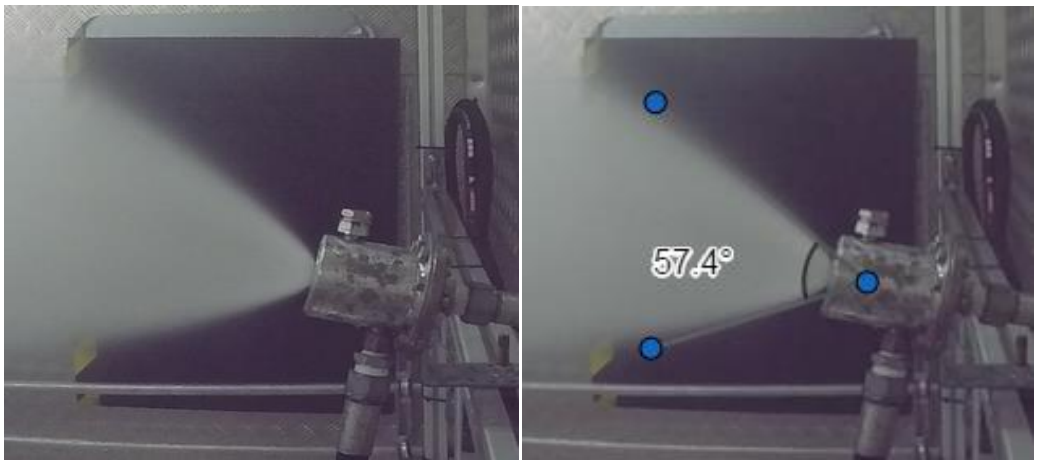

Stabilized cone of nozzle B1:2 for a P_{air}= 10 bar and P_{water}= 20 bar combination and cone opening angle.

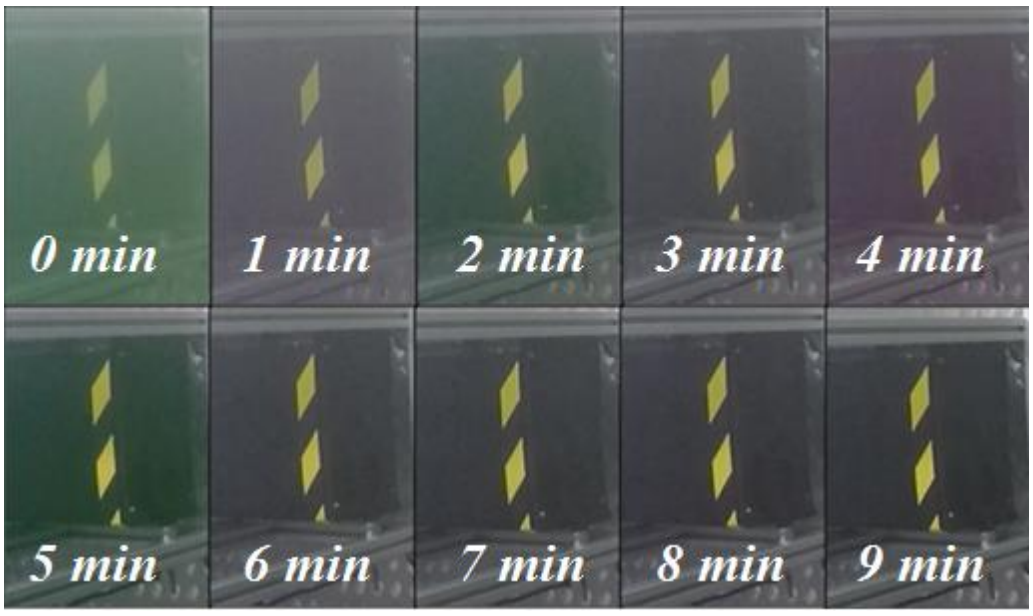

Time evolution of the fog generated with the B1:2 nozzle for a combination of P_{air}= 10 bar and P_{water}= 20 bar. The images show the concentration of fog in the room every minute since the shot was taken.

The pressurized water tank, with a capacity of 4.5 l of water, is emptied during shooting. The water flow rate obtained is 0.33 l/s. Figures show the cone stabilized during the shooting and the evolution of the fog with the time elapsed after the shot.

- **Test XVI**

NOZZLE	Model	B
	Scale	1:2
AIR PRESSURE		10 bar
WATER PRESSURE		25 bar

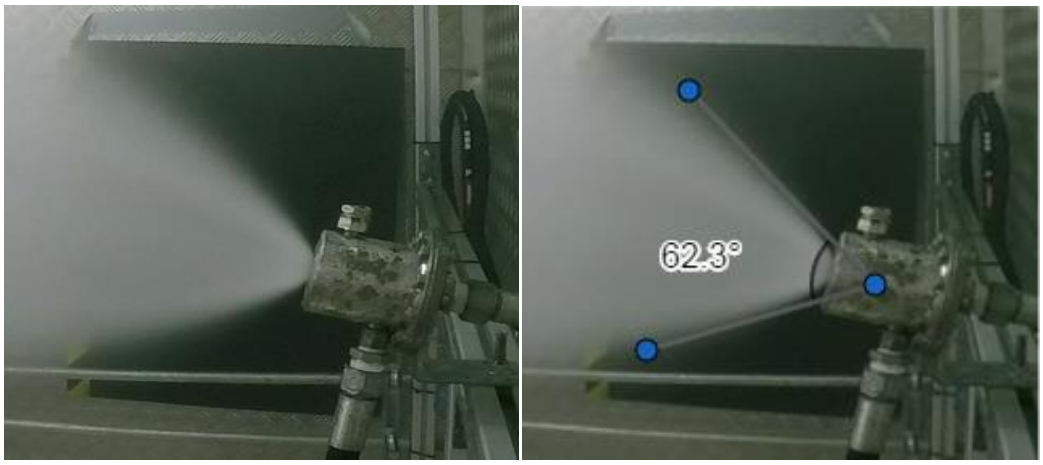

Stabilized cone of nozzle B1:2 for a P_{air}= 10 bar and P_{water}= 25 bar combination and cone opening angle.

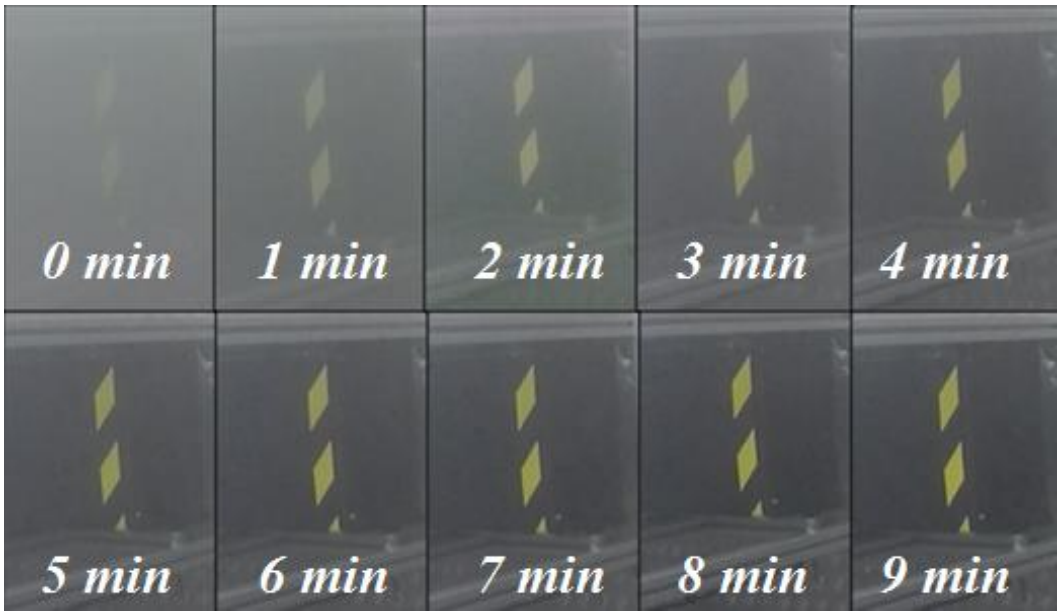

Time evolution of the fog generated with the B1:2 nozzle for a combination of P_{air}= 10 bar and P_{water}= 25 bar. The images show the concentration of fog in the room every minute since the shot was taken.

The pressurized water tank, with a capacity of 4.5 l of water, is emptied during shooting. The water flow rate obtained is 0.38 l/s. Figures show the cone stabilized during the shooting and the evolution of the fog with the time elapsed after the shot.

- **Test XVII**

NOZZLE	Model	B
	Scale	1:2
AIR PRESSURE		12 bar
WATER PRESSURE		3 bar

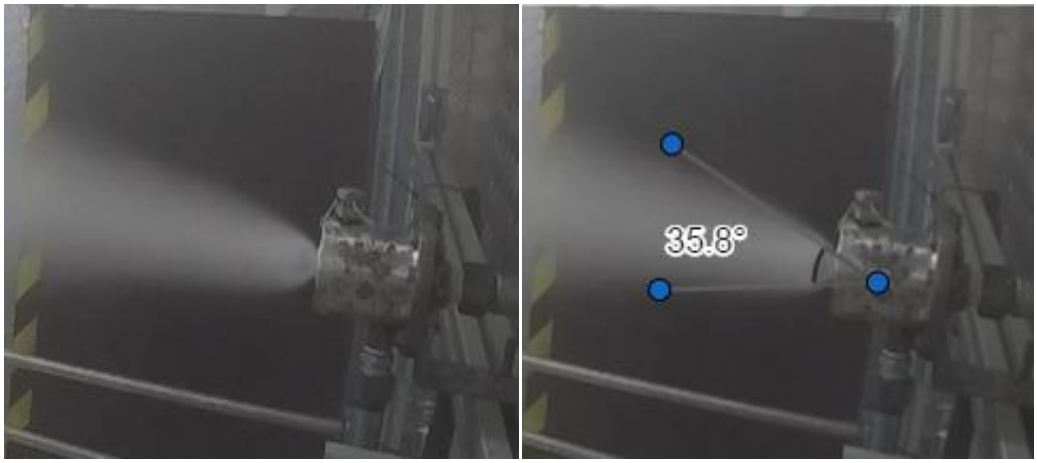

Stabilized cone of nozzle B1:2 for a P_{air}= 12 bar and P_{water}= 3 bar combination and cone opening angle.

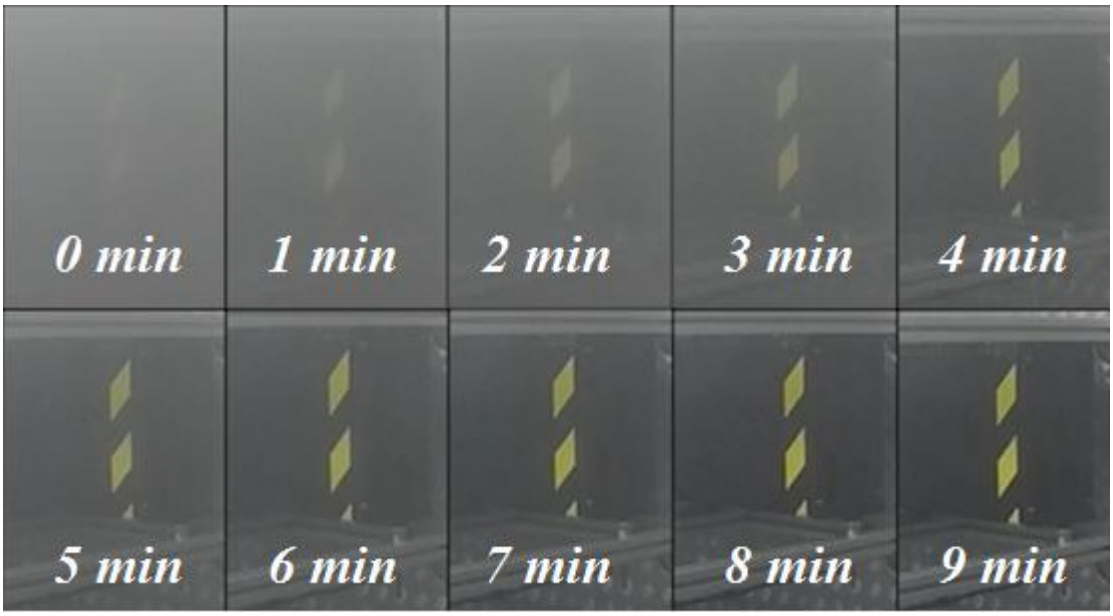

Time evolution of the fog generated with the B1:2 nozzle for a combination of P_{air}= 12 bar and P_{water}= 3 bar. The images show the concentration of fog in the room every minute since the shot was taken.

The pressurized water tank, with a capacity of 4.5 l of water, is not emptied during shooting. The flow maximun water flow rate obtained is lower than the sensitivity offered by the flow meters installed in the laboratory. Therefore, it has not been possible to obtain a numerical flow rate value. Figures show the cone stabilized during the shooting and the evolution of the fog with the time elapsed after the shot.

- **Test XVIII**

NOZZLE	Model	B
	Scale	1:2
AIR PRESSURE		15 bar
WATER PRESSURE		3 bar

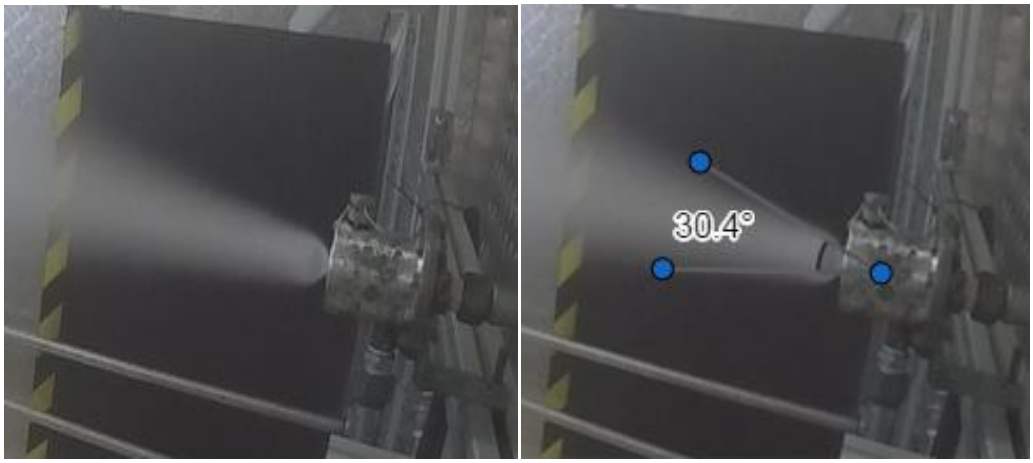

Stabilized cone of nozzle B1:2 for a P_{air}= 15 bar and P_{water}= 3 bar combination and cone opening angle.

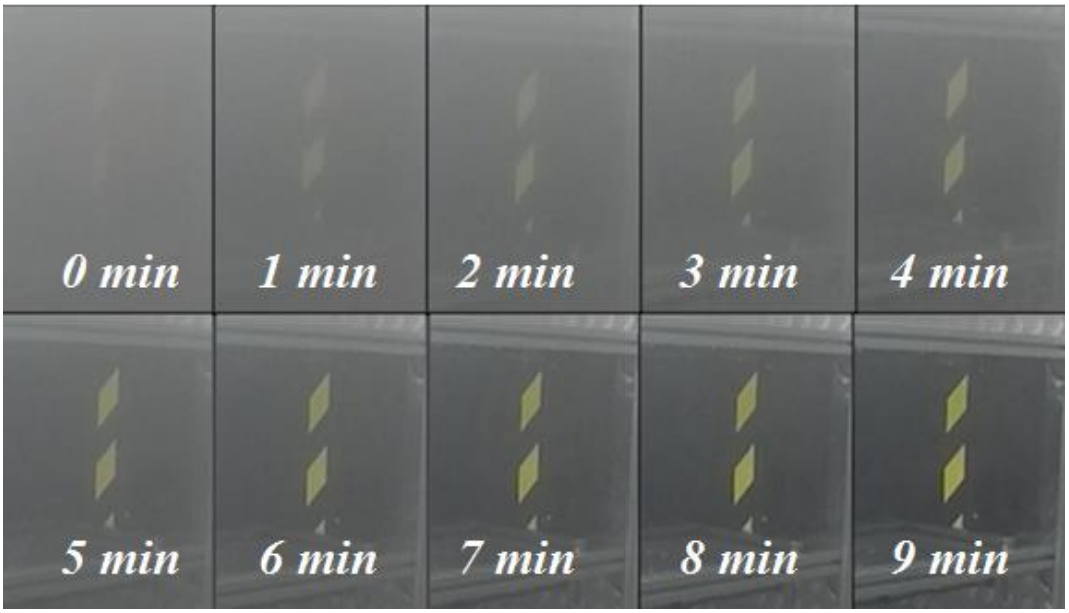

Time evolution of the fog generated with the B1:2 nozzle for a combination of P_{air}= 15 bar and P_{water}= 3 bar. The images show the concentration of fog in the room every minute since the shot was taken.

The pressurized water tank, with a capacity of 4.5 l of water, is not emptied during shooting. The flow maximun water flow rate obtained is lower than the sensitivity offered by the flow meters installed in the laboratory. Therefore, it has not been possible to obtain a numerical flow rate value Figures show the cone stabilized during the shooting and the evolution of the fog with the time elapsed after the shot.

- **Test IXX**

NOZZLE	Model	B
	Scale	1:2
AIR PRESSURE		19 bar
WATER PRESSURE		4 bar

Stabilized cone of nozzle B1:2 for a P_{air}= 19 bar and P_{water}= 4 bar combination and cone opening angle.

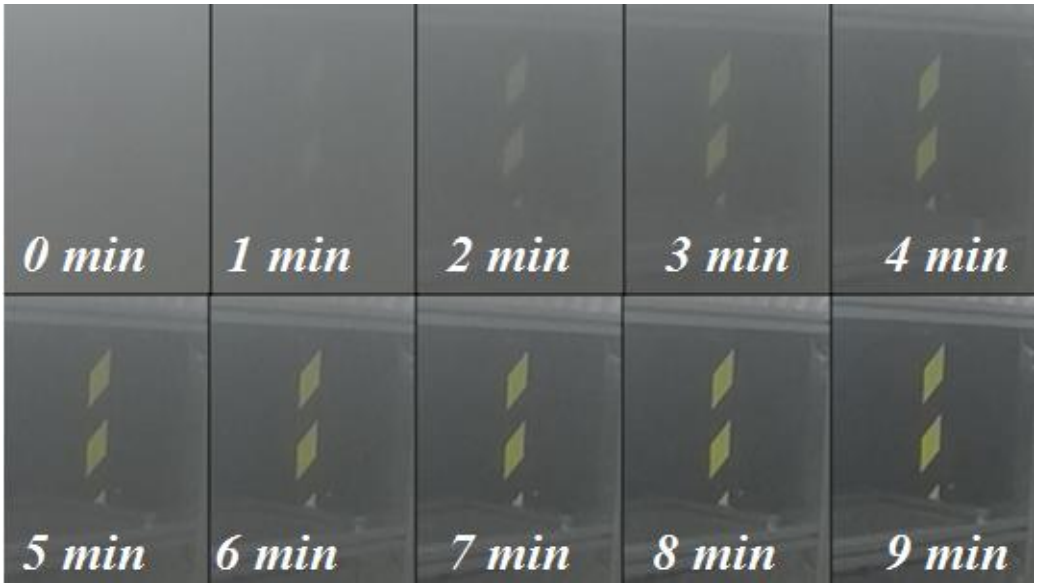

Time evolution of the fog generated with the B1:2 nozzle for a combination of P_{air}= 19 bar and P_{water}= 4 bar. The images show the concentration of fog in the room every minute since the shot was taken.

The pressurized water tank, with a capacity of 4.5 l of water, is not emptied during shooting. The flow maximun water flow rate obtained is lower than the sensitivity offered by the flow meters installed in the laboratory. Therefore, it has not been possible to obtain a numerical flow rate value. Figures show the cone stabilized during the shooting and the evolution of the fog with the time elapsed after the shot.

- **Test XX**

NOZZLE	Model	F
	Scale	1:2
AIR PRESSURE		5 bar
WATER PRESSURE		5 bar

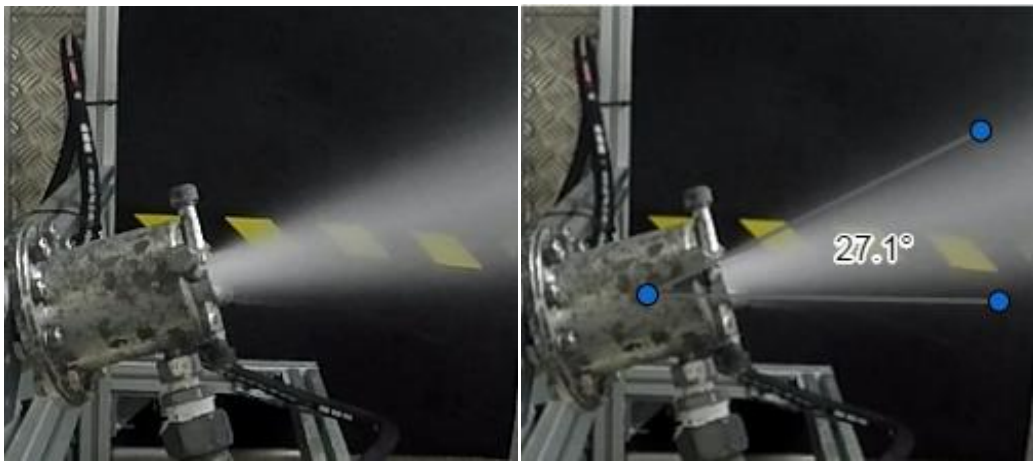

Stabilized cone of nozzle F1:2 for a P_{air}= 5 bar and P_{water}= 5 bar combination and cone opening angle.

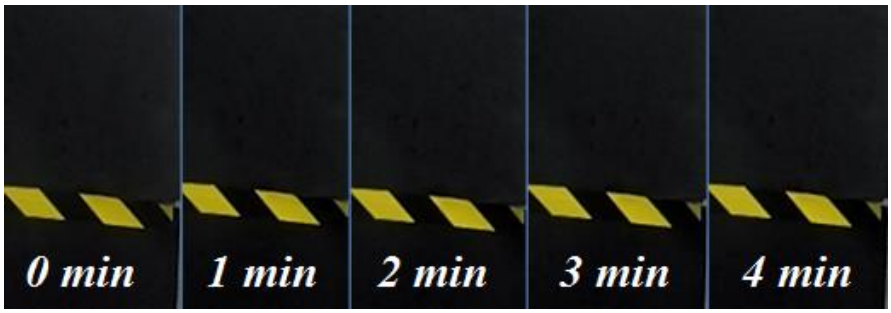

Time evolution of the fog generated with the F1:2 nozzle for a combination of P_{air}= 5 bar and P_{water}= 5 bar. The images show the concentration of fog in the room every minute since the shot was taken.

The pressurized water tank, with a capacity of 4.5 l of water, is not emptied during shooting. The water maximum flow rate obtained is 0.01 l/s. Figures show the cone stabilized during the shooting and the evolution of the fog with the time elapsed after the shot.

- **Test XXI**

NOZZLE	Model	F
	Scale	1:2
AIR PRESSURE		5 bar
WATER PRESSURE		10 bar

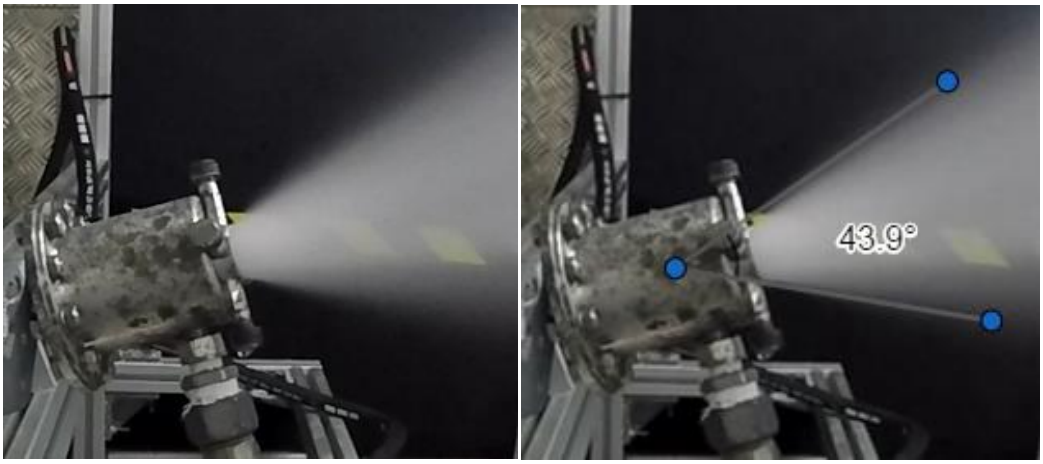

Stabilized cone of nozzle F1:2 for a P_{air}= 5 bar and P_{water}= 10 bar combination and cone opening angle.

Time evolution of the fog generated with the F1:2 nozzle for a combination of P_{air}= 5 bar and P_{water}= 10 bar. The images show the concentration of fog in the room every minute since the shot was taken.

The pressurized water tank, with a capacity of 4.5 l of water, is not emptied during shooting. The water maximum flow rate obtained is 0.20 l/s. Figures show the cone stabilized during the shooting and the evolution of the fog with the time elapsed after the shot.

- **Test XXII**

NOZZLE	Model	F
	Scale	1:2
AIR PRESSURE		5 bar
WATER PRESSURE		15 bar

Stabilized cone of nozzle F1:2 for a P_{air}= 5 bar and P_{water}= 15 bar combination and cone opening angle.

Time evolution of the fog generated with the F1:2 nozzle for a combination of P_{air}= 5 bar and P_{water}= 15 bar. The images show the concentration of fog in the room every minute since the shot was taken.

The pressurized water tank, with a capacity of 4.5 l of water, is not emptied during shooting. The water maximum flow rate obtained is 0.27 l/s. Figures show the cone stabilized during the shooting and the evolution of the fog with the time elapsed after the shot.

- **Test XXIII**

NOZZLE	Model	F
	Scale	1:2
AIR PRESSURE		5 bar
WATER PRESSURE		20 bar

Stabilized cone of nozzle F1:2 for a P_{air}= 5 bar and P_{water}= 20 bar combination and cone opening angle.

Time evolution of the fog generated with the F1:2 nozzle for a combination of P_{air}= 5 bar and P_{water}= 20 bar. The images show the concentration of fog in the room every minute since the shot was taken.

The pressurized water tank, with a capacity of 4.5 l of water, is emptied during shooting. The water flow rate obtained is 0.27 l/s. Figures show the cone stabilized during the shooting and the evolution of the fog with the time elapsed after the shot.

- **Test XXIV**

NOZZLE	Model	F
	Scale	1:2
AIR PRESSURE		10 bar
WATER PRESSURE		5 bar

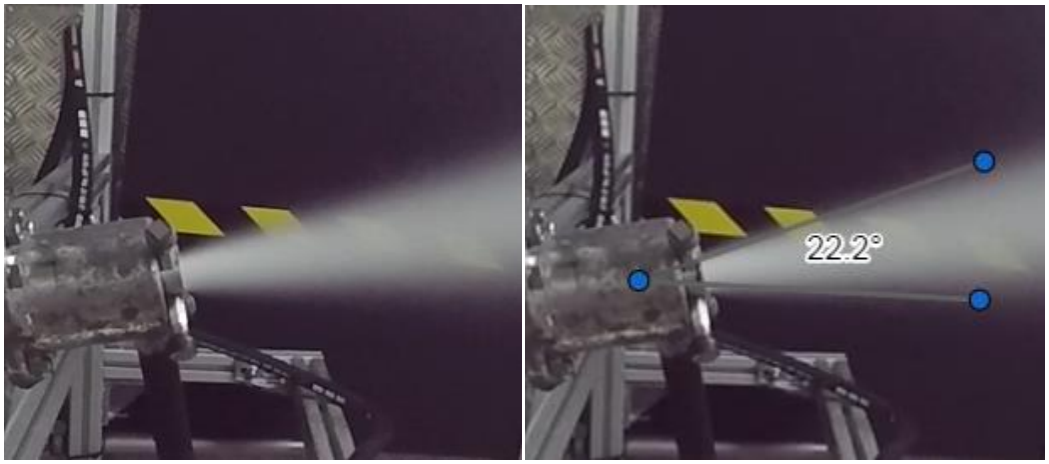

Stabilized cone of nozzle F1:2 for a P_{air}= 10 bar and P_{water}= 5 bar combination and cone opening angle.

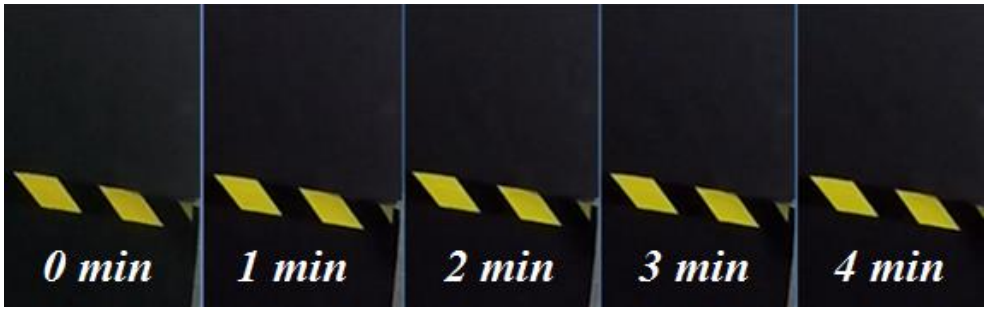

Time evolution of the fog generated with the F1:2 nozzle for a combination of Pair= 10 bar and Pwater= 5 bar. The images show the concentration of fog in the room every minute since the shot was taken.

The pressurized water tank, with a capacity of 4.5 l of water, is not emptied during shooting. The water maximum flow rate obtained is 0.14 l/s. Figures show the cone stabilized during the shooting and the evolution of the fog with the time elapsed after the shot.

- **Test XXV**

NOZZLE	Model	F
	Scale	1:2
AIR PRESSURE		10 bar
WATER PRESSURE		10 bar

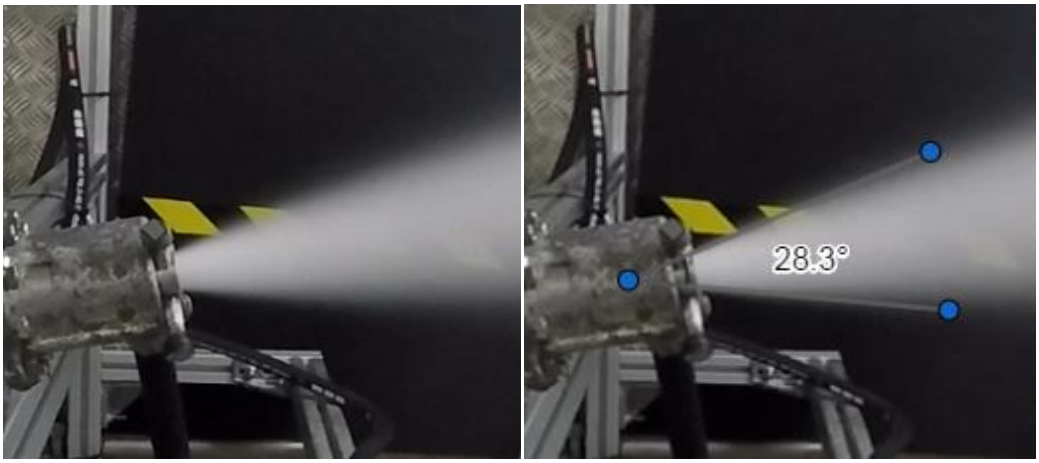

Stabilized cone of nozzle F1:2 for a P_{air}= 10 bar and P_{water}= 10 bar combination and cone opening angle.

Time evolution of the fog generated with the F1:2 nozzle for a combination of P_{air}= 10 bar and P_{water}= 10 bar. The images show the concentration of fog in the room every minute since the shot was taken.

The pressurized water tank, with a capacity of 4.5 l of water, is emptied during shooting. The water maximum flow rate obtained is 0.29 l/s. Figures show the cone stabilized during the shooting and the evolution of the fog with the time elapsed after the shot.

- **Test XXVI**

NOZZLE	Model	F
	Scale	1:2
AIR PRESSURE		10 bar
WATER PRESSURE		15 bar

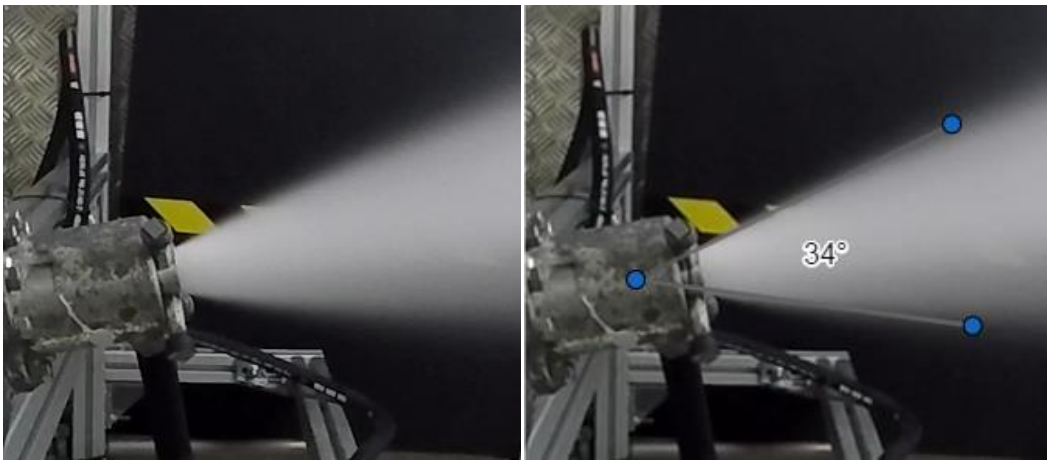

Stabilized cone of nozzle F1:2 for a P_{air}= 10 bar and P_{water}= 15 bar combination and cone opening angle.

Time evolution of the fog generated with the F1:2 nozzle for a combination of P_{air}= 10 bar and P_{water}= 15 bar. The images show the concentration of fog in the room every minute since the shot was taken.

The pressurized water tank, with a capacity of 4.5 l of water, is emptied during shooting. The water maximum flow rate obtained is 0.63 l/s. Figures show the cone stabilized during the shooting and the evolution of the fog with the time elapsed after the shot.

- **Test XXVII**

NOZZLE	Model	F
	Scale	1:2
AIR PRESSURE		10 bar
WATER PRESSURE		20 bar

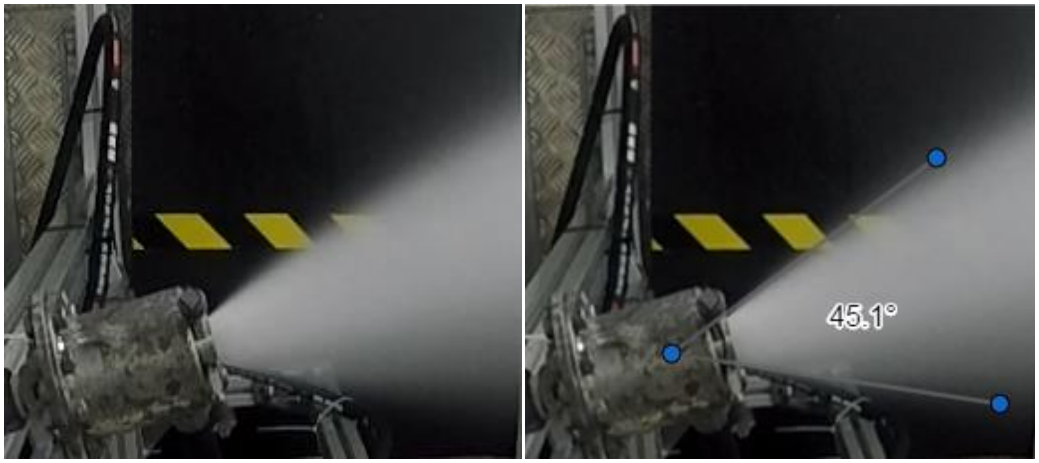

Stabilized cone of nozzle F1:2 for a P_{air}= 10 bar and P_{water}= 20 bar combination and cone opening angle.

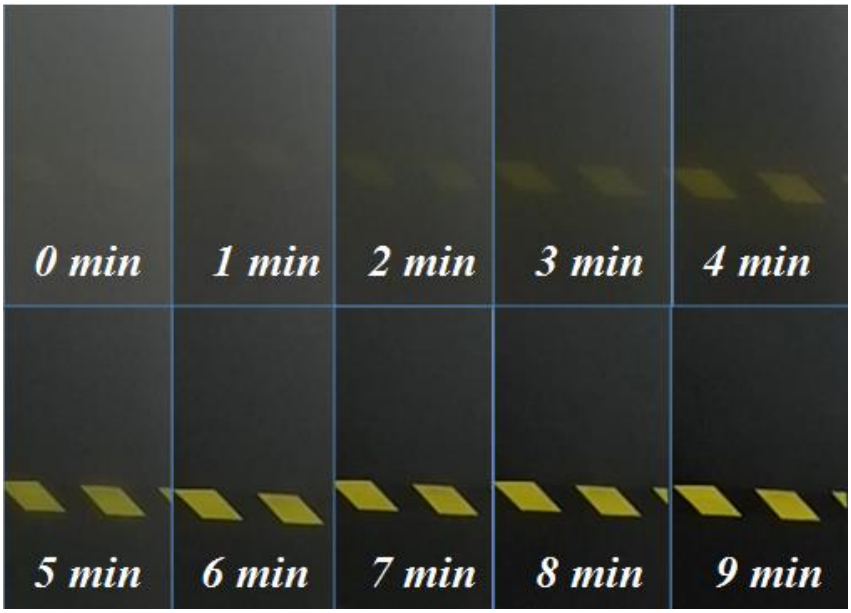

Time evolution of the fog generated with the F1:2 nozzle for a combination of P_{air}= 10 bar and P_{water}= 20 bar. The images show the concentration of fog in the room every minute since the shot was taken.

The pressurized water tank, with a capacity of 4.5 l of water, is emptied during shooting. The water maximum flow rate obtained is 0.66 l/s. Figures show the cone stabilized during the shooting and the evolution of the fog with the time elapsed after the shot.

- **Test XXVIII**

NOZZLE	Model	F
	Scale	1:2
AIR PRESSURE		15 bar
WATER PRESSURE		5 bar

Stabilized cone of nozzle F1:2 for a P_{air}= 15 bar and P_{water}= 5 bar combination and cone opening angle.

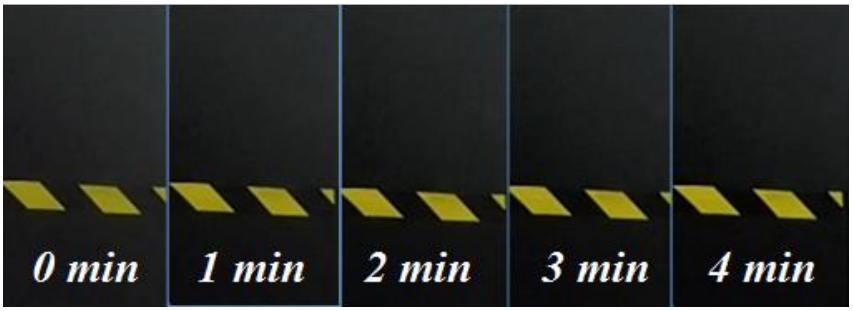

Time evolution of the fog generated with the F1:2 nozzle for a combination of P_{air}= 15 bar and P_{water}= 5 bar. The images show the concentration of fog in the room every minute since the shot was taken.

The pressurized water tank, with a capacity of 4.5 l of water, is emptied during shooting. The water maximum flow rate obtained is 0.44 l/s. Figures show the cone stabilized during the shooting and the evolution of the fog with the time elapsed after the shot.

- **Test XXIX**

NOZZLE	Model	F
	Scale	1:2
AIR PRESSURE		15 bar
WATER PRESSURE		10 bar

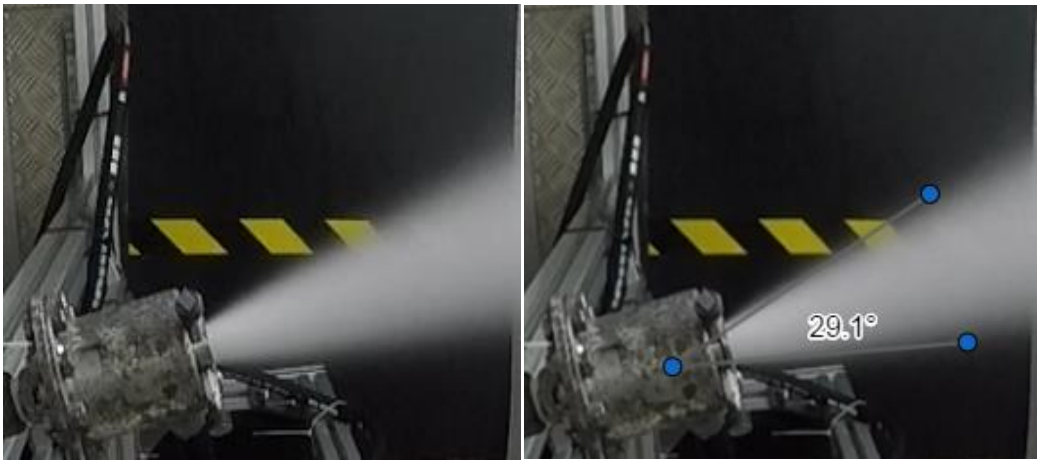

Stabilized cone of nozzle F1:2 for a P_{air}= 15 bar and P_{water}= 10 bar combination and cone opening angle.

Time evolution of the fog generated with the F1:2 nozzle for a combination of P_{air}= 15 bar and P_{water}= 10 bar. The images show the concentration of fog in the room every minute since the shot was taken.

The pressurized water tank, with a capacity of 4.5 l of water, is emptied during shooting. The water maximum flow rate obtained is 0.28 l/s. Figures show the cone stabilized during the shooting and the evolution of the fog with the time elapsed after the shot.

- **Test XXX**

NOZZLE	Model	F
	Scale	1:2
AIR PRESSURE		15 bar
WATER PRESSURE		15 bar

Stabilized cone of nozzle F1:2 for a P_{air}= 15 bar and P_{water}= 15 bar combination and cone opening angle.

Time evolution of the fog generated with the F1:2 nozzle for a combination of P_{air}= 15 bar and P_{water}= 15 bar. The images show the concentration of fog in the room every minute since the shot was taken.

The pressurized water tank, with a capacity of 4.5 l of water, is not emptied during shooting. The water maximum flow rate obtained is 0.27 l/s. Figures show the cone stabilized during the shooting and the evolution of the fog with the time elapsed after the shot

- **Test XXXI**

NOZZLE	Model	F
	Scale	1:2
AIR PRESSURE		15 bar
WATER PRESSURE		20 bar

Stabilized cone of nozzle F1:2 for a P_{air}= 15 bar and P_{water}= 20 bar combination and cone opening angle.

Time evolution of the fog generated with the F1:2 nozzle for a combination of P_{air}= 15 bar and P_{water}= 20 bar. The images show the concentration of fog in the room every minute since the shot was taken.

The pressurized water tank, with a capacity of 4.5 l of water, is emptied during shooting. The water maximum flow rate obtained is 0.41 l/s. Figures show the cone stabilized during the shooting and the evolution of the fog with the time elapsed after the shot.

- **Test XXXII**

NOZZLE	Model	F
	Scale	1:2
AIR PRESSURE		20 bar
WATER PRESSURE		5 bar

Stabilized cone of nozzle F1:2 for a P_{air}= 20 bar and P_{water}= 5 bar combination and cone opening angle.

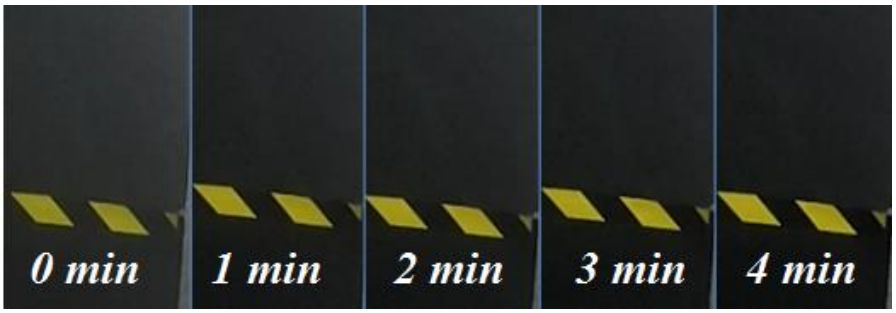

Time evolution of the fog generated with the F1:2 nozzle for a combination of P_{air}= 20 bar and P_{water}= 5 bar. The images show the concentration of fog in the room every minute since the shot was taken.

The pressurized water tank, with a capacity of 4.5 l of water, is emptied during shooting. The water maximum flow rate obtained is 0.33 l/s. Figures show the cone stabilized during the shooting and the evolution of the fog with the time elapsed after the shot

- **Test XXXIII**

NOZZLE	Model	F
	Scale	1:2
AIR PRESSURE		20 bar
WATER PRESSURE		10 bar

Stabilized cone of nozzle F1:2 for a P_{air}= 20 bar and P_{water}= 10 bar combination and cone opening angle.

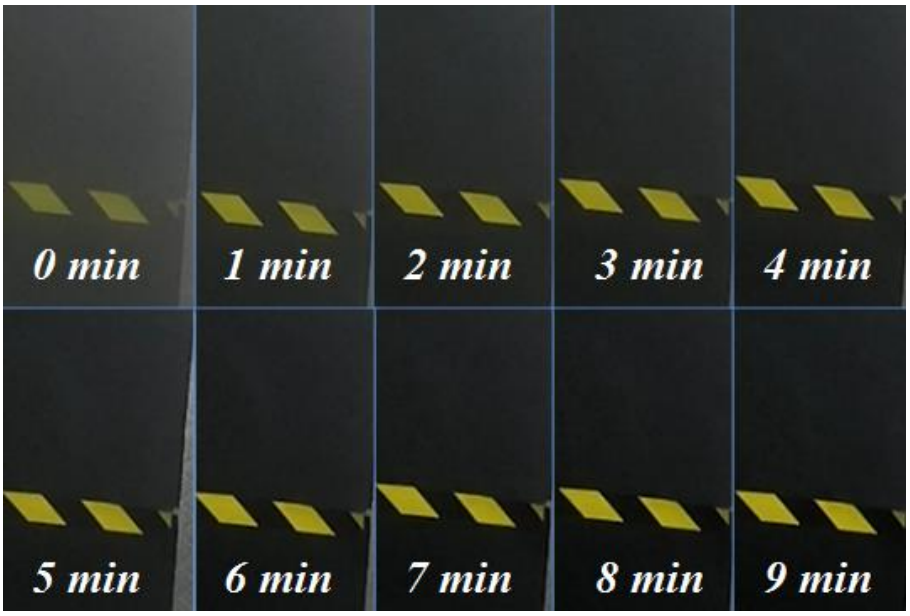

Time evolution of the fog generated with the F1:2 nozzle for a combination of P_{air}= 20 bar and P_{water}= 10 bar. The images show the concentration of fog in the room every minute since the shot was taken.

The pressurized water tank, with a capacity of 4.5 l of water, is emptied during shooting. The water maximum flow rate obtained is 0.24 l/s. Figures show the cone stabilized during the shooting and the evolution of the fog with the time elapsed after the shot.

- **Test XXXIV**

NOZZLE	Model	F
	Scale	1:2
AIR PRESSURE		20 bar
WATER PRESSURE		15 bar

Stabilized cone of nozzle F1:2 for a P_{air}= 20 bar and P_{water}= 15 bar combination and cone opening angle.

Time evolution of the fog generated with the F1:2 nozzle for a combination of P_{air}= 20 bar and P_{water}= 15 bar. The images show the concentration of fog in the room every minute since the shot was taken.

The pressurized water tank, with a capacity of 4.5 l of water, is emptied during shooting. The water maximum flow rate obtained is 0.29 l/s. Figures show the cone stabilized during the shooting and the evolution of the fog with the time elapsed after the shot.

- **Test XXXV**

NOZZLE	Model	F
	Scale	1:2
AIR PRESSURE		20 bar
WATER PRESSURE		20 bar

Stabilized cone of nozzle F1:2 for a P_{air}= 20 bar and P_{water}= 20 bar combination and cone opening angle.

Time evolution of the fog generated with the F1:2 nozzle for a combination of P_{air}= 20 bar and P_{water}= 20 bar. The images show the concentration of fog in the room every minute since the shot was taken.

The pressurized water tank, with a capacity of 4.5 l of water, is emptied during shooting. The water maximum flow rate obtained is 0.40 l/s. Figures show the cone stabilized during the shooting and the evolution of the fog with the time elapsed after the shot.

Annex B

Number of droplets for every size channel of the particle counter produced by the fog generated with the B1:2 nozzle to different combinations of air and water pressures of shot.

P_{air} = 2 bar

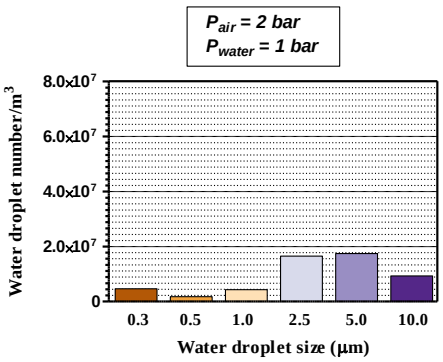

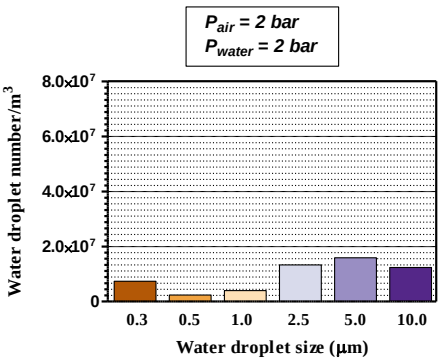

P_{air} = 3 bar

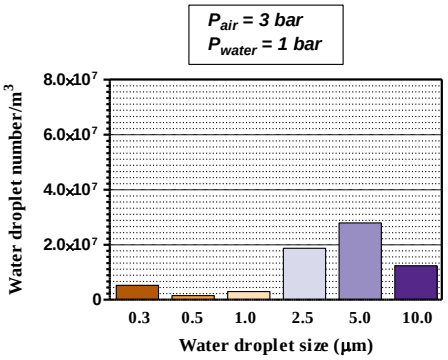

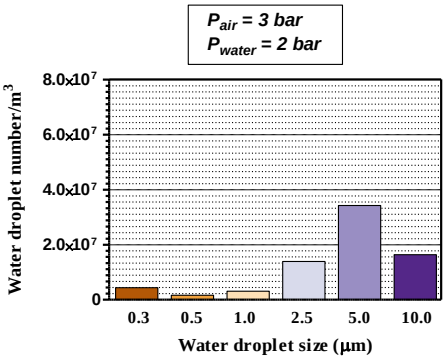

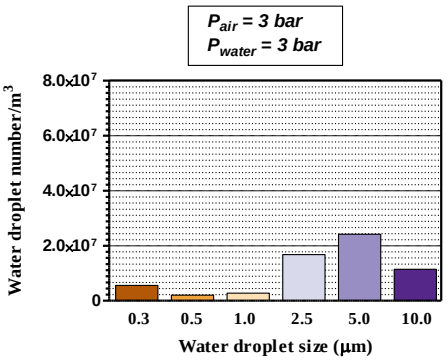

P_{air} = 4 bar

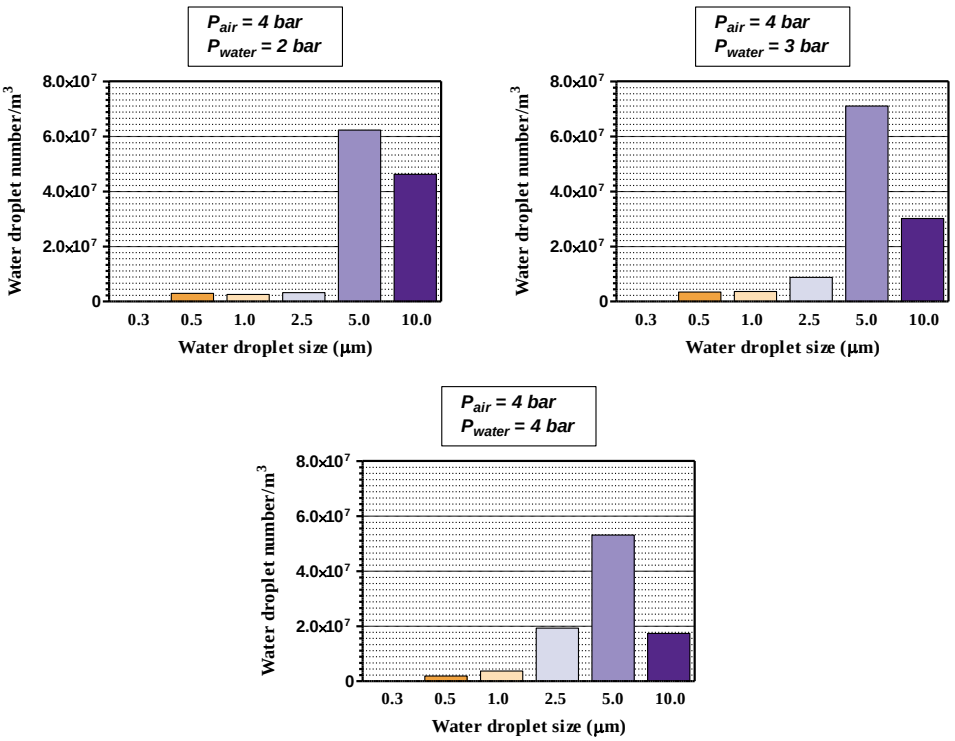

P_{air} = 6 bar

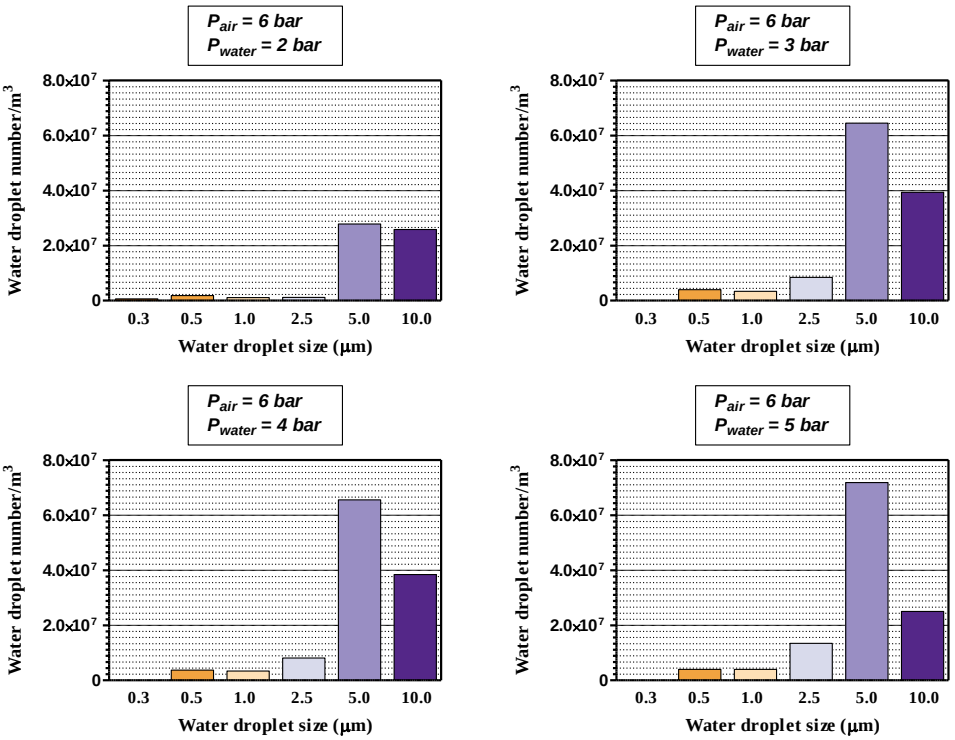

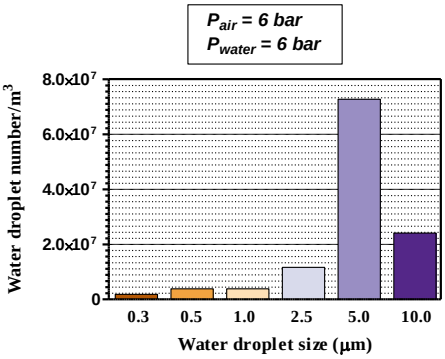
P_{air} = 6 bar
P_{water} = 6 bar
Water droplet number/m^3
8.0x10^7
6.0x10^7
4.0x10^7
2.0x10^7
0
0.3
0.5
1.0
2.5
5.0
10.0
Water droplet size (µm)

P_{air} = 8 bar

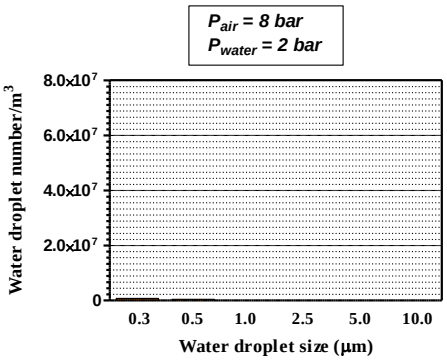
P_{air} = 8 bar
P_{water} = 2 bar
Water droplet number/m^3
8.0x10^7
6.0x10^7
4.0x10^7
2.0x10^7
0
0.3
0.5
1.0
2.5
5.0
10.0
Water droplet size (µm)

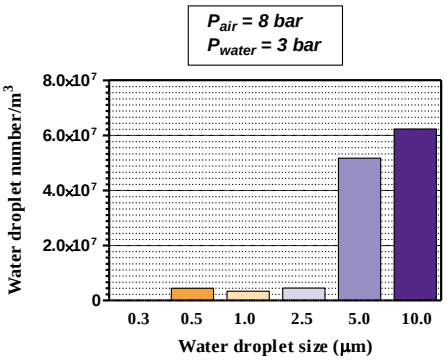
P_{air} = 8 bar
P_{water} = 3 bar
Water droplet number/m^3
8.0x10^7
6.0x10^7
4.0x10^7
2.0x10^7
0
0.3
0.5
1.0
2.5
5.0
10.0
Water droplet size (µm)

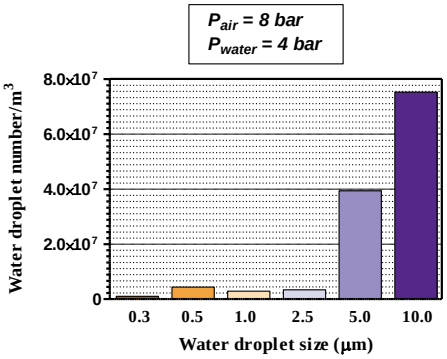
P_{air} = 8 bar
P_{water} = 4 bar
Water droplet number/m^3
8.0x10^7
6.0x10^7
4.0x10^7
2.0x10^7
0
0.3
0.5
1.0
2.5
5.0
10.0
Water droplet size (µm)

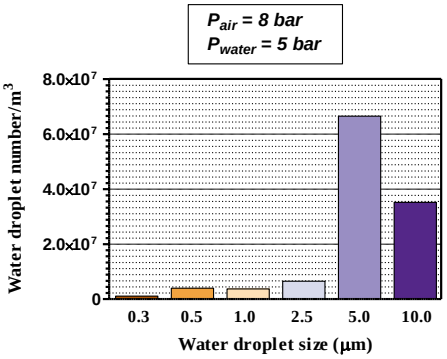
P_{air} = 8 bar
P_{water} = 5 bar
Water droplet number/m^3
8.0x10^7
6.0x10^7
4.0x10^7
2.0x10^7
0
0.3
0.5
1.0
2.5
5.0
10.0
Water droplet size (µm)

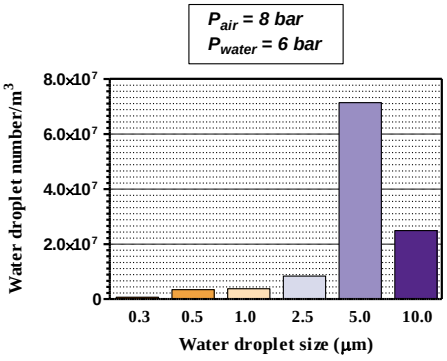
P_{air} = 8 bar
P_{water} = 6 bar
Water droplet number/m^3
8.0x10^7
6.0x10^7
4.0x10^7
2.0x10^7
0
0.3
0.5
1.0
2.5
5.0
10.0
Water droplet size (µm)

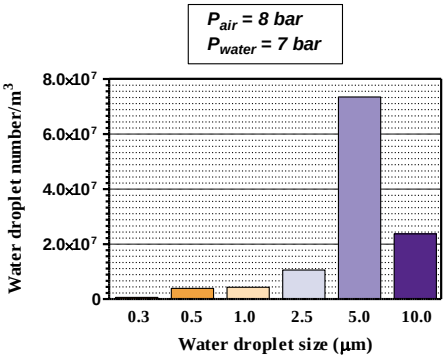
P_{air} = 8 bar
P_{water} = 7 bar
Water droplet number/m^3
8.0x10^7
6.0x10^7
4.0x10^7
2.0x10^7
0
0.3
0.5
1.0
2.5
5.0
10.0
Water droplet size (µm)

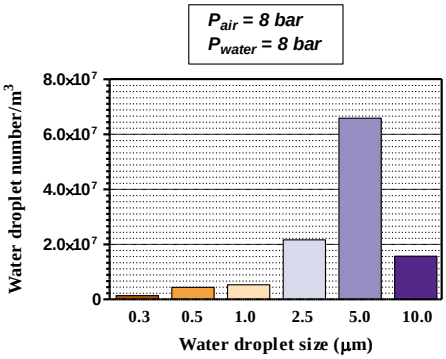
P_{air} = 8 bar
P_{water} = 8 bar
Water droplet number/m^3
8.0x10^7
6.0x10^7
4.0x10^7
2.0x10^7
0
0.3 0.5 1.0 2.5 5.0 10.0
Water droplet size (µm)

P_{air} = 10 bar

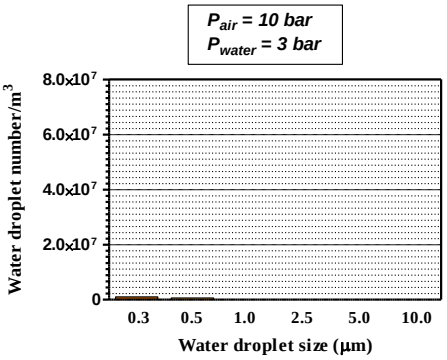
P_{air} = 10 bar
P_{water} = 3 bar
Water droplet number/m^3
8.0x10^7
6.0x10^7
4.0x10^7
2.0x10^7
0
0.3 0.5 1.0 2.5 5.0 10.0
Water droplet size (µm)

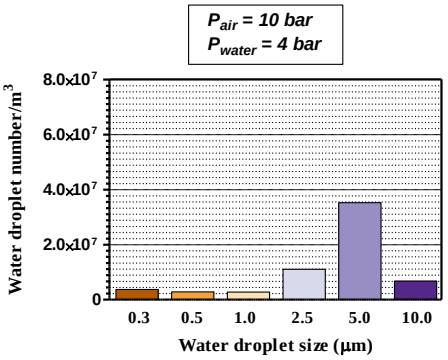
P_{air} = 10 bar
P_{water} = 4 bar
Water droplet number/m^3
8.0x10^7
6.0x10^7
4.0x10^7
2.0x10^7
0
0.3 0.5 1.0 2.5 5.0 10.0
Water droplet size (µm)

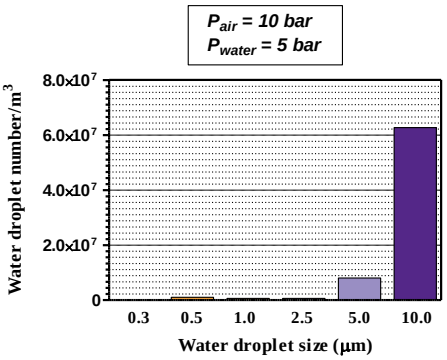
P_{air} = 10 bar
P_{water} = 5 bar
Water droplet number/m^3
8.0x10^7
6.0x10^7
4.0x10^7
2.0x10^7
0
0.3 0.5 1.0 2.5 5.0 10.0
Water droplet size (µm)

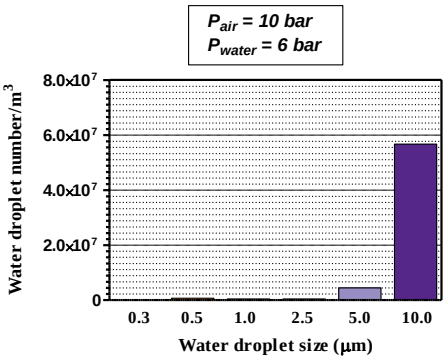
P_{air} = 10 bar
P_{water} = 6 bar
Water droplet number/m^3
8.0x10^7
6.0x10^7
4.0x10^7
2.0x10^7
0
0.3 0.5 1.0 2.5 5.0 10.0
Water droplet size (µm)

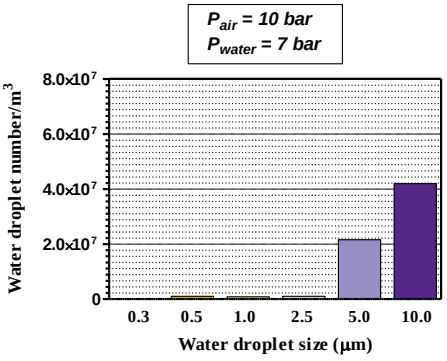
P_{air} = 10 bar
P_{water} = 7 bar
Water droplet number/m^3
8.0x10^7
6.0x10^7
4.0x10^7
2.0x10^7
0
0.3 0.5 1.0 2.5 5.0 10.0
Water droplet size (µm)

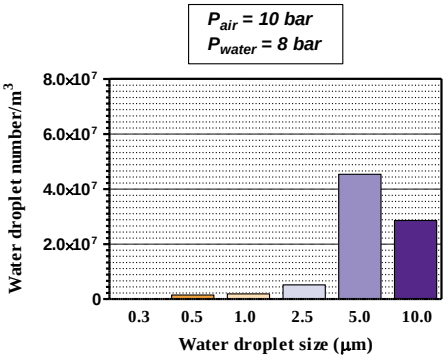
P_{air} = 10 bar
P_{water} = 8 bar
Water droplet number/m^3
8.0x10^7
6.0x10^7
4.0x10^7
2.0x10^7
0
0.3 0.5 1.0 2.5 5.0 10.0
Water droplet size (µm)

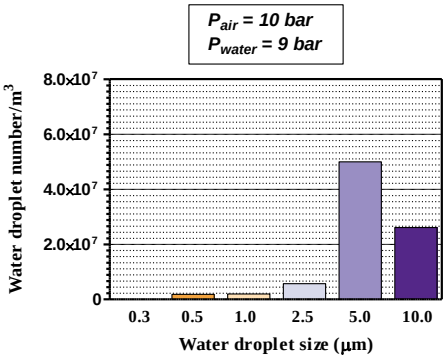
P_{air} = 10 bar
P_{water} = 9 bar
Water droplet number/m^3
8.0x10^7
6.0x10^7
4.0x10^7
2.0x10^7
0
0.3 0.5 1.0 2.5 5.0 10.0
Water droplet size (μm)

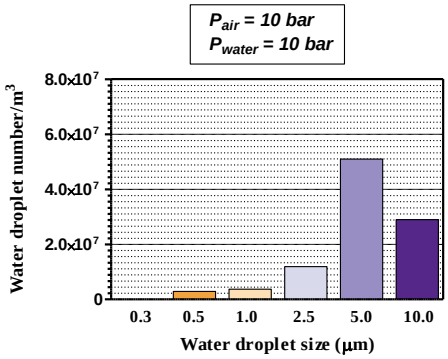
P_{air} = 10 bar
P_{water} = 10 bar
Water droplet number/m^3
8.0x10^7
6.0x10^7
4.0x10^7
2.0x10^7
0
0.3 0.5 1.0 2.5 5.0 10.0
Water droplet size (μm)

P_{air} = 12 bar

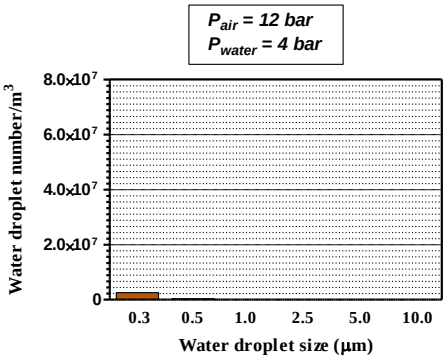
P_{air} = 12 bar
P_{water} = 4 bar
Water droplet number/m^3
8.0x10^7
6.0x10^7
4.0x10^7
2.0x10^7
0
0.3 0.5 1.0 2.5 5.0 10.0
Water droplet size (μm)

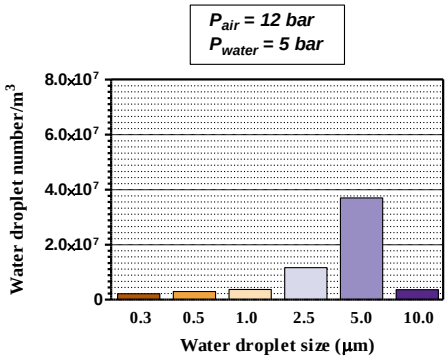
P_{air} = 12 bar
P_{water} = 5 bar
Water droplet number/m^3
8.0x10^7
6.0x10^7
4.0x10^7
2.0x10^7
0
0.3 0.5 1.0 2.5 5.0 10.0
Water droplet size (μm)

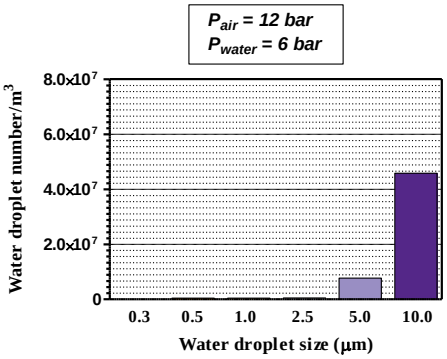
P_{air} = 12 bar
P_{water} = 6 bar
Water droplet number/m^3
8.0x10^7
6.0x10^7
4.0x10^7
2.0x10^7
0
0.3 0.5 1.0 2.5 5.0 10.0
Water droplet size (μm)

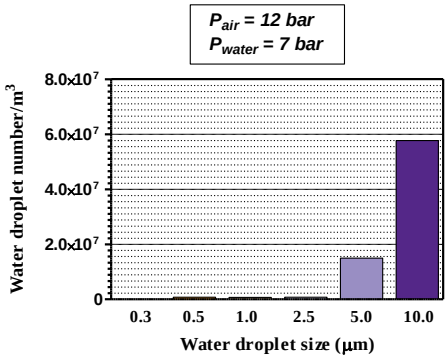
P_{air} = 12 bar
P_{water} = 7 bar
Water droplet number/m^3
8.0x10^7
6.0x10^7
4.0x10^7
2.0x10^7
0
0.3 0.5 1.0 2.5 5.0 10.0
Water droplet size (μm)

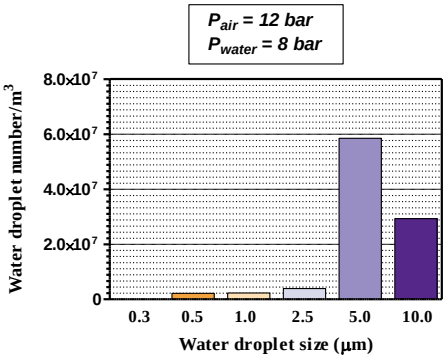
P_{air} = 12 bar
P_{water} = 8 bar
Water droplet number/m^3
8.0x10^7
6.0x10^7
4.0x10^7
2.0x10^7
0
0.3 0.5 1.0 2.5 5.0 10.0
Water droplet size (μm)

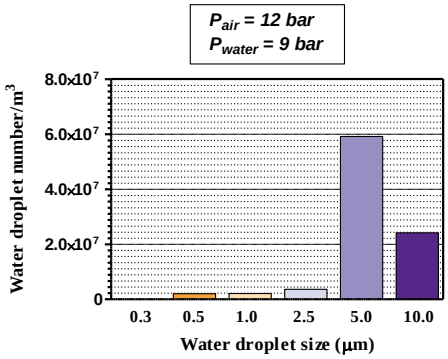
P_{air} = 12 bar
P_{water} = 9 bar
Water droplet number/m^3
8.0x10^7
6.0x10^7
4.0x10^7
2.0x10^7
0
0.3 0.5 1.0 2.5 5.0 10.0
Water droplet size (μm)

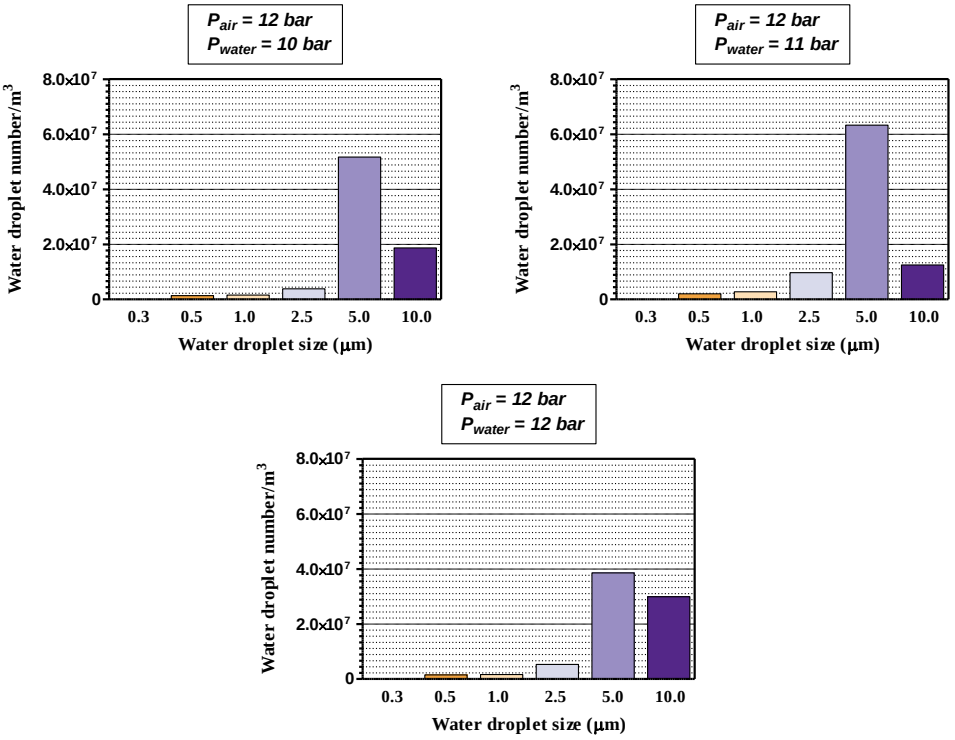
P_{air} = 12 bar
P_{water} = 10 bar
P_{air} = 12 bar
P_{water} = 11 bar
P_{air} = 12 bar
P_{water} = 12 bar
Water droplet number/m^3
8.0x10^7
6.0x10^7
4.0x10^7
2.0x10^7
0
0.3
0.5
1.0
2.5
5.0
10.0
Water droplet size (μm)

P_{air} = 14 bar

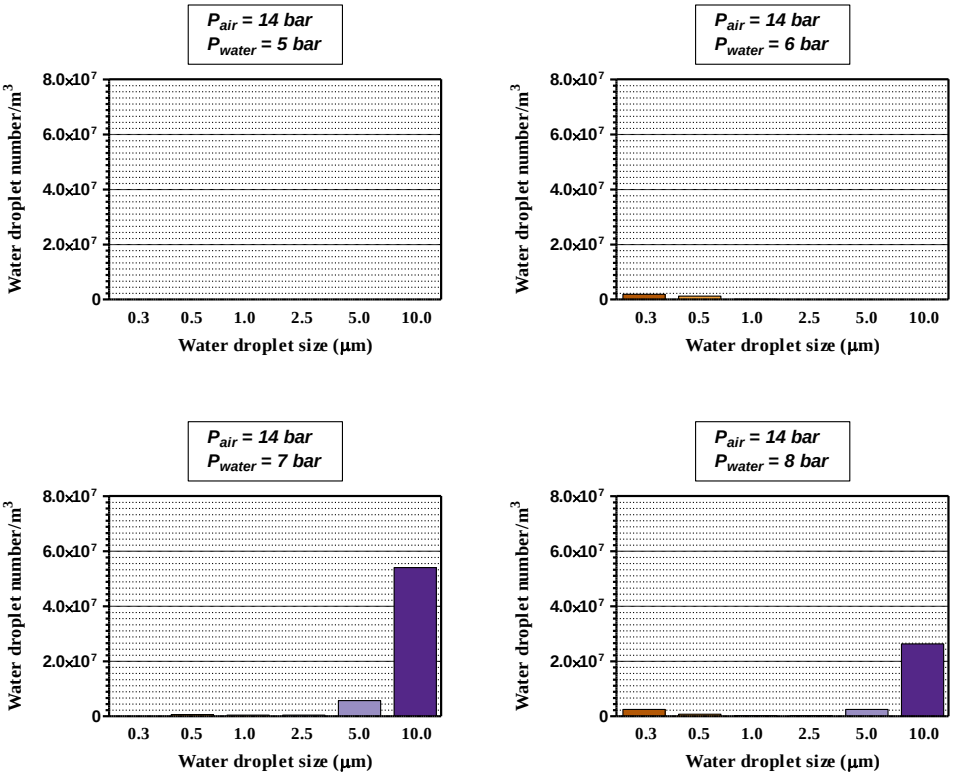
P_{air} = 14 bar
P_{water} = 5 bar
P_{air} = 14 bar
P_{water} = 6 bar
P_{air} = 14 bar
P_{water} = 7 bar
P_{air} = 14 bar
P_{water} = 8 bar
Water droplet number/m^3
8.0x10^7
6.0x10^7
4.0x10^7
2.0x10^7
0
0.3
0.5
1.0
2.5
5.0
10.0
Water droplet size (μm)

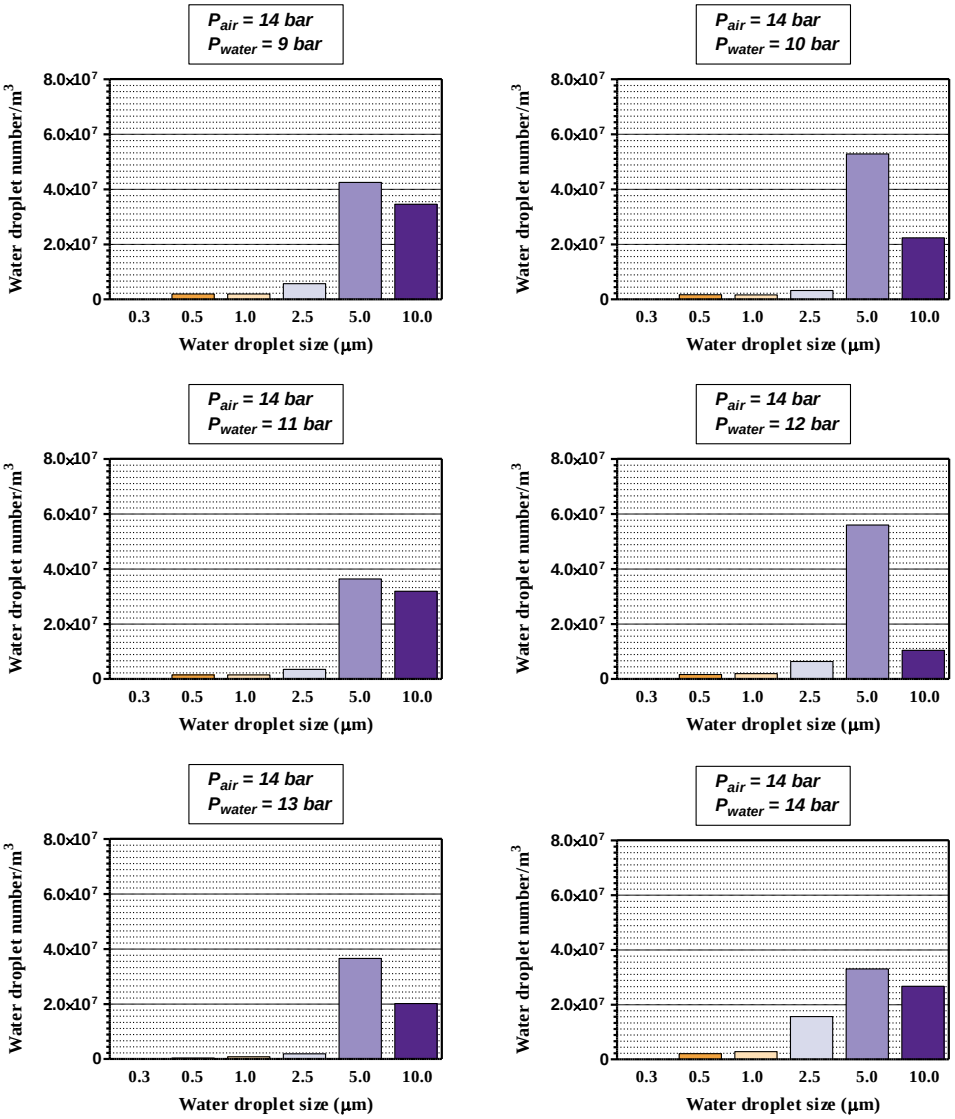
P_{air} = 14 bar
P_{water} = 9 bar
P_{air} = 14 bar
P_{water} = 10 bar
P_{air} = 14 bar
P_{water} = 11 bar
P_{air} = 14 bar
P_{water} = 12 bar
P_{air} = 14 bar
P_{water} = 13 bar
P_{air} = 14 bar
P_{water} = 14 bar
Water droplet number/m^3
8.0x10^7
6.0x10^7
4.0x10^7
2.0x10^7
0
0.3
0.5
1.0
2.5
5.0
10.0
Water droplet size (μm)

Percentage of droplets for every size channel of the particle counter produced by the fog generated with the B1:2 nozzle to different combinations of air and water pressures of shot .

P_{air} = 2 bar

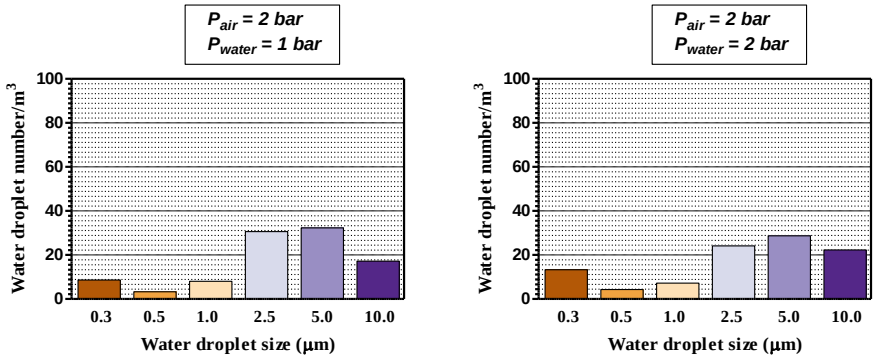

P_{air} = 3 bar

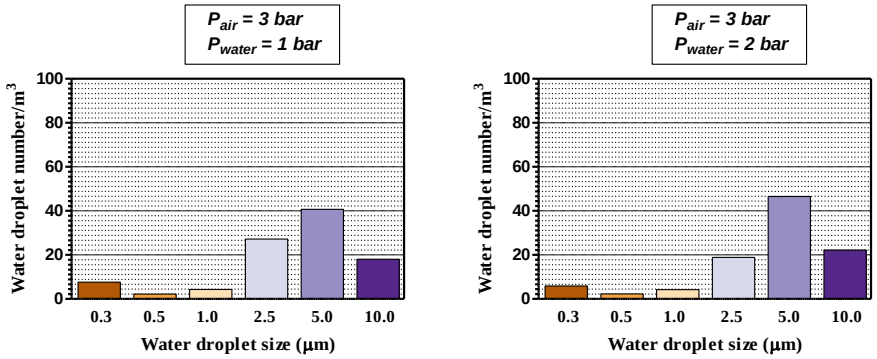

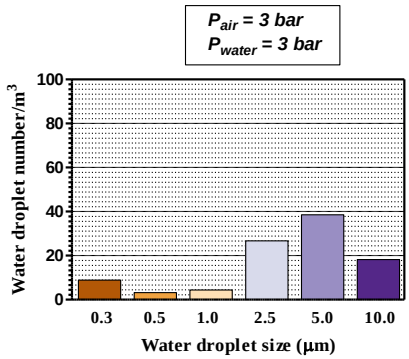

P_{air} = 4 bar

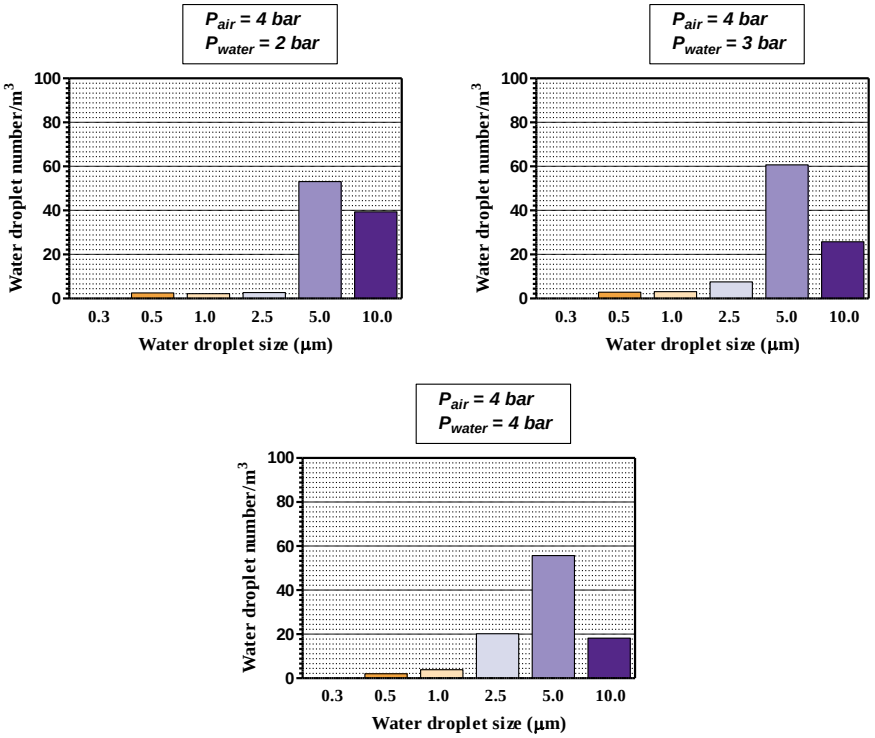

P_{air} = 6 bar

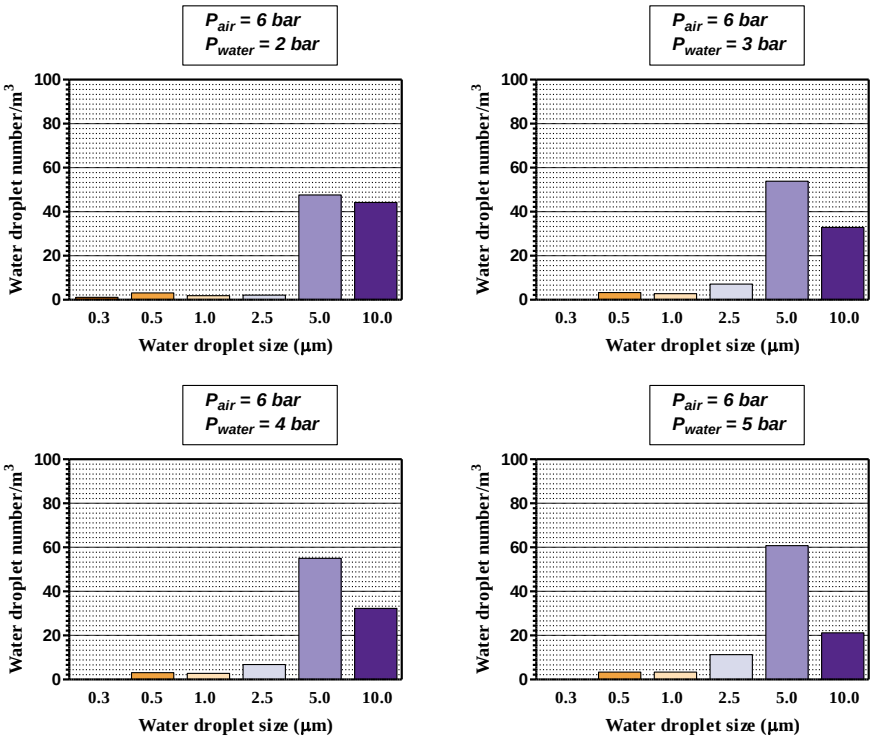

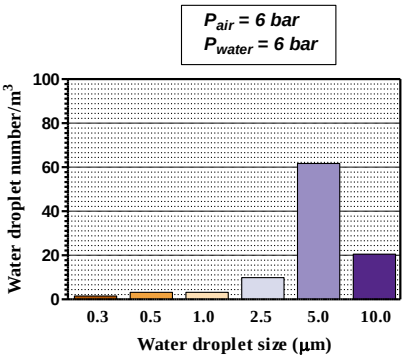
P_{air} = 6 bar
P_{water} = 6 bar
Water droplet number/m^3
100
80
60
40
20
0
0.3
0.5
1.0
2.5
5.0
10.0
Water droplet size (µm)

P_{air} = 8 bar

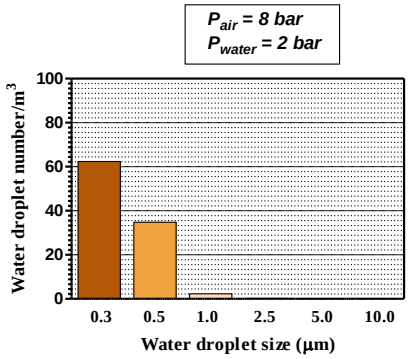
P_{air} = 8 bar
P_{water} = 2 bar
Water droplet number/m^3
100
80
60
40
20
0
0.3
0.5
1.0
2.5
5.0
10.0
Water droplet size (µm)

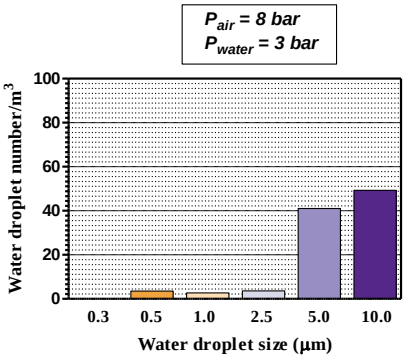
P_{air} = 8 bar
P_{water} = 3 bar
Water droplet number/m^3
100
80
60
40
20
0
0.3
0.5
1.0
2.5
5.0
10.0
Water droplet size (µm)

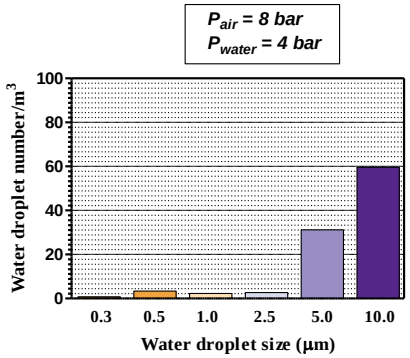
P_{air} = 8 bar
P_{water} = 4 bar
Water droplet number/m^3
100
80
60
40
20
0
0.3
0.5
1.0
2.5
5.0
10.0
Water droplet size (µm)

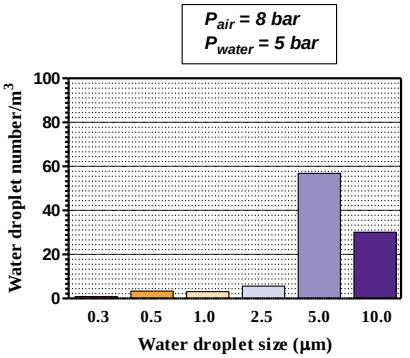
P_{air} = 8 bar
P_{water} = 5 bar
Water droplet number/m^3
100
80
60
40
20
0
0.3
0.5
1.0
2.5
5.0
10.0
Water droplet size (µm)

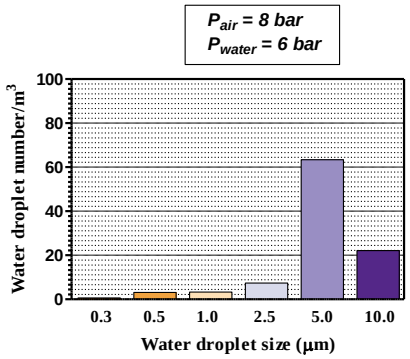
P_{air} = 8 bar
P_{water} = 6 bar
Water droplet number/m^3
100
80
60
40
20
0
0.3
0.5
1.0
2.5
5.0
10.0
Water droplet size (µm)

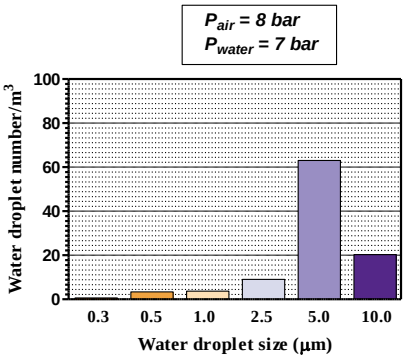
P_{air} = 8 bar
P_{water} = 7 bar
Water droplet number/m^3
100
80
60
40
20
0
0.3
0.5
1.0
2.5
5.0
10.0
Water droplet size (µm)

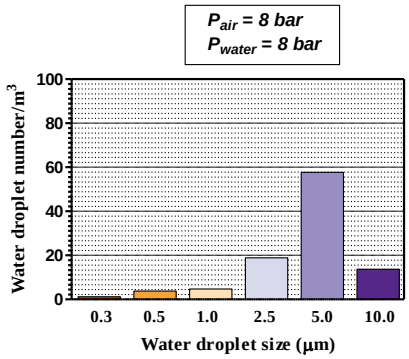
P_{air} = 8 bar
P_{water} = 8 bar
Water droplet number/m^3
100
80
60
40
20
0
0.3
0.5
1.0
2.5
5.0
10.0
Water droplet size (µm)

P_{air} = 10 bar

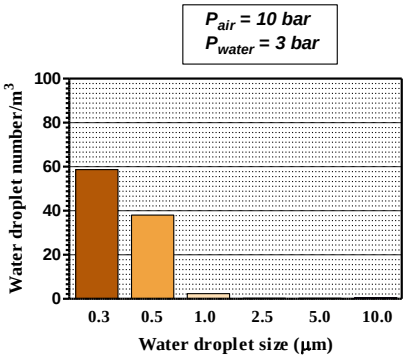
P_{air} = 10 bar
P_{water} = 3 bar
Water droplet number/m^3
100
80
60
40
20
0
0.3
0.5
1.0
2.5
5.0
10.0
Water droplet size (µm)

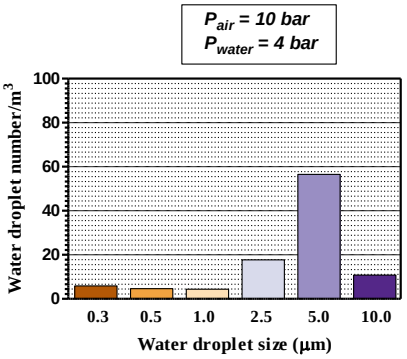
P_{air} = 10 bar
P_{water} = 4 bar
Water droplet number/m^3
100
80
60
40
20
0
0.3
0.5
1.0
2.5
5.0
10.0
Water droplet size (µm)

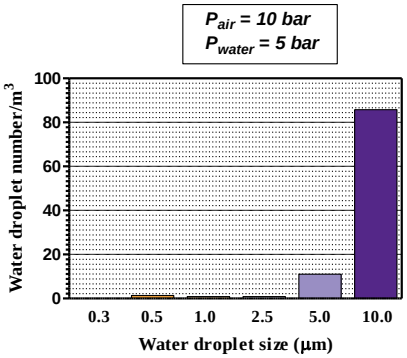
P_{air} = 10 bar
P_{water} = 5 bar
Water droplet number/m^3
100
80
60
40
20
0
0.3
0.5
1.0
2.5
5.0
10.0
Water droplet size (µm)

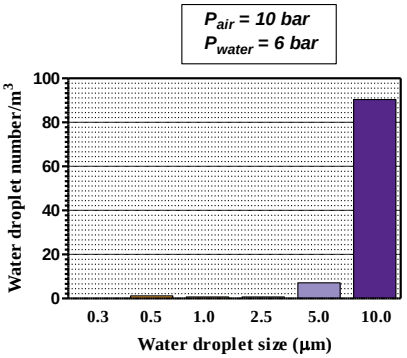
P_{air} = 10 bar
P_{water} = 6 bar
Water droplet number/m^3
100
80
60
40
20
0
0.3
0.5
1.0
2.5
5.0
10.0
Water droplet size (µm)

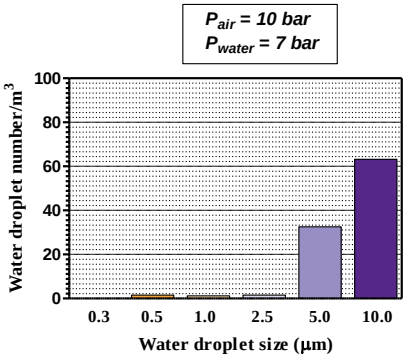
P_{air} = 10 bar
P_{water} = 7 bar
Water droplet number/m^3
100
80
60
40
20
0
0.3
0.5
1.0
2.5
5.0
10.0
Water droplet size (µm)

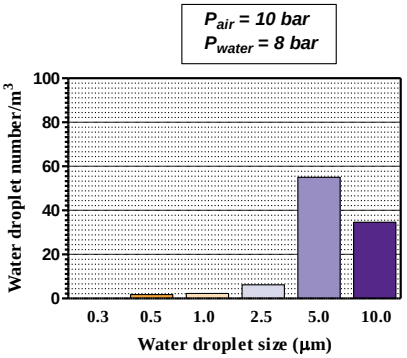
P_{air} = 10 bar
P_{water} = 8 bar
Water droplet number/m^3
100
80
60
40
20
0
0.3
0.5
1.0
2.5
5.0
10.0
Water droplet size (µm)

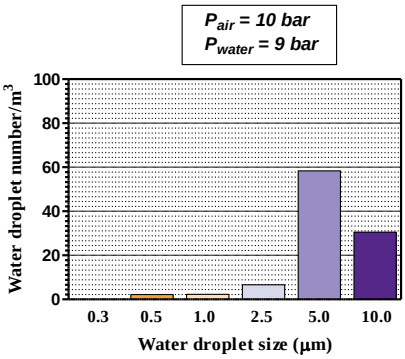
P_{air} = 10 bar
P_{water} = 9 bar
Water droplet number/m^3
0
20
40
60
80
100
0.3
0.5
1.0
2.5
5.0
10.0
Water droplet size (µm)

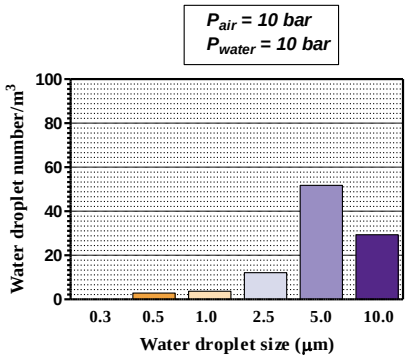
P_{air} = 10 bar
P_{water} = 10 bar
Water droplet number/m^3
0
20
40
60
80
100
0.3
0.5
1.0
2.5
5.0
10.0
Water droplet size (µm)

P_{air} = 12 bar

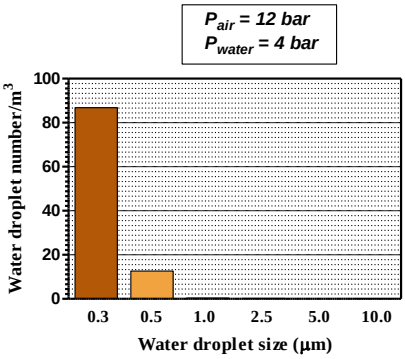
P_{air} = 12 bar
P_{water} = 4 bar
Water droplet number/m^3
0
20
40
60
80
100
0.3
0.5
1.0
2.5
5.0
10.0
Water droplet size (µm)

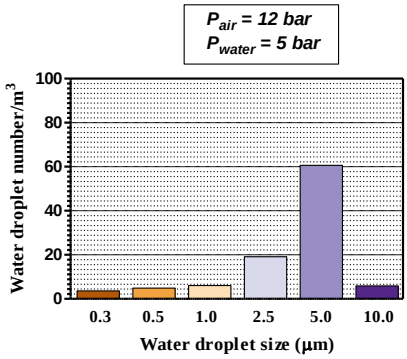
P_{air} = 12 bar
P_{water} = 5 bar
Water droplet number/m^3
0
20
40
60
80
100
0.3
0.5
1.0
2.5
5.0
10.0
Water droplet size (µm)

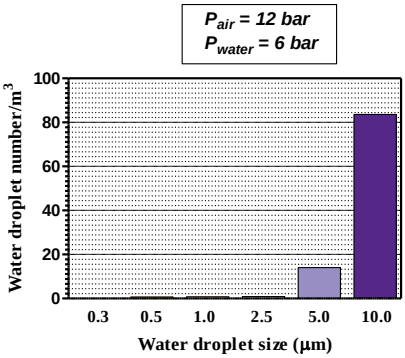
P_{air} = 12 bar
P_{water} = 6 bar
Water droplet number/m^3
0
20
40
60
80
100
0.3
0.5
1.0
2.5
5.0
10.0
Water droplet size (µm)

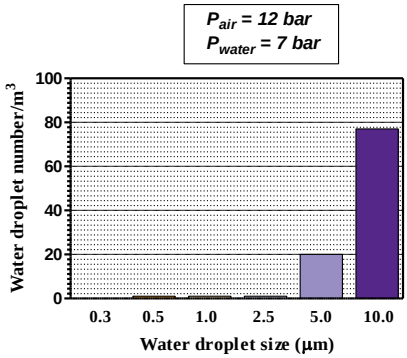
P_{air} = 12 bar
P_{water} = 7 bar
Water droplet number/m^3
0
20
40
60
80
100
0.3
0.5
1.0
2.5
5.0
10.0
Water droplet size (µm)

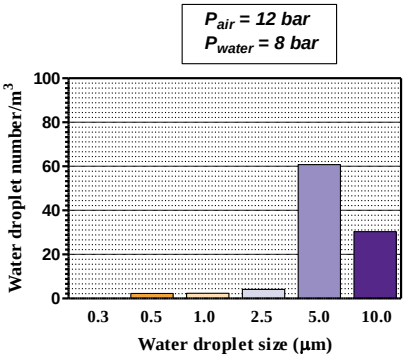
P_{air} = 12 bar
P_{water} = 8 bar
Water droplet number/m^3
0
20
40
60
80
100
0.3
0.5
1.0
2.5
5.0
10.0
Water droplet size (µm)

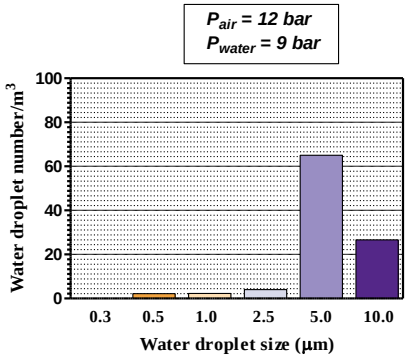
P_{air} = 12 bar
P_{water} = 9 bar
Water droplet number/m^3
0
20
40
60
80
100
0.3
0.5
1.0
2.5
5.0
10.0
Water droplet size (µm)

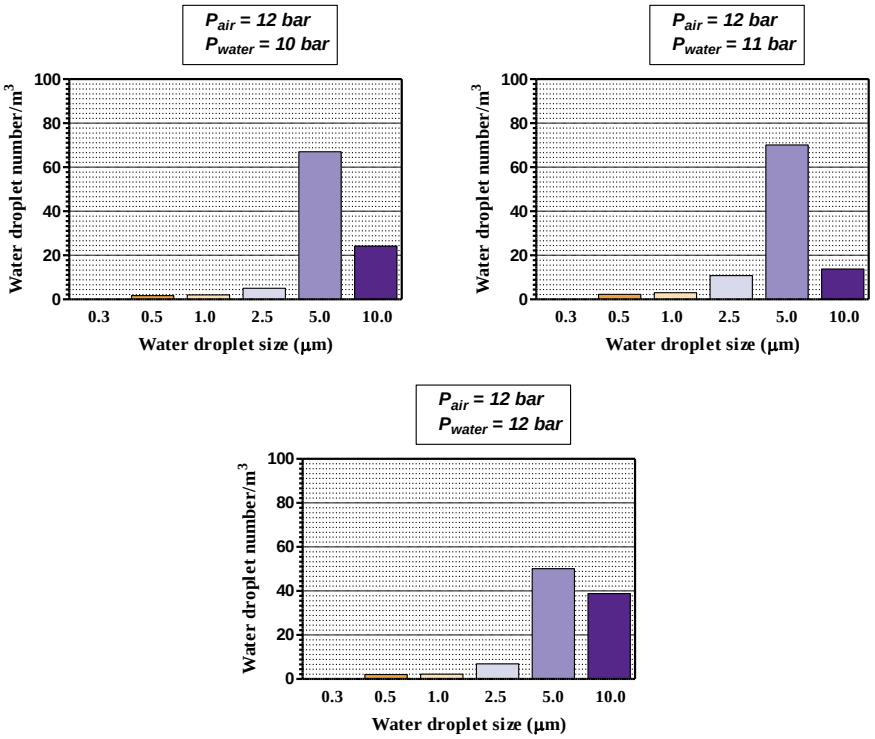
P_{air} = 12 bar
P_{water} = 10 bar
P_{air} = 12 bar
P_{water} = 11 bar
P_{air} = 12 bar
P_{water} = 12 bar
Water droplet number/m^3
Water droplet size (µm)
0.3 0.5 1.0 2.5 5.0 10.0
0 20 40 60 80 100

P_{air} = 14 bar

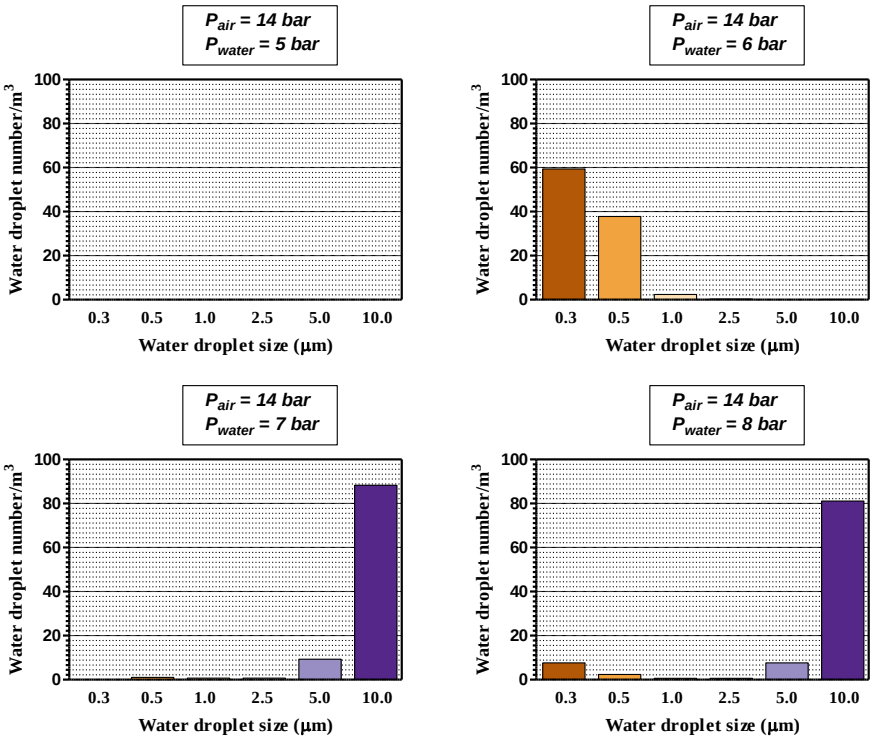
P_{air} = 14 bar
P_{water} = 5 bar
P_{air} = 14 bar
P_{water} = 6 bar
P_{air} = 14 bar
P_{water} = 7 bar
P_{air} = 14 bar
P_{water} = 8 bar
Water droplet number/m^3
Water droplet size (µm)
0.3 0.5 1.0 2.5 5.0 10.0
0 20 40 60 80 100

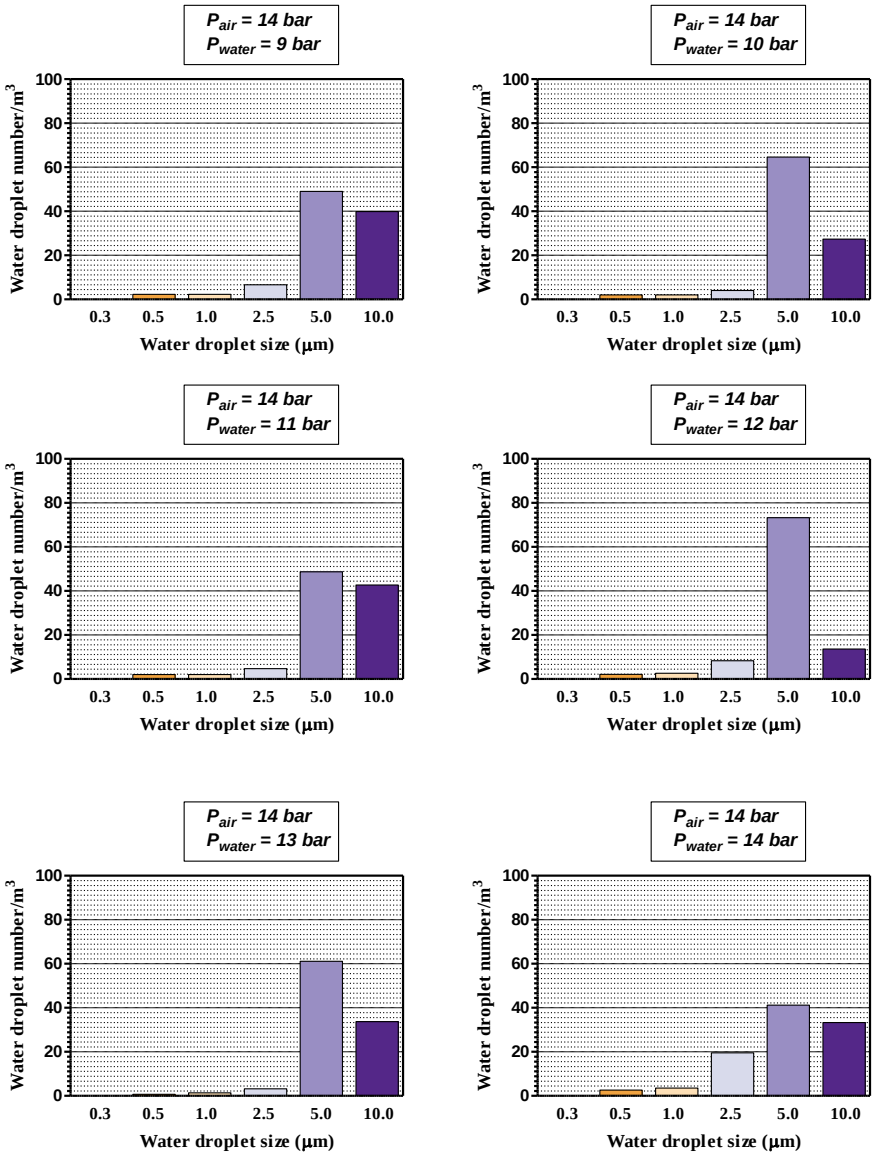
P_{air} = 14 bar
P_{water} = 9 bar
P_{air} = 14 bar
P_{water} = 10 bar
P_{air} = 14 bar
P_{water} = 11 bar
P_{air} = 14 bar
P_{water} = 12 bar
P_{air} = 14 bar
P_{water} = 13 bar
P_{air} = 14 bar
P_{water} = 14 bar
Water droplet number/m^3
0
20
40
60
80
100
0.3
0.5
1.0
2.5
5.0
10.0
Water droplet size (µm)